
Numerical Analyzes and Experimental Investigations of Air Foil Journal Bearings

Zur Erlangung des akademischen Grades Doktor-Ingenieur (Dr.-Ing.)
Genehmigte Dissertation von Marcel Mahner aus Marburg
Tag der Einreichung: 02.02.2021, Tag der Prüfung: 12.05.2021

1. Gutachten: Prof. Dr.-Ing. Bernhard Schweizer
2. Gutachten: Prof. Dr.-Ing. Wilfried Becker
Darmstadt – D17



TECHNISCHE
UNIVERSITÄT
DARMSTADT

Mechanical Engineering
Department
Institute of Applied
Dynamics

Numerical Analyzes and Experimental Investigations of Air Foil Journal Bearings

Accepted doctoral thesis by Marcel Mahner

1. Review: Prof. Dr.-Ing. Bernhard Schweizer
2. Review: Prof. Dr.-Ing. Wilfried Becker

Date of submission: 02.02.2021

Date of thesis defense: 12.05.2021

Darmstadt – D17

Bitte zitieren Sie dieses Dokument als:

URN: urn:nbn:de:tuda-tuprints-185925

URL: <http://tuprints.ulb.tu-darmstadt.de/id/eprint/18592>

Dieses Dokument wird bereitgestellt von tuprints,

E-Publishing-Service der TU Darmstadt

<http://tuprints.ulb.tu-darmstadt.de>

tuprints@ulb.tu-darmstadt.de

CC-BY-NC-ND 4.0 International

For my grandma Lore

Erklärungen laut Promotionsordnung

§8 Abs. 1 lit. c PromO

Ich versichere hiermit, dass die elektronische Version meiner Dissertation mit der schriftlichen Version übereinstimmt.

§8 Abs. 1 lit. d PromO

Ich versichere hiermit, dass zu einem vorherigen Zeitpunkt noch keine Promotion versucht wurde. In diesem Fall sind nähere Angaben über Zeitpunkt, Hochschule, Dissertationsthema und Ergebnis dieses Versuchs mitzuteilen.

§9 Abs. 1 PromO

Ich versichere hiermit, dass die vorliegende Dissertation selbstständig und nur unter Verwendung der angegebenen Quellen verfasst wurde.

§9 Abs. 2 PromO

Die Arbeit hat bisher noch nicht zu Prüfungszwecken gedient.

Darmstadt, 02.02.2021

M. Mahner

Preface

This thesis is a synopsis of the subsequent publications in peer-reviewed journals:

- I M. Mahner, P. Li, A. Lehn, B. Schweizer, Numerical and Experimental Investigations on Preload Effects in Air Foil Journal Bearings. ASME. J. Eng. Gas Turbines Power. March 2018; 140(3): 032505. [1]
- II M. Mahner, A. Lehn, and B. Schweizer, Thermogas- and thermohydrodynamic simulation of thrust and slider bearings: Convergence and efficiency of different reduction approaches. Tribology International, 2016. 93: pp. 539-554. [2]
- III M. Mahner, M. Bauer, and B. Schweizer, Numerical Analyzes and Experimental Investigations on the Fully-Coupled Thermo-Elasto-Gasdynamical Behavior of Air Foil Journal Bearings, Mechanical Systems and Signal Processing 149 (2021): 107221. [3]
- IV M. Mahner, M. Bauer, A. Lehn, B. Schweizer, An experimental investigation on the influence of an assembly preload on the hysteresis, the drag torque, the lift-off speed and the thermal behavior of three-pad air foil journal bearings. Tribology International, 2019. vol. 137: pp. 113-126. [4]

These publications are based on the work which has been accomplished during my occupation as a research assistant at the Institute of Applied Dynamics at the Technical University of Darmstadt.

Zusammenfassung

Zur Lagerung schnelldrehender Rotoren in Turbomaschinenanwendungen werden häufig radiale Folien-Luftlager eingesetzt. Wie im Fall hydrodynamischer Öllager, treten auch bei Folien-Luftlagern unter Umständen subharmonische Schwingungen sowie durch den Fluidfilm induzierte Instabilitäten des Rotors auf. Zur Reduktion der Amplitude dieser subharmonischen Schwingungen und zur Steigerung der kritischen Drehzahl, bei der erstmals fluidfilminduzierte Instabilitäten auftreten, werden die radialen Folien-Luftlager häufig vorgespannt. Im Rahmen dieser Arbeit wird der Einfluss einer Montagevorspannung auf das thermo-elasto-gasdynamische Verhalten radialer Dreiflächen-Folien-Luftlager numerisch und experimentell untersucht. Das dreidimensionale thermo-elasto-gasdynamische Lagermodell beinhaltet die Beschreibung der Deformation von Top- und Bumpfoil sowie die Berechnung der Druck- und Temperaturverteilung im Luftfilm sowie die Temperaturverteilung in den umgebenden Komponenten. Letzteres umfasst den Rotor, das Lagergehäuse sowie das Top- und Bumpfoil. Um den Berechnungsaufwand zur Lösung des sich ergebenden nichtlinearen integro-partiellen Differentialgleichungssystems zu reduzieren, werden verschiedene Verfahren zur mathematischen Reduktion der dreidimensionalen Energiegleichung und der verallgemeinerten Reynoldsgleichung angewendet und im Hinblick auf die Berechnungszeit und den numerischen Fehler miteinander verglichen. Die sich ergebenden Gleichungen werden mithilfe der Finite-Elemente-Methode gelöst. Zur Validierung der Berechnungsergebnisse werden Messungen auf zwei unterschiedlichen Prüfständen durchgeführt. Mithilfe des ersten Prüfstands - dem Hystereseprüfstand - werden Hysteresekurven verschieden stark vorgespannter radialer Dreiflächen-Folien-Luftlager bei stehendem Lagerzapfen gemessen. Das numerische Modell der Folienstruktur wird durch einen Vergleich der gemessenen und berechneten Hysteresekurven, Steifigkeiten und Reibungsverlusten (Dämpfungen) validiert. Mithilfe eines zweiten Prüfstands - dem automatisierten Hochgeschwindigkeitsprüfstands - wird der Einfluss der Montagevorspannung auf das Reibmoment und auf das thermische Verhalten von radialen Dreiflächen-Folien-Luftlagern untersucht. Um das thermische Modell des Dreiflächen-Folien-Luftlagers zu validieren, werden die gemessenen und berechneten Lagertemperaturen miteinander verglichen.

Abstract

Self-acting air foil journal bearings are an important component in high-speed, oil-free turbomachinery applications. For rotors supported in air foil journal bearings, subharmonic vibrations and fluid-film induced instabilities of the rotor-bearing system may occur. In order to decrease the amplitude of these subharmonic vibrations and to increase the onset speed of the fluid-film induced instabilities, a preload is often introduced in air foil journal bearings. In this study, the effect of an assembly preload on the thermo-elasto-gasdynamics behavior of a three-pad air foil journal bearing is investigated numerically and experimentally. The 3D thermo-elasto-gasdynamics bearing model comprises the description of bump and top foil deflection and the calculation of the pressure and temperature distribution in the air film as well as the temperature distributions in the surrounding structure, namely in the rotor, in the bearing sleeve and in the top and bump foil. Temperature distributions in the air film and in the surrounding structure are obtained from the 3D energy equation and appropriate heat equations. To reduce the computational effort for the solution of the governing system of nonlinear integro-partial differential equations, different approaches for a mathematical reduction of the 3D energy equation and the generalized Reynolds equation are applied and compared with respect to computation time and accuracy. The governing equations are solved by the finite element method. In order to validate the numerical results, different experiments are accomplished on two different test rigs. Using the first test rig - the hysteresis device - hysteresis curves of differently preloaded three-pad air foil journal bearings are measured at zero running speed. The numerical model of the elastic foil structure is validated by a comparison between measured and predicted hysteresis curves, foil structural stiffness and frictional loss (damping). On a second test rig - the automated high-speed test rig - the effect of the assembly preload on the drag torque and on the thermal behavior of three-pad air foil journal bearings is investigated experimentally. For the purpose of validating the thermal model of the preloaded three-pad air foil journal bearing, measured and predicted bearing temperatures are compared.

Acknowledgments

Firstly, I like to thank my academic supervisor Prof. Dr.-Ing. Bernhard Schweizer for the opportunity to write this work and for introducing me to the air foil bearing research. I am grateful for your support during my occupation at your institute and in the time hereafter.

I would like to thank Prof. Dr.-Ing. Wilfried Becker for reviewing this work. During the master's course, it were your lectures in which I learned the theoretical and mathematical fundamentals I needed to build the structural mechanics part of the numerical model presented in this work.

I would like to express my deep appreciation to Prof. Dr.-Ing. Richard Markert. During your lectures, you inspired my fascination for the field of structural dynamics and rotor-dynamics. In these lectures, I received the fundamental education I needed to work in this field of research. I deeply acknowledge your support and the valuable discussions during my occupation at the institute and in the time hereafter. Thank you also for the motivating words in the final phase of finishing this thesis.

I would like to thank my former colleagues at the Institute of Applied Dynamics for the many interesting discussions and the great time. I would like to especially thank Maria Rauck and Helga Lorenz for always providing me assistance in all organizational and accounting requests. For their technical support in the laboratory, I would like to thank Jochen Ott and Wolfgang Hess. I would like to thank Andreas Lehn for introducing me to the theory of air foil thrust bearings and for the many valuable discussions during our common time at the institute.

I would like to express my deepest appreciation to my former colleague Marcel Bauer. I really enjoyed our valuable, interesting and productive discussions in our shared office. Thank you for your support during the setup of the foil bearing test rig, during the accomplishments of the experiments and for your support in building a foil bearing manufacturing. I am thankful for still having you as a discussion partner and a dear friend.

Finally, I would like to thank my parents for their love, their assistance and their motivating words. I would like to thank my wife and my daughter for their love and support, although I spent a lot of our free time by finishing this work. I am for ever thankful for your understanding and motivation.

Contents

Preface	vii
Acknowledgments	xiii
List of Publications	xvii
Authors' Contributions	xxi
Nomenclature	xxiii
1. Introduction	1
1.1. Technology of Air Foil Bearings	1
1.2. Preload Concepts for Air Foil Journal Bearings	3
1.3. Objectives and Structure of the Thesis	5
1.3.1. Outline of Paper I	8
1.3.2. Outline of Paper II	14
1.3.3. Outline of Paper III	19
1.3.4. Outline of Paper IV	23
2. Results	29
2.1. Preload Effects on the Bearing Stiffness and Damping	29
2.1.1. Foil Structural Stiffness and Damping at Zero Running Speed	29
2.1.2. Overall Bearing Stiffness and Damping in Airborne Operation	33
2.2. Preload Effects on the Thermal Behavior	34
2.2.1. Efficient Reduction Approaches for Fluid Film Bearings	34
2.2.2. Thermo-Elasto-Gasdynamic Behavior of Preloaded Air Foil Journal Bearing	36
2.3. Preload Effects on the Drag Torque and on the Lift-Off-Speed of Air Foil Journal Bearings	39
3. Conclusion and Outlook	45

References	47
Appendix A. Effect of the Bump Foil Initial Radius on the Bearing Performance	53
Appendix B. Effect of the Bump Height on the Bearing Performance	57
Paper I	63
Paper II	73
Paper III	91
Paper IV	125

List of Publications

The subsequent list gives an overview of all publications by the author of this synopsis, including conference and journal papers as well as the bachelor and master thesis. The four publications which are subject of this synopsis are colored in green and numerated as paper I-IV.

M. Mahner, Qualifizierung und Optimierung einer Farbauftragseinrichtung zur Durchführung von Machbarkeitsuntersuchungen zum Mikroprägen, Bachelor Thesis, 2011, DHBW Mannheim.

M. Mahner, Berechnung der Temperaturverteilung eines mit Luft betriebenen Axiallagers, Master Thesis, 2013, Technical University of Darmstadt.

O. Alber and M. Mahner (2014), Description of sub- and superharmonic motion in rotor-stator contact using Fourier series, ZAMM - Journal of Applied Mathematics and Mechanics / Zeitschrift für Angewandte Mathematik und Mechanik 94(11): 945-950.

M. Mahner, A. Lehn, and B. Schweizer, Reduction Approaches for Thermogasdynamic Lubrication Problems. Proc. Appl. Math. Mech., 2015. 15: pp. 405-406.

Paper II: M. Mahner, A. Lehn, and B. Schweizer, Thermogas- and thermohydrodynamic simulation of thrust and slider bearings: Convergence and efficiency of different reduction approaches, Tribology International, 2016, 93: pp. 539-554. [2]

M. Mahner, P. Li, A. Lehn and B. Schweizer, Elastogasdynamic Model for Air Foil Journal Bearings: Hysteresis Prediction Including Preloading Effects, STLE 71st Annual Meeting and Exhibition, 2016, Las Vegas, Nevada, USA.

A. Lehn, M. Mahner, and B. Schweizer, Elasto-gasdynamics modeling of air foil thrust bearings with a two-dimensional shell model for top and bump foil, *Tribology International*, 2016, 100: pp. 48-59.

A. Lehn, M. Mahner, and B. Schweizer, A Contribution to the Thermal Modeling of Bump Type Air Foil Bearings: Analysis of the Thermal Resistance of Bump Foils, *Journal of Tribology*, 2017, 139(6): pp. 061702-061702-10.

M. Mahner, P. Li, A. Lehn and B. Schweizer, Numerical and Experimental Investigations on Preload Effects in Air Foil Journal Bearings, *ASME Turbo Expo: Power for Land, Sea, and Air*, Volume 7A (2017): Structures and Dynamics.

Paper I: M. Mahner, P. Li, A. Lehn, B. Schweizer, Numerical and Experimental Investigations on Preload Effects in Air Foil Journal Bearings, *ASME. J. Eng. Gas Turbines Power*, March 2018, 140(3): 032505. [1]

A. Lehn, M. Mahner, and B. Schweizer, A thermo-elasto-hydrodynamic model for air foil thrust bearings including self-induced convective cooling of the rotor disk and thermal runaway, *Tribology International*, 2018, 119: p. 281-298.

A. Lehn, M. Mahner, and B. Schweizer, Characterization of static air foil thrust bearing performance: an elasto-gasdynamics analysis for aligned, distorted and misaligned operating conditions. *Arch Appl Mech* (2018) 88:705–728.

Paper IV: M. Mahner, M. Bauer, A. Lehn, B. Schweizer, An experimental investigation on the influence of an assembly preload on the hysteresis, the drag torque, the lift-off speed and the thermal behavior of three-pad air foil journal bearings, *Tribology International*, 2019, vol. 137: pp. 113-126. [4]

P. Zeise, M. Mahner, M. Bauer, M. Rieken, and B. Schweizer, A Reduced Model for Air Foil Journal Bearings for Time-Efficient Run-Up Simulations, *Proceedings of the ASME Turbo Expo 2019: Turbomachinery Technical Conference and Exposition*. Volume 7B: Structures and Dynamics. Phoenix, Arizona, USA. June 17–21, 2019, V07BT34A004,

ASME.

M. Rieken, M. Mahner, and B. Schweizer, Thermal Optimization of Air Foil Thrust Bearings Using Different Foil Materials, Proceedings of the ASME Turbo Expo 2019: Turbomachinery Technical Conference and Exposition. Volume 7B: Structures and Dynamics. Phoenix, Arizona, USA. June 17–21, 2019. V07BT34A031, ASME.

P. Zeise, M. Mahner, M. Bauer, M. Rieken, and B. Schweizer, A reduced semi-analytical gas foil bearing model for transient run-up simulations, 12th International Conference on Vibrations in Rotating Machinery (2020), London, CRC Press.

Paper III: M. Mahner, M. Bauer, and B. Schweizer, Numerical Analyzes and Experimental Investigations on the Fully-Coupled Thermo-Elasto-Gasdynamical Behavior of Air Foil Journal Bearings, Mechanical Systems and Signal Processing 149 (2021): 107221. [3]

The authors' contributions to the four above in green marked publications, which are subject of this synopsis, are summarized next.

Authors' Contributions

Paper I: M. Mahner, P. Li, A. Lehn, B. Schweizer, Numerical and Experimental Investigations on Preload Effects in Air Foil Journal Bearings, ASME. J. Eng. Gas Turbines Power, March 2018, 140(3): 032505.

Marcel Mahner: Conception; Literature review; Formal analysis; Investigation; Methodology; Software; Mechanical design of test rig; Conduction of experiments; Validation; Visualization; Writing - original draft; Writing - review & editing.

Pu Li: Support in the mechanical design of the test rig; Support in the conduction of experiments.

Andreas Lehn: Support in the conception phase; Proofreading.

Bernhard Schweizer: Conception; Methodology; Proofreading.

Paper II: M. Mahner, A. Lehn, and B. Schweizer, Thermogas- and thermohydrodynamic simulation of thrust and slider bearings: Convergence and efficiency of different reduction approaches, Tribology International, 2016, 93: pp. 539-554.

Marcel Mahner: Conception; Literature review; Formal analysis; Investigation; Methodology; Software; Verification; Visualization; Writing - original draft; Writing - review & editing.

Andreas Lehn: Conception; Methodology; Literature Review; Proofreading.

Bernhard Schweizer: Conception; Methodology; Proofreading.

Paper III: M. Mahner, M. Bauer, and B. Schweizer, Numerical Analyzes and Experimental Investigations on the Fully-Coupled Thermo-Elasto-Gasdynamic Behavior of Air Foil Journal Bearings, Mechanical Systems and Signal Processing 149 (2021): 107221.

Marcel Mahner: Conception; Literature review; Formal analysis; Investigation; Methodology; Software; Validation; Visualization; Writing - original draft; Writing - review & editing.

Marcel Bauer: Investigation; Proofreading.

Bernhard Schweizer: Conception; Methodology; Proofreading.

Paper IV: M. Mahner, M. Bauer, A. Lehn, B. Schweizer, An experimental investigation on the influence of an assembly preload on the hysteresis, the drag torque, the lift-off speed and the thermal behavior of three-pad air foil journal bearings, Tribology International, 2019, vol. 137: pp. 113-126.

Marcel Mahner: Conception; Literature review; Methodology; Mechanical Design of test rig; Conduction of Experiments; Investigation; Software; Verification; Visualization; Writing - original draft; Writing - review & editing.

Marcel Bauer: Conduction of Experiments; Investigation; Proofreading.

Andreas Lehn: Support in the conception phase.

Bernhard Schweizer: Conception; Methodology; Proofreading.

Nomenclature

A_{pad}	pad area [m ²]
E	Young's modulus [N/m ²]
F_b	bearing load [N]
F_y, F_z	resulting fluid film forces on the rotor in y - and z -direction [N]
F_b	bearing load [N]
$F_{s_{hor}}$	horizontal force on the rotor shaft [N]
H	thickness of top and bump foil [m]
M	bending moment about the z -axis, related to the beamshell width [N]
N	normal force, related to the beamshell width [N/m]
Q	shear force, related to the beamshell width [N/m]
$\Delta l_{\bar{z}}$	dimensionless length of a finite element across the fluid film
$\bar{e}_r, \bar{T}, \bar{e}_r, \bar{p}$	Relative error in temperature and pressure
\dot{q}	heat flux [W/m ²]
c_p	isobaric heat capacity [J/(kg K)]
e_r	rotor eccentricity [m]
k	heat conductivity [W/(m ² K)]
p_y, p_z	pressure on the beamshell in y and z -direction [Pa]
r_b	bump foil radius [m]

r_i	bearing sleeve inner radius [m]
r_r	rotor radius [m]
r_t	top foil radius [m]
s	material coordinate [m]
$s_{b_{hor}}$	relative displacement bewteen shaft and bearing sleeve [m]
u	displacement in the global y - or z -direction [m]
x_a, y_a, z_a	longitudinal, transversal and cross-film coordinate of the fluid film [m]
$\Delta\varphi$	rotation about the global x -axis [rad]
Ω	rotor angular velocity [s^{-1}]
α_s	shear correction factor
γ_r	angle under which the bearing load is applied [rad]
κ	beamshell bending strain [m^{-1}]
ν	Poisson's ratio
ψ	angle between the rotor normal and the z -axis [rad]
ε, γ	beamshell normal and shear strain
η	dynamic viscosity [Pa s]
Ω	angular velocity of the shaft ($\Omega = n\pi/30$) [s^{-1}]
φ_0, φ	orientation of the beamshell cross section about the global x -axis in the initial and in the current configuration [rad]
h_i	gap function of the i -th bearing pad [m]
i	$i = 1, 2, 3$ indicating the three top foils
L_t, b_t	top foil length and width [m]
n	rotational speed of the shaft [rpm]
p_a	ambient pressure [Pa]

p_i pressure in the i -th bearing pad [Pa]

r_r, r_i rotor radius and bearing sleeve inner radius [m]

1. Introduction

In this section, the reader is firstly introduced to the air foil bearing technology. This comprises the description of the general function, design and industrial application as well as a discussion of the advantages and disadvantages of air foil journal bearings. Afterwards, different preload concepts from literature are presented and discussed in context of the assembly preload proposed within this work. Then, the objectives of this thesis are motivated and the structure of the thesis is explained. Since this thesis is a synopsis of the papers listed above, the content of the papers will be outlined and their contribution to the thesis objectives will be presented.

1.1. Technology of Air Foil Bearings

Air foil bearings are self-acting aerodynamic bearings. They are applied as thrust or journal bearings. In contrast to rigid air bearings, an elastic foil structure is placed between the journal or rotor thrust surface and the bearing surface. The foil structure consists of a top foil and an underlying setup which induces compliance and damping to the foil bearing, see Fig. 1.1. When the shaft rotates, the air sticking on the rotor is trapped into the convergent air gap between the smooth top foil and the rotor. This leads to a pressure built-up which balances the load acting on the rotor. The pressure also acts on the top foil causing a deformation of the foil structure. The displacement of the rotor under the acting load as well as the deformation of the foil structure generate the resultant air gap.

According to the design of the compliant structure different air foil bearing types are distinguished. The subsequent list gives an overview of common foil bearing types [5, 6]:

- Bump-type foil bearings, see Fig. 1.1
- Mesh-type foil bearings
- Cantilever-type foil bearings
- Leaf-type foil bearings

- Compression spring foil bearings

At present, bump-type foil bearings are one of the most common foil bearing types. Bump-type foil journal bearings consist of one or several pairs of bump and top foils, see Fig. 1.1. The bump foil is a corrugated foil which induces compliance and friction to the bearing [4]. While circular one-pad air foil journal bearings show a high load capacity, three-pad designs are characterized by an improved whirl stability [7]. In this study, preloaded three-pad bump-type foil journal bearings will be investigated.

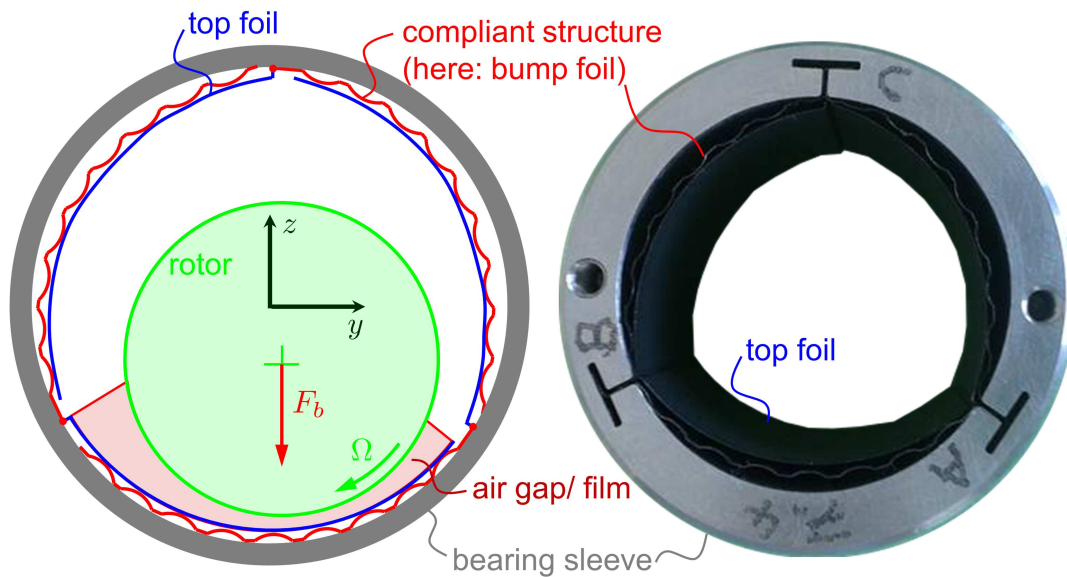


Figure 1.1.: Bump-type three-pad air foil journal bearing with top and bump foils

Air foil bearings have many advantages compared to oil lubricated bearings which arise mainly from the omission of oil and from the elastic foil structure [4]. Air foil bearings are environmentally friendly [8] and can be used in applications where an oil-free medium is mandatory like in compressors for fuel cells [4]. Incorporating air bearings instead of oil bearings in machines can significantly reduce the maintenance effort. Advantageously, an oil supply system is not necessary [9]. Furthermore, the maximum operating temperature of oil bearings is limited due to oil degradation, see [8]. In contrast, the operating temperature of air bearings is only restricted by the maximum tolerable temperature of the surrounding materials and the coatings of the top foil and the rotor [4].

These advantages of air foil bearings are countered by several downsides [4]. Compared to oil bearings of the same nominal size, air foil bearings have a smaller load capacity [6]. This is caused by the smaller air viscosity. Therefore, rotors supported in air foil bearings must either have a larger journal diameter or operate at higher speeds [4]. Thus, air foil bearings are mainly used in low load, high speed applications like in micro-gas turbines, see e.g. [10].

Owing to the low heat capacity of air, the thermal behavior of air foil bearings is a crucial issue, see e.g. [6, 4]. Although the drag torque of air bearings is rather low after rotor lift-off, the low heat capacity of air can lead to a significant increase in the bearing temperature [4]. The temperature increase may lead to a thermal instability resulting in a catastrophic bearing failure, see e.g. [11, 12].

In air foil journal bearings, sliding friction between the top foil and the rotor occurs until the rotor lifts off. The boundary and mixed lubrication occurring before rotor lift-off lead to large startup and shutdown torques as well as to wear on the top foil and the rotor, see e.g. [13].

1.2. Preload Concepts for Air Foil Journal Bearings

Rotors supported by air foil journal bearings often show subharmonic vibrations and fluid film induced instabilities, see e.g. [14]. Figure 1.2 shows a measured Campbell diagram of a turbo compressor supported in two air foil journal bearings. As can be seen from the figure, distinctive subharmonic vibrations occur besides the unbalance induced synchronous oscillations. These subharmonic vibrations can be traced back either to the non-linear behavior of the foil structure or of the air film. The air film induced subharmonic vibrations are also known as whirl/whip phenomena. As shown in Fig. 1.2, the amplitudes of the fluid film induced whirl/whip oscillations are moderate compared to the synchronous vibrations. The whirl/whip vibrations may lead to an instability of the rotor-bearing system at higher rotational speeds leading to large rotor amplitudes which may cause a rotor failure.

The application of a mechanical preload in air foil journal bearings can significantly reduce the amplitudes of sup- and superharmonic motions. Furthermore, the onset speed of the rotor instabilities may be increased, as shown, for example, by Sim et al. [15]. In this study, a mechanical preload is introduced to a three-pad air foil journal bearing by using top and bump foils whose nominal, initial radii (r_t , r_b) are larger than the inner radius of the bearing sleeve r_i and the outer radius of the shaft r_s [1], see the initial configuration of top and bump foil in Fig. 1.3. This initial configuration refers to the undeformed state of top and bump foil after their manufacturing [1]. During the assembly process of top

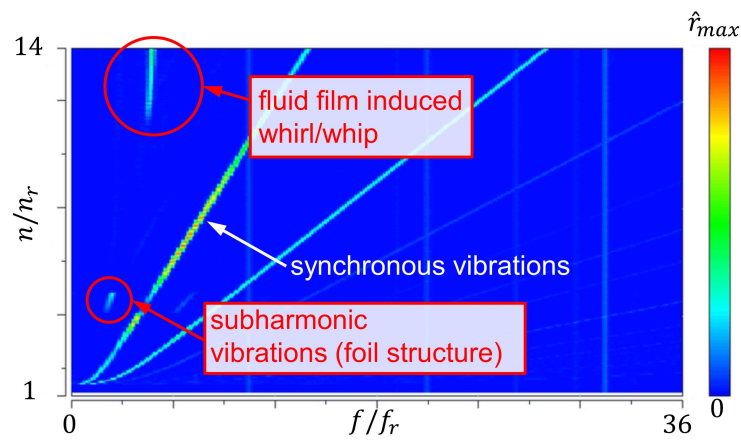


Figure 1.2.: Measured Campbell diagram of a turbo compressor supported in two air foil journal bearings

and bump foil, the foils are elastically bended into the bearing sleeve. In order to assemble the air foil journal bearing on the shaft, the top and bump foils are pushed against the bearing sleeve. After this assembly force is released, the top and bump foils will elastically unbend and the top foils will contact the rotor. This deformed state of top and bump foil is referred to as the assembly configuration, see Fig. 1.3. In the assembly configuration, the top foil contacts the shaft surface and consequently there is no initial clearance between the top foil and the shaft [1], see Fig. 1.3. Due to the described assembly preload the elastic foil structural stiffness and damping increase [1].

The assembly preload investigated in this study differs from other preloading mechanisms of air foil journal bearings presented in literature [11, 17, 18, 19, 10, 20, 21, 22]. In these studies the preload is introduced by using shims underneath the foil structure [10, 20], providing a lobe in the bearing sleeve inner contour [18, 19], actively displacing the bump foil in radial direction [21, 22, 23, 24] or by using an oversized shaft [11, 17]. These techniques either locally [18, 19, 10, 20, 21, 22, 23, 24], see Fig. 1.4a), or globally [11, 17, 23], see Fig. 1.4b), reduce the operating air film thickness leading to an increase in the air film stiffness. Additionally, the foil structural stiffness is increased slightly. The reduced bearing clearance significantly increases the risk of a thermal runaway induced by thermal and centrifugal growth of the rotor. The assembly preload presented in this study increases mainly the foil structural stiffness, while the bearing clearance is not affected.

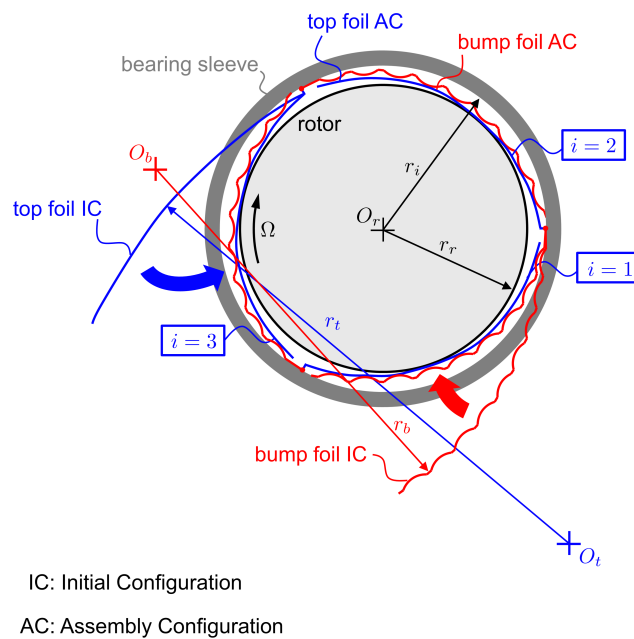


Figure 1.3.: Preloaded three-pad air foil journal bearing in the initial and in the assembly configuration [16, 1]

1.3. Objectives and Structure of the Thesis

In this thesis, the effect of an assembly preload on the thermo-elasto-gasdynamics behavior of a preloaded three-pad air foil journal bearing will be investigated numerically and experimentally. Therefore, a comprehensive 3D thermo-elasto-gasdynamics bearing model as well as two different bearing test rigs are developed.

Basically, this thesis is based on four major publications [1, 2, 3, 4]. In paper I-III [1, 2, 3] different aspects of the 3D thermo-elasto-gasdynamics bearing model are presented. The 3D thermo-elasto-gasdynamics bearing model comprises the description of bump and top foil deflection and the calculation of the pressure and temperature distribution in the air film as well as the temperature distribution in the surrounding structure, namely in the rotor, in the bearing sleeve and in the top and bump foil. Figure 1.5 illustrates the different modeling aspects and domains considering the example of a three-pad air foil journal bearing. The corresponding paper, in which the particular part of the numerical model is presented, is indicated in the figure.

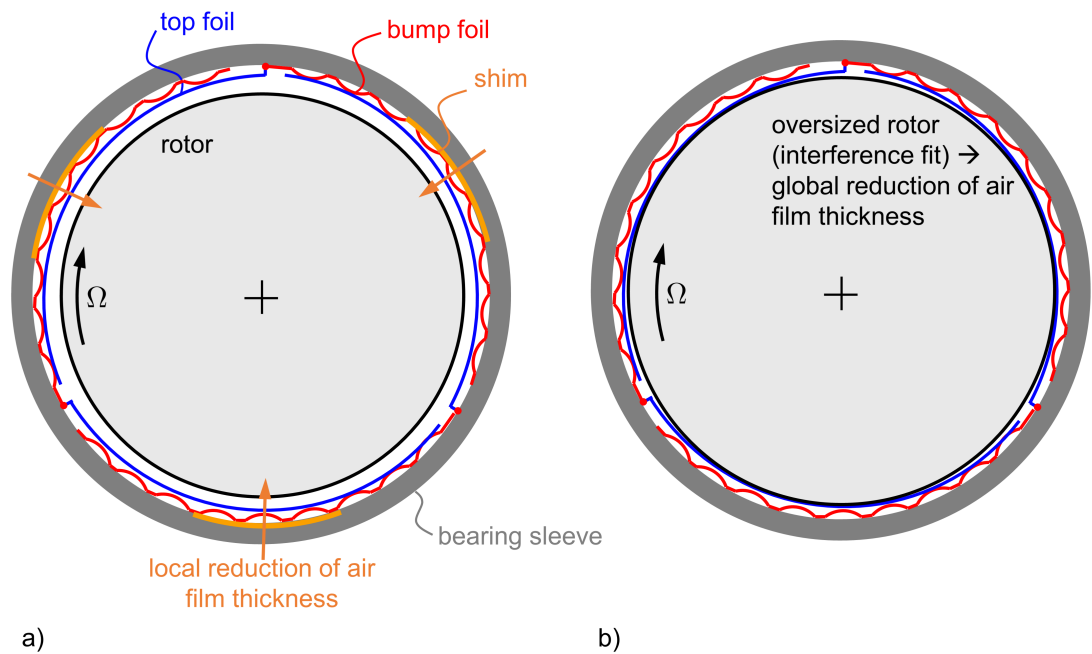


Figure 1.4.: Alternative preload techniques by using shims (a) or an oversized shaft (b)

As shown in Fig. 1.5, the elasto-gasdynamic bearing model is presented in paper I [1]. In this model, bump and top foil deflection are described by the beamshell theory according to Reissner [25]. Furthermore, the model considers the contact between bump and top foil as well as between bump foil and bearing sleeve using an augmented Lagrange approach as well as Coulomb's law of friction. The pressure distribution is described by the Reynolds equation for compressible fluids. The Reynolds equation and the structural mechanical equations of the foil structure are coupled by the gap function between top foil and rotor. In paper I, isothermal conditions are assumed first. The system of partial differential equations is solved by a finite element approach. For the purpose of validating the structural mechanical model of the elastic foil structure, hysteresis measurements are performed on a special test rig. Furthermore, the effect of the assembly preload on the bearing hysteresis, the foil structural stiffness and frictional loss (damping) as well as on the bearing drag torque are investigated numerically by a comparison of two differently preloaded three-pad air foil journal bearings. In addition, the overall bearing stiffness is evaluated for these bearings.

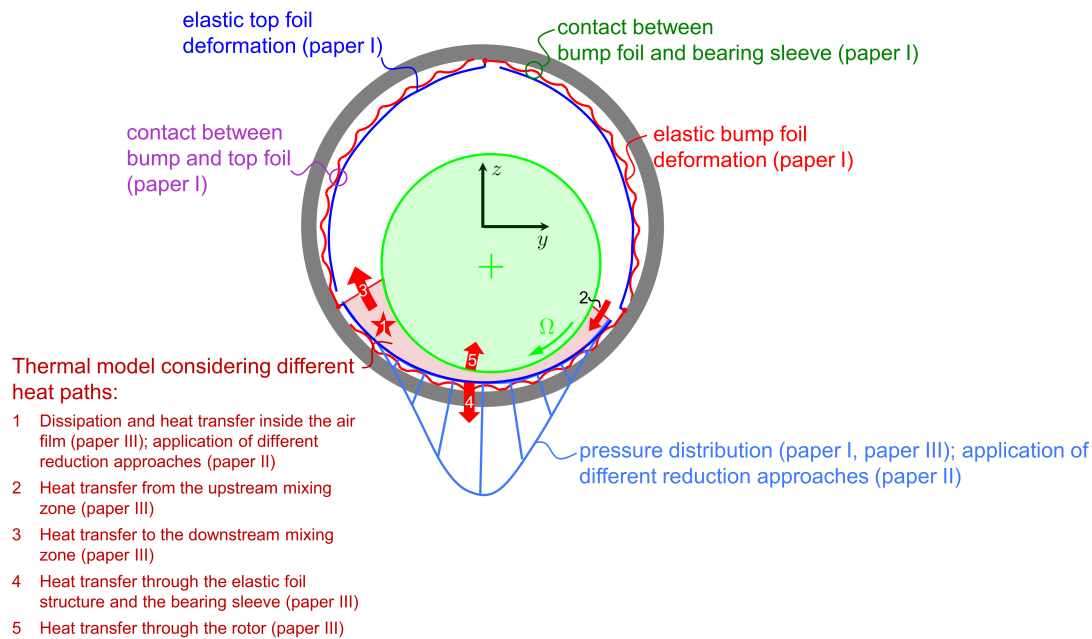


Figure 1.5.: Modeling aspects of a three-pad air foil journal bearing with specification of the corresponding paper, in which the particular part of the numerical model is presented

In order to describe the thermal behavior of air foil bearings, it is mandatory to solve the 3D energy equation in conjunction with the generalized Reynolds equation according to Dowson [26]. The solution of the governing system of nonlinear integro-partial differential equations requires a high computational effort and is often connected with numerical instabilities. Therefore, different reduction approaches for reducing the dimension of the governing equation system are presented in paper II [2]. These approaches are compared with respect to numerical efficiency, accuracy and convergence behavior using the examples of an air foil thrust bearing and an oil slider bearing. For the air foil thrust bearing, the foil structure is assumed to be rigid. Furthermore, simplified boundary conditions are applied to the 3D energy equation. The approach with the best numerical efficiency is applied in the thermo-elasto-gasdynamical air foil journal bearing model presented in paper III [3].

In paper III [3], the overall thermo-elasto-gasdynamics air foil journal bearing model is presented. To calculate the temperature distribution of the air foil journal bearing, the elasto-gasdynamics bearing model presented in paper I [1] is complemented by the 3D energy equation for the air film and appropriate heat equations for the surrounding structure, namely the rotor, the top and bump foil and the bearing sleeve. To account for the temperature induced change of density and viscosity across the air film, the generalized Reynolds equation according to Dowson is used in this study instead of the ordinary Reynolds equation for compressible fluids. The computational effort for the solution of the generalized Reynolds equation in conjunction with the 3D energy equation is reduced by transferring the Averaging Approach developed in paper II [2] to air foil journal bearings. While the bearing sleeve is modeled as a lumped thermal mass, 2D partial differential heat equations are used for the rotor, the top foil and for the bump foil. Furthermore, a model for the thermal contact resistance for the contact between bump foil and top foil as well as between bump foil and bearing sleeve are developed based on the formula derived by Lehn et al. [27]. The governing system of partial differential equations is solved by a finite element approach. An artificial diffusion approach is applied to reduce numerical instabilities – well known in connection with convection-diffusion problems. Using the developed 3D thermo-elasto-gasdynamics bearing model, the thermal behavior of a preloaded three-pad air foil journal bearing is investigated. The numerical model is validated using the measurement results presented in paper IV [4].

In paper IV [4], an automated high-speed test rig for air foil journal bearings is presented which can run at speeds up to 60,000 rpm. Using this test rig, the effect of the assembly preload on the bearing drag torque, the bearing lift-off speed and on the thermal behavior is investigated by a comparison of the measurement results of two differently preloaded three-pad air foil journal bearings. Furthermore, the foil structural stiffness and damping of these bearings are compared using the test rig presented in paper I [1].

Summarizing, the effect of the assembly preload on the thermo-elasto-gasdynamics model is studied using a comprehensive numerical model and two highly automated test rigs which are presented in papers I-IV. Figure 1.6 gives a schematic overview of the four papers and their contribution to the overall scientific question of the influence of the assembly preload on the thermo-elasto gasdynamics bearing behavior. In the subsequent sections, the numerical and experimental methods applied in the four papers are outlined.

1.3.1. Outline of Paper I

In paper I [1], an elasto-gasdynamics model of a three-pad air foil journal bearing is presented. The elasto-gasdynamics model incorporates the description of the gasdynamics

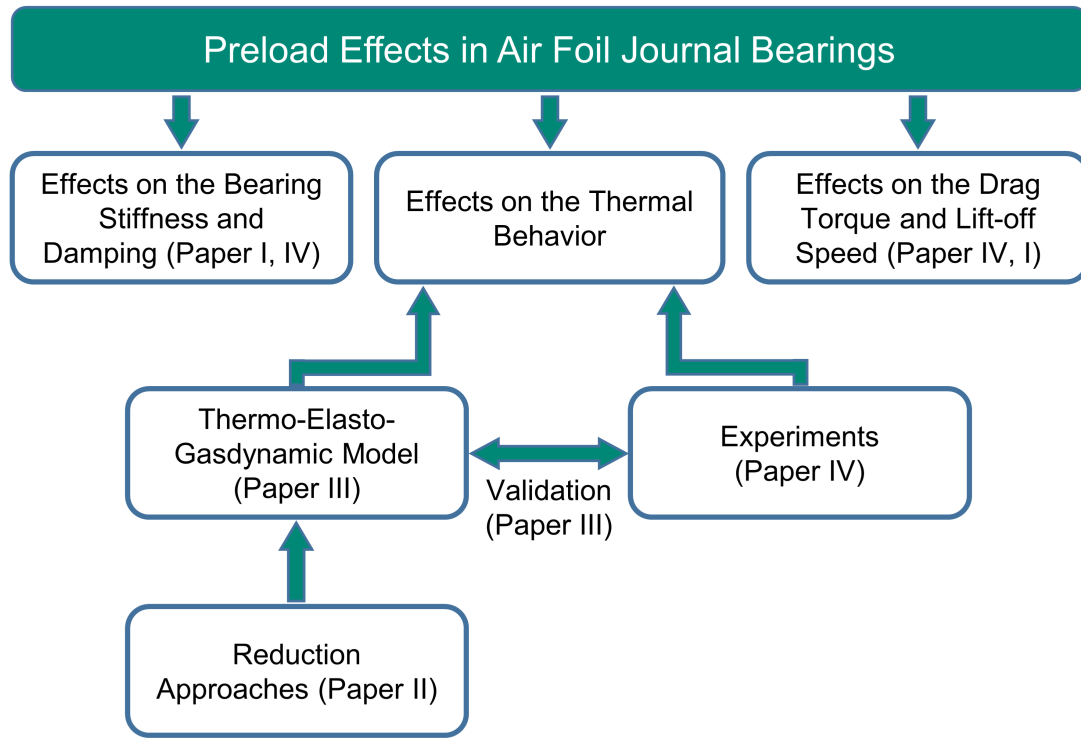


Figure 1.6.: Schematic Overview of the contribution of the four papers on the overall scientific question on the influence of the assembly preload

pressure distribution in the convergent gap between top foil and shaft as well as the description of the elastic deformation of bump and top foil. In paper I, thermal effects, which in general have a crucial influence on the bearing performance, will be neglected in order to focus on the effects arising from the elastic foil structure. Under this assumption, the pressure distribution in the gas film in the i -th bearing pad (length L_t , width b_t) is described by the Reynolds equation for compressible fluids [1]

$$\begin{aligned}
 & \frac{\partial}{\partial x_{a_i}} \left(\frac{1}{1 + \varepsilon_{t_i}} \frac{p_i h_i^3}{\eta_{a_i}} \frac{\partial p_i}{\partial x_{a_i}} \right) + \frac{\partial}{\partial y_{a_i}} \left(\frac{p_i h_i^3}{\eta_{a_i}} \frac{\partial p_i}{\partial y_{a_i}} \right) \\
 & = -6r_r \Omega \frac{\partial(p_i h_i)}{\partial x_{a_i}} \quad \forall i = 1, 2, 3
 \end{aligned} \tag{1.1}$$

rical nonlinearities. While the deformations are large, the membrane, bending and shear stress are assumed to be small [3]. Thus, linear elastic material behavior is considered [3]. Furthermore, Reissner-Mindlin kinematics are assumed. Based on the results obtained in [32, 33], the deformations are considered to be constant across the foil width. The plane strain theory is applied since the top and bump foil width is significantly larger than the foil height [3]. With these assumptions, the general 3D theory of elasticity is reduced to the nonlinear 1D beamshell theory according to Reissner, see [25, 34, 35, 1]. Using this theory, the deformation of bump and top foil at every material coordinate s is described by the two displacements u and v in the global y - and z -direction and by the rotation $\Delta\varphi = \varphi - \varphi_0$ about the global x -axis, where φ and φ_0 denote the orientation of the beamshell cross section about the global x -axis in the initial and in the current configuration [3]. The two displacements and the rotation are calculated from the following three coupled partial differential equations [3]

$$\frac{\partial}{\partial s} [N \cos(\varphi) + Q \sin(\varphi)] = -p_y(1 + \varepsilon), \quad (1.3)$$

$$\frac{\partial}{\partial s} [N \sin(\varphi) - Q \cos(\varphi)] = -p_z(1 + \varepsilon), \quad (1.4)$$

$$\frac{\partial M}{\partial s} = (1 + \varepsilon)Q - \gamma N, \quad (1.5)$$

which represent the equilibrium of forces in the y - and z -direction (Eqs. (1.3) and (1.4)) as well as the equilibrium of momentum about the x -axis (Eq. (1.5)), see Fig. 1.8. N , Q and M are the normal and the shear force as well as the bending moment about the global x -axis, see Fig 1.8. p_y and p_z denote the pressure on the beamshell in the global y - and z -direction. Note, that Eq. (1.3)-(1.5) are valid for top and bump foil. In order to distinguish between bump and top foil hereafter, the subscripts b and t are introduced in paper III [3]. In general, the pressures p_{y_t} and p_{z_t} on the top foil result from the aerodynamic pressure p and the shear stress in the air film. For the investigated three-pad air foil journal bearing, the top foil deformation due to the shear stress is negligible. Hence, only the aerodynamic pressure p acting on the top foil is considered in this study. The two-dimensional pressure distribution p_i obtained from the Reynolds equation (1.1) for each bearing pad is averaged across the bearing width according to [3]

$$\bar{p}_i = \frac{1}{b_t} \int_0^{b_t} p_i dy_{a_i} \quad \forall i = 1, \dots, 3. \quad (1.6)$$

From the averaged pressure \bar{p}_i , the pressure components p_{y_t} and p_{z_t} are calculated.

The leading edge of bump and top foil are assumed as free ends whereas the trailing edges are mounted in suspensions, see Fig. 1.9. Bump and top foil are restricted to move

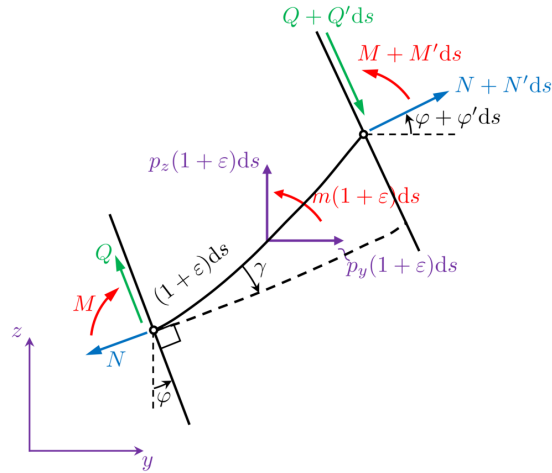


Figure 1.8.: Free body diagram of an infinitesimal beamshell segment [25, 1]

in normal and in tangential direction at the trailing edges. The deformation of the top and bump foil mounting suspension due to bending moments is taken into account. The mounting suspension is modeled as a torsional spring with the stiffness k_φ , see Fig. 1.9.

The partial differential equations (1.3)-(1.5) are formulated for each bump and segment of the three bump foils. At the intersection of bump and segment, appropriate coupling conditions for the stress resultants N , Q and M as well as for the kinematic variables u , v and φ are applied, see Fig. 1.10.

The contact between bump and top foil as well as the contact between bump foil and bearing sleeve are modeled by a node-to-surface approach. The no-penetration condition in normal direction is enforced using an augmented Lagrange approach [36, 35]. In tangential direction, the friction force is calculated using Coulomb's law of friction. The signum function in the friction law is regularized using an elastic slip approach, see Wriggers [35].

For the prediction of the static hysteresis of air foil journal bearings, the rotational speed of the shaft is set to zero ($\Omega = 0$). Therefore, the shaft contacts the top foil surface since the air film is not considered. Due to friction reduction coatings on the top foil and the shaft, their contact is assumed to be frictionless. The no penetration condition between the shaft and the top foil is enforced using a penalty approach [3].

The governing set of differential and algebraic equations is solved using a fully coupled nonlinear finite element approach.

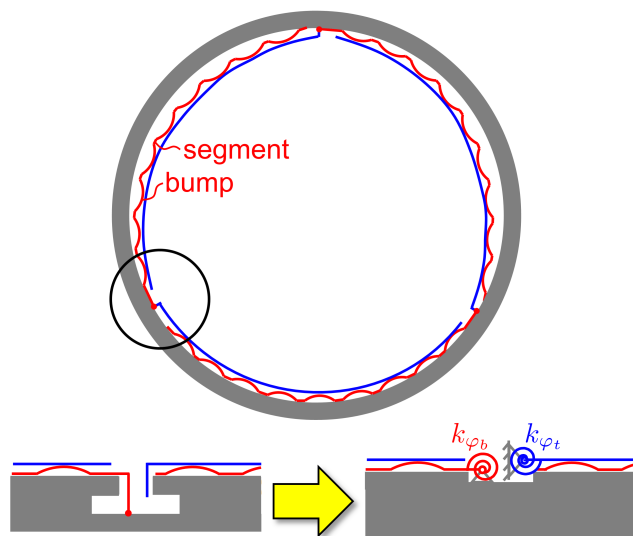


Figure 1.9.: Location of the top and bump foil mounting suspensions as well as illustration of the boundary conditions of top and bump foil [3]

In paper I [1], the effect of the assembly preload on the static hysteresis and on the aerodynamic performance of a preloaded three-pad air foil journal bearing is investigated numerically using the elasto-gasdynamics model described above. Therefore, the stiffness, the damping and the drag torque of two differently preloaded bearings are compared. While the bearing sleeve and the bump foils have the same dimensions, the two air foil journal bearings differ in the nominal radius of the top foil.

In order to analyze the stiffness and damping of the foil structure at zero running speed, hysteresis simulations are performed by quasi-statically applying a harmonic displacement to the rotor shaft. By plotting the resulting reaction force on the shaft over the shaft displacement, hysteresis curves are obtained. The slope of these curves and the area enclosed by the hysteresis loops correspond with the foil structural stiffness and the energy dissipation during one hysteresis cycle. The latter mainly determines the bearing damping.

Furthermore, hysteresis curves at a rotational speed of $n = 60,000$ rpm are calculated. By a comparison of the static hysteresis curves at zero running speed with the curves at $n = 60,000$ rpm, conclusion on the effect of the air film on the overall bearing stiffness and damping are drawn. In addition, the drag torque at different bearing loads for the two differently preloaded bearing are compared based on the numerical results.

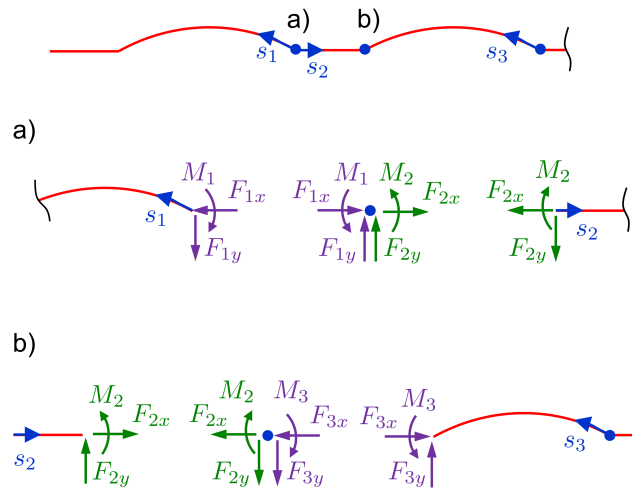


Figure 1.10.: Free body diagram at the leading (a) and the trailing (b) edge of bump and segment [3]

For the purpose of validating the elastic model of the foil structure, load-deflection tests are accomplished experimentally and compared with numerically predicted hysteresis curves. The measurements are performed on an automated hysteresis device shown in Fig. 1.11. In this device, the air foil journal bearing is clamped in a housing which is mounted on a linear guiding [1]. A motion is applied to the housing by a hybrid linear actuator. The shaft is rigidly mounted on a radial force sensor equipped with strain gauges. The relative motion between bearing and shaft is measured by two perpendicular eddy current sensors.

During the hysteresis measurement, the shaft is automatically moved by the hybrid linear actuator until a specified maximum bearing load is reached [1]. Afterwards, the direction of the displacement is reversed. This procedure is repeated until closed hysteresis loops are achieved.

The main results presented in paper I [1] are briefly summarized in section 2.1 to give an overview of the effect of the assembly preload on the bearing hysteresis.

1.3.2. Outline of Paper II

As stated in section 1.3.2, thermal effects are neglected in paper I [1] to focus on the influences arising from the nonlinear behavior of the elastic foil structure. In general,

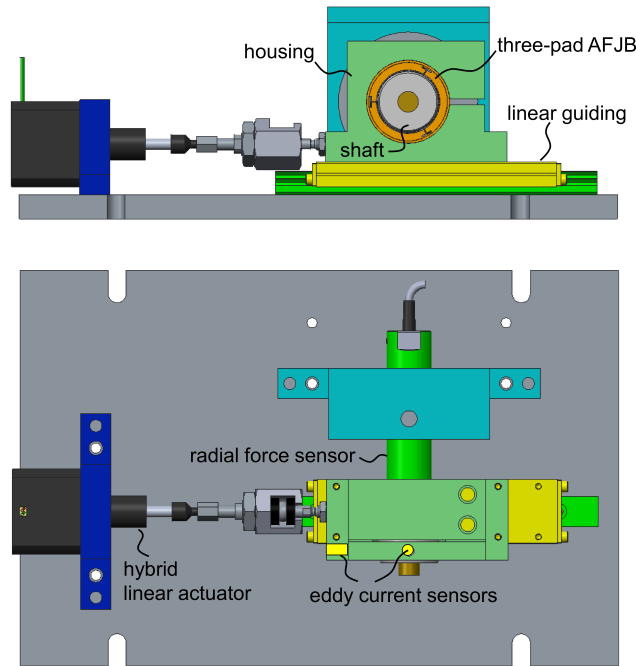


Figure 1.11.: Device for the automated measurement of air foil journal bearing hystereses [1]

thermal effects have a crucial influence on the performance of air foil bearings. In order to study the thermo-gasdynamic behavior of air foil bearings, the 3D energy equation [3]

$$\begin{aligned}
 \rho_i c_{p_i} \left(\frac{\partial T_{a_i}}{\partial x_{a_i}} v_{x_{a_i}} + \frac{\partial T_{a_i}}{\partial y_{a_i}} v_{y_{a_i}} \right) = & \quad (1.7) \\
 \frac{\partial p_i}{\partial x_{a_i}} v_{x_{a_i}} + \frac{\partial p_i}{\partial y_{a_i}} v_{y_{a_i}} + k_{a_i} \left(\frac{\partial^2 T_{a_i}}{\partial y_{a_i}^2} + \frac{\partial^2 T_{a_i}}{\partial z_{a_i}^2} \right) + \\
 \eta_{a_i} \left[\left(\frac{\partial v_{x_{a_i}}}{\partial z_{a_i}} \right)^2 + \left(\frac{\partial v_{y_{a_i}}}{\partial z_{a_i}} \right)^2 \right] \quad \forall i = 1, \dots, 3.
 \end{aligned}$$

has to be solved to get the air film temperature T_{a_i} . As for the Reynolds equation 1.1, the 3D energy equation is formulated in the local Cartesian coordinates x_{a_i} , y_{a_i} and z_{a_i} of the i -th bearing pad, see Fig. 1.7. Note, that some terms in the 3D energy equation (1.7) have

been neglected following an order of magnitude analysis by Lehn [6] and Dowson [26]. In Eq. (1.7), c_{p_i} and k_{a_i} depict the isobaric heat capacity and the heat conductivity of the air film in the i -th bearing pad. According to Dowson [26], the circumferential and axial fluid film velocity $v_{x_{a_i}}$ and $v_{y_{a_i}}$ in Eq. (1.7) are calculated from a simplified form of the Navier-Stokes equation.

The change of the air density ρ_i and viscosity η_{a_i} with the air film temperature is described by the ideal gas equation and the Sutherland equation, respectively. Since the Reynolds equation (1.1) does not account for the change of density and viscosity across the fluid film height, a more general form of the Reynolds equation is necessary to account for thermal effects on the pressure distribution [3]. Therefore, the general Reynolds equation according to Dowson [26] is applied in this work [3]:

$$\begin{aligned} & \frac{\partial}{\partial x_{a_i}} \left[(F_{2_i} + G_{1_i}) \frac{\partial p_i}{\partial x_{a_i}} \right] + \frac{\partial}{\partial y_{a_i}} \left[(F_{2_i} + G_{1_i}) \frac{\partial p_i}{\partial y_{a_i}} \right] \\ & = -\frac{\partial}{\partial x_{a_i}} \left[r_r \Omega \left(\frac{F_{3_i} + G_{2_i}}{F_{0_i}} - G_{3_i} \right) \right] \quad \forall i = 1, \dots, 3. \end{aligned} \quad (1.8)$$

In this equation, the change of the fluid viscosity η_i and the fluid density ρ_i across the fluid film is accounted for by the quantities F_{0_i} - F_{3_i} and G_{1_i} - G_{3_i} which are defined by the following integral expressions [26]:

$$F_{0_i} = \int_0^{h_i} \frac{dz_{a_i}}{\eta_{a_i}}, \quad (1.9)$$

$$F_{1_i} = \int_0^{h_i} \frac{z_{a_i}}{\eta_{a_i}} dz_{a_i}, \quad (1.10)$$

$$F_{2_i} = \int_0^{h_i} \frac{\rho_i z_{a_i}}{\eta_{a_i}} (z_{a_i} - z_{a_i}^*) dz_{a_i}, \quad (1.11)$$

$$F_{3_i} = \int_0^{h_i} \frac{\rho_i z_{a_i}}{\eta_{a_i}} dz_{a_i}, \quad (1.12)$$

$$G_{1_i} = \int_0^{h_i} \left[z_{a_i} \frac{\partial \rho_i}{\partial z_{a_i}} \left(\int_0^{z_{a_i}} \frac{z_{a_i}}{\eta_{a_i}} dz_{a_i} - z_{a_i}^* \int_0^{z_{a_i}} \frac{dz_{a_i}}{\eta_{a_i}} \right) \right] dz_{a_i}, \quad (1.13)$$

$$G_{2_i} = \int_0^{h_i} \left(z_{a_i} \frac{\partial \rho_i}{\partial z_{a_i}} \int_0^{z_{a_i}} \frac{dz_{a_i}}{\eta_{a_i}} \right) dz_{a_i}, \quad (1.14)$$

$$G_{3_i} = \int_0^{h_i} z_{a_i} \frac{\partial \rho_i}{\partial z_{a_i}} dz_{a_i}, \quad (1.15)$$

with

$$z_{a_i}^* = \frac{F_{1_i}}{F_{0_i}}. \quad (1.16)$$

These integrals are evaluated across the fluid film height h_i .

The 3D energy equation (1.7) and the generalized Reynolds equation (1.8) together with the Dowson integrals (1.9)-(1.15) represent a system of nonlinear integro-partial differential equations. Solving this system by a finite element approach entails a high computational effort [37, 38]. Due to the nonlinearity of the problem, also convergence problems are frequently observed.

In paper II [2], mainly two different reduction methods – namely an *Averaging Approach* and a *Polynomial Approach* – are presented. These approaches are used to reduce the dimension of the governing system of nonlinear integro-partial differential equations and in order to stabilize the solution process. In that paper, these approaches are applied to efficiently calculate the pressure and temperature field in the fluid film of an air foil thrust bearing pad and an oil slider bearing. This synopsis will focus on the application of the two methods to the air foil thrust bearing, see Fig. 1.12. For the application to oil bearings, the reader is kindly referred to the original publication [2].

For simplicity, the deformation of the elastic foil structure of the air foil thrust bearing pad is neglected in paper II [2]. Therefore, it is assumed that the air film height h does not change due to the aerodynamic pressure acting on the top foil. Furthermore, ideal thermal boundary conditions are applied at the pad inlet as well as at the interfaces to the surrounding structure. Hence, the temperature distribution in the surrounding structure is not calculated in paper II [2].

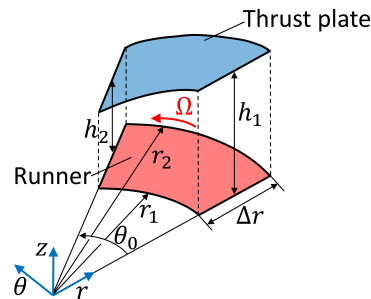


Figure 1.12.: Geometry of an air thrust bearing pad [39]

The *Averaging Approach* is based on averaging the fluid temperature across the fluid film according to Lee and Kim [40]. Within this approach, the 3D energy equation is

solved without using any reduction techniques so that a 3D temperature distribution is obtained. The 3D temperature field $T_a(r, \theta, z)$ is averaged across the fluid film

$$T_{a,avg}(r, \theta) = \int_0^h T_a(r, \theta, z) dz \quad (1.17)$$

yielding a 2D temperature field $T_{a,avg}(r, \theta)$. Herein, r , θ and z denote the radial, the circumferential and the cross-film coordinate of the investigated air foil thrust bearing pad, see Fig. 1.12. Based on the 2D temperature field, fluid density and viscosity in the generalized Reynolds equation and in the 3D energy equation are calculated by means of appropriate constitutive equations. Hence, fluid density ρ and fluid viscosity η are only functions of r and θ . As a consequence, the generalized Reynolds equation is reduced to the classical compressible Reynolds equation [40].

Within the Polynomial Approach, fluid temperature, density, and fluidity (reciprocal of viscosity) are approximated by Legendre polynomials of order N across the fluid film [41, 37, 42]. The polynomial coefficients are calculated using the values of temperature, density and fluidity at the $N + 1$ Lobatto points across the fluid film [2, 39].

Using the polynomial approximations for fluidity and density, the Dowson integrals in the generalized Reynolds equation (1.8) are calculated using a Lobatto point quadrature method. The generalized Reynolds equation is solved by the finite element method [2, 39].

Three different approaches – namely the Quadrature Method, Modified Quadrature Method the Point Collocation Method and the Galerkin method – are used to simplify and reduce the 3D energy equation [2, 39]. Within the Quadrature Method, the 3D energy equation is solved without reduction; only density and fluidity are approximated by Legendre polynomials [2, 39]. In context of the Modified Quadrature Method additional simplifications are introduced to the 3D energy equation (1.7). Within the Point Collocation Method and the Galerkin method, fluidity, density and temperature are approximated by Legendre polynomials so that the 3D energy equation is solved in 2D space [2, 39].

The Point Collocation Method is based on the approach of Elrod [37]. To calculate the temperature at the Lobatto points, the 3D energy equation is discretized across the fluid film using the method of weighted residuals with Dirac delta functions as weighting functions [37, 42, 39]. Therefore, the 3D energy equation is reduced to a set of $N - 1$ 2D partial differential equations for the $N + 1$ unknown temperatures at the Lobatto points [39]. The remaining two unknown temperatures at the top and bottom of the fluid film are determined by the boundary conditions [2, 39]. The set of 2D partial differential equations is solved by a finite element approach.

In context of the Galerkin approach Legendre polynomials across the fluid film are used as weighting functions to obtain a weak form of the energy equation [41, 42, 2, 39].

Thereby, the 3D energy equation is reduced to a set of $N + 1$ 2D partial differential equations [39]. Neumann boundary conditions at the runner or at the thrust plate are incorporated using the weak formulation for the heat conduction term [39]. Dirichlet boundary conditions at the runner or the thrust plate are implemented by formulating the Dirichlet boundary conditions as Neumann boundary conditions using a penalty approach [2, 39]. As for the Point Collocation Method, the set of $N + 1$ 2D partial differential equations is solved by a finite element approach [2, 39].

The different reduction approaches introduced above are compared with respect to the numerical efficiency, the accuracy and the convergence behavior in paper II [2], see section 2.2.1.

1.3.3. Outline of Paper III

In paper III [3], a fully-coupled elasto-gasdynamics model of a three-pad air foil journal bearing is presented. Therefore, the elasto-gasdynamics model introduced in paper I [1] is extended by a thermal model for the air film and for the surrounding structure. For the reduction of the governing equation, the Averaging Approach from paper II [2] is applied.

To account for the thermal effects on the pressure distribution, the general Reynolds equation according to Dowson (1.8) is used in paper III [3] instead of the simple Reynolds equation for compressible fluids (1.1) introduced in paper I [1]. In paper III [3], the air film height h is defined as the actual normal distance between the rotor and the top foil taking into account the rotor eccentricity e_r under the bearing load F_b as well as the deformation of the foil structure. The elastic model of bump and top foil as well as the contact model between bump foil and bearing sleeve and between bump and top foil are taken from paper I [1]. In addition, the friction occurring in the contact region between rotor and top foil is taken into account in paper III [3]. Furthermore, the radial displacement of the top foil mounting suspension is considered in paper III [3]. In contrast to paper I [1], the actual position of the rotor is found from the equilibrium of forces

$$\begin{bmatrix} F_y \\ F_z \end{bmatrix} + F_b \begin{bmatrix} \sin(\gamma_r) \\ -\cos(\gamma_r) \end{bmatrix} = \begin{bmatrix} 0 \\ 0 \end{bmatrix} \quad (1.18)$$

in y - and z -direction.

Herein, γ_r describes the angle under which the bearing load is applied, see Fig. 1.7. The forces F_y and F_z result from the air film pressure between the rotor and the three bearing pads. These are calculated from the 2D pressure distribution by using the relationships

[3]

$$\begin{bmatrix} F_y \\ F_z \end{bmatrix} = \sum_{i=1}^3 \begin{bmatrix} - \iint_{A_{pad_i}} p_i \sin(\psi) \, dA \\ \iint_{A_{pad_i}} p_i \cos(\psi) \, dA \end{bmatrix}. \quad (1.19)$$

In the above equation, $A_{pad_i} \approx L_{t_i} b$ denotes the area of the i -th bearing pad [3].

The 3D energy equation (1.7) is used to calculate the temperature distribution in each air film. As shown by Salehi et al. [43], about 75 – 80 % of the heat which is generated in each air film is conducted into the surrounding structure and a cooling flow. Hence, it is important that the different heat paths through the surrounding structure are correctly accounted for in thermo-elasto-gasdynamic air foil journal bearing models. Figure 1.5 gives an overview of the different heat paths in a three-pad air foil journal bearing. Besides the convective heat transfer from the air which enters and leaves each bearing pad, the heat is transferred to the rotor and the foil structure by conduction. The temperature in these components is described by using appropriate heat equations which will be shortly summarized hereafter.

Due to the high rotational speed of the rotor, the temperature T_r of the rotor is assumed to be constant in circumferential direction [3]. Therefore, the 2D axisymmetric energy equation [3]

$$k_r \left(\frac{\partial^2 T_r}{\partial r^2} + \frac{1}{r} \frac{\partial T_r}{\partial r} + \frac{\partial^2 T_r}{\partial z_r^2} \right) = 0 \quad (1.20)$$

is applied for calculating the temperature distribution of the rotor. Herein, k_r represents the thermal conductivity of the rotor. Equation (1.20) is solved on the rotor domain which is shown in Fig. 1.13. Note, that the local rotor axis z_r shows in the same direction as the global x -axis and the local y_{a_i} -axis of each fluid film respectively, see Fig. 1.7. This figure also shows the heat transfer at the rotor boundaries. This comprises the heat transfer from the air foil journal bearing to the rotor and from the rotor to the ambient air. The heat transfer from the air foil journal bearing is calculated by averaging the heat flux at the air film/rotor interface in circumferential direction. In the region next to the air foil journal bearing, the heat is transferred to the ambient air by forced convection induced by the high rotational speed of the shaft. The corresponding heat transfer coefficient is calculated from an appropriate Nusselt relationship [15]. The axial rotor ends are assumed to be adiabatic.

In paper III [3], the effect of the thermal and centrifugal expansion on the governing air film height is considered. Since the temperature distribution and the centrifugal load are

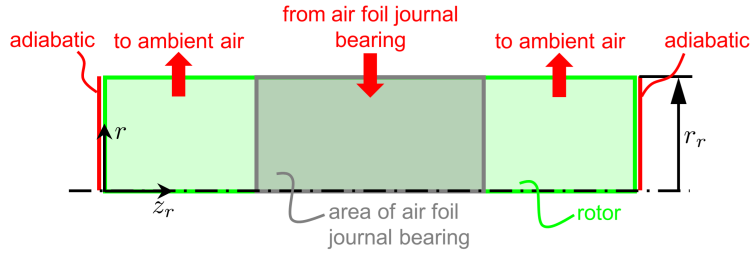


Figure 1.13.: Rotor domain and heat transfer at the rotor boundaries [3]

axisymmetric, the axial and radial rotor deformation are calculated from the Lamé-Navier equations [3].

Due to the small thickness, the temperature distribution of top and bump foil are described by 2D heat equations. For the top foil, the curvature can be neglected in the 2D heat equations [3]

$$k_{t_i} H_{t_i} \left(\frac{\partial^2 T_{t_i}}{\partial s_{t_i}^2} + \frac{\partial^2 T_{t_i}}{\partial y_{t_i}^2} \right) = -\dot{q}_{t_{in_i}} + \dot{q}_{t_{out_i}}, \quad (1.21)$$

$$\forall i = 1, \dots, 3,$$

since the top foil height is considerably smaller than the overall radius of the top foil. Note, that the s_{t_i} - and y_{t_i} -coordinate of the top foil correspond with the x_{a_i} - and y_{a_i} -coordinate of the air film. The axial top foil ends are assumed to be adiabatic, while at the top foil leading edge, the heat is transferred through the mounting suspension to the bearing sleeve. At the trailing edge, the top foil temperature equals the inlet air film temperature. The quantity $\dot{q}_{t_{in_i}}$ in Eq. (1.21) depicts the heat flux from each air film to the adjacent top foil. The outgoing heat flux $\dot{q}_{t_{out_i}}$ is transferred to the bump foil.

It is assumed that the heat leaves the top foil only in the regions where the bumps contact the top foil, see Fig. 1.14. The corresponding thermal contact resistance is calculated using an analytical formula. The derivation of the formula is based on the assumption that the heat in the contact region of bump and top foil is transferred by the small air film near the contact points, see [6, 27]: In [6, 27] it is shown that the thermal resistance of the solid contact is significantly larger than the thermal resistance of the neighboring air film. Thus, the thermal resistance of the air film determines the overall thermal behavior of the bump and top foil contact [3]. The thermal resistance of the air film is mainly determined by the air film height between top and bump foil in the contact region, see

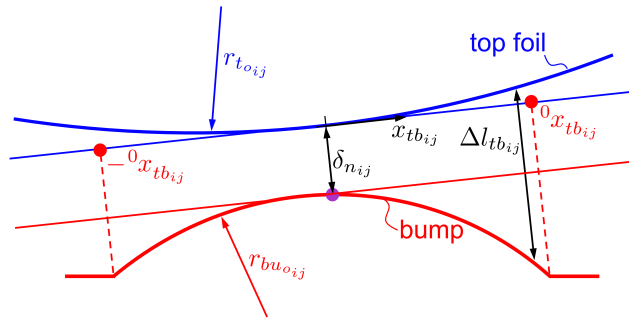


Figure 1.14.: Contact region between the top foil and a single bump [3]

Fig. 1.14. Therefore, the air film height in the contact region is described by an analytical formula that accounts for the actual curvature of bump and top foil [3]. From the air film height, the thermal resistance can be derived by integration of the infinitesimal thermal conductance in the contact region and building the reciprocal of the governing thermal conductance [3].

As explained above, the heat from the top foil $\dot{q}_{t_{out_i}}$ is transferred to the bump foil in the contact region, see Fig. 1.14. As for the top foil, the temperature distribution of the bump foil is described by a 2D heat equation. In Eq. (1.21), the curvature of the top foil is neglected since the top foil radius is significantly larger than the top foil thickness. The same holds for the bump foil segments [3]. In contrast, the curvature has to be considered in the 2D heat equation of each bump. Therefore, a 2D heat equation for each bump and segment are derived. At the intersection of bump and top foil, appropriate coupling constraints for the temperature and the heat flux are formulated.

The bearing sleeve is modeled as a lumped thermal mass. The heat which is transferred to the bearing sleeve from the bump foil and the top foil, is conducted through the bearing sleeve and transferred to the ambient air [3]. The corresponding heat transfer coefficient is determined from experiments. Furthermore, the thermal expansion of the bearing sleeve is considered and accounted for in the calculation of the governing air film height between top foil and rotor.

The governing system of nonlinear integro-partial differential equation is reduced by the Averaging Approach presented in paper II [2]. Hence, the general Reynolds equation according to Dowson (1.8) is reduced to the simple Reynolds equation for compressible fluids (1.1). Furthermore, the fluid velocity expressions in the 3D energy equation of the air film (1.7) are simplified [3].

The governing equations are discretized by a finite element approach. The physical domains are discretized using different types and different numbers of finite elements [3]. For the nonlinear beamshell equations (1.3)-(1.5), quintic Lagrange elements are used to avoid shear locking [3]. All other equations are discretized with quadratic Lagrange elements. In order to prevent numerical instabilities in connection with convection-diffusion problems an artificial diffusion approach is applied in paper III [3].

Figure 1.15 illustrates the numerical solution procedure of the fully-coupled thermo-elasto-gasdynamics problem. As depicted, a segregated solution procedure is applied. In context of this procedure, the total number of dependent variables and corresponding equations is divided into three segregated groups [3]:

1. Elasto-gasdynamics variables and equations: Top and bump foil displacement, rotor eccentricity, air film pressure.
2. Thermal variables and equations: Air film temperature, top and bump foil temperature, rotor temperature, bearing sleeve temperature and expansion.
3. Lamé-Navier equations of the rotor: Centrifugal and thermal rotor expansion.

Each group of equations is solved for the corresponding variables using a fully-coupled solution approach, while the variables of the other groups are held constant [3]. The group of variables introduced above define the sub-steps of the solution procedure. The sub-steps 1-3 are repeated until a global convergence of all variables is achieved. In each sub-step, a damped Newton-Raphson approach is applied, in which the Jacobian matrix is calculated analytically [3].

Using the described numerical model, the thermo-elasto-gasdynamics behavior of a heavily preloaded three-pad air foil journal is investigated. First, the static bearing stiffness and hysteresis is analyzed. Afterwards, the temperature distribution in the different bearing components are investigated for different bearing loads at a rotational speed of 35 krpm.

For the purpose of validating the numerical model, experiments with a heavily preloaded bearing are accomplished on the hysteresis device presented in paper I [1], see section 1.3.1. Furthermore, the predicted temperature distribution are validated against measurement results from paper IV [4]. These results have been obtained by using an automated high-speed test rig which runs at speeds up to 60 krpm [4].

1.3.4. Outline of Paper IV

In paper IV [4], the influence of the assembly preload on the bearing hysteresis, on the drag torque and on the thermal behavior are investigated experimentally. The two

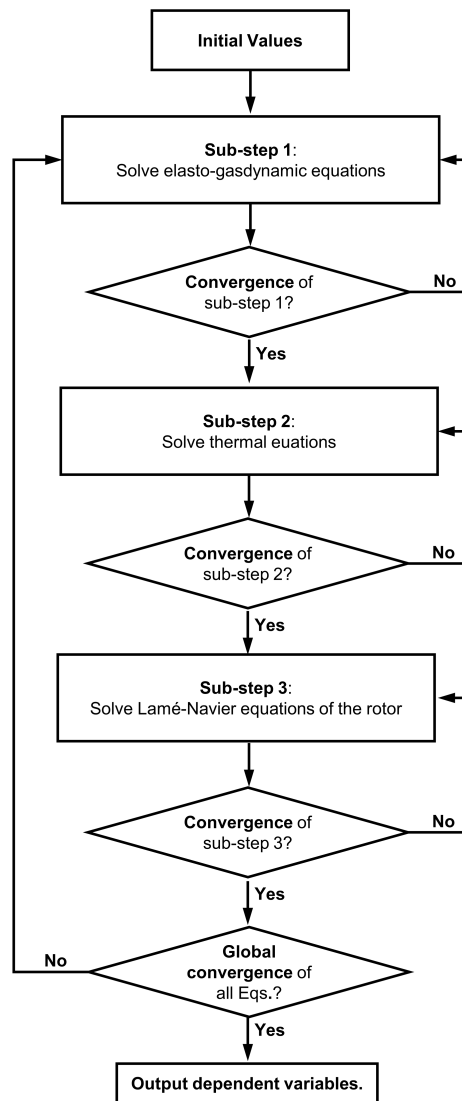


Figure 1.15.: Flowchart of the solution procedure in the last study step [3]

bearings differ only in their nominal top foil radii creating different assembly preloads, while the nominal bump foil radius and the preload induced by the bump foil shape are

equal.

The measurements are realized on two different test rigs. For quantifying the assembly preload and its effect on the static bearing hysteresis at zero running speed, the hysteresis device from paper I [1] is used, see section 1.3.1. The effect of the assembly preload on the bearing drag torque and on the thermal behavior at different bearing loads is studied with a second test rig, see Fig. 1.16 and 1.17. This automated high-speed test rig, which runs at speeds up to 60 krpm, is capable of measuring the bearing drag torque, the horizontal and vertical displacement of the bearing and different temperatures of the rotor and the bearing at different rotor speeds and bearing loads [4]. The test rig consists of a ball bearing supported rotor which is run by an AC motor spindle.

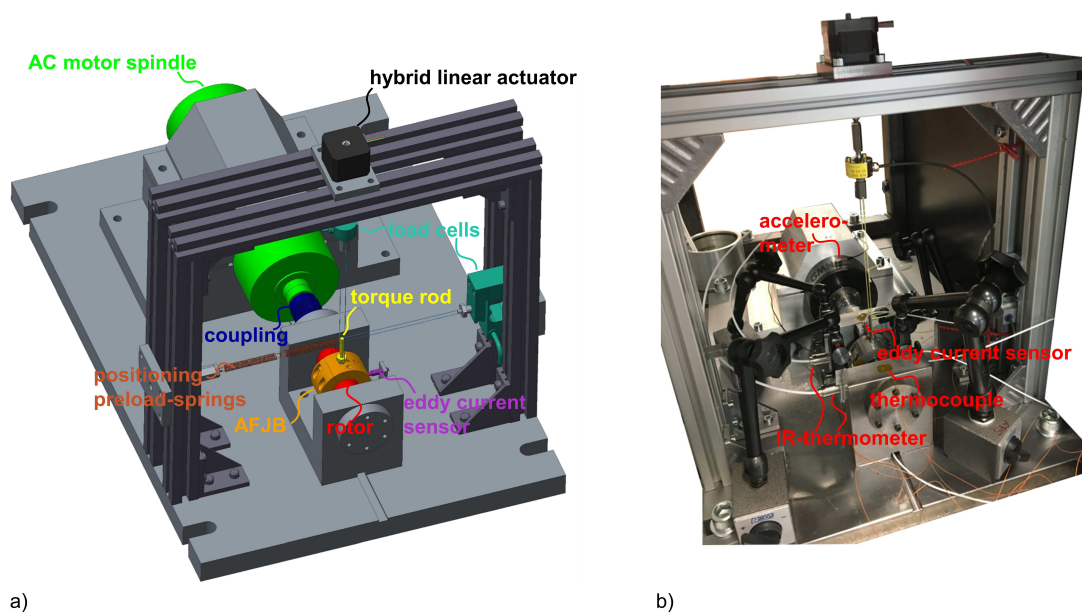


Figure 1.16.: CAD-model (a) and photo (b) of the automated high-speed air foil journal bearing test rig [4]

The investigated air foil journal bearing is located in the middle of a rotor. A divided bearing sleeve is used to allow for a simple and fast assembling and disassembling of the foil bearing on the rotor [4]. A torque rod can be attached to the bearing sleeve at different angular locations. The free end of the torque rod is connected to a load cell via a horizontal cable. Thereby, the bearing drag torque is measured. Furthermore, two serially

The rotor temperature is measured with two infrared thermometers.

The test procedure for each bearing comprises four steps, see [4]: A sequence of start-stop cycles to assure that the top foil and rotor coating are broken in, the measurement of the drag torque of the run-in bearing, the acquisition of the steady state bearing temperatures and a static hysteresis measurement at zero running speed to quantify the effect of the assembly preload on the bearing foil structural stiffness and the frictional loss.

In the first step, the rotor is subjected to a sequence of start-stop-cycles at speeds up to 40 krpm. During these cycles, different loads are applied to the air foil journal bearing. The sequence of start-stop-cycles is stopped when no significant change of the maximum rotor temperature is detected anymore. This assures that the top foil coating is broken in.

In the second step, the drag torque of the bearings is acquired with the described test rig. Note, that no thermocouples are used in this step at the bump and top foils to assure that the torque measurement will not be affected by an eventual increase in the preload by the thermocouples. The drag torque measurements are accomplished during one start-stop-cycle of the rotor. The bearing torque is measured for the two bearings at different loads up to 30 N.

In the third step, the thermal behavior of the lightly and the heavily preloaded bearing under steady state conditions is analyzed for bearing loads up to 30 N in steps of 10 N. The temperature measurements are accomplished at a rotor speed of $n_r = 35$ krpm. At the rotor startup, the air foil journal bearing is not subjected to a load. When the final rotor speed is reached, the particular load is applied to the bearing using a specified loading schema. This is done to ensure that the bearing operates at a defined point of the bearing hysteresis curve. This is especially important for a comparison with the simulation results in paper III [3], see section 1.3.3.

In the last step, static hysteresis measurements of the two bearings are accomplished using the hysteresis device first presented in paper I [1], see section 1.3.1.

The experimental results are used to study the effect of the assembly preload on the bearing hysteresis, the drag torque, the lift-off-speed and on the thermal behavior.

2. Results

As shown in Fig. 1.6 and discussed in section 1.3, the effect of an assembly preload on the thermo-elasto-gasdynamics behavior is studied numerically and experimentally in papers I-IV [2, 1, 3, 4]. In this section, the main results of the paper I-IV are briefly summarized.

Firstly, the effect of the assembly preload on the bearing stiffness and damping is presented in section 2.1. As shown in Fig. 1.6, this effect is studied numerically in paper I [1] as well as experimentally in paper IV [4]. Within this investigation, thermal effects are neglected.

In the second step, the influence of the assembly preload on the thermal behavior is presented in section 2.2. Figure 1.6 shows that papers II-IV [2, 3, 4] contribute to the understanding of the thermal behavior of air foil journal bearings either numerically (paper II/III) or experimentally (paper IV).

Finally, the effect of the assembly preload on the drag torque and on the lift-off speed of three-pad air foil journal bearings will be summarized in section 2.3 based on the experimental results from paper IV [4], see Fig. 1.6.

In the subsequent studies, the assembly preload is changed by using different top foils with different radii. For the effect of further preload parameters on the bearing performance, the reader is referred to appendix A and appendix B.

2.1. Preload Effects on the Bearing Stiffness and Damping

In this section, the effect of the assembly preload on the bearing stiffness and damping is discussed. Firstly, the foil structural stiffness and damping are investigated using the numerical model presented in paper I/III [1, 3] as well as the introduced hysteresis test rig, see section 1.3.1. Afterwards, the overall bearing stiffness and damping during airborne bearing operation are analyzed numerically for two differently preloaded bearings.

2.1.1. Foil Structural Stiffness and Damping at Zero Running Speed

In order to study the foil structural stiffness and damping of three-pad air foil journal bearings, load-deflection simulations and experiments are performed in paper I [1], in

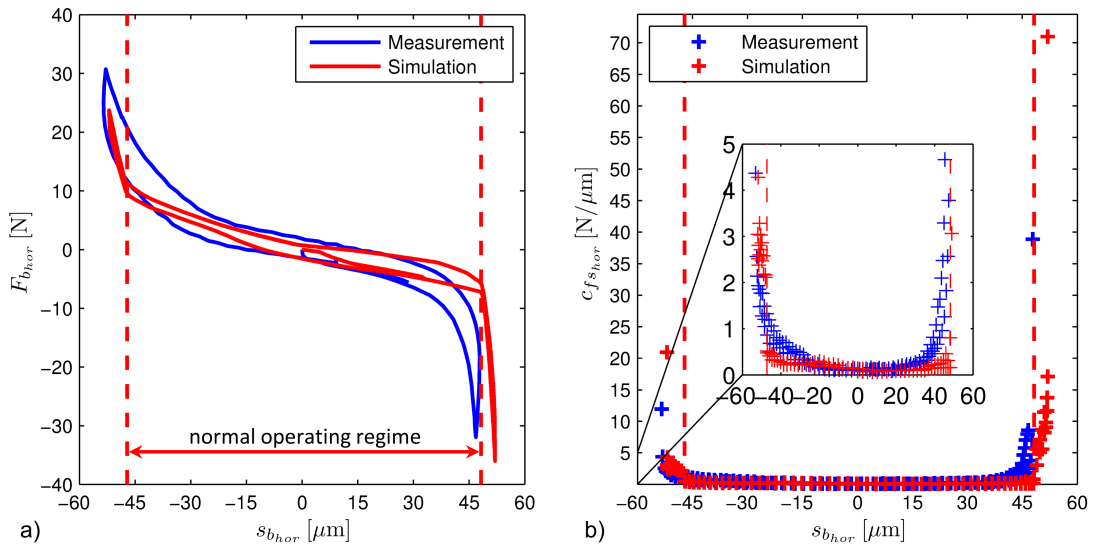


Figure 2.1.: Measured and predicted hysteresis curves (a) and foil structural stiffness (b) of the lightly preloaded three-pad air foil journal bearing from paper I [1]

paper III [3] and in paper IV [4]. In this section, the results from these papers are briefly summarized.

In context of the load-deflection tests, the non-rotating shaft is quasi-statically and harmonically displaced in the direction of a top foil center. When plotting the corresponding reaction force $F_{s_{hor}}$ on the shaft in the direction of the applied motion over the relative displacement $s_{b_{hor}}$, characteristic hysteresis curves of the air foil journal bearing are obtained, see Fig. 2.1a). Figure 2.1a) shows the measured and predicted hysteresis curve of a lightly preloaded three-pad air foil journal bearing investigated in paper I [1]. The foil structural stiffness c_F is derived from the hysteresis curves by using first-order central differences [1]. Figure 2.1b) depicts the foil structural stiffness over the relative displacement. For moderate bearing loads - the normal operating regime - the stiffness is rather low and nearly constant. For larger loads, which occur during shock loads, the stiffness increases significantly. The elastic foil structural stiffness at moderate loads is caused by the assembly preload. For bearings which are not preloaded, the stiffness would be zero in this area. For larger bearing loads, more bumps contact the bearing sleeve. This explains the rise in the bearing stiffness.

The area enclosed by the hysteresis loop in Fig. 2.1 equals the energy dissipation

during one cycle [1]. The energy dissipation is caused by the frictional losses in the contact between bump and top foil as well as between bump foil and bearing sleeve. The dissipation corresponds with the bearing damping.

As shown in Fig. 2.1, predicted and measured hysteresis curves agree well. The small differences in the stiffness might be traced back to manufacturing errors of the bump foil which significantly affect the size of the normal operating regime [1]. In addition, the boundary conditions at the top and bump foil leading edge influence the foil structural stiffness in the normal operating regime [3]. The discrepancies in the dissipated energy might be traced back to the uncertainty in the coefficient of friction between bump and top foil as well as between bump foil and bearing sleeve [1]. Furthermore, the friction between top foil and rotor have been neglected in this study. According to Conlon et al. [44, 45], the friction between rotor and top foil affects the bearing damping.

To reduce the differences between the predicted and measured stiffness and damping, the foil structural model presented in paper I [1] is improved in context of paper III [3], see section 1.3.3: On the one hand, the friction between rotor and top foil is taken into account following the findings by Conlon et al. [44, 45]. On the other hand, the radial displacement of the mounting suspension of the top foil is considered. Figure 2.2 shows the predicted and measured hysteresis curves (a) and the foil structural stiffness of a heavily preloaded bearing. The measurement results are originally taken from paper IV [4]. Note, that the results for the test bearings from paper I [1] and paper III [3] can not be compared with respect to the effect of the assembly preload since both bearings differ significantly in the number of bumps, in the bump pitch as well as in the overall bump and top foil radii. As can be seen from Fig. 2.2, the measured and predicted hysteresis curves and the foil structural stiffness agree favorably indicating that the effect of the friction between top foil and rotor has to be taken into account [44, 45].

Figure 2.3 shows the measured hysteresis curves and the foil structural stiffness for a lightly and a heavily preloaded three-pad air foil journal bearing, see paper IV [4]. Note, that the depicted hysteresis curves and the foil structural stiffness curves of the heavily preloaded bearing are the same as the measured curves in Fig. 2.2. The lightly and the heavily preloaded bearing differ only in their nominal top foil radii creating different assembly preloads, while the nominal bump foil radius and the preload induced by the bump foil shape are equal [4]. The top foil radius of the heavily preloaded bearing is about two times larger than the top foil radius of the lightly preloaded bearing. As can be seen in Fig. 2.3, both hysteresis curves show a quite similar distance between the bearing displacement at the maximum and the minimum bearing load. This indicates that the higher assembly preload does not significantly influence maximum rotor displacement at shock loads. This is an important difference to other preload concepts which are based on an either local [18, 19, 10, 20, 21, 22, 23, 24] or global [11, 17, 23] reduction of the

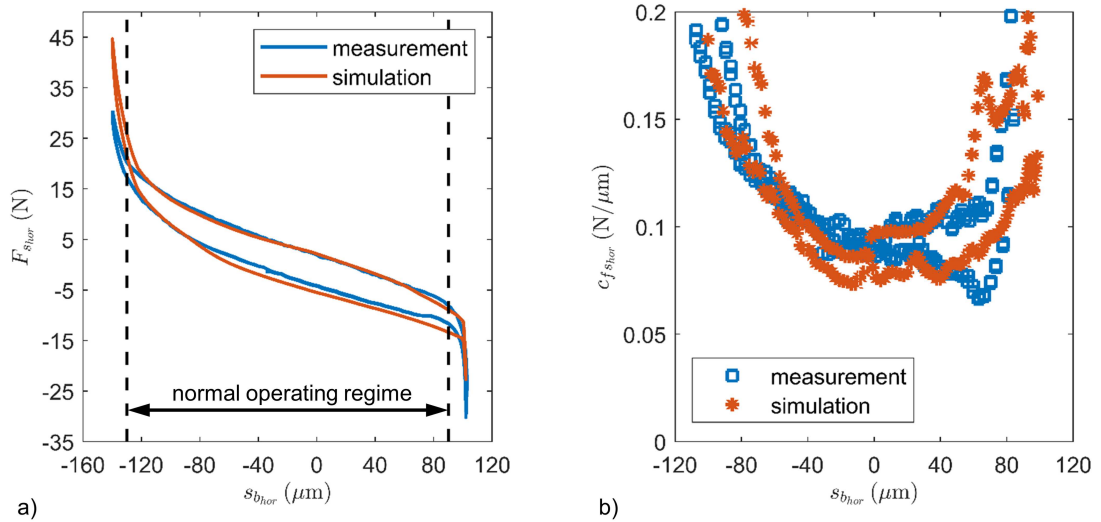


Figure 2.2.: Measured and predicted hysteresis curves (a) and foil structural stiffness (b) of the heavily preloaded three-pad air foil journal bearing from paper III [3]

operating air film thickness.

In contrast, the assembly preload is aimed to increase the foil structural stiffness in the normal operating regime. As depicted in Fig. 2.3b), the foil structural stiffness in the normal operating regime increases significantly with the assembly preload. While the foil structural stiffness differs for small loads and bearing displacements, the foil structural stiffness of the lightly and the heavily preloaded bearing are approaching for higher loads and displacements [4]. Thus, the foil structural stiffness gets more and more dominated by the bump foil, which are the same for both bearing types, as the number of bumps coming into contact with either the top foil or the bearing sleeve increases [4], see Fig. 2.3.

The dissipated energy of the heavily preloaded bearing equals 1.3 mJ, while for the lightly preloaded bearing a dissipated energy of 1.1 mJ is obtained [4]. As expected, the larger assembly preload leads to a rise of the normal forces in the contact between bump and top foil as well as between bump foil and bearing sleeve. Consequently, the friction forces and the frictional loss increase which will result in a higher bearing damping [4].

In this section, the influence of the assembly preload on the bearing stiffness and damping has been explained based on measurement results from paper IV [4]. For a numerical investigation on the bearing stiffness and damping, the reader is referred to paper I [1].

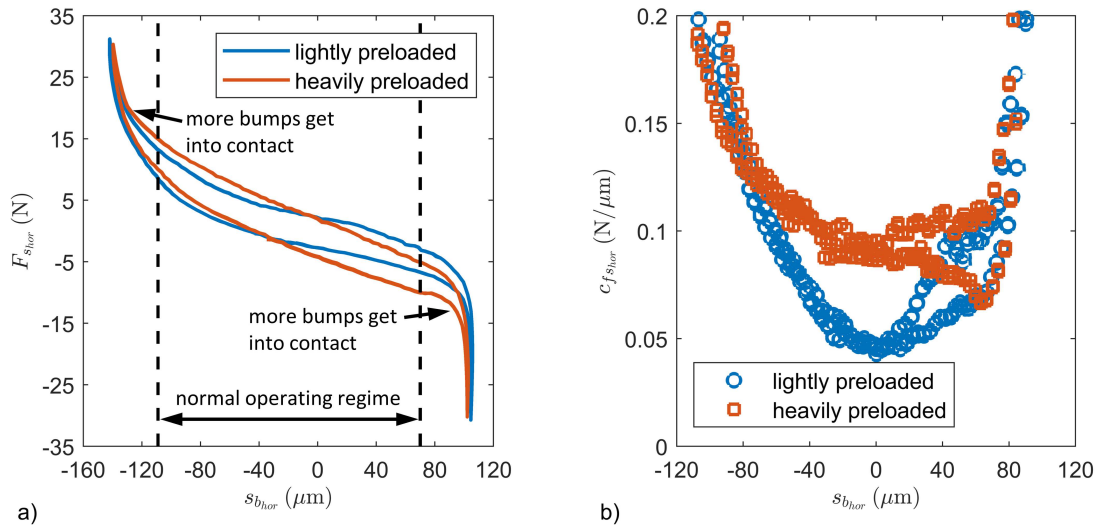


Figure 2.3.: Measured hysteresis curves (a) and foil structural stiffness (b) for the lightly and the heavily preloaded bearing from paper IV [4]

2.1.2. Overall Bearing Stiffness and Damping in Airborne Operation

In section 2.1.1, the stiffness and damping of the foil structure has been analyzed by load-deflection simulations and measurements at zero running-speed. During airborne operation, the overall bearing stiffness is determined by the foil structural stiffness as well as by the stiffness of the air film. In a simplified model, the air film and the foil structure can be regarded as two serially combined springs. To analyze the effect of the air film on the overall bearing stiffness and damping, load-deflection simulations with a rotating shaft ($n = 60,000$ rpm) are conducted in paper I [1] and compared with the results of static load-deflection simulations at zero running speed. In this section, the main results of this analysis from paper I [1] are briefly summarized.

The load-deflection simulations are performed for two differently preloaded bearings. Again, the lightly preloaded bearing and the heavily preloaded bearing differ only in the top foil radii. The top foil radius of the heavily preloaded bearing is about two times larger than the top foil radius of the lightly preloaded bearings. The static hysteresis curves and the foil structural stiffness of the lightly preloaded bearing are depicted in Fig. 2.1.

Figure 2.4 depicts the resultant force F_r on the shaft in the direction of the prescribed displacement over the shaft eccentricity e_r for the static load-deflection simulations as

well as for the simulations with a rotating shaft. For the same shaft displacement, the reaction force F_r is larger for the rotating shaft compared to the simulations with the non-rotating shaft [1]. This can be traced back to the additional air film between rotor and top foil which leads to a larger deflection of the foil structure.

As in the case of the static load-deflection simulations at zero running-speed, the bearing damping is significantly increased due to the assembly preload, see Fig. 2.4. The friction losses are larger as in the case of the static load-deflection simulation at zero running-speed, see Fig. 2.4. This can be explained by the different pressure distributions on the top foil [1]: For the static load-deflection test, the top foil contacts the shaft at small areas which leads to a very localized contact pressure distribution on the top foil. In case of the rotating shaft, the pressure distribution in the fluid film leads to a smooth and non-localized pressure distribution. Due to this pressure distribution, more bumps are in contact either with the bearing sleeve or the top foil leading to a larger friction loss.

As can be obtained from Fig.2.4, the effect of the air film on the overall bearing stiffness depends on the assembly preload [1]: For lightly preloaded bearings, the overall stiffness is effected by the fluid film while for heavily preloaded bearings the effect is rather small, see Fig. 2.4. For more details on the overall bearing stiffness and their dependence on the assembly preload, the reader is referred to the original manuscript [1].

2.2. Preload Effects on the Thermal Behavior

The effect of the assembly preload on the bearing stiffness and damping has been performed under isothermal conditions. Hence, thermal effects have been neglected in these investigations. In the next step, the influence of the assembly preload on the thermal behavior of air foil journal bearing will be investigated numerically and experimentally. As described in section 1.3.2, reduction approaches are mandatory to efficiently solve the system of nonlinear integro-partial differential equations which builds the thermo-elasto gasdynamic bearing model. The numerical error and the computation time of these approaches are summarized in section 2.2.1. Afterwards, the thermal behavior of preloaded air foil journal bearings will be investigated numerically and experimentally, see section 2.2.2.

2.2.1. Efficient Reduction Approaches for Fluid Film Bearings

The numerical efficiency of the different reduction approaches summarized in section 1.3.2, is evaluated using a thermo-gasdynamic model of an air foil thrust bearing pad, see Fig. 1.12. The numerical model is briefly summarized in section 1.3.2. For more details

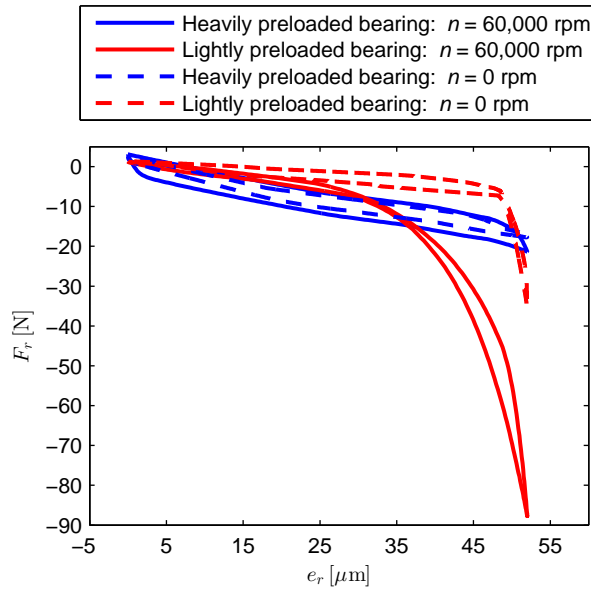


Figure 2.4.: Predicted hysteresis curves with rotating and non-rotating shaft of the lightly and the heavily preloaded bearing from paper I [1]

on the numerical model, the reader is referred to the original paper [2]. The results presented in this section have first been published in paper II [2].

The numerical efficiency is compared by evaluating the computation time and the accuracy of the different approaches. Figure 2.5 shows the relative error in temperature $\bar{e}_{r,T}^{Av}(\Delta l_{\bar{z}})$ (left) and pressure $\bar{e}_{r,T}^{Av}(\Delta l_{\bar{z}})$ (right) over the cross-film element length $\Delta l_{\bar{z}}$ for the Averaging Approach. The numbers next to the errors are the corresponding computation times. As can be seen from Fig. 2.5, the errors are quite small, even for small element numbers across the air film [2]. This can be traced back to the low heat conductivity of air. Thereby, the temperature varies only little across the air film [2]. As expected, the errors in temperature and pressure decrease with the cross-film element number while the computation time increases.

The results for the Quadrature Method (Quad [2]), the Modified Quadrature Method (Quad,mod [2]), the Point Collocation Method (Col) and the Galerkin method (Gal) are summarized in Fig. 2.6 and 2.7. Figure 2.6 shows the relative error in temperature (left) and pressure (right) over the order N of the Legendre polynomials. Figure 2.7 depicts the corresponding computation times. As can be seen, the errors decrease with the polynomial

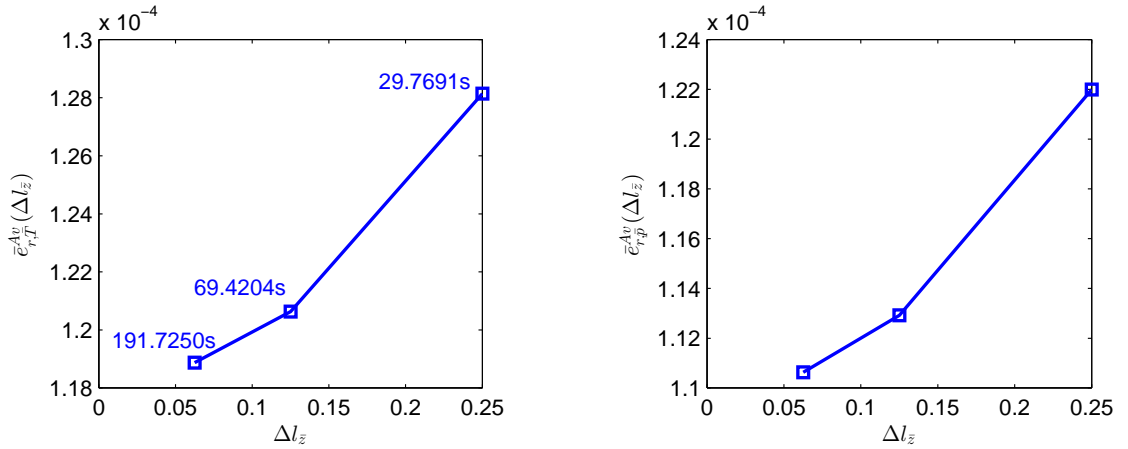


Figure 2.5.: Relative error in temperature (left) and pressure (right) for the Averaging Approach over the element size [2]

order while the computation times increase [2].

As can be seen from Fig. 2.5- 2.7, all reduction approaches yield a significant reduction in the computation time compared to the unreduced finite element model (computation time: 2227.72 s), see [2]. Very low computation times and moderate errors are achieved with the Averaging Approach and with the Galerkin method. In contrast to the Galerkin Method, the implementation of the Averaging Approach in the thermo-elasto-gasdynamics model is quite simple. Consequently, the Averaging Approach is applied in the thermo-elasto-gasdynamics model of preloaded air foil journal bearings presented in section 1.3.3. The results obtained with this model will be discussed in the subsequent section.

2.2.2. Thermo-Elasto-Gasdynamics Behavior of Preloaded Air Foil Journal Bearing

In paper III [3] and paper IV [4], the thermal behavior of preloaded three-pad air foil journal bearings is studied both numerically and experimentally. Therefore, the thermo-elasto-gasdynamics model summarized in section 1.3.3 as well as the automated high-speed test rig presented in section 1.3.4 are used. Within the two papers, the lightly and the heavily preloaded bearing, whose hysteresis curves are presented in Fig. 2.3, are investigated with respect to the temperature distribution in the air film and the surrounding structure. In this section, the results from paper III [3] and paper IV [4]

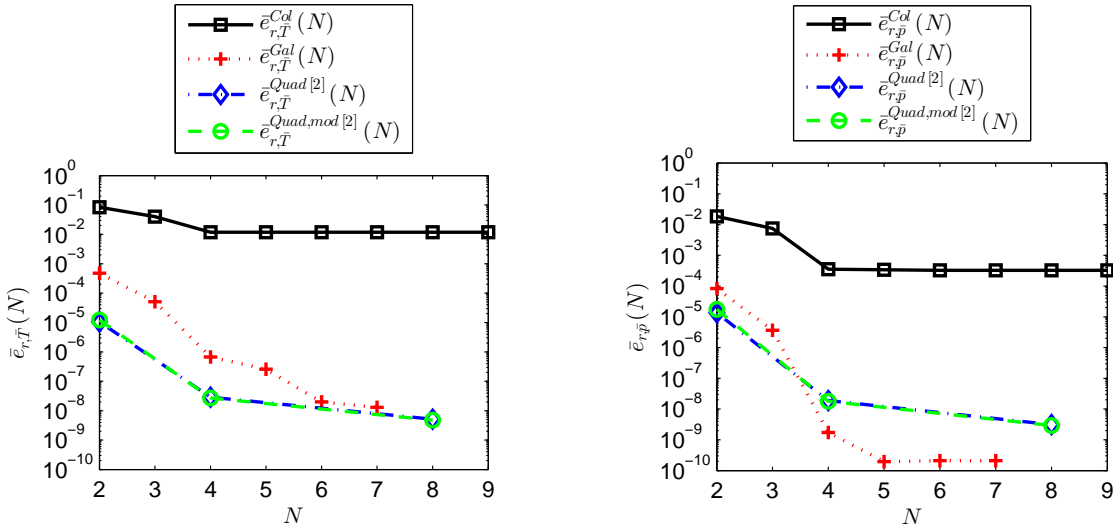


Figure 2.6.: Relative error in temperature (left) and pressure (right) for the Quadrature Method, the Modified Quadrature Method, the Point Collocation Method and the Galerkin method over the polynomial order N [2]

regarding the thermal behavior of preloaded three-pad air foil journal bearings are briefly summarized.

Figure 2.8 shows the predicted and measured temperatures of the first bearing pad (a), of the second and third bump foil (b) and of the bearing sleeve and the rotor (c) over the bearing load for the heavily preloaded bearing at a rotational speed of 35 krpm. The pad numbers in relation to the loading direction are depicted in Fig. 1.7. As can be seen, the predicted and measured temperatures show a good agreement.

As can be seen in Fig. 2.8, the temperatures of the top and bump foil increase with increasing bearing load [3]. The temperature rise in the first bearing pad is significantly larger than in the other bearing pads, since the bearing load is directed towards the center of the first pad. Besides the loading condition, the rise of the temperature of the first bump foil may be explained by a second effect [3]: Due to the load, the distance between the contacting points decreases. Thereby, the thermal resistance at the contact points between top and bump foil as well as between bump foil and bearing sleeve decreases. This leads to a rise of the bump foil temperature and the bearing sleeve temperature.

In order to study the effect of the assembly preload on the thermal behavior of three-pad air foil journal bearings, additional temperature measurements with the lightly

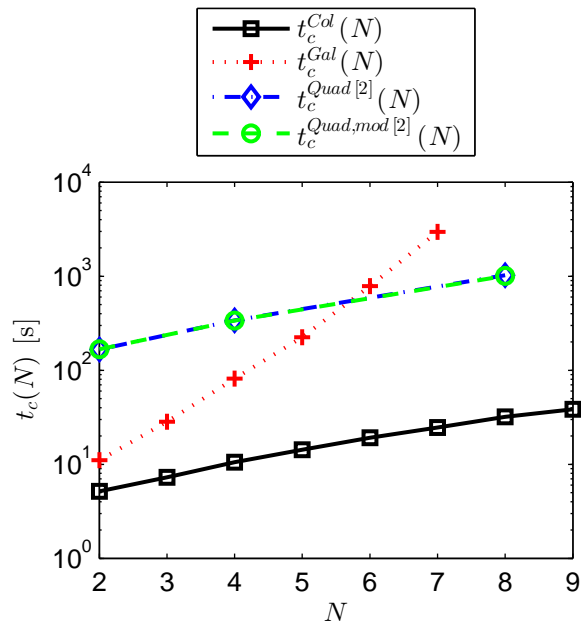


Figure 2.7.: Computation time for the Quadrature Method, the Modified Quadrature Method, the Point Collocation Method and the Galerkin method over the polynomial order N [2].

preloaded bearing are accomplished in paper IV [4]. Figure 2.9 shows the measured temperature increase for the lightly (a) and the heavily (b) preloaded bearing over the bearing load [4]. The temperature differences between the heavily and the lightly preloaded bearing are depicted in Fig. 2.9c). As can be obtained from the figures, the bearing and rotor temperature are not affected significantly by the assembly preload [4]. For both components, the temperature difference between the lightly and the heavily preloaded bearing falls within the measurement uncertainty [4]. This holds especially for higher bearing loads. Concluding, the assembly preload has no significant influence on the thermal behavior of air foil journal bearings after bearing lift-off. This is a significant advantage over other preloading mechanisms which are based on an either local [18, 19, 10, 20, 21, 22, 23, 24] or global [11, 17, 23] reduction of the air film thickness, see Fig. 1.4. As shown by Radil et al. [11] as well as by Keun and San Andrés [12], these techniques suffer from the risk of a thermal runaway induced by the thermal growth of the rotor in combination with the reduced bearing clearance. This can lead to a catastrophic

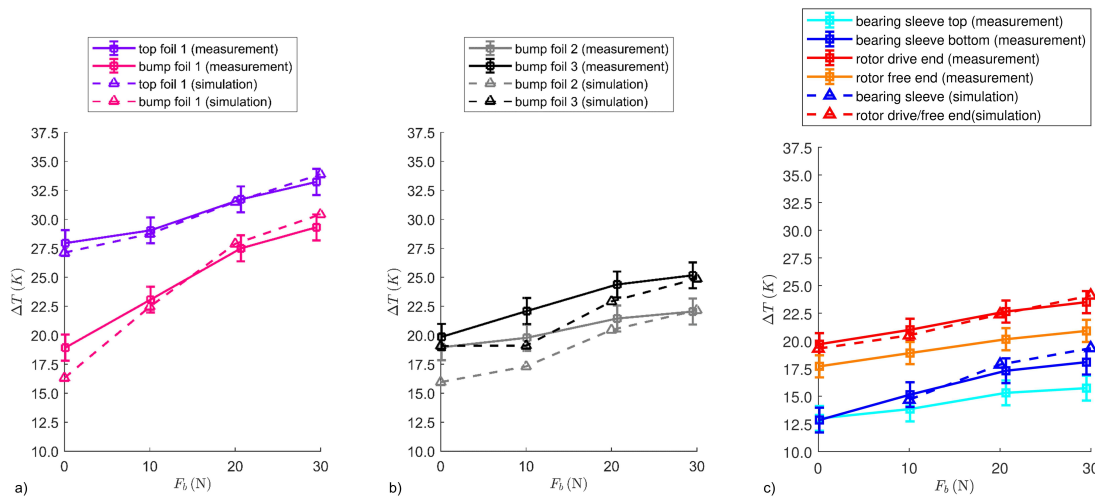


Figure 2.8.: Measured and predicted temperatures of the first bearing pad (a), of the second and third bump foil (b) and of the bearing sleeve and the rotor (c) for the heavily preloaded bearing [3]. Measurement results from paper IV [4].

bearing failure.

2.3. Preload Effects on the Drag Torque and on the Lift-Off-Speed of Air Foil Journal Bearings

Besides the thermal behavior and the bearing hysteresis, the effect of the assembly preload on the bearing drag torque and lift-off speed is investigated experimentally in paper IV [4]. Using the automated high-speed test rig described in section 1.3.4, Stribeck curves for the lightly and the heavily preloaded bearing are obtained during start-stop-cycles at different bearing loads. From these curves, the lift-off speed, the drag torque during airborne operation as well as the shutdown torque are determined. In this section, the main results from paper IV [4] regarding the bearing drag torque and lift-off speed are summarized.

Figure 2.10 depicts the bearing lift-off speed for the lightly and the heavily preloaded bearing over the bearing load. For the lightly preloaded bearing, the lift-off speed increases nearly linearly with the bearing load [4]. As shown in Fig. 2.10, the lift-off speed of the heavily preloaded bearing is smaller compared to the lift of speed of the lightly preloaded

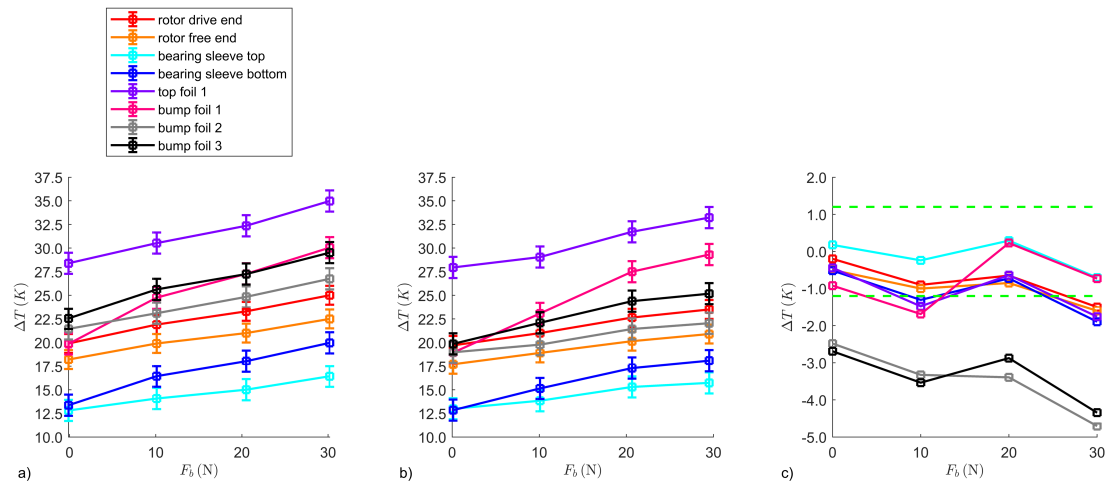


Figure 2.9.: Measured temperature increase for the lightly (a) and the heavily (b) preloaded bearing over the bearing load. The temperature difference between the heavily and the lightly preloaded bearing are shown in c). The dashed lines indicate the measurement uncertainty of the thermocouples [4].

bearing for bearing loads larger than 0 N [4]. This might be traced back to the larger initial top foil radius of the heavily preloaded bearing leading to an improved air flow at the pad inlet. Also San Andrés and Norsworthy [46] obtained only slight differences in the lift-off speed of differently shim-preloaded air foil journal bearings.

Figure 2.11 shows the airborne part of the Stribeck curve for different loads and assembly preloads [4]. In Fig. 2.11, the lift-off speeds from Fig. 2.10 are shown as dashed lines. As one can see, the airborne drag torque increases significantly with the bearing load [4]. As can be obtained from the figures, the assembly preload does not affect the drag torque significantly. The airborne drag torque and the rotational speed determine the power dissipation in the air film which leads to the temperature increase in the bearing. The fact that the assembly preload does not affect the airborne drag torque significantly, confirms that the effect of the preload on the bearing temperature is negligible as well, see section 2.2. For a numerical investigation of the assembly preload on the bearing drag torque during airborne operation for two differently preloaded bearings, the reader is referred to paper I [1].

Figure 2.12 depicts the measured and fitted shutdown torque of the lightly and the

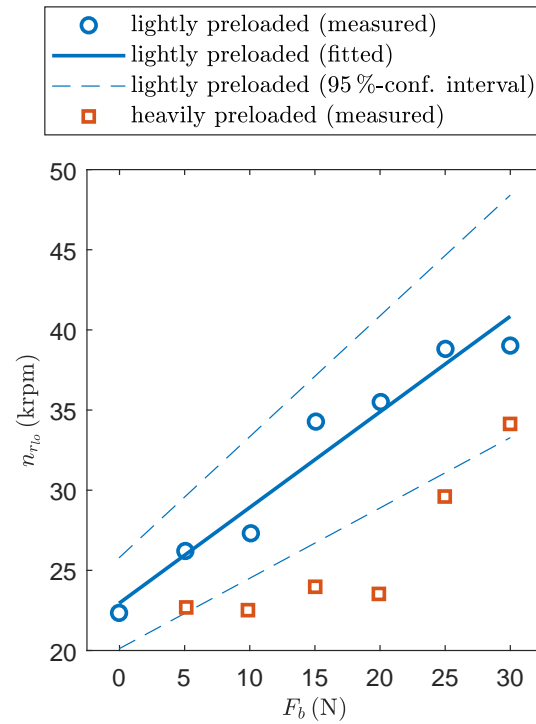


Figure 2.10.: Measured and fitted lift-off speed for the lightly and the heavily preloaded bearing over the bearing load [4]

heavily preloaded bearing over the bearing load [4]. Additionally, the confidence intervals of the linear regression of the shutdown torque are depicted by dashed lines in Fig. 2.12. The shutdown torque of both bearings increases linearly with the bearing load [47, 4]. As expected, the shutdown torque of the heavily preloaded bearing is slightly larger compared to the lightly preloaded bearing [4].

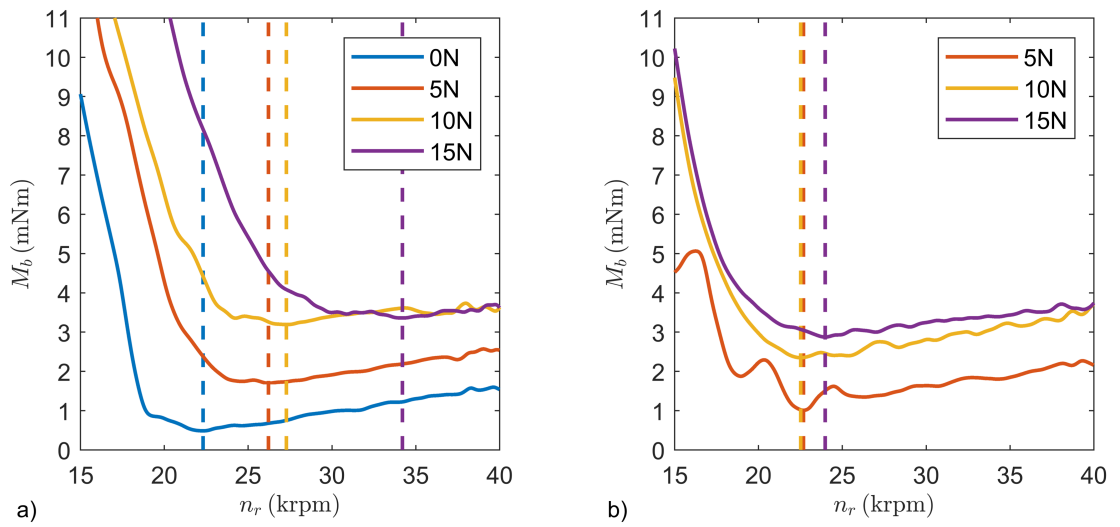


Figure 2.11.: Measured airborne drag torque of the lightly (a) and the heavily (b) preloaded bearing over the rotational speed for different bearing loads. Dashed lines mark the lift-off speeds from Fig. 2.10 [4].

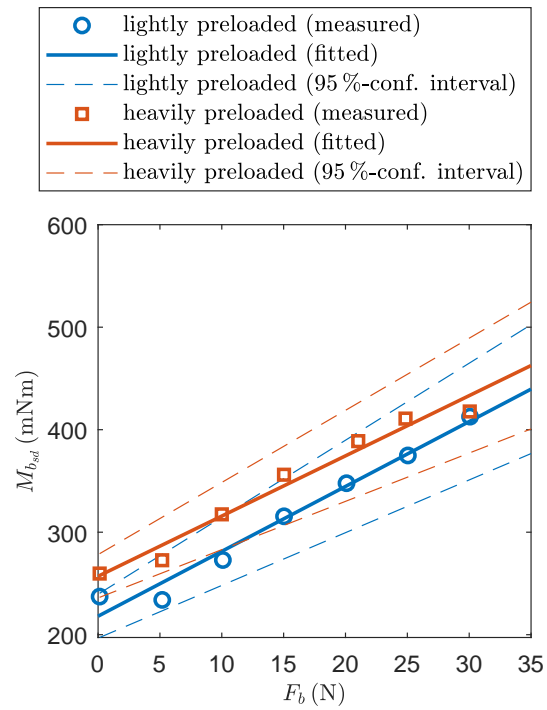


Figure 2.12.: Measured and fitted shutdown torque of the heavily and the lightly preloaded bearing over the bearing load [4]

3. Conclusion and Outlook

In context of this synopsis, the effect of the assembly preload on the thermo-elasto-gasdynamics behavior of preloaded three-pad air foil journal bearings has been discussed. This discussion has been based on the numerical and experimental methods and results from paper I-IV [1, 2, 3, 4].

The presented numerical model captures the aerodynamic pressure generation in the air film, the deformation of the elastic foil structure under the aerodynamic pressure as well as the temperature distribution in the air film and in the surrounding components.

In a first step, the elasto-gasdynamics behavior has been studied [1]. In this study isothermal conditions have been assumed. The pressure distribution in the air films has been calculated from the Reynolds equation for compressible fluids. To obtain the deformation of the elastic foil structure, the beamshell theory according to Reissner [25] has been applied [1]. The contact between bump and top foil as well as between bump foil and bearing sleeve has been modeled by an augmented Lagrange approach. Furthermore, friction has been taken into account using Coulomb's law of friction.

In a next step, the elasto-gasdynamics model from paper I [1] has been extended by a thermal model for the air films and the surrounding structure. Therefore, the 3D heat equation for the air film as well as appropriate heat equations for the rotor, the elastic foil structure and the bearing sleeve have been applied and coupled to the elasto-gasdynamics model [3]. Furthermore, the thermal expansion of rotor and bearing sleeve have been taken into account. In order to reduce the computational effort which goes along with the numerical solution of the governing system of integro-partial differential equation, the Averaging Approach – see paper II [2] – has been used. In paper II [2], different reduction approaches have been compared with respect to the accuracy and numerical efficiency.

Besides the numerical investigations performed with the described thermo-elasto-gasdynamics model, experiments have been accomplished on two different test rigs [1, 3, 4]: On the hysteresis test rig, load-deflection tests have been conducted to determine the bearing stiffness and damping [1]. The automated high-speed test rig has been used for determining the effect of the assembly preload on the lift-off speed, the drag torque and the thermal behavior of preloaded three-pad air foil journal bearings experimentally [4]. With the results from both test rigs, the thermo-elasto-gasdynamics model has been

validated [1, 3].

The predicted and measured hysteresis curves, stiffness diagrams and bearing temperature agree well validating the thermo-elasto-gasdynamics bearing model [1, 3]. As has been shown in this synopsis, the assembly preload significantly increases the bearing stiffness and damping as intended. Advantageously, the bearing drag torque during airborne operation, the bearing temperature as well as the lift-off speed are not affected by the assembly preload. This stands in contrast to other preloading techniques which are based on an either local [18, 19, 20, 21, 22, 23, 24] or global [11, 17, 23] reduction of the air film height. Air foil bearings which are preloaded in this manner often suffer from thermal runaway caused by small bearing clearances.

In further studies, the effect of the assembly preload on the rotordynamic behavior has to be evaluated. Therefore, reduced numerical bearing models are mandatory in order to be used within run-up simulations of rotor-bearing-systems. First approaches are presented in [48, 49]. Furthermore, the dynamic behavior of rotors supported by preloaded air foil journal bearings has to be analyzed experimentally using appropriate test rigs.

References

- [1] M. Mahner, P. Li, A. Lehn, B. Schweizer, Numerical and experimental investigations on preload effects in air foil journal bearings, *Journal of Engineering for Gas Turbines and Power* 140 (3) (2018) 032505–1–032505–9. doi:10.1115/1.4037965.
- [2] M. Mahner, A. Lehn, B. Schweizer, Thermogas- and thermohydrodynamic simulation of thrust and slider bearings: Convergence and efficiency of different reduction approaches, *Tribology International* 93 (2016) 539–554. doi:10.1016/j.triboint.2015.02.030.
- [3] M. Mahner, M. Bauer, B. Schweizer, Numerical analyzes and experimental investigations on the fully-coupled thermo-elasto-gasdynamic behavior of air foil journal bearings, *Mechanical Systems and Signal Processing* 149 (2021) 107221.
- [4] M. Mahner, M. Bauer, A. Lehn, B. Schweizer, An experimental investigation on the influence of an assembly preload on the hysteresis, the drag torque, the lift-off speed and the thermal behavior of three-pad air foil journal bearings, *Tribology International* 137 (2019) 113–126.
- [5] K. Feng, Prediction of static and dynamic performance and thermohydrodynamic analysis of gas foil bearings, Ph.d. thesis, University of Tokyo (2009).
- [6] A. Lehn, Air foil thrust bearings: A thermo-elasto-hydrodynamic analysis, Ph.d. thesis, Technical University Darmstadt (2017).
- [7] H. Heshmat, W. Shapiro, S. Gray, Development of foil journal bearings for high load capacity and high speed whirl stability, *Journal of Lubrication Technology* 104 (2) (1982) 149–156, 10.1115/1.3253173. doi:10.1115/1.3253173. URL <http://dx.doi.org/10.1115/1.3253173>
- [8] D. Kim, S. Park, Hydrostatic air foil bearings: Analytical and experimental investigation, *Tribology International* 42 (3) (2009) 413–425. doi:10.1016/j.triboint.2008.08.001.

-
- [9] C. Dellacorte, M. J. Valco, Load capacity estimation of foil air journal bearings for oil-free turbomachinery applications, *Tribology Transactions* 43 (4) (2000) 795–801. doi:10.1080/10402000008982410.
- [10] T. H. Kim, L. San Andrés, Effects of a mechanical preload on the dynamic force response of gas foil bearings: Measurements and model predictions, *Tribology Transactions* 52 (4) (2009) 569–580. doi:10.1080/10402000902825721.
- [11] K. Radil, S. Howard, B. Dykas, The role of radial clearance on the performance of foil air bearings, *Tribology Transactions* 45 (4) (2002) 485–490. doi:10.1080/10402000208982578.
- [12] K. Ryu, L. San Andrés, On the failure of a gas foil bearing: High temperature operation without cooling flow, *Journal of Engineering for Gas Turbines and Power* 135 (11) (2013) 112506–1 – 112506–10. doi:10.1115/1.4025079.
- [13] C. Dellacorte, Composition optimization of chromium carbide based solid lubricant coatings for foil gas bearings at temperatures up to 650 °C, Report Contractor Report No. 179649, NASA (1987).
- [14] C. Baum, H. Hetzler, W. Seemann, On the stability of balanced rigid rotors in air foil bearings, in: 11th International Conference on Vibrations in Rotating Machines (SIRM), Magdeburg, Germany, Feb, 2015, pp. 23–25.
- [15] K. Sim, L. Yong-Bok, T. Ho Kim, J. Lee, Rotordynamic performance of shimmed gas foil bearings for oil-free turbochargers, *Journal of Tribology* 134 (3) (2012) 031102–1 – 031102–11. doi:10.1115/1.4005892.
- [16] M. Mahner, P. Li, A. Lehn, B. Schweizer, Numerical and experimental investigations on preload effects in air foil journal bearings, in: ASME Turbo Expo, Vol. Volume 7A: Structures and Dynamics, Place of Conference, 2017, p. V07AT34A006, 10.1115/GT2017-63284. doi:10.1115/GT2017-63284.
URL <http://dx.doi.org/10.1115/GT2017-63284>
- [17] D. Rubio, L. San Andrés, Bump-type foil bearing structural stiffness: Experiments and predictions, *Journal of Engineering for Gas Turbines and Power* 128 (3) (2006) 653–660. doi:10.1115/1.2056047.
- [18] D. Kim, Parametric studies on static and dynamic performance of air foil bearings with different top foil geometries and bump stiffness distributions, *Journal of Tribology* 129 (2) (2007) 354. doi:10.1115/1.2540065.

-
-
- [19] D. Kim, D. Lee, Design of three-pad hybrid air foil bearing and experimental investigation on static performance at zero running speed, *Journal of Engineering for Gas Turbines and Power* 132 (12) (2010) 122504. doi:10.1115/1.4001066.
- [20] K. Sim, B. Koo, J. Sung Lee, T. Ho Kim, Effects of mechanical preloads on the rotordynamic performance of a rotor supported on three-pad gas foil journal bearings, *Journal of Engineering for Gas Turbines and Power* 136 (12) (2014) 122503–122503–8. doi:10.1115/1.4027745.
- [21] K. Feng, H.-Q. Guan, Z.-L. Zhao, T.-Y. Liu, Active bump-type foil bearing with controllable mechanical preloads, *Tribology International* 120 (2018) 187–202.
- [22] H. Guan, T. Liu, T. Zhang, K. Feng, Z. Guo, Vibration control for rotor mounted on a novel active bump type foil bearing with controllable mechanical preloads, in: *ASME Turbo Expo 2018: Turbomachinery Technical Conference and Exposition*, Vol. Volume 7B: Structures and Dynamics, Place of Conference, 2018, p. V07BT34A028. doi:10.1115/GT2018-75894.
URL <http://dx.doi.org/10.1115/GT2018-75894>
- [23] J. Park, K. Sim, A feasibility study of controllable gas foil bearings with piezoelectric materials via rotordynamic model predictions, in: *ASME Turbo Expo 2018: Turbomachinery Technical Conference and Exposition*, Vol. Volume 7B: Structures and Dynamics, Place of Conference, 2018, p. V07BT34A034. doi:10.1115/GT2018-76273.
URL <http://dx.doi.org/10.1115/GT2018-76273>
- [24] H. Sadri, H. Schlums, M. Sinapius, Design characteristics of an aerodynamic foil bearing with adaptable bore clearance, in: *ASME Turbo Expo 2018: Turbomachinery Technical Conference and Exposition*, Vol. Volume 7B: Structures and Dynamics, Place of Conference, 2018, p. V07BT34A031. doi:10.1115/GT2018-76204.
URL <http://dx.doi.org/10.1115/GT2018-76204>
- [25] E. Reissner, On one-dimensional finite-strain beam theory: the plane problem, *Journal of Applied Mathematics and Physics (ZAMP)* 23 (5) (1972) 795–804.
- [26] D. Dowson, A generalized reynolds equation for fluid-film lubrication, *International Journal of Mechanical Sciences* 4 (2) (1962) 159–170. doi:[https://doi.org/10.1016/S0020-7403\(62\)80038-1](https://doi.org/10.1016/S0020-7403(62)80038-1).
URL <http://www.sciencedirect.com/science/article/pii/S0020740362800381>

-
- [27] A. Lehn, M. Mahner, B. Schweizer, A thermo-elasto-hydrodynamic model for air foil thrust bearings including self-induced convective cooling of the rotor disk and thermal runaway, *Tribology International* 119 (2018) 281–298. doi:<https://doi.org/10.1016/j.triboint.2017.08.015>.
URL <http://www.sciencedirect.com/science/article/pii/S0301679X17303936>
- [28] H. Heshmat, J. A. Walowit, O. Pinkus, Analysis of gas-lubricated foil journal bearings, *Journal of Lubrication Technology* 105 (1983) 647–655.
- [29] S. Le Lez, M. Arghir, J. Frene, A new bump-type foil bearing structure analytical model, *Journal of Engineering for Gas Turbines and Power* 129 (4) (2007) 1047–1057. doi:10.1115/1.2747638.
- [30] L. San Andrés, T. H. Kim, Analysis of gas foil bearings integrating fe top foil models, *Tribology International* 42 (1) (2009) 111–120. doi:10.1016/j.triboint.2008.05.003.
- [31] S. Aksoy, M. F. Aksit, A fully coupled 3d thermo-elastohydrodynamics model for a bump-type compliant foil journal bearing, *Tribology International* 82 (2015) 110–122. doi:10.1016/j.triboint.2014.10.001.
- [32] M. Carpino, L. A. Medvetz, J.-P. Peng, Effects of membrane stresses in the prediction of foil bearing performance©, *Tribology Transactions* 37 (1) (1994) 43–50. doi:10.1080/10402009408983264.
- [33] D.-H. Lee, Y.-C. Kim, K.-W. Kim, The static performance analysis of foil journal bearings considering three-dimensional shape of the foil structure, *Journal of Tribology* 130 (3) (2008) 031102–031102–10. doi:10.1115/1.2913538.
- [34] A. Libai, J. G. Simmonds, *The nonlinear theory of elastic shells*, Cambridge university press, 2005.
- [35] P. Wriggers, *Computational Contact Mechanics*, Springer-Verlag, Berlin, Heidelberg, 2006.
- [36] D. P. Bertsekas, *Constrained Optimization and Lagrange Multiplier Methods*, Computer Science and Applied Mathematics, Academic Press, Inc., San Diego, 1982.
- [37] H. G. Elrod, *Efficient numerical method for computation of thermohydrodynamics of laminar lubricating films*, Tech. rep., NASA Lewis Research Center (1989).

-
-
- [38] K. Feng, S. Kaneko, A thermohydrodynamic sparse mesh model of bump-type foil bearings, *Journal of Engineering for Gas Turbines and Power* 135 (2) (2013).
- [39] M. Mahner, A. Lehn, B. Schweizer, Reduction approaches for thermogasdynamic lubrication problems, *Proc. Appl. Math. Mech.* 15 (2015) 405–406. doi:10.1002/pamm.201510193.
URL <http://dx.doi.org/10.1002/pamm.201510193>
- [40] D. Lee, D. Kim, Three-dimensional thermohydrodynamic analyses of rayleigh step air foil thrust bearing with radially arranged bump foils, *Tribology Transactions* 54 (3) (2011) 432–448. doi:10.1080/10402004.2011.556314.
- [41] H. G. Elrod, D. E. Brewster, Thermohydrodynamic analysis for laminar lubricating films, Tech. rep., NASA Technical Memorandum 88845 (1986).
- [42] L. E. Moraru, Numerical prediction and measurements in the lubrication of aeronautical engine and transmission components, Ph.D. thesis, University of Toledo (2005).
- [43] M. Salehi, E. Swanson, H. Heshmat, Thermal features of compliant foil bearings—theory and experiments, *Journal of Tribology* 123 (3) (2001) 566. doi:10.1115/1.1308038.
- [44] M. Conlon, A. Dadouche, W. Dmochowski, R. Payette, J.-P. Bédard, B. Liko, Experimental evaluation of foil bearing performance: Steady-state and dynamic results, in: *ASME Turbo Expo 2009: Power for Land, Sea, and Air*, American Society of Mechanical Engineers, 2009, pp. 981–992.
- [45] M. Conlon, A. Dadouche, W. Dmochowski, R. Payette, J.-P. Bédard, A comparison of the steady-state and dynamic performance of first-and second-generation foil bearings, in: *ASME Turbo Expo 2010: Power for Land, Sea, and Air*, American Society of Mechanical Engineers, 2010, pp. 453–462.
- [46] L. San Andrés, J. Norsworthy, Measurement of drag torque, lift off speed and rotor-dynamic force coefficients in a shimmed bfb, in: *IFTToMM International Conference on Rotor Dynamics*, Proceedings of the 9th IFTToMM International Conference on Rotor Dynamics, Springer International Publishing, 2015, pp. 909–919.
- [47] C. Dellacorte, V. Lukaszewicz, M. J. Valco, K. C. Radil, H. Heshmat, Performance and durability of high temperature foil air bearings for oil-free turbomachinery, *Tribology Transactions* 43 (4) (2000) 774–780. doi:10.1080/10402000008982407.

-
- [48] P. Zeise, M. Mahner, M. Bauer, M. Rieken, B. Schweizer, A reduced model for air foil journal bearings for time-efficient run-up simulations, in: ASME Turbo Expo 2019: Turbomachinery Technical Conference and Exposition, Vol. Volume 7B: Structures and Dynamics, Phoenix, Arizona, USA, 2019.
- [49] P. Zeise, M. Mahner, M. Bauer, M. Rieken, B. Schweizer, A reduced semi-analytical gas foil bearing model for transient run-up simulations, in: 12th International Conference on Vibrations in Rotating Machinery, CRC Press, London, 2020, pp. 575–587.

A. Effect of the Bump Foil Initial Radius on the Bearing Performance

For investigating the effect of an increased bump foil radius on the bearing hysteresis, on the foil structural stiffness, on the shutdown torque and on the bearing and rotor temperature, additional tests are accomplished. The dimensions of the test bearing equal the dimensions of the lightly preloaded bearing from paper IV [4], except for the bump foil radius. For this test, the bump foil radius is increased to $r_b = 34$ mm.

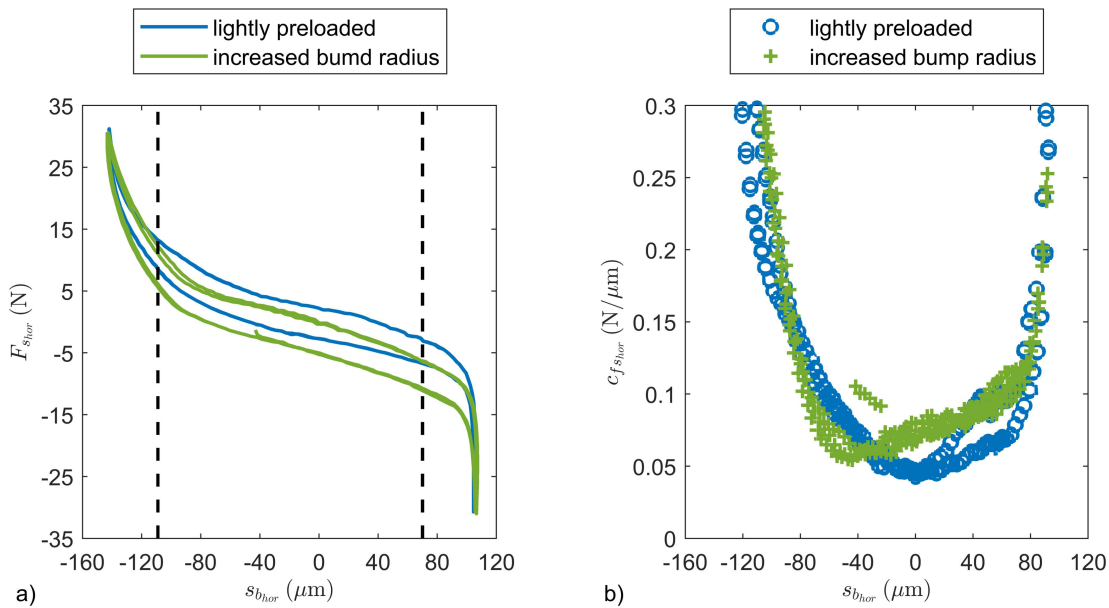


Figure A.1.: Measured hysteresis curves (a) and foil structural stiffness (b) for the lightly preloaded bearing and for the bearing with increased bump radius. The dashed lines indicate the normal operating regime of both bearings.

As shown in Figs. A.1-A.3, the foil structural stiffness at small bearing displacements is increased, while the shutdown torque as well as the bearing and rotor temperature are not significantly affected by the increased bump foil radius.

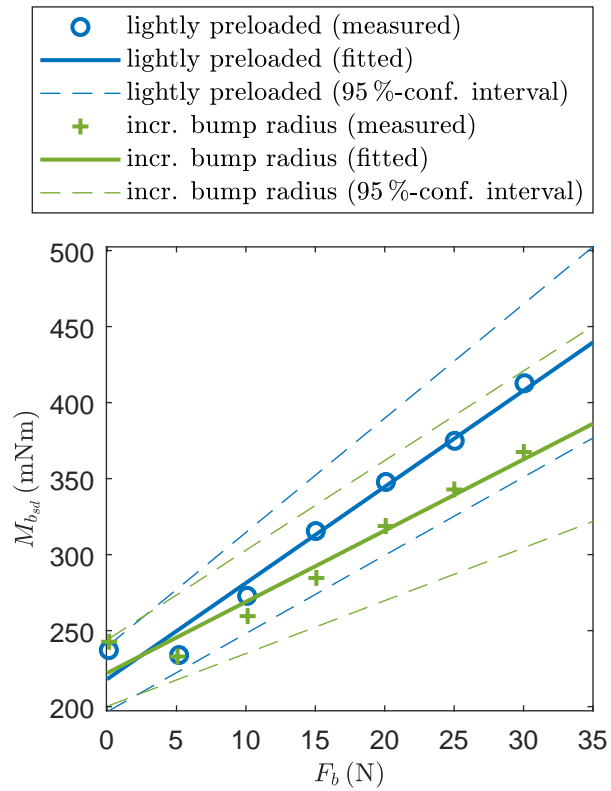


Figure A.2.: Measured and fitted shutdown torque of the lightly preloaded bearing and of the bearing with increased bump radius over the bearing load

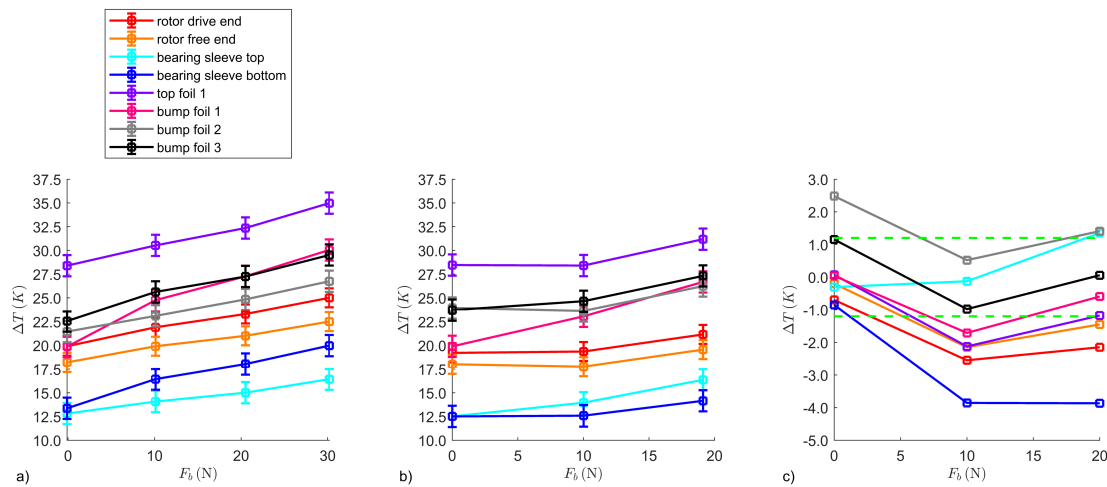


Figure A.3.: Measured temperature increase for the heavily preloaded bearing (a) and for the bearing with increased bump radius (b) over the bearing load. The temperature differences between the heavily preloaded bearing and the bearing with increased bump radius are depicted in c).

B. Effect of the Bump Height on the Bearing Performance

Now, the effect of an increased bump height on the bearing hysteresis, the lift-off speed, the shutdown torque and on the thermal behavior is discussed. The geometry of the investigated bearing equals the dimensions of the heavily preloaded bearing from paper IV [4], except for the bump height. Each bump is about $27\ \mu\text{m}$ higher than the corresponding bump of the heavily preloaded bearing.

Figure B.1 shows the hysteresis (a) and the foil structural stiffness (b) of the heavily preloaded bearing and of the bearing with increased bump height. As can be seen in Fig. B.1a), the bearing normal operating regime (dashed lines) is reduced by about $29\ \mu\text{m}$. This corresponds to the above mentioned rise in the bump height of about $27\ \mu\text{m}$. The foil structural stiffness at zero displacement increases by 32.56%, while the frictional loss decreases from 1.4 mJ to 1 mJ. The latter decrease can be traced back to the reduced overall displacement of the bearing sleeve.

The lift off-speed of the heavily preloaded bearing and of the bearing with increased bump height are depicted in Fig. B.2 over the bearing load. As shown in Fig. B.2 the lift-off speed of the bearing with increased bump height rises with the bearing load for $F_b \leq 20\ \text{N}$.

Figure B.3 shows the measured and the fitted shutdown torque over the bearing load for the heavily preloaded bearing and for the bearing with increased bump height. As expected, the shutdown torque of the bearing with increased bump height is larger than the shutdown torque of the heavily preloaded bearing.

The temperature increase of the different bearing components and of the rotor are depicted in Fig. B.4 for the heavily preloaded bearing (a) and for the bearing with increased bump height (b). The temperature differences between the heavily preloaded bearing and the bearing with increased bump height are depicted in Fig. 2.9c). The dashed lines indicate the measurement uncertainty of the thermocouples. As can be seen from the figure, the bearing and rotor temperatures rise caused by the smaller operating regime of the bearing with the increased bearing preload. This proves that a global reduction of the air film height leads to larger bearing temperatures with the risk of a thermal

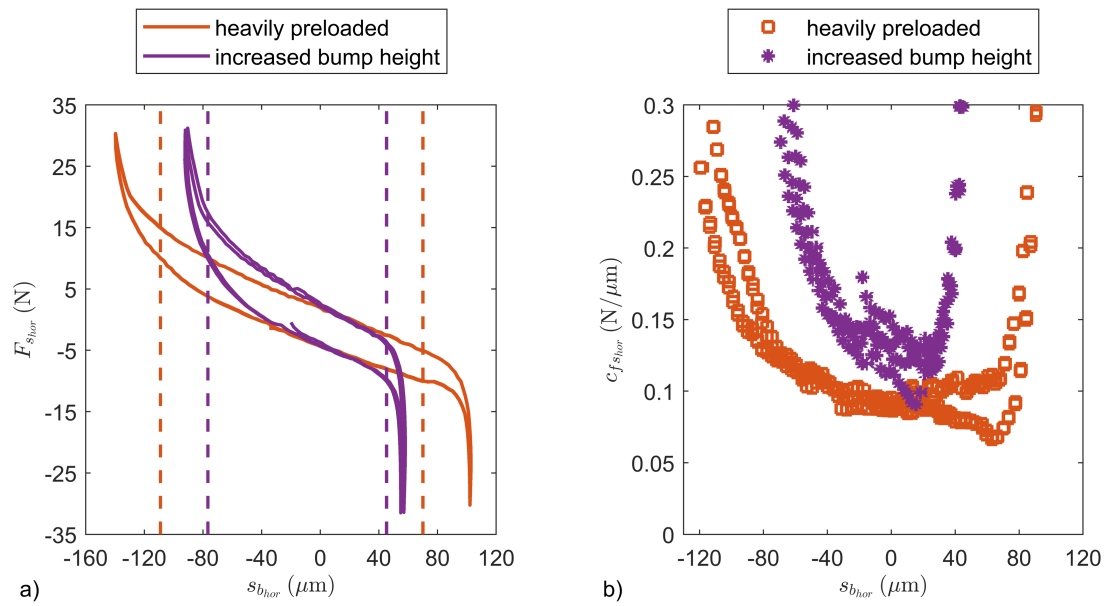


Figure B.1.: Measured hysteresis curves (a) and foil structural stiffness (b) for the heavily preloaded bearing and for the bearing with increased bump height. The dashed lines indicate the normal operating regime for both bearings.

instability [11, 12].

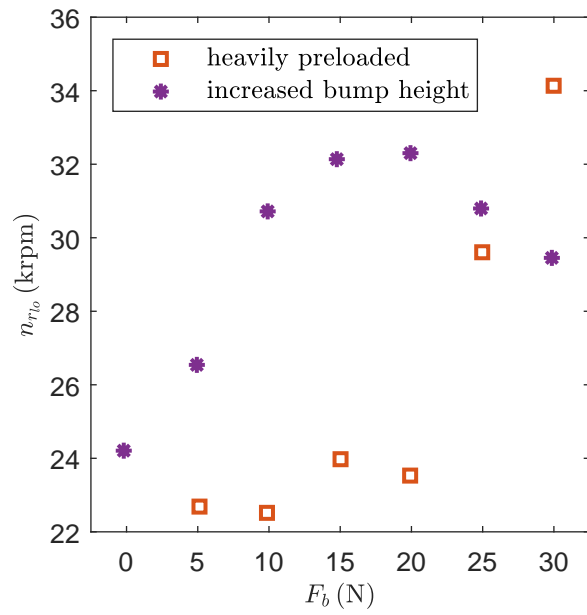


Figure B.2.: Measured lift-off speed for the heavily preloaded bearing and for the bearing with increased bump height over the bearing load

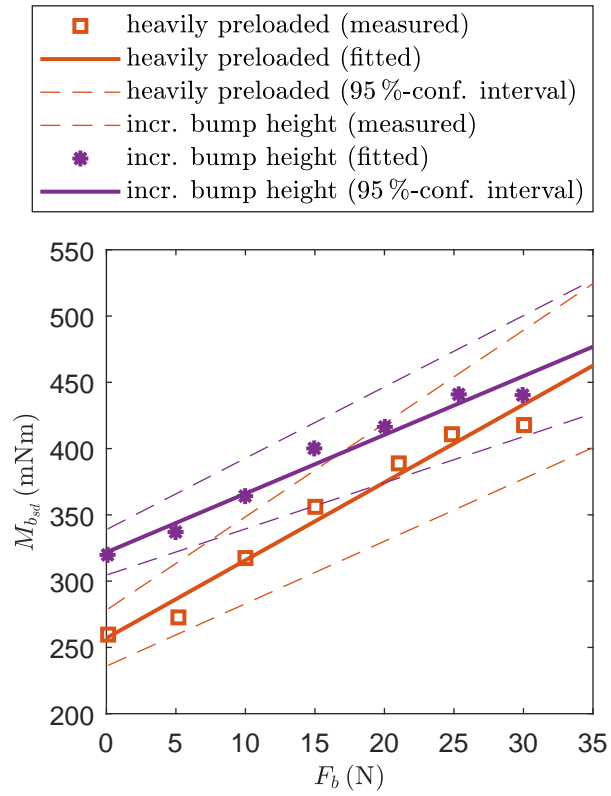


Figure B.3.: Measured and fitted shutdown torque of the heavily preloaded bearing and of the bearing with increased bump height over the bearing load

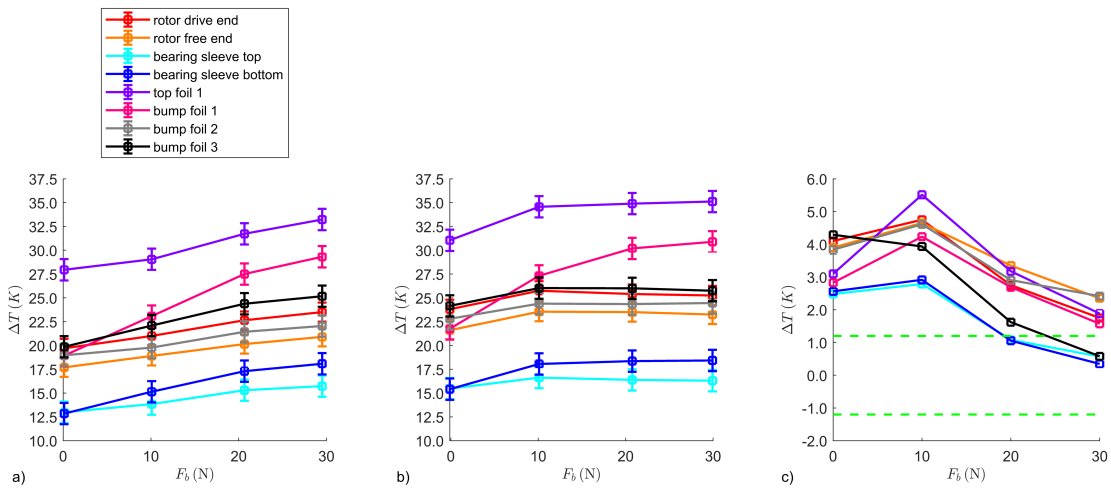


Figure B.4.: Measured temperature increase for the heavily preloaded bearing (a) and for the bearing with increased bump height (b) over the bearing load. The temperature differences between the heavily preloaded bearing and the bearing with increased bump height are depicted in c).



Paper I

M. Mahner, P. Li, A. Lehn, B. Schweizer, Numerical and Experimental Investigations on Preload Effects in Air Foil Journal Bearings, ASME. J. Eng. Gas Turbines Power, March 2018, 140(3): 032505.

©2018. This manuscript version is made available under the CCC license 1092849-1.

Marcel Mahner¹

Department of Mechanical Engineering,
Institute of Applied Dynamics,
Technical University of Darmstadt,
Otto-Berndt-Straße 2,
Darmstadt 64287, Germany
e-mail: mahner@ad.tu-darmstadt.de

Pu Li

Department of Mechanical Engineering,
Institute of Applied Dynamics,
Technical University of Darmstadt,
Otto-Berndt-Straße 2,
Darmstadt 64287, Germany
e-mail: li@ad.tu-darmstadt.de

Andreas Lehn

Department of Mechanical Engineering,
Institute of Applied Dynamics,
Technical University of Darmstadt,
Otto-Berndt-Straße 2,
Darmstadt 64287, Germany
e-mail: lehn@ad.tu-darmstadt.de

Bernhard Schweizer

Department of Mechanical Engineering,
Institute of Applied Dynamics,
Technical University of Darmstadt,
Otto-Berndt-Straße 2,
Darmstadt 64287, Germany
e-mail: schweizer@ad.tu-darmstadt.de

Numerical and Experimental Investigations on Preload Effects in Air Foil Journal Bearings

A detailed elastogasdynamic model of a preloaded three-pad air foil journal bearing is presented. Bump and top foil deflections are herein calculated with a nonlinear beam-shell theory according to Reissner. The two-dimensional pressure distribution in each bearing pad is described by the Reynolds equation for compressible fluids. The assembly preload is calculated by simulating the assembly process of top foil, bump foil, and shaft. Most advantageously, there is no need for the definition of an initial radial clearance in the presented model. With this model, the influence of the assembly preload on the static bearing hysteresis as well as on the aerodynamic bearing performance is investigated. For the purpose of model validation, the predicted hysteresis curves are compared with measured curves. The numerically predicted and the measured hysteresis curves show a good agreement. The numerical predictions exhibit that the assembly preload increases the elastic foil structural stiffness (in particular for moderate shaft displacements) and the bearing damping. It is observed that the effect of the fluid film on the overall bearing stiffness depends on the assembly preload: For lightly preloaded bearings, the fluid film affects the overall bearing stiffness considerably, while for heavily preloaded bearings the effect is rather small for a wide range of reaction forces. Furthermore, it is shown that the assembly preload increases the friction torque significantly.

[DOI: 10.1115/1.4037965]

1 Introduction

Air foil journal bearings are frequently used to support shafts in rotating devices, for instance in microgas turbines or in rotor systems for fuel cell applications, where oil-free bearings are mandatory, see, e.g., Refs. [1] and [2]. Air bearings have different advantages compared to oil bearings. They are simple and inexpensive to produce, and they provide a minor maintenance effort [1]. Due to the elastic foil structure, air foil journal bearings have the ability to accommodate journal misalignment and radial growth induced by thermal and centrifugal effects, see, e.g., Ref. [3].

In order to increase the onset speed of subsynchronous motions and to decrease the subsynchronous rotor oscillations, three-pad configurations are often used instead of simple circular one-pad designs, see Ref. [4]. Three-pad air foil journal bearings consist of a rigid bearing sleeve and three pairs of bump and top foil, see Fig. 1. The bump foil is a corrugated foil, which induces compliance and damping to the bearing. The top foil provides a smooth surface for the gasdynamic pressure generation.

For different reasons, an assembly preload of top and bump foil is introduced in air foil journal bearings by using top and bump foils whose nominal, initial radii (r_t , r_b) are larger than the inner radius of the bearing sleeve r_i and the outer radius of the shaft r_s , see the initial configuration of top and bump foil in Fig. 1. This initial configuration refers to the undeformed state of top and bump foil after their manufacturing and before their assembly in the bearing sleeve. During the assembly process of top and bump foil, the foils are elastically bended into the bearing sleeve. In

order to assemble the air foil journal bearing on the shaft, the top and bump foils are pushed against the bearing sleeve manually. After this assembly force is released, the top and bump foils will elastically unbend, and the top foils will contact the rotor, see the assembly configuration in Fig. 1. This leads to an interference between the shaft and the elastic foil structure [2,3]: the top foil contacts the shaft surface, and consequently, there is no initial clearance between the top foil and the shaft, see Fig. 1. Due to the initial deformation of top and bump foil in the assembly configuration, the elastic foil structural stiffness and damping increases. It is important to note that the assembly preload discussed here differs from the definition of the aerodynamic preload in other works, see, e.g., Refs. [5–8]. In these works, the aerodynamic preload was defined as a wedge, which is introduced either by shimming of the bump foil or by providing a lobe in the bearings sleeve. The shimming of the bump foil mainly leads to an increase in the overall bearing stiffness and damping and a decreasing radial clearance [6]. While the shimming of the bump foil does not increase the elastic foil structural stiffness significantly, it mainly affects the stiffness of the air film which leads to an increase in the overall bearing stiffness. Contrarily, the assembly preload increases the elastic foil structural stiffness for small shaft displacements.

As a consequence of the assembly preload—especially discussed within this paper—the stiffness of the bearing for small shaft eccentricities as well as the bearing damping is increased. In order to predict the influence of the assembly preload on the bearing hysteresis and on the aerodynamic bearing performance, a detailed elastogasdynamic bearing model is mandatory.

A crucial aspect concerning the development of a comprehensive air foil bearing model is the description of bump and top foil deflections due to the gasdynamic pressure acting on the top foil. In the past decades, many analytical and numerical models were

¹Corresponding author.

Contributed by the Structures and Dynamics Committee of ASME for publication in the JOURNAL OF ENGINEERING FOR GAS TURBINES AND POWER. Manuscript received July 19, 2017; final manuscript received July 25, 2017; published online October 17, 2017. Editor: David Wisler.

established in order to describe the static and dynamic behavior of the compliant foil structure. These models can be divided in three groups regarding their level of detail: elastic foundation type models, detailed analytical models, and numerical models based on a finite element approach.

In simple elastic foundation type models, the bump foil is modeled as an elastic foundation, while the top foil is assumed to follow the bump deflection and is therefore not modeled at all. The stiffness of the foundation is calculated based on beam models for a single bump with different assumptions regarding the boundary conditions of the bump [9–13].

Besides the simple elastic foundation type models, comprehensive analytical models of the bump foil, which account for the kinematic and kinetic coupling between the bumps were developed by different authors, e.g., see Refs. [14–16]. These models were used in order to study the static and dynamic behavior of the bump foil. The results obtained with these models showed that the bump stiffness depends on the load distribution on the top foil and that the bump stiffness decreases from the fixed end to the free end. Furthermore, it was observed that the deformation of the segments between adjacent bumps significantly affects the bump foil stiffness.

The previously mentioned works assumed that the top foil follows the bump deflections. Consequently, the top foil sagging effect and a potential top foil lift off were not taken into account in these models. Different authors investigated the effect of the top foil deflection on the performance of air foil bearings using finite element models for the top foil, see, e.g., Refs. [17–19]. In these works, the bump foil was modeled using continuous elastic foundation type models [17], discrete springs [18], or more comprehensive analytical models as discussed above [19]. These works showed that the top foil deflection in air foil journal bearings is approximately constant along the bearing width. This indicated that one-dimensional (1D) structural models might be appropriate in order to describe the foil deflections in air foil journal bearings. In a recent study, Leister et al. [20] developed a 1D runtime efficient model of the foil structure by dividing the top foil in segments whose length are equal to the bump pitch. An analytical expression for the deflection of the top foil segments was derived by these authors.

In the past decade, different finite element models of the bump foil were presented in order to accurately determine the stiffness

and damping properties of the elastic foil structure [21,22] or to accomplish detailed elastogasdynamic studies [23,24].

While a lot of different top and bump foil models were developed in the past, relatively few investigations on the effect of an assembly preload on the hysteresis as well as on the aerodynamic performance of air foil journal bearings were accomplished. Radil et al. [2] analyzed the effect of an assembly preload experimentally. They used an oversized shaft which consequently produces an interference with the top foil. Therefore, the top foil is pushed against the shaft surface by the bump foils creating an assembly preload. This preload was indirectly measured by defining a radial clearance as the half distance between the stiff areas in a hysteresis loop. They observed that there exists an optimum radial clearance at which the load capacity reaches a maximum. Rubio and San Andrés [3] accomplished load-deflection tests with different shaft diameters in order to study the influence of a preload on the stiffness of an air foil journal bearing. Furthermore, they introduced a simple model for predicting the stiffness for different bearing deflections by modeling the bumps as springs whose stiffness was calculated using Iordanoff's formula [11]. The bearing preload was accounted for by a precompression of the springs due to the larger shaft diameter. Predictions and experimental results showed a good agreement. Feng and Kaneko [19] calculated an effective radial clearance based on the results of a load-deflection test which was then used in their elasto-aerodynamic model of an air foil journal bearing. Kim [7] was the first who introduced an aerodynamic preload to a three-pad air foil journal bearing by lobing of the bearing sleeve. He numerically showed that the preloaded three-pad air foil journal bearing has a higher onset speed of instability compared to a simple one pad-design. In a further study, Kim and Lee [8] extended the preloaded three-pad air foil journal bearing design by an external air injection at each top foil center. In a recent work, Mahner et al. [25] introduced an elastogasdynamic bearing model which accounts for an assembly preload. The model predictions were compared to hysteresis measurements showing a good agreement.

In this manuscript, a detailed elastogasdynamic model of a preloaded three-pad air foil journal bearing will be presented. This model correctly accounts for an assembly preload by a geometrical exact representation of the top and the bump foil initial configuration. The assembly preload is predicted by calculating the top and bump foil deflections due to the assembly process using the nonlinear 1D beamshell theory according to Reissner [26,27]. The pressure distribution in each bearing pad is described by the Reynolds equation for compressible fluids. Both, the nonlinear beamshell equations as well as the Reynolds equation are solved with a fully coupled nonlinear finite element approach. With this model, the effect of the assembly preload on the static hysteresis and on the aerodynamic performance of a preloaded three-pad air foil journal bearing will be discussed. For the purpose of model validation, load-deflection tests are accomplished experimentally and compared with numerical model predictions. Most advantageously, there is no need for the definition of an initial radial clearance between the top foil and the shaft within the presented model: The actual clearance (gap function) can be obtained from the current top foil configuration and the current shaft position only. In previous models, see, e.g., Refs. [18] and [19], the gap function was calculated based on the assumption of an initial radial clearance. In these models, the initial radial clearance was either empirically obtained following geometrical considerations [18] or derived from hysteresis measurements [19]. Since the gap function has a crucial influence on the aerodynamic bearing performance [2], it is important to accurately account for the actual radial clearance in an air foil journal bearing model.

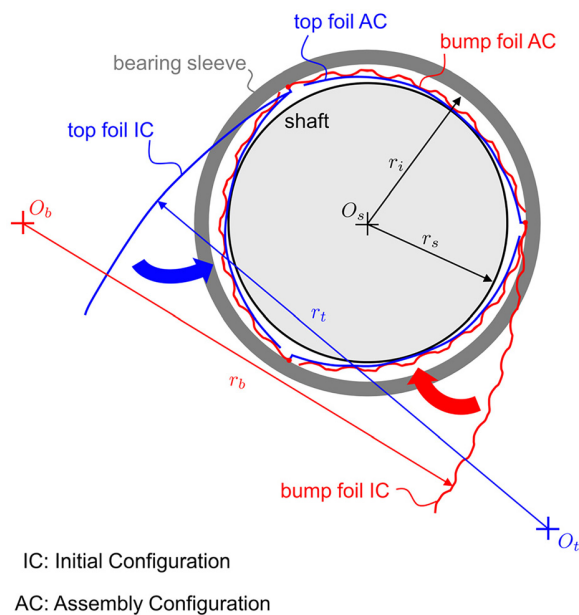


Fig. 1 Preloaded three-pad air foil journal bearing with top and bump foils in initial configuration and in assembly configuration

2 Elastogasdynamic Bearing Model

The elastogasdynamic model incorporates the description of the gasdynamic pressure distribution in the convergent gap between top foil and shaft as well as the description of the elastic

deformation of bump and top foil. In this paper, thermal effects, which in general have a crucial influence on the bearing performance, will be neglected in order to focus on the effects arising from the elastic foil structure. Assuming isothermal conditions and an ideal gas behavior, the pressure distribution in the gas film in the i th bearing pad (length L_i , width b_i) is described by the Reynolds equation for compressible fluids

$$\frac{1}{1 + \varepsilon_i} \frac{\partial}{\partial s_i} \left(\frac{1}{1 + \varepsilon_i} \frac{p_i h_i^3}{\eta} \frac{\partial p_i}{\partial s_i} \right) + \frac{\partial}{\partial z} \left(\frac{p_i h_i^3}{\eta} \frac{\partial p_i}{\partial z} \right) = - \frac{6r_s \Omega}{1 + \varepsilon_i} \frac{\partial(p_i h_i)}{\partial s_i} \quad \forall i = 1, 2, 3 \quad (1)$$

with the boundary conditions

$$\begin{aligned} p_i(s_i = 0, z) \\ = p_i(s_i = L_i, z) = p_i(s_i, z = 0) = p_i(s_i, z = b_i) = p_a \\ \forall i = 1, 2, 3 \end{aligned} \quad (2)$$

Herein, p_i denotes the pressure in the i th bearing pad; η represents the dynamic viscosity of air at a constant temperature; r_s and Ω denote the radius and the angular velocity of the shaft. Furthermore, p_a is the ambient pressure. Since the Reynolds equation is projected onto the deformed top foil surface, the elongation of the top foil in normal direction is accounted for by the factor $1/(1 + \varepsilon_i)$ in the Reynolds equation (1), where ε_i denotes the normal strain of each top foil. s_i and z are the tangential and axial coordinates of the top foil. h_i represents the gap function which is obtained from the distance between the current shaft position and the current top foil position

$$h_i = \sqrt{(x_i + u_i - x_{O_s})^2 + (y_i + v_i - y_{O_s})^2} - r_s \quad (3)$$

Herein, x_i and y_i denote the global x - and y -coordinates of the i th top foil in the initial configuration. The entities u_i and v_i are the displacement of the i th top foil in x - and y -direction. x_{O_s} and y_{O_s} represent the global x - and y -coordinates of the shaft center in the current configuration.

Since the current position of the top foil is calculated based on the initial undeformed top foil configuration by considering the deformation during the assembly process, the gap functions result only from the top foil and the shaft displacement. There is no need for the definition of an initial radial clearance. In case of the preloaded three-pad air foil journal bearing, discussed within this

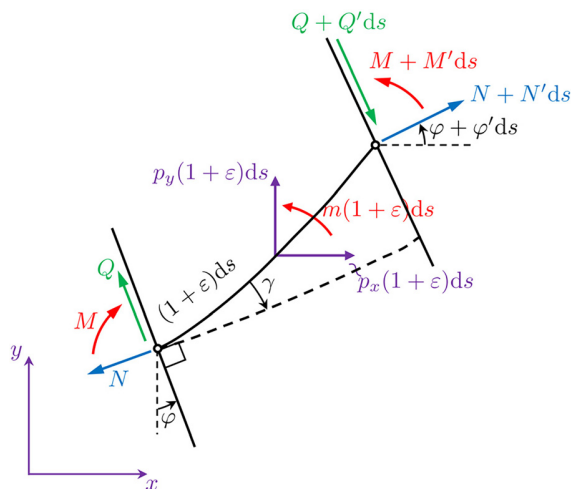


Fig. 2 Free body diagram of an infinitesimal beamshell segment [26]

paper, there is no initial radial clearance between the top foil and the shaft: The top foil contacts the shaft even in the unloaded, perfectly aligned case. Boundary and mixed lubrication regimes occurring due to high loads or during rotor start-up or shut-down are neglected in this study. For the predictions of the aerodynamic bearing performance, full-film lubrication is assumed. In a further study, boundary and mixed lubrication regimes will be considered by using an appropriate approach, see, e.g., [28,29].

Assuming a constant foil thickness, Reissner–Mindlin kinematics, and plane strain assumption along the bearing width, the deformation of bump and top foil is described by the nonlinear 1D beamshell theory according to Reissner [26,27]. The assumption of plain strain in axial direction is justified by the stiffening effect due to the membrane forces in the top and bump foil as already observed in Refs. [17] and [23]. A geometrically nonlinear theory is mandatory, since large deformations occur during the assembly process of top and bump foil due to the assembly preload. While the deformations are large, it is assumed that the normal, shear, and bending strains remain small. The assumption of Reissner–Mindlin kinematics yields the following kinematic relations for the beamshell

$$\varepsilon = (x' + u') \cos \varphi + (y' + v') \sin(\varphi) - 1 \quad (4)$$

$$\gamma = (x' + u') \sin \varphi - (y' + v') \cos(\varphi) \quad (5)$$

$$\kappa = \varphi' - \varphi'_0 \quad (6)$$

x and y denote the global coordinates of the beamshell in the initial configuration. u and v are the displacement of the beamshell along the x - and the y -axes, respectively. The entity φ expresses the orientation of the cross section in the current configuration, while φ_0 is the cross section orientation in the initial configuration. ε , γ , and κ denote the normal, shear, and bending strain. $(\cdot)'$ = $\partial(\cdot)/\partial s$ represent the partial derivative with respect to the tangential beamshell coordinate s .

The principle of virtual work yields the equilibrium equations

$$[N \cos(\varphi) + Q \sin(\varphi)]' = -p_x(1 + \varepsilon) \quad (7)$$

$$[N \sin(\varphi) - Q \cos(\varphi)]' = -p_y(1 + \varepsilon) \quad (8)$$

$$M' = (1 + \varepsilon)Q - \gamma N - m(1 + \varepsilon) \quad (9)$$

Equations (7) and (8) describe the force equilibrium in x - and y -directions, whereas Eq. (9) represents the equilibrium of moments about the z -axis. N , Q , and M are the normal and the shear force as well as the bending moment about the z -axis, see Fig. 2. Note, that N , Q , and M are related to the beamshell width.

The moment load density is denoted by m . The pressure on the beamshell in x - and y -directions is represented by p_x and p_y , respectively. In case of the elastogasdynamic bearing model, the pressures p_{x_i} and p_{y_i} on the i th top foil are obtained from the solution of the Reynolds equation (1). Since the beamshell theory is only one-dimensional, the two-dimensional pressure distribution obtained from the Reynolds equation (1) is averaged along the bearing width

$$\bar{p}_i = \frac{1}{b_i} \int_{z=0}^{b_i} p_i dz \quad \forall i = 1, 2, 3 \quad (10)$$

yielding an average pressure \bar{p}_i in the i th bearing pad [18,30]. With the averaged pressure \bar{p}_i , the pressures p_{x_i} and p_{y_i} on the i th top foil can be obtained from

$$p_{x_i}(1 + \varepsilon_i) = \sin(\varphi_i)(1 + \varepsilon_i)\bar{p}_i - \gamma_i \cos(\varphi_i)\bar{p}_i \quad (11)$$

$$p_{y_i}(1 + \varepsilon_i) = -\cos(\varphi_i)(1 + \varepsilon_i)\bar{p}_i - \gamma_i \sin(\varphi_i)\bar{p}_i \quad (12)$$

with the index i ($i = 1, 2, 3$) indicating the three top foils.

With the assumption of small strains and considering isotropic material behavior, the linear constitutive equations are given by

$$N = \frac{EH}{1 - \nu^2} \varepsilon \quad (13)$$

$$M = \frac{EH^3}{12(1 - \nu^2)} \kappa \quad (14)$$

$$Q = \alpha_s GH \gamma \quad (15)$$

where E and ν are the elastic modulus and the Poisson's ratio of the beamshell material. The thickness of top and bump foil is denoted by H . α_s represents the shear correction factor.

The leading edge of bump and top foil are assumed as free ends, whereas the trailing edges are attached to the bearing sleeve.

The contact between bump and top foil as well as the contact between bump foil and bearing sleeve are modeled by a node-to-surface approach. The no-penetration condition in normal direction is enforced using an augmented Lagrange approach [31,32] which allows for the separation of bump and top foil as well as for the separation of bump foil and bearing sleeve. In tangential direction, the friction force is calculated using Coulomb's law of friction

$$F_T = -\mu \frac{\dot{g}_T}{|\dot{g}_T|} F_N \quad (16)$$

Herein, F_T and F_N denote the tangential and normal force at each contact point; μ is the coefficient of friction; \dot{g}_T represents the relative tangential velocity of a contact slave node with respect to the master surface. The signum function in the friction law is regularized using an elastic slip approach, see Ref. [32].

For the prediction of the static hysteresis of air foil journal bearings, the rotational speed of the shaft is set to zero ($\Omega = 0$). Therefore, the shaft contacts the top foil surface since no air film is considered. Due to friction reduction coatings on the top foil and the shaft, their contact is assumed to be frictionless. The no penetration condition between the shaft and the top foil is enforced using a penalty approach.

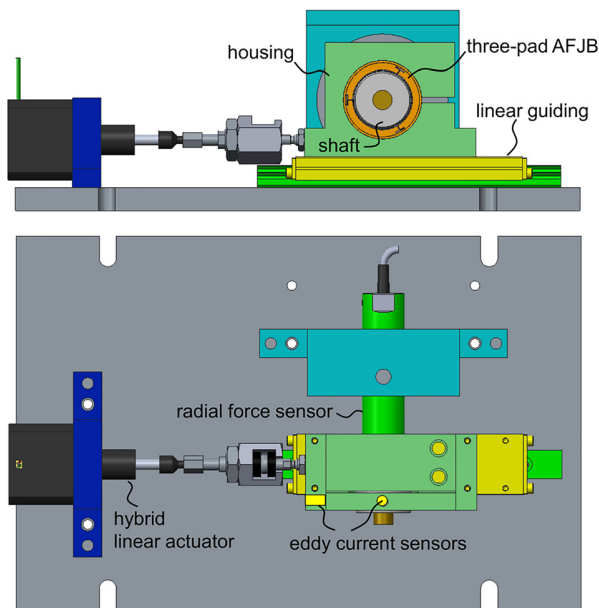


Fig. 3 Device for the automated measurement of air foil journal bearing hystereses

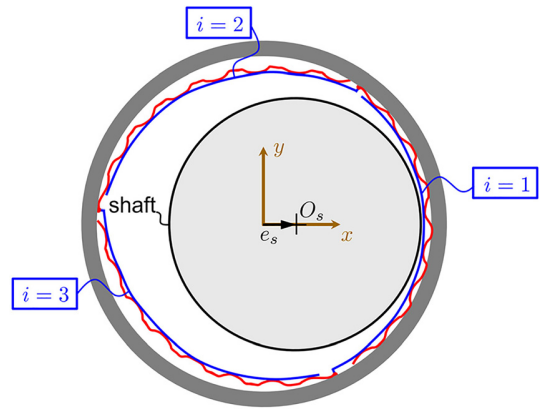


Fig. 4 Direction of shaft displacement in the load-deflection test

The governing set of differential and algebraic equations is solved using a fully coupled nonlinear finite element approach.

3 Experimental Setup and Procedure

In this study, hysteresis curves are measured using an automated device shown in Fig. 3. In this device, the air foil journal bearing is clamped in a housing which is mounted on a linear guiding. A motion is applied to the housing by a hybrid linear actuator (stepper motor, step size: $1.5 \mu\text{m}$). The shaft is rigidly mounted on a radial force sensor equipped with strain gauges (sensitivity: 99.6255 mV/N). The relative motion between bearing and shaft is measured by two perpendicular eddy current sensors (sensitivity: 10.5972 V/mm , 10.1533 V/mm).

During the hysteresis measurement, the shaft is automatically moved by the hybrid linear actuator by a fixed number of steps. The force on the shaft as well as the relative displacement between the shaft and the housing are simultaneously measured for 1 s after each movement of the hybrid linear actuator (sampling rate: 1000 Hz). Afterward, the measured quantities are averaged. This procedure is automatically repeated until the hysteresis curve reaches a closed loop.

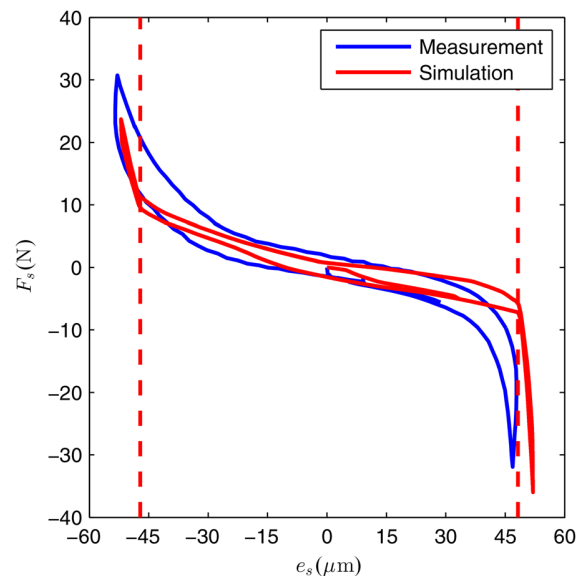


Fig. 5 Measured and predicted hysteresis curve of the lightly preloaded three-pad air foil journal bearing

Table 1 Parameters of the lightly preloaded three-pad air foil journal bearing

Parameter	Value
Overall bearing parameters	
Bearing width, b	27 mm
Shaft radius, r_s	15 mm
Bearing sleeve inner radius, r_i	15.739 mm
Number of pads	3
Top and bump foil parameters	
Top foil radius, r_t	15 mm
Top foil length, L_t	31.098 mm
Number of bumps per bump foil	8
Bump foil radius, r_b	24.828 mm
Segment length, a_{se}	1.145 mm
Bump height, h_b	0.513 mm
Bump pitch, a_p	3.848 mm
Top and bump foil thickness, H	100 μm
Top foil coating thickness, H_{cot}	40 μm
Elastic modulus of top and bump foil, E	$2.1 \times 10^{11} \text{ N/m}^2$
Poisson's ratio of top and bump foil, ν	0.3
Shear correction factor of top and bump foil, α_s	5/6

4 Experimental Model Validation

To validate the presented structural model of top and bump foil, the predicted and measured static hysteresis curves are compared.

A numerical prediction of the static hysteresis is achieved with the previously described bearing model by quasi-statically moving the nonrotating shaft with the harmonic function $e_s = \hat{e}_s \sin(2\pi t)$ in the direction of the top foil center of the first bearing pad, see Fig. 4. Herein, \hat{e}_s denotes the amplitude of the harmonic shaft displacement. Since inertia effects are neglected, the mathematical problem is frequency independent. Therefore, t is regarded as a nondimensional parameter here. The simulations are accomplished until the hysteresis curve reaches a closed loop.

Note, that the assembly process of top and bump foil is simulated before the hysteresis calculation is accomplished in order to calculate the assembly configuration of top and bump foil, see Fig. 1.

Figure 5 shows the measured and the numerically predicted hysteresis curves of the lightly preloaded three-pad air foil journal bearing whose parameters are summarized in Table 1. F_s denotes

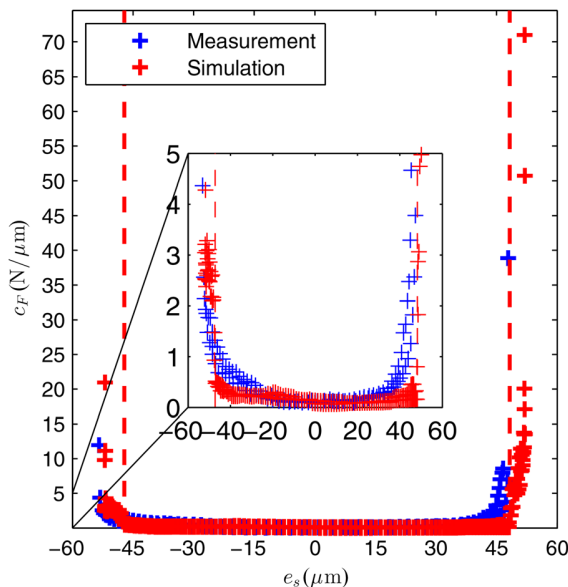


Fig. 6 Measured and predicted elastic foil structural stiffness of the lightly preloaded three-pad air foil journal bearing

the resulting reaction force on the shaft in the direction of the applied shaft motion. The area enclosed by the hysteresis loop represents the friction loss W_D which determines the bearing damping. The elastic foil structural stiffness c_F is derived from the hysteresis curves by using first-order central differences. The results are depicted in Fig. 6. As can be detected from Figs. 5 and 6, both, simulation and measurement, exhibit that the elastic foil structural stiffness increases with the shaft displacement e_s . For moderate shaft displacements ($-47 \mu\text{m} < e_s < 48 \mu\text{m}$ for the simulation), the stiffness is rather low and nearly constant. For larger displacements, the stiffness increases significantly. The elastic foil structural stiffness at moderate shaft displacements is caused by the assembly preload. Without an assembly preload, the stiffness would be zero in this area. For larger shaft displacements, more bumps contact the bearing sleeve. This explains the rise in the bearing stiffness. When nearly all bumps are in contact with the bearing sleeve, the stiffness is significantly increased. Predicted and measured hysteresis curves show a rather good agreement. The differences in the friction loss might be traced back to the uncertainty of the coefficient of friction. Furthermore, the friction between the shaft and the top foils is neglected in this study. This might also be a reason for the differences in the enclosed area of the hysteresis loop. Conlon et al. [33,34] experimentally obtained that the friction between the shaft and the top foil has an effect on the bearing damping.

The discrepancies in the stiffness might stem from manufacturing and assembly errors. Manufacturing errors of the bump foil mainly affect the bump height which has a crucial influence on the shaft displacement at which the significant increase of the stiffness will occur. The transition from the area of small stiffness to the area of large stiffness is smoother in the measurement compared to the simulation. This might be caused by a small misalignment ($< 7 \mu\text{m}$) between the shaft and the bearing sleeve in the experimental setup.

5 Effect of the Assembly Preload on the Static Bearing Hysteresis

To show the effect of the assembly preload of top and bump foil on the static bearing hysteresis, an additional load-deflection simulation with a larger assembly preload is accomplished at zero running speed ($\Omega = 0$). Top and bump foil radius of this heavily preloaded air foil journal bearing are $r_t = r_b = 50 \text{ mm}$. All other

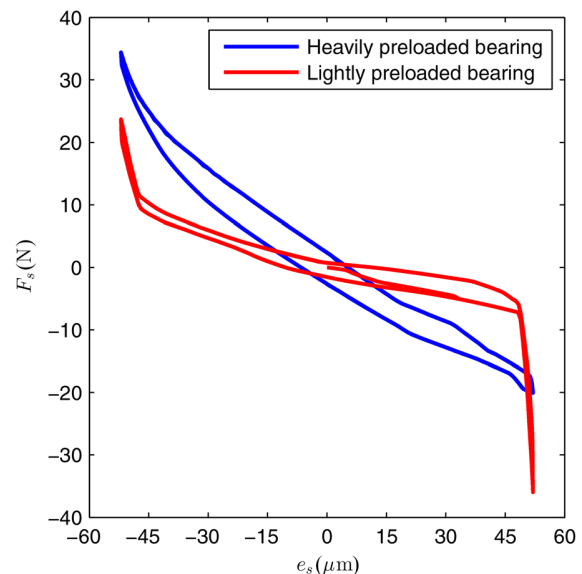


Fig. 7 Hysteresis curves for different assembly preloads of top and bump foil

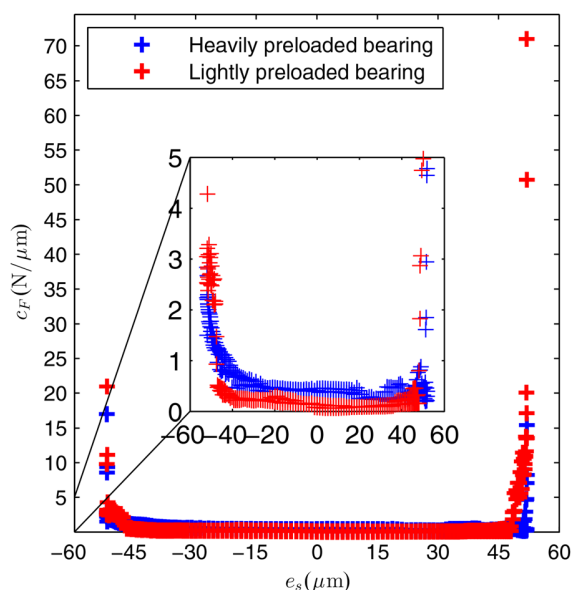


Fig. 8 Elastic foil structural stiffness for different assembly preloads of top and bump foil

bearing parameters are the same as in the lightly preloaded case, see Table 1.

Figures 7 and 8 depict the hysteresis curves and the elastic foil structural stiffness for the lightly and the heavily preloaded three-pad air foil journal bearing over the shaft displacement e_s . As can be seen from the figures, the elastic foil structural stiffness for moderate shaft displacements and the area enclosed by the hysteresis loop significantly increases with the assembly preload: the elastic foil structural stiffness, c_F , is increased by a factor of approximately 3 at zero shaft displacement. The friction loss rises by a factor of 1.77 to $W_D = 0.43$ mJ. The rise of the bearing damping is mainly caused by the larger friction forces due to the assembly preload. The larger friction forces as well as geometrically nonlinear effects induced by the assembly preload explain the increase of the elastic foil structural stiffness.

Although the assembly preload is increased, the heavily preloaded bearing has a smaller maximum force compared to the

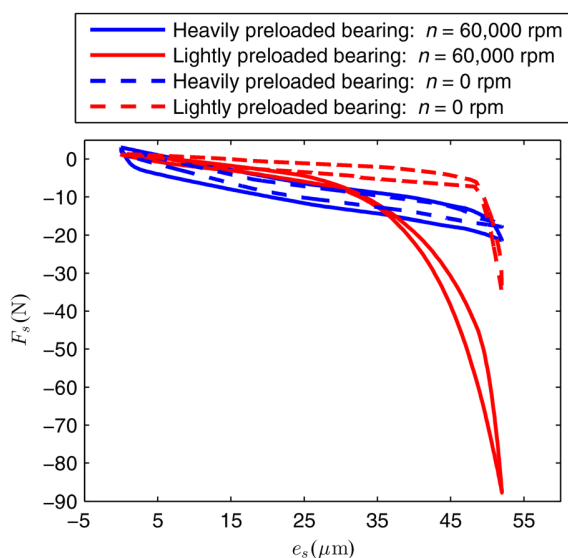


Fig. 9 Hysteresis curves with rotating and nonrotating shaft for different assembly preloads of top and bump foil

lightly preloaded bearing. For the heavily preloaded bearing, there is no significant increase in the stiffness for the depicted shaft displacement. This effect is caused by the larger bump and top foil deformation during the assembly process of top and bump foil for the heavily preloaded bearing. This bending deformation leads to a flattening of the bump foil due to which the clearance between the bump foil and the bearing sleeve in the assembly configuration will increase.

6 Effect of the Assembly Preload on the Aerodynamic Bearing Performance

In order to investigate the effect of the air film on the bearing stiffness and on the bearing damping, load-deflection simulations with a rotating shaft ($n = 60,000$ rpm, approximated lift-off speed from measurements: 20,000–25,000 rpm) are accomplished along with static load-deflection simulations at zero running speed. For both cases, the shaft displacement is described by the harmonic function $e_s = \hat{e}_s/2 [1 - \cos(2\pi t)]$. To calculate the pressure distribution in the air film, the Reynolds equation (1) is solved fully coupled with the structural model of top and bump foil. The numerical simulations are accomplished with $\eta = 19.25 \times 10^{-6}$ Pa-s and $p_a = 1 \times 10^5$ Pa. Again, the simulations are accomplished until the hysteresis curve reaches a closed loop.

Figure 9 depicts the resultant force F_s on the shaft in the direction of the applied motion over the shaft displacement e_s for the static load-deflection simulations as well as for the simulations with a rotating shaft.

For the same shaft displacement, the reaction force F_s is larger for the rotating shaft compared to the simulations with the nonrotating shaft. For the lightly preloaded bearing, the calculated minimum film thickness at the maximum force of $F_s = -87.74$ N is $h_{\min} = 1.95$ μm thus indicating that the load capacity is already nearly reached. The highly preloaded bearing has a minimum film thickness of $h_{\min} = 3.51$ μm at force of $F_s = -21.28$ N.

As in the case of the static load-deflection simulations at zero running-speed, the bearing damping is significantly increased due to the assembly preload, see Fig. 9. For the lightly preloaded bearing, the friction loss with rotating shaft is $W_D = 0.15$ mJ, while for the heavily preloaded bearing a friction loss of $W_D = 0.26$ mJ is obtained from the hysteresis curve. The friction losses are larger

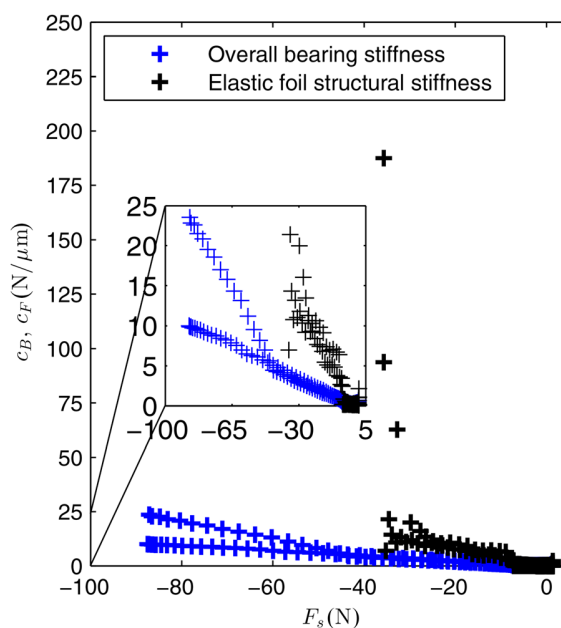


Fig. 10 Overall bearing stiffness and elastic foil structural stiffness for the lightly preloaded bearing

as in the case of the static load-deflection simulation at zero running-speed, see Fig. 9 (lightly preloaded bearing: $W_D=0.11$ mJ, heavily preloaded bearing: $W_D=0.13$ mJ). This can be explained by the different pressure distributions on the top foil: For the static load-deflection test, the top foil contacts the shaft at small areas which leads to a very localized contact pressure distribution on the top foil. In case of the rotating shaft, the pressure distribution in the fluid film leads to a smooth and nonlocalized pressure distribution. Due to this pressure distribution, more bumps are in contact either with the bearing sleeve or the top foil leading to a larger friction loss. For the same shaft displacement, the force F_s is larger for the running shaft compared to the nonrotating shaft leading to a larger area enclosed by the hysteresis loop.

Contrarily, Conlon et al. [33,34] showed experimentally that the overall bearing damping is smaller than the structural damping. The authors concluded that the friction between the shaft and the top foil in case of the structural testings leads to the detected increase of the structural damping. Since the friction between the shaft and the top foil has been neglected in this study, the presented model cannot predict this effect.

Figures 10 and 11 present the overall bearing stiffness, c_B , for the lightly and the heavily preloaded bearing over the reaction force F_s . The overall bearing stiffness stems from the fluid film and from the elastic foil structure. The figures also show the elastic foil structural stiffness c_F obtained from the static load-deflection simulations at zero running speed. As can be obtained from the figures, the bearing preload significantly affects the impact of the fluid film on the overall bearing stiffness.

For the lightly preloaded bearing, see Fig. 10, the elastic foil structural stiffness is larger than the overall bearing stiffness for $|F_s| > 7.2$ N. This result correlates with the experimental findings of Conlon et al. [33,34]. The decrease of the stiffness due to the air film is plausible since the elastic foil structure and the fluid film can be considered as two serially arranged nonlinear springs, see, e.g., Ref. [35]. Nevertheless, the elastic foil structural stiffness is slightly smaller than the overall bearing stiffness for $|F_s| < 7.2$ N. This effect can be traced back to the dependency of the elastic foil structural stiffness on the load distribution as already experimentally and numerically shown by several authors, see, e.g., Refs. [14], [16], and [36]. The load distributions on the top foil at an equal reaction force F_s in case of the load deflection

tests with rotating and with nonrotating shaft are different due to two main reasons: On the one hand, the forces perpendicular to the reaction force F_s are unequal. On the other hand, the fluid film pressure acting on the top foil is smoother and less localized compared to the contact pressure between the top foil and the shaft in case of the static load-deflection tests at zero running-speed. Consequently, more bumps are in contact either with the top foil or the bearing sleeve in case of the rotating shaft. Furthermore, the fluid film stiffness is larger than the elastic foil structural stiffness for $|F_s| < 7.2$ N. Both increases of the stiffness compared to the elastic foil structural stiffness lead to the fact that the overall bearing stiffness is larger than the elastic foil structural stiffness for $|F_s| < 7.2$ N.

For the heavily preloaded bearing, see Fig. 11, the bearing stiffness and the elastic foil structural stiffness show very similar values for a wide range of reaction forces F_s except for the area of decreasing overall bearing stiffness. This indicates that the overall bearing stiffness is primary determined by the elastic foil structural stiffness for a wide range of reaction forces. Otherwise, in the area of decreasing overall bearing stiffness, the overall bearing stiffness is larger than the elastic foil structural stiffness. This can again be explained by the differences between the fluid film pressure distribution and the contact pressure distribution leading to an increase in the number of active bumps in the case of the rotating shaft. Furthermore, the fluid film stiffness is larger than the elastic foil structural stiffness in the area of decreasing overall bearing stiffness. Again, both effects lead to the increase of the overall bearing stiffness compared to the elastic foil structural stiffness.

Figure 12 shows the friction torque M_s on the shaft for the lightly and the heavily preloaded bearing over the shaft displacement e_s . Due to the assembly preload, the friction torque is significantly increased. Note, that while the shaft displacement in case of the lightly and the heavily preloaded bearing are the same, the shaft force F_s is larger for the lightly preloaded bearing for $e_s > 37.6$ μm , see Fig. 9. As a consequence of the larger friction torque of the heavily preloaded bearing, the temperature rise in the bearing will be larger leading to a risk of a thermal runaway.

Since the contact forces between the top foil and the shaft are larger for the heavily preloaded case, the starting torque will increase significantly. Furthermore, the assembly preload reduces the load capacity of the bearing.

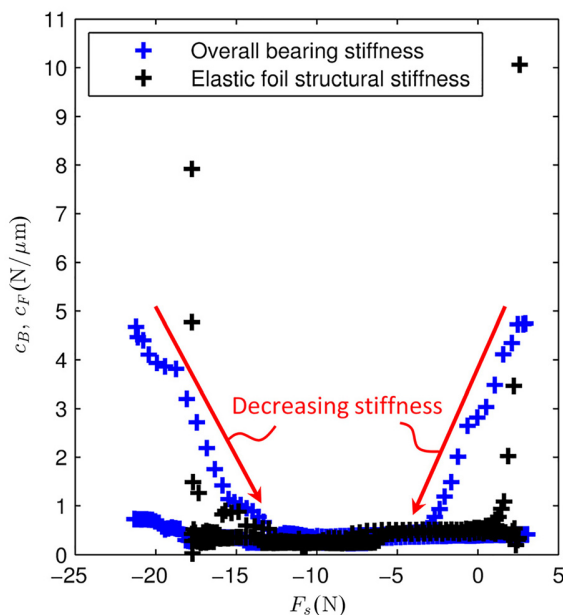


Fig. 11 Overall bearing stiffness and elastic foil structural stiffness for the heavily preloaded bearing

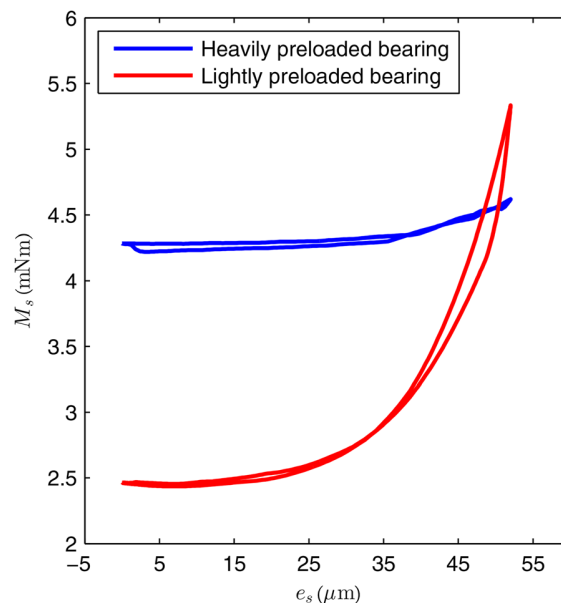


Fig. 12 Friction torque on the shaft for different assembly preloads of top and bump foil

7 Conclusions

A detailed elastogasdynamic model of a preloaded three-pad air foil journal bearing has been presented. This model correctly accounts for the effect of an assembly preload by using a geometrically nonlinear beamshell theory. The initial geometry of top and bump foil has been accounted for in order to calculate the assembly preload. Most advantageously, there is no need for the definition of an initial radial clearance in the presented model. The pressure distribution in the fluid film between shaft and top foil has been described by the Reynolds equation for compressible fluids. The set of differential equations has been solved with a fully coupled nonlinear finite element approach.

For the purpose of model validation, a numerically predicted static hysteresis curve has been compared with a measurement. The results show a good agreement. Furthermore, load-deflection simulations with different levels of assembly preload have been accomplished. The results show that the assembly preload significantly increases the elastic foil structural stiffness for moderate shaft displacements as well as the bearing damping.

To show the effect of the assembly preload on the aerodynamic bearing performance, load-deflection simulations with a rotating shaft have also been realized. The effect of the fluid film on the overall bearing stiffness depends on the assembly preload; for lightly preloaded bearings, the overall stiffness is affected by the fluid film, while for heavily preloaded bearings the effect is rather small for a wide range of reaction forces. It has further been shown that a larger assembly preload leads to a significant rise in the friction and starting torque.

Nomenclature

a_p = bump pitch (m)
 a_{se} = segment length (m)
 b = bearing width (m)
 c_B, c_F = overall bearing stiffness and elastic foil structural stiffness (N/m)
 E = elastic modulus (N/m²)
 \hat{e}_s = amplitude of the harmonic shaft displacement (m)
 e_s = shaft displacement (m)
 F_N = normal force at a contact slave node (N)
 F_s = reaction force on the shaft in the direction of the applied shaft motion (N)
 F_T = tangential force at a contact slave node (friction force) (N)
 \dot{g}_T = relative tangential velocity of a contact slave node (m/s)
 H = thickness of top and bump foil (m)
 h_b = bump height (m)
 h_i = gap function of the i th bearing pad (m)
 H_{cot} = top foil coating thickness (m)
 $i = 1, 2, 3$ indicating the three top foils
 L_t, b_t = top foil length and width (m)
 m = moment load density about the z -axis (N/m)
 M = bending moment about the z -axis, related to the beamshell width (N)
 M_s = friction torque on the shaft (Nm)
 n = rotational speed of the shaft (rpm)
 N = normal force, related to the beamshell width (N/m)
 \bar{p}_i = averaged pressure in the i th bearing pad (Pa)
 p_a = ambient pressure (Pa)
 p_i = pressure in the i th bearing pad (Pa)
 p_x, p_y = pressure on the beamshell in x - and y -directions (Pa)
 p_{x_i}, p_{y_i} = pressure on the i th top foil in x - and y -directions (Pa)
 Q = shear force, related to the beamshell width (N/m)
 r_s, r_i = shaft radius and bearing sleeve inner radius (m)
 r_t, r_b = top and bump foil radius (m)
 s, s_t = tangential coordinates (m)
 t = nondimensional parameter
 u, v = displacement of the beamshell along the x - and y -axes (m)

u_i, v_i = displacement of the i th top foil along the x - and y -axes (m)
 W = bearing load (N)
 W_D = friction loss (bearing damping) (J)
 x, y = global x - and y -coordinates of the beamshell in the initial configuration (m)
 x_{O_s}, y_{O_s} = global x - and y -coordinates of the shaft center (m)
 z = axial coordinate of the top foil (m)
 α_s = shear correction factor
 ϵ, κ = beamshell normal and shear strain
 η = dynamic viscosity (Pa s)
 κ = beamshell bending strain (m⁻¹)
 μ = coefficient of friction
 ν = Poisson's ratio
 φ_0, φ = orientation of the beamshell cross section about the global z -axis in the initial and in the current configuration (rad)
 Ω = angular velocity of the shaft ($\Omega = n\pi/30$) (s⁻¹)
 $(\cdot)'$ = derivative with respect to s

References

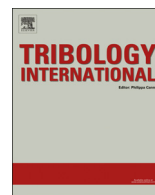
- [1] Dellacorte, C., and Valco, M. J., 2000, "Load Capacity Estimation of Foil Air Journal Bearings for Oil-Free Turbomachinery Applications," *Tribol. Trans.*, **43**(4), pp. 795–801.
- [2] Radil, K., Howard, S., and Dykas, B., 2002, "The Role of Radial Clearance on the Performance of Foil Air Bearings," *Tribol. Trans.*, **45**(4), pp. 485–490.
- [3] Rubio, D., and San Andrés, L., 2006, "Bump-Type Foil Bearing Structural Stiffness: Experiments and Predictions," *ASME J. Eng. Gas Turbines Power*, **128**(3), pp. 653–660.
- [4] Heshmat, H., Shapiro, W., and Gray, S., 1982, "Development of Foil Journal Bearings for High Load Capacity and High Speed Whirl Stability," *ASME J. Lubr. Technol.*, **104**(2), pp. 149–156.
- [5] Kim, T. H., and San Andrés, L., 2009, "Effects of a Mechanical Preload on the Dynamic Force Response of Gas Foil Bearings: Measurements and Model Predictions," *Tribol. Trans.*, **52**(4), pp. 569–580.
- [6] Sim, K., Koo, B., Sung Lee, J., and Ho Kim, T., 2014, "Effects of Mechanical Preloads on the Rotordynamic Performance of a Rotor Supported on Three-Pad Gas Foil Journal Bearings," *ASME J. Eng. Gas Turbines Power*, **136**(12), p. 122503.
- [7] Kim, D., 2007, "Parametric Studies on Static and Dynamic Performance of Air Foil Bearings With Different Top Foil Geometries and Bump Stiffness Distributions," *ASME J. Tribol.*, **129**(2), pp. 354–364.
- [8] Kim, D., and Lee, D., 2010, "Design of Three-Pad Hybrid Air Foil Bearing and Experimental Investigation on Static Performance at Zero Running Speed," *ASME J. Eng. Gas Turbines Power*, **132**(12), p. 122504.
- [9] Walowit, J. A., and Anno, J. N., 1975, *Modern Developments in Lubrication Mechanics*, Applied Science Publisher Ltd., London.
- [10] Heshmat, H., Walowit, J. A., and Pinkus, O., 1983, "Analysis of Gas-Lubricated Foil Journal Bearings," *ASME J. Lubr. Technol.*, **105**(4), pp. 647–655.
- [11] Iordnaoff, I., 1999, "Analysis of an Aerodynamic Compliant Foil Thrust Bearing: Method for a Rapid Design," *ASME J. Tribol.*, **121**(4), pp. 816–822.
- [12] Kim, D., Ezeka, C., and Kumar, M., 2007, "Revisit to Stiffness of Bump Foils in Air Foil Bearings," *ASME Paper No. IJTC2007-44319*.
- [13] Arghir, M., Deville, L., and Pion, J.-B., 2007, "About the Stiffness of Bumps in Aerodynamic Foil Bearings," Society of Tribologists and Lubrication Engineers (STLE) 70th Annual Meeting and Exhibition, Dallas, TX, May 17–21.
- [14] Ku, C.-P. R., and Heshmat, H., 1992, "Compliant Foil Structural Stiffness Analysis—Part I: Theoretical Model Including Strip and Variable Bump Foil Geometry," *ASME J. Tribol.*, **114**(2), pp. 394–400.
- [15] Ku, C. P. R., and Heshmat, H., 1994, "Structural Stiffness and Coulomb Damping in Compliant Foil Journal Bearings: Theoretical Considerations," *Tribol. Trans.*, **37**(3), pp. 525–533.
- [16] Le Lez, S., Arghir, M., and Frene, J., 2007, "A New Bump-Type Foil Bearing Structure Analytical Model," *ASME J. Eng. Gas Turbines Power*, **129**(4), pp. 1047–1057.
- [17] Carpino, M., Medvetz, L. A., and Peng, J.-P., 1994, "Effects of Membrane Stresses in the Prediction of Foil Bearing Performance," *Tribol. Trans.*, **37**(1), pp. 43–50.
- [18] San Andrés, L., and Kim, T. H., 2009, "Analysis of Gas Foil Bearings Integrating FE Top Foil Models," *Tribol. Int.*, **42**(1), pp. 111–120.
- [19] Feng, K., and Kaneko, S., 2010, "Analytical Model of Bump-Type Foil Bearings Using a Link-Spring Structure and a Finite-Element Shell Model," *ASME J. Tribol.*, **132**(2), p. 021706.
- [20] Leister, T., Baum, C., and Seemann, W., 2016, "Computational Analysis of Foil Air Journal Bearings Using a Runtime-Efficient Segmented Foil Model," International Symposium on Transport Phenomena and Dynamics of Rotating Machinery (ISROMAC), Honolulu, HI, Apr. 10–15.
- [21] Le Lez, S., Arghir, M., and Frene, J., 2007, "Static and Dynamic Characterization of a Bump-Type Foil Bearing Structure," *ASME J. Tribol.*, **129**(1), pp. 75–83.
- [22] Żywica, G., 2011, "The Static Performance Analysis of the Foil Bearing Structure," *Acta Mech. Autom.*, **5**(4), pp. 119–122.

- [23] Lee, D.-H., Kim, Y.-C., and Kim, K.-W., 2008, "The Static Performance Analysis of Foil Journal Bearings Considering Three-Dimensional Shape of the Foil Structure," *ASME J. Tribol.*, **130**(3), p. 031102.
- [24] Lehn, A., Mahner, M., and Schweizer, B., 2016, "Elasto-Gasdynamics Modeling of Air Foil Thrust Bearings With a Two-Dimensional Shell Model for Top and Bump Foil," *Tribol. Int.*, **100**, pp. 48–59.
- [25] Mahner, M., Li, P., Lehn, A., and Schweitzer, B., 2016, "Elastogasdynamic Model for Air Foil Journal Bearings: Hysteresis Prediction Including Preloading Effects," Society of Tribologists and Lubrication Engineers (STLE), *71st Annual Meeting and Exhibition*, Las Vegas, NV, May 15–19.
- [26] Reissner, E., 1972, "On One-Dimensional Finite-Strain Beam Theory: The Plane Problem," *J. Appl. Math. Phys. (ZAMP)*, **23**(5), pp. 795–804.
- [27] Libai, A., and Simmonds, J. G., 2005, *The Nonlinear Theory of Elastic Shells*, Cambridge University Press, Cambridge, UK.
- [28] Hu, Y.-Z., and Zhu, D., 2000, "A Full Numerical Solution to the Mixed Lubrication in Point Contacts," *ASME J. Tribol.*, **122**(1), pp. 1–9.
- [29] Xiong, S., Wang, Q. J., Liu, W. K., Yang, Q., Vaidyanathan, K., Zhu, D., and Lin, C., 2006, "Approaching Mixed Elastohydrodynamic Lubrication of Smooth Journal-Bearing Systems With Low Rotating Speed," *Tribol. Trans.*, **49**(4), pp. 598–610.
- [30] San Andrés, L., and Kim, T. H., 2007, "Improvements to the Analysis of Gas Foil Bearings: Integration of Top Foil 1D and 2D Structural Models," *ASME Paper No. GT2007-27249*.
- [31] Bertsekas, D. P., 1982, "Constrained Optimization and Lagrange Multiplier Methods," *Computer Science and Applied Mathematics*, Academic Press, San Diego, CA.
- [32] Wriggers, P., 2006, *Computational Contact Mechanics*, Springer-Verlag, Berlin.
- [33] Conlon, M., Dadouche, A., Dmochowski, W., Payette, R., and Bédard, J.-P., 2009, "A Comparison of the Steady-State and Dynamic Performance of First- and Second-Generation Foil Bearings," *ASME Paper No. GT2010-23683*.
- [34] Conlon, M., Dadouche, A., Dmochowski, W., Payette, R., Bédard, J.-P., and Liko, B., 2010, "Experimental Evaluation of Foil Bearing Performance: Steady-State and Dynamic Results," *ASME Paper No. GT2009-60186*.
- [35] Hoffmann, R., Munz, O., Pronobis, T., Barth, E., and Liebich, R., 2016, "A Valid Method of Gas Foil Bearing Parameter Estimation: A Model Anchored on Experimental Data," *Proc. Inst. Mech. Eng. Part C*, epub.
- [36] Ku, C. P. R., and Heshmat, H., 1993, "Compliant Foil Bearing Structural Stiffness Analysis-Part II: Experimental Investigation," *ASME J. Tribol.*, **115**(3), pp. 364–369.

Paper II

M. Mahner, A. Lehn, and B. Schweizer, Thermogas- and thermohydrodynamic simulation of thrust and slider bearings: Convergence and efficiency of different reduction approaches, Tribology International, 2016, 93: pp. 539-554.

©2016. This manuscript version is made available under the CC-BY-NC-ND 4.0 license
<http://creativecommons.org/licenses/by-nc-nd/4.0/>



Thermogas- and thermohydrodynamic simulation of thrust and slider bearings: Convergence and efficiency of different reduction approaches



Marcel Mahner*, Andreas Lehn, Bernhard Schweizer

Technical University Darmstadt, Department of Mechanical Engineering, Institute of Applied Dynamics, Otto-Berndt-Strasse 2, 64287 Darmstadt, Germany

ARTICLE INFO

Article history:

Received 10 September 2014

Received in revised form

24 February 2015

Accepted 27 February 2015

Available online 9 March 2015

MSC:

00-01

99-00

Keywords:

Fluid film bearings

Thermogasdynamic

Thermohydrodynamic

Reduction approaches

ABSTRACT

The pressure and temperature distribution in gas thrust and oil slider bearings are described by the generalized Reynolds equation according to Dowson and the 3D energy equation. In this paper, two different approaches are presented in order to reduce the dimension of the governing nonlinear integro-differential equation system and in order to stabilize the solution process. In the first reduction approach, the temperature in the fluid is averaged across the fluid film according to Lee and Kim. In the second approach, Legendre polynomials are used to approximate temperature, density and fluidity across the fluid film. The reduction techniques are compared with respect to numerical efficiency, accuracy and convergence behavior.

© 2015 Elsevier Ltd. All rights reserved.

1. Introduction

In many technical applications with rotating devices (gas turbines, turbochargers, etc., see e.g. [1–3]), oil thrust bearings are used to support a shaft in the axial direction. To describe the pressure and temperature distribution in the fluid film of oil thrust bearings, the geometry of thrust bearing pads is frequently simplified and the finite slider bearing is used to analyze and optimize thrust bearing pads, see for instance Ezzat and Rohde [4]. For low loads and low rotational speeds, the pressure field in the oil film of slider bearings may satisfactorily be described by the classical isothermal Reynolds equation. For higher loads and speeds, an isothermal approach is, however, not sufficient, because temperature/viscosity-dependency has to be taken into account to obtain reliable pressure distributions, see Huebner [5]. In this case, the pressure and temperature field are described by the generalized Reynolds equation according to Dowson [6] and the 3D energy equation.

Instead of oil thrust bearings, gas thrust bearings are often used in order to reduce costs, weight and maintenance effort. Gas thrust bearings may advantageously be applied in low-load applications, e.g. in air cycle machines, in gas turbines or in rotor systems for fuel cell applications [7,8]. For gas thrust bearings, considering

temperature effects is often necessary, because of the temperature/viscosity-dependency of the gas and due to the fact that the density of the gas is a function of pressure and temperature. As for oil bearings, the generalized Reynolds equation and the 3D energy equation have to be used to compute the pressure and temperature field in gas thrust bearings.

The generalized Reynolds equation in combination with the 3D energy equation mathematically represents a nonlinear integro-differential equation system for both the thermohydrodynamic and the thermogasdynamic case. Solving this integro-differential equation system by a finite element approach entails a high computational effort, see e.g. Elrod [9] and Feng and Kaneko [10]. Due to the nonlinearity of the problem, also convergence problems are frequently observed.

Based on a Galerkin approach, Elrod and Brewe [11] describe a numerically efficient method to solve the generalized Reynolds equation in combination with the 3D energy equation for the case that Dirichlet boundary conditions are assumed at the top and bottom of the fluid film. In their approach, they take into account the temperature/viscosity-dependency, but they neglect the temperature and pressure dependency of the fluid density. Temperature and fluidity are approximated by Legendre polynomials of order three across the fluid film. Thereby, the integrals occurring in the generalized Reynolds equation are calculated using a Lobatto point quadrature method. The 3D energy equation is reduced to 2D space by enforcing the moments of the energy equation to be zero, see [11]. Moraru [12] has shown that for the

* Corresponding author. Tel.: +49 6151 16 4215.

E-mail address: mahner@sds.tu-darmstadt.de (M. Mahner).

Nomenclature

A_U, B_U	dimensionless constants in the Ubbelohde–Walther relation (66)	p_a	ambient pressure (Pa)
A_{ij}	second order tensor, $A_{ij} = P_j(\zeta_i)$	p^*	averaged pressure across the fluid film (Pa)
A_{pad}	pad surface area (m ²)	r, θ, z	cylindrical coordinates (m, rad, m)
B	width of the oil slider bearing (m)	r_1, r_2	inner and outer radius of the thrust bearing pad (m)
C	fluid specific constant in the Sutherland equation (29) (K)	t	time (s)
D_i	discretization across the fluid film	t_c	simulation time (s)
F_0, F_1	Dowson integrals (m/(Pa s), m ² /(Pa s))	u, v	longitudinal and transverse fluid velocities in the oil slider bearing (m/s)
F_2, F_3	Dowson integrals (kg/(Pa s), kg/(Pa s m))	v_r	radial fluid velocity (m/s)
G_1, G_2, G_3	Dowson integrals (kg/(Pa s), kg/(Pa s m), kg/m ²)	v_θ	circumferential fluid velocity (m/s)
I_{ji}	inverse tensor of A_{ij} , $I_{ji} = (A^{-1})_{ji}$	w	fluid velocity in the z-direction (m/s)
L	length of the oil slider bearing (m)	x, y, z	Cartesian coordinates (m)
N	maximum polynomial order in the polynomial approximation for temperature, density and fluidity across the fluid film	z^*	ratio of Dowson integrals, $z^* = F_1/F_0$ (m)
$N_{a,\bar{r}}, N_{a,\bar{\theta}}$	number of nodes used for the estimation of the relative error in temperature and pressure	$\Delta l_{\bar{r}}, \Delta l_{\bar{\theta}}$	dimensionless length of a finite element in the \bar{r} -, $\bar{\theta}$ - and ζ -direction
$P_j(\zeta)$	j -th Legendre polynomial	$\Delta l_{\bar{z}}$	dimensionless length of a finite element in the \bar{z} -direction
$Pe_{\bar{r}}^e, Pe_{\bar{\theta}}^e$	element Péclet number in the \bar{r} -, $\bar{\theta}$ - and ζ -direction	Δr	difference between outer and inner pad radius, $\Delta r = r_2 - r_1 = \text{const.}$ (m)
Pe_{ζ}^e	ζ -direction	Ω	angular velocity of the runner (1/s)
R_{th}	thermal resistivity of the rotor (K/W)	Φ_{cyl}	dissipation term in the energy equation (21) (N/(m ² s))
T	fluid temperature (K)	θ_0	pad angle (rad)
T_0, T_1	reference temperatures in the relations (67) and (68) (K)	α	fluidity of the fluid (1/(Pa s))
T_R	reference temperature in the Sutherland equation (29) (K)	$\tilde{\alpha}_j$	polynomial coefficients of the j -th Legendre polynomial in the approximation for fluidity
T_m	averaged temperature across the fluid film (K)	β	expression defined by equation (12) (Pa)
T_a	inlet temperature (K)	β^*	average of β across the fluid film (Pa)
\hat{T}_j	polynomial coefficients of the j -th Legendre polynomial in the approximation for temperature	$\delta(\zeta - \zeta_i)$	Dirac-delta functions across the fluid film
U_1	longitudinal runner velocity of the oil slider bearing (m/s)	η	dynamic viscosity (Pa s)
$V_{\theta 1}, V_{\theta 2}$	circumferential velocities of the runner and the thrust plate (m/s)	η_0	dynamic viscosity at inlet temperature T_a (Pa s)
$V_{r 1}, V_{r 2}$	radial velocities of the runner and the thrust plate (m/s)	η_R	dynamic reference viscosity in the Sutherland equation (29), related to T_R (Pa s)
c_p	specific heat capacity of the fluid (J/(kg K))	λ	fluid heat conductivity (W/(m K))
$\dot{e}_{conv.}$	heat flux per fluid volume due to convection and compression (W/m ³)	ν_0, ν_1	kinematic viscosity at the temperatures T_0 and T_1 (m ² /s)
\dot{e}_{comp}	heat flux per fluid volume due to dissipation and conduction (W/m ³)	ρ	fluid density (kg/m ³)
$\dot{e}_{dis}, \dot{e}_{cond}$	heat flux per fluid volume due to dissipation and conduction (W/m ³)	$\hat{\rho}_j$	polynomial coefficients of the j -th Legendre polynomial in the approximation for density
$\bar{e}_{r,\bar{r}}, \bar{e}_{r,\bar{\theta}}$	relative error in temperature and pressure	\mathcal{D}_i^{col}	weighting function for the Point Collocation Method, $\mathcal{D}_i^{col} = \delta(\zeta - \zeta_i)$
f_2	Neumann boundary condition at the thrust plate	\mathcal{D}_i^{gal}	weighting function for the Galerkin Method, $\mathcal{D}_i^{gal} = P_i(\zeta)$
g_1	Dirichlet boundary condition at the runner	ζ	dimensionless coordinate across the fluid film, $\zeta \in [-1, 1]$
h	fluid film thickness (m)	ζ^*	dimensionless ratio of Dowson integrals, $\zeta^* = \tilde{F}_1/\tilde{F}_0$
h_1, h_2	inlet and outlet fluid film thickness (m)	ζ_i	i -th Lobatto-point
p	pressure in the fluid film (Pa)	$\bar{\cdot}$	dimensionless variables
		\cdot	dimensionless Dowson integrals for $\zeta \in [-1, 1]$

case of two moments, the approach of Elrod and Brewe may also be interpreted as a Galerkin method. The resulting 2D partial differential equations are solved by a finite difference method. Results of the reduction method discussed in [11] for the infinitely wide inclined slider bearing show good agreement with simulations results carried out without reduction techniques [11]. In [9], however, numerical instabilities in connection with this reduction method are reported for the slider bearing of finite width.

In a subsequent work, Elrod [9] describes a modification of the reduction approach presented in [11]. In [9], the temperature and the fluidity are approximated by Legendre polynomials of arbitrary order. Instead of reducing the 3D energy equation using moments

of the energy equation, a point collocation method is applied in [9]. The resulting 2D partial differential equations are solved by a finite difference method. The results obtained with this method show good agreement with corresponding results from the literature.

Moraru [12] extends the approach presented in [9] to compressible fluids and takes also into account the temperature/density-dependency. In [12], a 2D formulation of the energy equation neglecting the heat conduction and the fluid flow transverse to the surface motion is used. In contrast to [9,11], the density is approximated in [12] by Legendre polynomials across the fluid film also. The governing partial differential equations are

solved in [12] by a finite difference approach with some modifications compared to Elrod [9] concerning the finite difference formulation. The results are compared with the corresponding results in [9] and with simulation results of a thermoelastohydrodynamic lubrication problem [12].

Feng and Kaneko [10] use the approach of Moraru [12] for calculating the temperature and pressure distribution in a multi-wound foil bearing taking into account foil deflections. They assume the density to be constant across the fluid film. In contrast to Moraru [12], Feng and Kaneko [10] discuss a 3D problem. They discretize the governing partial differential equations with a finite difference method.

Lee and Kim [13] calculate the temperature and pressure field in an air foil thrust bearing using an alternative reduction approach. They consider change of viscosity and density across and along the fluid film. The energy equation is solved in 3D. The resultant temperature field is averaged across the fluid film yielding a 2D temperature field. Viscosity and density in the generalized Reynolds equation are calculated based on this averaged 2D temperature field by using appropriate constitutive equations. Due to this averaging method, the generalized Reynolds equation can be replaced by the classical compressible Reynolds equation.

In this paper, mainly two different reduction methods, namely an *Averaging Approach* and a *Polynomial Approach*, are discussed in order to efficiently calculate the pressure and temperature field in fluid films of gas thrust and oil slider bearings.

Concerning the *Averaging Approach* presented in this paper, a modified form of the averaging approach introduced by Lee and Kim [13] is applied to the 3D energy equation and the generalized Reynolds equation. In contrast to Lee and Kim [13], where the averaged temperature is only used for calculating the viscosity and the density in the generalized Reynolds equation, we use these values also in the 3D energy equation.

Concerning the *Polynomial Approach*, the approaches of Elrod, Brewe and Moraru [9,11,12] are applied in a modified form in order to reduce the computational effort for solving the nonlinear integro-differential equation system. As proposed in [12], fluid temperature, density and fluidity are approximated by Legendre polynomials. Therefore, the integrals in the generalized Reynolds equation are numerically calculated using a Lobatto point quadrature method. For calculating the temperatures at the Lobatto points, the 3D energy equation has to be solved. In this paper, four different methods – namely the *Quadrature Method*, the *Modified Quadrature Method*, the *Point Collocation Method* and the *Galerkin Method* – are discussed in context with the *Polynomial Approach* to simplify and reduce the 3D energy equation.

The *Galerkin Method* is based on the reduction approach presented by Elrod [11]. The Galerkin approach described in [11] for polynomials of order three is extended to polynomials of arbitrary order. In contrast to [11], where monomials are used as weighting functions, Legendre polynomials are applied as weighting functions. The governing 2D partial differential equations are solved with a finite element approach.

In contrast to Elrod [9] and Moraru [12], where only Dirichlet boundary conditions are used at the top and bottom of the fluid film, we discuss the *Point Collocation Method* for arbitrary boundary conditions, i.e. we also consider Neumann and Robin boundary conditions.

In the context with the *Quadrature Method* and the *Modified Quadrature Method*, the temperature field is solved in 3D by a finite element approach so that only fluidity and density have to be approximated by Legendre polynomials. Therefore, the integrals in the generalized Reynolds equation and the fluid velocities can be calculated by means of a Lobatto point quadrature method. An

additional simplification for the 3D energy equation is applied in the *Modified Quadrature Method*.

The different reduction approaches presented in this paper are compared in detail with respect to numerical efficiency, accuracy and convergence behavior for both the gas thrust and the oil slider bearing.

2. Thermogasdynamic thrust and thermohydrodynamic slider bearing models

The pressure and temperature field in gas and oil bearings are generally described by the Navier–Stokes equations, the continuity equation, the energy equation and appropriate constitutive equations. Based on these equations, the governing integro-differential equation system for gas thrust bearings can be derived by making use of the well-known fluid film hypotheses, for thin films, see Section 2.1. In Section 2.2, the corresponding integro-differential equation system is derived for the case of oil slider bearings.

2.1. Thermogasdynamic model for gas thrust bearings

Thrust bearings consist of a runner and a thrust plate. The thrust plate is divided into several pads. In this paper, only one pad is modeled, see Fig. 1. The Navier–Stokes equations and the continuity equation can be reduced by employing the well-known assumptions for thin fluid films (see e.g. [6]):

1. The fluid is a Newtonian fluid.
2. There is no slip between the fluid and the rigid surfaces of the bearing.
3. Inertia and body forces are neglected compared to viscous and pressure forces.
4. The gradients of the circumferential and radial velocities across the fluid film are considerably larger than all other velocity gradients.

In [6], the generalized Reynolds equation is presented for Cartesian coordinates. Analogous to [6], the generalized Reynolds equation can be derived for cylindrical coordinates (r, θ, z) , which finally results in (see [5])

$$\begin{aligned} \frac{1}{r} \frac{\partial}{\partial r} \left[r(F_2 + G_1) \frac{\partial p^*}{\partial r} \right] + \frac{1}{r^2} \frac{\partial}{\partial \theta} \left[(F_2 + G_1) \frac{\partial p^*}{\partial \theta} \right] \\ = \left[\frac{\partial(\rho V_r)_2}{\partial r} + \frac{1}{r} (\rho V_r)_2 + \frac{1}{r} \frac{\partial(\rho V_\theta)_2}{\partial \theta} \right] \\ - \frac{1}{r} \frac{\partial}{\partial r} \left[r \frac{(V_{r2} - V_{r1})(F_3 + G_2)}{F_0} + r V_{r1} G_3 \right] \\ - \frac{1}{r} \frac{\partial}{\partial \theta} \left[\frac{(V_{\theta2} - V_{\theta1})(F_3 + G_2)}{F_0} + V_{\theta1} G_3 \right] \\ + [\rho w]_2 - [\rho w]_1 + \int_0^h \frac{\partial \rho}{\partial t} dz. \end{aligned} \quad (1)$$

Herein, ρ denotes the fluid density. $V_{\theta1}$ and V_{r1} as well as $V_{\theta2}$ and V_{r2} are the circumferential and radial velocities of the runner and the thrust plate, respectively, see Fig. 1. Furthermore, p^* denotes the averaged pressure across the fluid film, see [6]. w terms the fluid velocity in the z -direction. The expressions F_0 to F_3 and G_1 to G_3 describe integral expressions across the fluid film:

$$F_0 = \int_0^h \frac{dz}{\eta}, \quad (2)$$

$$F_1 = \int_0^h \frac{z}{\eta} dz, \quad (3)$$

$$F_2 = \int_0^h \frac{\rho z}{\eta} (z - z^*) dz, \quad (4)$$

$$F_3 = \int_0^h \frac{\rho z}{\eta} dz, \quad (5)$$

$$G_1 = \int_0^h \left[z \frac{\partial \rho}{\partial z} \left(\int_0^z \frac{z}{\eta} dz - z^* \int_0^z \frac{dz}{\eta} \right) \right] dz, \quad (6)$$

$$G_2 = \int_0^h \left(z \frac{\partial \rho}{\partial z} \int_0^z \frac{dz}{\eta} \right) dz, \quad (7)$$

$$G_3 = \int_0^h z \frac{\partial \rho}{\partial z} dz, \quad (8)$$

with

$$z^* = \frac{F_1}{F_0}, \quad (9)$$

and

$$h = h_1 - \frac{h_1 - h_2}{\theta_0} \theta. \quad (10)$$

Note that h denotes the fluid film thickness for the inclined thrust bearing pad, where h_1 and h_2 represent the inlet and the outlet film thickness, respectively. θ_0 is the pad angle, see Fig. 1. η denotes the dynamic viscosity of the fluid. The 3D pressure distribution $p = p(r, \theta, z)$ can be obtained from the 2D pressure field $p^* = p^*(r, \theta)$ by using the relationship

$$p(r, \theta, z) = p^*(r, \theta) + (\beta(r, \theta, z) - \beta^*(r, \theta)) \quad (11)$$

with

$$\beta = \frac{2}{3} \eta \left[\left(\frac{\partial w}{\partial z} - \frac{1}{r} \frac{\partial}{\partial r} (r v_r) \right) + \left(\frac{\partial w}{\partial z} - \frac{1}{r} \frac{\partial v_\theta}{\partial \theta} \right) \right] + \int \left[\frac{1}{r} \frac{\partial}{\partial r} \left(r \eta \frac{\partial v_r}{\partial z} \right) + \frac{1}{r} \frac{\partial}{\partial \theta} \left(\eta \frac{\partial v_\theta}{\partial z} \right) \right] dz, \quad (12)$$

where β^* describes the mean value of β across the fluid film, see [6]. Note that v_r and v_θ represent the radial and circumferential fluid velocities, respectively. The generalized Reynolds equation (1) can be simplified by specifying the boundary conditions for the fluid velocities (see [5])

$$v_r(r, \theta, z=0) = V_{r1} = 0, \quad v_r(r, \theta, z=h) = V_{r2} = 0, \quad (13)$$

$$v_\theta(r, \theta, z=0) = V_{\theta1} = r\Omega, \quad v_\theta(r, \theta, z=h) = V_{\theta2} = 0, \quad (14)$$

$$w(r, \theta, z=0) = 0, \quad w(r, \theta, z=h) = 0, \quad (15)$$

with Ω describing the angular velocity of the runner. Further simplification can be achieved by introducing the following additional assumptions:

5. The pressure across the fluid film is approximately constant ($p \approx p^*$, see [6]).
6. The flow is stationary ($\partial \rho / \partial t = 0$).

As a consequence, the generalized Reynolds equation can be reduced to

$$\frac{1}{r} \frac{\partial}{\partial r} \left[r(F_2 + G_1) \frac{\partial p}{\partial r} \right] + \frac{1}{r^2} \frac{\partial}{\partial \theta} \left[(F_2 + G_1) \frac{\partial p}{\partial \theta} \right] = \Omega \frac{\partial}{\partial \theta} \left[\frac{(F_3 + G_2)}{F_0} - G_3 \right], \quad (16)$$

with the boundary conditions

$$p(r=r_1, \theta) = p(r=r_2, \theta) = p_a, \quad (17)$$

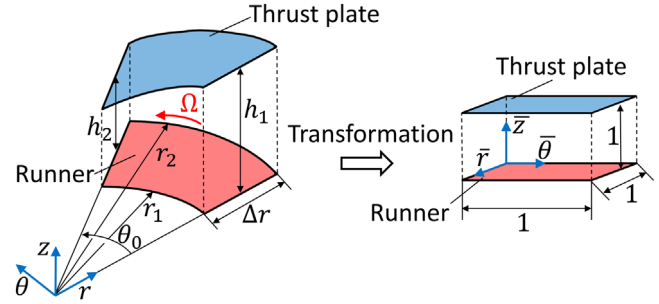


Fig. 1. Transformation of the pad geometry using relations (30) and (31) for the inclined gas thrust bearing.

$$p(r, \theta = 0) = p(r, \theta = \theta_0) = p_a. \quad (18)$$

Herein, r_1 and r_2 denote the inner and the outer radius of the thrust bearing, respectively, see Fig. 1. p_a represents the ambient pressure. Solving the Navier–Stokes equations by making use of the assumptions 1–6 and the boundary conditions (13)–(14) yields the fluid velocities

$$v_r = \frac{\partial p}{\partial r} \left(\int \frac{z}{\eta} dz - z^* \int \frac{dz}{\eta} \right), \quad (19)$$

$$v_\theta = \frac{1}{r} \frac{\partial p}{\partial \theta} \left(\int \frac{z}{\eta} dz - z^* \int \frac{dz}{\eta} \right) - \frac{r\Omega}{F_0} \int \frac{dz}{\eta} + r\Omega. \quad (20)$$

The temperature distribution in the fluid film is generally described by the 3D energy equation, which reads in cylindrical coordinates

$$\rho c_p \left(\frac{\partial T}{\partial t} + v_r \frac{\partial T}{\partial r} + \frac{v_\theta}{r} \frac{\partial T}{\partial \theta} + w \frac{\partial T}{\partial z} \right) = \left(\frac{\partial p}{\partial t} + v_r \frac{\partial p}{\partial r} + \frac{v_\theta}{r} \frac{\partial p}{\partial \theta} \right) + \Phi_{cyl} + \frac{1}{r} \frac{\partial}{\partial r} \left(\lambda r \frac{\partial T}{\partial r} \right) + \frac{1}{r^2} \frac{\partial}{\partial \theta} \left(\lambda r \frac{\partial T}{\partial \theta} \right) + \frac{\partial}{\partial z} \left(\lambda \frac{\partial T}{\partial z} \right). \quad (21)$$

In the above equation, T terms the fluid temperature, c_p describes the specific heat capacity of the fluid and λ is the fluid heat conductivity. Φ_{cyl} denotes the dissipation term. The 3D energy equation (21) can be simplified by making use of the assumptions 1–6 and by applying the subsequent additional assumptions:

7. As a result of the high circumferential fluid velocity, heat conduction can be neglected compared to heat convection in the θ -direction, see [5].
8. As a result of the low fluid velocity in the z -direction, convection can be neglected compared to conduction in the z -direction.

Making use of the assumptions 1–6 and applying an order of magnitude analysis, see [6], the dissipation term Φ_{cyl} can be simplified to

$$\Phi_{cyl} = \eta \left[\left(\frac{\partial v_r}{\partial z} \right)^2 + \left(\frac{\partial v_\theta}{\partial z} \right)^2 \right]. \quad (22)$$

With the above assumptions, the energy equation (21) is finally reduced to

$$\rho c_p \left(v_r \frac{\partial T}{\partial r} + \frac{v_\theta}{r} \frac{\partial T}{\partial \theta} \right) = \left(v_r \frac{\partial p}{\partial r} + \frac{v_\theta}{r} \frac{\partial p}{\partial \theta} \right) + \eta \left[\left(\frac{\partial v_r}{\partial z} \right)^2 + \left(\frac{\partial v_\theta}{\partial z} \right)^2 \right] + \frac{1}{r} \frac{\partial}{\partial r} \left(\lambda r \frac{\partial T}{\partial r} \right) + \frac{\partial}{\partial z} \left(\lambda \frac{\partial T}{\partial z} \right), \quad (23)$$

with the idealized boundary conditions

$$T(r, \theta = 0, z) = T_a, \quad (24)$$

$$\frac{\partial T}{\partial r} \Big|_{r=r_1} = \frac{\partial T}{\partial r} \Big|_{r=r_2} = 0, \tag{25}$$

$$\lambda \frac{\partial T}{\partial z} \Big|_{z=0} = \frac{T(r, \theta, z=0) - T_a}{R_{th} A_{pad}}, \tag{26}$$

$$\frac{\partial T}{\partial z} \Big|_{z=h} = 0. \tag{27}$$

It should be mentioned that $A_{pad} = 1/2\theta_0(r_2^2 - r_1^2)$ terms the pad surface area. T_a represents the pad inlet temperature of the fluid. R_{th} denotes the thermal resistivity of the rotor. The Robin boundary condition (26) states that the heat conduction at the bottom of the fluid film equals the heat flux through the runner. According to Huebner [5], only one boundary condition has to be considered in the θ -direction, because the heat conduction in this direction ($1/r^2 \lambda \partial^2 T / \partial \theta^2$) is neglected. Temperature and pressure dependencies of the fluid properties are described by appropriate constitutive equations. Hence, additional assumptions are introduced:

- 9. The fluid is an ideal gas.
- 10. Viscosity η changes only with temperature, not with pressure.
- 11. Specific heat capacity c_p and heat conductivity λ are assumed to be constant.

Temperature and pressure dependency of the density are therefore described by the ideal gas equation

$$\rho = \frac{p}{RT}, \tag{28}$$

with R denoting the ideal gas constant. The temperature/viscosity-dependency is described by the Sutherland equation, see [14]:

$$\eta = \eta_R \frac{T_R + C}{T + C} \left(\frac{T}{T_R} \right)^{3/2}. \tag{29}$$

In the above equation, η_R represents a reference viscosity, which is related to the reference temperature T_R . C is a fluid specific constant.

Next, Eqs. (2)–(8), Eqs. (16)–(20), and Eqs. (21)–(29) are written in dimensionless form by introducing the subsequent relations:

$$r = r_1 + (r_2 - r_1)\bar{r} = r_1 + \Delta r \bar{r}, \quad \theta = \theta_0 \bar{\theta}, \quad z = h \bar{z}, \tag{30}$$

$$h = h_2 \bar{h}, \tag{31}$$

$$p = p_a(1 + \bar{p}), \quad T = T_a(1 + \bar{T}), \quad \eta = \eta_R \bar{\eta}, \quad \rho = \rho_0 \bar{\rho}, \tag{32}$$

$$v_r = r_2 \Omega \bar{v}_r, \quad v_\theta = r_2 \Omega \bar{v}_\theta. \tag{33}$$

It should be stressed that ρ_0 denotes the reference density at the pad inlet. The solution space is transformed from the (r, θ, z) -space to the dimensionless $(\bar{r}, \bar{\theta}, \bar{z})$ -space by making use of the relations (30) and (31), see Fig. 1.

Using the above relations, the generalized Reynolds equation (16) is expressed by

$$\begin{aligned} & \frac{\rho_0 h_2^3 p_a}{\eta_R (\Delta r)^2} \frac{\partial}{\partial \bar{r}} \left[\bar{h}^3 (r_1 + \Delta r \bar{r}) (\bar{F}_2 + \bar{G}_1) \frac{\partial \bar{p}}{\partial \bar{r}} \right] \\ & + \frac{\rho_0 h_2^3 p_a}{(r_1 + \Delta r \bar{r}) \theta_0^2 \eta_R} \frac{\partial}{\partial \bar{\theta}} \left[\bar{h}^3 (\bar{F}_2 + \bar{G}_1) \frac{\partial \bar{p}}{\partial \bar{\theta}} \right] \\ & = \frac{\Omega (r_1 + \Delta r \bar{r}) h_2 \rho_0}{\theta_0} \frac{\partial}{\partial \bar{\theta}} \left[\bar{h} \left(\frac{\bar{F}_3 + \bar{G}_2}{\bar{F}_0} - \bar{G}_3 \right) \right], \end{aligned} \tag{34}$$

with the boundary conditions

$$\bar{p}(\bar{r} = 0, \bar{\theta}) = \bar{p}(\bar{r} = 1, \bar{\theta}) = 0, \tag{35}$$

$$\bar{p}(\bar{r}, \bar{\theta} = 0) = \bar{p}(\bar{r}, \bar{\theta} = 1) = 0, \tag{36}$$

and the dimensionless integrals

$$\bar{F}_0 = \int_0^1 \frac{d\bar{z}}{\bar{\eta}}, \tag{37}$$

$$\bar{F}_1 = \int_0^1 \frac{\bar{z}}{\bar{\eta}} d\bar{z}, \tag{38}$$

$$\bar{F}_2 = \int_0^1 \frac{\bar{\rho} \bar{z}}{\bar{\eta}} (\bar{z} - \bar{z}^*) d\bar{z}, \tag{39}$$

$$\bar{F}_3 = \int_0^1 \frac{\bar{\rho} \bar{z}}{\bar{\eta}} d\bar{z}, \tag{40}$$

$$\bar{G}_1 = \int_0^1 \left[\bar{z} \frac{\partial \bar{p}}{\partial \bar{z}} \left(\int_0^{\bar{z}} \frac{\bar{z}}{\bar{\eta}} d\bar{z} - \bar{z}^* \int_0^{\bar{z}} \frac{d\bar{z}}{\bar{\eta}} \right) \right] d\bar{z}, \tag{41}$$

$$\bar{G}_2 = \int_0^1 \left(\bar{z} \frac{\partial \bar{p}}{\partial \bar{z}} \int_0^{\bar{z}} \frac{d\bar{z}}{\bar{\eta}} \right) d\bar{z}, \tag{42}$$

$$\bar{G}_3 = \int_0^1 \bar{z} \frac{\partial \bar{p}}{\partial \bar{z}} d\bar{z}, \tag{43}$$

with

$$\bar{z}^* = \frac{\bar{F}_1}{\bar{F}_0}. \tag{44}$$

Using the relations (30)–(33), the energy equation (23) is transformed to

$$\begin{aligned} & \rho_0 r_2 \Omega c_p \bar{p} T_a \left[\bar{v}_r \frac{\partial \bar{T}}{\Delta r \partial \bar{r}} + \frac{\bar{v}_\theta}{(r_1 + \Delta r \bar{r}) \theta_0} \left(\frac{\partial \bar{T}}{\partial \bar{\theta}} - \frac{\partial \bar{T}}{\partial \bar{z}} \frac{\partial \bar{h}}{\partial \bar{\theta}} \right) \right] \\ & = p_a r_2 \Omega \left(\bar{v}_r \frac{\partial \bar{p}}{\Delta r \partial \bar{r}} + \frac{\bar{v}_\theta}{(r_1 + \Delta r \bar{r}) \theta_0} \frac{\partial \bar{p}}{\partial \bar{\theta}} \right) \\ & + \frac{(r_2 \Omega)^2 \eta_R}{h_2^2 \bar{h}^2 \bar{\eta}} \left[\left(\frac{\partial \bar{v}_r}{\partial \bar{z}} \right)^2 + \left(\frac{\partial \bar{v}_\theta}{\partial \bar{z}} \right)^2 \right] \\ & + T_a \lambda \left[\frac{1}{(r_1 + \Delta r \bar{r}) (\Delta r)^2} \frac{\partial}{\partial \bar{r}} \left((r_1 + \Delta r \bar{r}) \frac{\partial \bar{T}}{\partial \bar{r}} \right) + \frac{1}{h_2^2 \bar{h}^2} \frac{\partial^2 \bar{T}}{\partial \bar{z}^2} \right], \end{aligned} \tag{45}$$

with the velocities

$$\bar{v}_r = \frac{h_2^2 \bar{h}^2 p_a}{\eta_R \Delta r r_2 \Omega} \frac{\partial \bar{p}}{\partial \bar{r}} \left(\int_0^{\bar{z}} \frac{\bar{z}}{\bar{\eta}} d\bar{z} - \bar{z}^* \int_0^{\bar{z}} \frac{d\bar{z}}{\bar{\eta}} \right), \tag{46}$$

$$\begin{aligned} \bar{v}_\theta & = \frac{h_2^2 \bar{h}^2 p_a}{(r_1 + \Delta r \bar{r}) \theta_0 \eta_R r_2 \Omega} \frac{\partial \bar{p}}{\partial \bar{\theta}} \left(\int_0^{\bar{z}} \frac{\bar{z}}{\bar{\eta}} d\bar{z} - \bar{z}^* \int_0^{\bar{z}} \frac{d\bar{z}}{\bar{\eta}} \right) \\ & - \frac{(r_1 + \Delta r \bar{r})}{r_2 \bar{F}_0} \int_0^{\bar{z}} \frac{d\bar{z}}{\bar{\eta}} + \frac{(r_1 + \Delta r \bar{r})}{r_2}, \end{aligned} \tag{47}$$

and the boundary conditions

$$\bar{T}(\bar{r}, \bar{\theta} = 0, \bar{z}) = 0, \tag{48}$$

$$\frac{T_a}{\Delta r} \frac{\partial \bar{T}}{\partial \bar{r}} \Big|_{\bar{r}=0} = \frac{T_a}{\Delta r} \frac{\partial \bar{T}}{\partial \bar{r}} \Big|_{\bar{r}=1} = 0, \tag{49}$$

$$\lambda \frac{T_a}{h_2 \bar{h}} \frac{\partial \bar{T}}{\partial \bar{z}} \Big|_{\bar{z}=0} = \frac{T_a \bar{T}(\bar{r}, \bar{\theta}, \bar{z}=0)}{R_{th} A_{pad}}, \tag{50}$$

$$\frac{T_a}{h_2 \bar{h}} \frac{\partial \bar{T}}{\partial \bar{z}} \Big|_{\bar{z}=1} = 0. \tag{51}$$

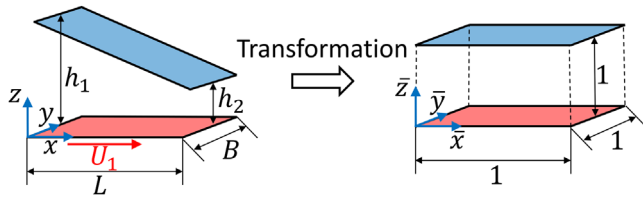


Fig. 2. Transformation of the pad geometry using the relations (31) and (54) for the inclined oil slider bearing.

Using the relations (32) yields the dimensionless ideal gas equation

$$\bar{\rho} = \frac{1 + \bar{p}}{1 + \bar{T}} \quad (52)$$

and the dimensionless Sutherland equation

$$\bar{\eta} = \frac{T_R + C}{C + T_a(1 + \bar{T})} \left[\frac{T_a}{T_R}(1 + \bar{T}) \right]^{3/2} \quad (53)$$

The 13 equations (34), (37)–(43), (45)–(47) and (52), (53) describe a nonlinear integro-differential equation system for the dimensionless pressure \bar{p} , the dimensionless temperature \bar{T} , the dimensionless viscosity $\bar{\eta}$, the dimensionless density $\bar{\rho}$, the dimensionless velocities \bar{v}_r and \bar{v}_θ as well as for the dimensionless integrals \bar{F}_0 to \bar{F}_3 and \bar{G}_1 to \bar{G}_3 .

2.2. Thermohydrodynamic model for oil slider bearings

The geometry of an inclined oil slider bearing is shown in Fig. 2. Instead of the relations (30), the solution space is transformed from the (x, y, z) -space to the dimensionless $(\bar{x}, \bar{y}, \bar{z})$ -space by applying the relations

$$x = L\bar{x}, \quad y = B\bar{y}, \quad z = h\bar{z}. \quad (54)$$

Herein L and B denote the length and the width of the inclined oil slider bearing, respectively, see Fig. 2.

Similar to the thermogasdynamic model for thrust bearings, see Section 2.1, the following assumptions are used for oil slider bearings, see [5,6]:

1. The fluid is an incompressible Newtonian fluid.
2. There is no slip between the fluid and the rigid surfaces of the bearing.
3. Inertia and body forces are neglected compared to viscous and pressure forces.
4. The gradients of the transverse and longitudinal velocities across the fluid film are considerably larger than all other velocity gradients.
5. The pressure across the fluid film is nearly constant.
6. The fluid flow is stationary.
7. As a result of the high fluid velocity in the x -direction, heat conduction can be neglected compared to heat convection in the x -direction.
8. As a result of the low fluid velocity in the z -direction, convection can be neglected compared to conduction in the z -direction.
9. Viscosity η changes only with temperature and not with pressure. For general lubrication problems, dependency of the viscosity on the pressure must also be taken into account. For the investigated oil slider bearing and for the considered boundary conditions (see the numerical example in Section 4.2), the change of viscosity due to pressure increase is significantly smaller than the change of viscosity due to

temperature increase. Hence, viscosity is assumed to be only a function of temperature here.

10. Specific heat capacity and heat conductivity are assumed to be constant.
11. Temperature/density-dependency can be neglected.
12. There is no cavitation in the fluid film.

With these assumptions and with the relations (31), (32) and (54) using $\bar{\rho} = 1$ and $\eta_R = \eta_0 = \eta(T_a)$, we get the subsequent dimensionless incompressible generalized Reynolds equation

$$\frac{p_a h_2^3}{\eta_0 L^2} \frac{\partial}{\partial \bar{x}} \left[\bar{h}^3 \bar{F}_2 \frac{\partial \bar{p}}{\partial \bar{x}} \right] + \frac{p_a h_2^3}{\eta_0 B^2} \frac{\partial}{\partial \bar{y}} \left[\bar{h}^3 \bar{F}_2 \frac{\partial \bar{p}}{\partial \bar{y}} \right] = \frac{h_2}{L} \frac{\partial}{\partial \bar{x}} \left[\bar{h} U_1 \bar{F}_3 \right], \quad (55)$$

with the dimensionless integrals (37)–(40) and the boundary conditions

$$\bar{p}(\bar{x} = 0, \bar{y}) = \bar{p}(\bar{x} = 1, \bar{y}) = 0, \quad (56)$$

$$\bar{p}(\bar{x}, \bar{y} = 0) = \bar{p}(\bar{x}, \bar{y} = 1) = 0. \quad (57)$$

Herein, the fluid film thickness \bar{h} is defined by

$$\bar{h} = \frac{h_1}{h_2} - \left(\frac{h_1}{h_2} - 1 \right) \bar{x}. \quad (58)$$

Using assumptions 1–12 as well as the relations (31), (32) and (54), the dimensionless energy equation reads as follows:

$$\rho c_p U_1 T_a \left[\frac{\bar{u}}{L} \left(\frac{\partial \bar{T}}{\partial \bar{x}} - \frac{\partial \bar{T}}{\partial \bar{z}} \frac{\partial \bar{h}}{\partial \bar{x}} \right) + \frac{\bar{v}}{B} \frac{\partial \bar{T}}{\partial \bar{y}} \right] = \frac{\eta_0 \bar{\eta} U_1^2}{(h_2 \bar{h})^2} \left[\left(\frac{\partial \bar{u}}{\partial \bar{z}} \right)^2 + \left(\frac{\partial \bar{v}}{\partial \bar{z}} \right)^2 \right] + \frac{\lambda T_a}{B^2} \frac{\partial^2 \bar{T}}{\partial \bar{y}^2} + \frac{\lambda T_a}{(h_2 \bar{h})^2} \frac{\partial^2 \bar{T}}{\partial \bar{z}^2}, \quad (59)$$

with the boundary conditions

$$\bar{T}(\bar{x} = 0, \bar{y}, \bar{z}) = 0, \quad (60)$$

$$\frac{T_a}{B} \frac{\partial \bar{T}}{\partial \bar{y}} \Big|_{\bar{y}=0} = \frac{T_a}{B} \frac{\partial \bar{T}}{\partial \bar{y}} \Big|_{\bar{y}=1} = 0, \quad (61)$$

$$T(\bar{x}, \bar{y}, \bar{z} = 0) = 0, \quad (62)$$

$$\frac{T_a}{h_2 \bar{h}} \frac{\partial \bar{T}}{\partial \bar{z}} \Big|_{\bar{z}=1} = 0 \quad (63)$$

and the dimensionless velocities

$$\bar{u} = \frac{u}{U_1} = \frac{p_a (h_2 \bar{h})^2}{\eta_0 L U_1} \frac{\partial \bar{p}}{\partial \bar{x}} \int \frac{\bar{z}}{\bar{\eta}} d\bar{z} - \left(\frac{1}{\bar{F}_0} + \frac{p_a (h_2 \bar{h})^2}{L U_1 \eta_0} \bar{z}^* \frac{\partial \bar{p}}{\partial \bar{x}} \right) \int \frac{d\bar{z}}{\bar{\eta}} + 1, \quad (64)$$

$$\bar{v} = \frac{v}{u_1} = \frac{p_a (h_2 \bar{h})^2}{B U_1 \eta_0} \frac{\partial \bar{p}}{\partial \bar{y}} \left(\int \frac{\bar{z}}{\bar{\eta}} d\bar{z} - \bar{z}^* \int \frac{d\bar{z}}{\bar{\eta}} \right). \quad (65)$$

In the above equations, U_1 denotes the velocity of the runner. In contrast to the gas thrust bearing model, the runner is assumed to have a constant temperature, namely the inlet temperature T_a , see [4]. The temperature/viscosity-dependency is described by the Ubbelohde-Walther relation:

$$\bar{\eta}(\bar{T}) = 10^{-6} \rho \left[10^{10 [A_U - B_U \log_{10}(T_a(1 + \bar{T}))]} \right] \quad (66)$$

with the constants

$$A_U = \log_{10}(\log_{10}(\nu_0 + 0.6)) + b \log_{10}(T_0) \quad (67)$$

and

$$B_U = \frac{\log_{10}(\log_{10}(\nu_1 + 0.6)) - \log_{10}(\log_{10}(\nu_0 + 0.6))}{\log_{10}(T_0) - \log_{10}(T_1)} \quad (68)$$

according to DIN 51563, see [5]. Note that ν_0 and ν_1 denote the kinematic velocities at the temperatures T_0 and T_1 , respectively. Summarizing: the pressure and temperature distribution in an oil slider bearing is described by the generalized Reynolds equation (55) and the corresponding Dowson integrals (37)–(40), the 3D energy equation (59), the equations for the longitudinal and transverse velocities (64) and (65) as well as by the Ubbelohde–Walther relation (66). These equations represent a nonlinear integro-differential equation system consisting of nine equations for the unknown quantities \bar{p} , $\bar{F}_0 - \bar{F}_3$, \bar{T} , \bar{u} , \bar{v} and $\bar{\eta}$.

3. Reduction approaches

In this section, mainly two reduction approaches are discussed. In the first approach, the fluid temperature T is averaged across the fluid film, see [13]. In the second approach, the fluid temperature T , the fluidity $1/\eta$ and – in case of gas bearings – the density ρ are approximated by Legendre polynomials, see [9,11,12]. Different modifications of the second approach are presented. The first and the second approach are described in detail for the gas thrust bearing, which represents the more general case. For the reason of a concise representation, only results are presented for the oil slider bearing. For the following analysis, dimensionless variables are used according to Eqs. (30)–(33).

3.1. Averaging approach

This approach is based on averaging the fluid temperature across the fluid film, see [13]. Within this approach, the 3D energy equation (45) is solved without using any reduction techniques so that a 3D temperature distribution is obtained. This 3D temperature field is averaged across the fluid film

$$\bar{T}_m(\bar{r}, \bar{\theta}) = \int_0^1 \bar{T}(\bar{r}, \bar{\theta}, \bar{z}) d\bar{z} \quad (69)$$

yielding a 2D temperature field $\bar{T}_m(\bar{r}, \bar{\theta})$. Fluid density and viscosity in the generalized Reynolds equation (34) and the 3D energy equation (45) are calculated with the 2D temperature distribution by means of the constitutive equations (52) and (53). As a consequence, the generalized Reynolds equation is reduced to the classical compressible Reynolds equation (see [13])

$$\begin{aligned} & \frac{\rho_0 h_2^3 p_a}{\eta_R (\Delta r)^2} \frac{\partial}{\partial \bar{r}} \left[\bar{h}^{-3} (r_1 + \Delta r \bar{r}) \frac{1 + \bar{p}}{\bar{\eta}(\bar{T}_m)(1 + \bar{T}_m)} \frac{\partial \bar{p}}{\partial \bar{r}} \right] \\ & + \frac{\rho_0 h_2^3 p_a}{(r_1 + \Delta r \bar{r}) \theta_0^2 \eta_R} \frac{\partial}{\partial \bar{\theta}} \left[\bar{h}^{-3} \frac{1 + \bar{p}}{\bar{\eta}(\bar{T}_m)(1 + \bar{T}_m)} \frac{\partial \bar{p}}{\partial \bar{\theta}} \right] \\ & = \frac{6 \Omega (r_1 + \Delta r \bar{r}) h_2 \rho_0}{\theta_0} \frac{\partial}{\partial \bar{\theta}} \left(\bar{h} \frac{1 + \bar{p}}{1 + \bar{T}_m} \right). \end{aligned} \quad (70)$$

Due to the *Averaging Approach*, the integrals (37)–(43) have not to be calculated. Hence, the nonlinear integro-differential equation system is reduced to seven equations (instead of 13 for the unreduced model). In contrast to Lee and Kim [13], where the averaged temperature is only used for calculating the viscosity and the density in the generalized Reynolds equation, we use these values also in the 3D energy equation and for calculating the fluid velocities. Hence, fluid density ρ and fluid viscosity η are only

functions of r and θ . The velocities (46) and (47) are reduced to

$$\bar{v}_r = \frac{h_2^2 \bar{h}^2 p_a}{2 \eta_R \bar{\eta}(\bar{T}_m) \Delta r r_2 \Omega} \frac{\partial \bar{p}}{\partial \bar{r}} (\bar{z}^2 - \bar{z}), \quad (71)$$

$$\begin{aligned} \bar{v}_\theta = & \frac{h_2^2 \bar{h}^2 p_a}{2 (r_1 + \Delta r \bar{r}) \theta_0 r_2 \eta_R \bar{\eta}(\bar{T}_m) \Omega} \frac{\partial \bar{p}}{\partial \bar{\theta}} (\bar{z}^2 - \bar{z}) \\ & - \frac{(r_1 + \Delta r \bar{r})}{r_2} \bar{z} + \frac{(r_1 + \Delta r \bar{r})}{r_2}. \end{aligned} \quad (72)$$

Remark on the discretization approach and the solution procedure: The 3D energy equation (45) is discretized by 3D hexahedral Lagrange elements of order two (information on the number of elements is provided in Sections 4.1 and 4.2). The Reynolds equation (70) is discretized by 2D quadrilateral Lagrange elements of order two (information on the number of elements is provided in Sections 4.1 and 4.2). Here, the finite element software COMSOL Multiphysics is used for discretizing the field equations. A segregated solution approach is applied for solving the discretized system, i.e. the resulting finite element system is solved in a blockwise manner:

- *Stage 1:* In the first solution step, pressure is kept constant and the 3D energy equation (45) is solved for the temperature.
- *Stage 2:* In the second solution step, the 3D temperature field from stage 1 is averaged across the fluid film and the mean 2D temperature field $\bar{T}_m(\bar{r}, \bar{\theta})$ is calculated with Eq. (69). Based on the 2D temperature field, fluid density and viscosity are calculated as a function of \bar{r} and $\bar{\theta}$.
- *Stage 3:* In the third solution step, the 2D pressure field is calculated based on the 2D viscosity and density fields from stage 2 by solving the compressible Reynolds equation (70).

Stages 1–3 are repeated until global convergence of all variables is achieved.

3.2. Polynomial approach

In this approach, fluid temperature T , density ρ , and fluidity $1/\eta$ are approximated by Legendre polynomials, see [11,9,12]:

$$\bar{T}(\bar{r}, \bar{\theta}, \zeta) = \sum_{j=0}^N \hat{T}_j(\bar{r}, \bar{\theta}) P_j(\zeta), \quad (73)$$

$$\bar{\rho}(\bar{r}, \bar{\theta}, \zeta) = \sum_{j=0}^N \hat{\rho}_j(\bar{r}, \bar{\theta}) P_j(\zeta), \quad (74)$$

$$\frac{1}{\bar{\eta}} = \bar{\alpha}(\bar{r}, \bar{\theta}, \zeta) = \sum_{j=0}^N \hat{\alpha}_j(\bar{r}, \bar{\theta}) P_j(\zeta), \quad (75)$$

with the Legendre polynomial of order n

$$P_n(\zeta) = \frac{1}{2^n n!} \frac{d^n}{d\zeta^n} (\zeta^2 - 1)^n. \quad (76)$$

Herein, \hat{T}_j , $\hat{\rho}_j$ and $\hat{\alpha}_j$ denote the polynomial coefficients of the j -th Legendre polynomial for temperature, density and fluidity, respectively. N represents the maximum polynomial order in the polynomial approximations. Legendre polynomials fulfill the orthogonality relation

$$\int_{-1}^1 P_i(\zeta) P_j(\zeta) d\zeta = 0 \quad \forall i \neq j. \quad (77)$$

In order to apply the orthogonality relation to the current problem, the $(\bar{r}, \bar{\theta}, \bar{z})$ -space with $\bar{z} \in [0, 1]$ is transformed to the $(\bar{r}, \bar{\theta}, \zeta)$ -space with $\zeta \in [-1, 1]$ by using the transformation

$$\zeta = 2\bar{z} - 1. \tag{78}$$

The $N + 1$ polynomial coefficients \hat{T}_j , $\hat{\rho}_j$ and $\hat{\alpha}_j$ may in a straightforward manner be calculated by applying an interpolation technique with $N + 1$ Lobatto points, see [11]. The $N + 1$ Lobatto points can be subdivided into the $N - 1$ internal points and the two points at $\zeta = -1$ and $\zeta = 1$. The $N - 1$ internal Lobatto points are the roots of the first derivative of the N -th Legendre polynomial. Hence, fluid temperature, density and fluidity at the Lobatto point ζ_i can be calculated by

$$\bar{T}(\bar{r}, \bar{\theta}, \zeta_i) = A_{ij} \hat{T}_j(\bar{r}, \bar{\theta}) \quad \forall i = 0, \dots, N, \tag{79}$$

$$\bar{\rho}(\bar{r}, \bar{\theta}, \zeta_i) = A_{ij} \hat{\rho}_j(\bar{r}, \bar{\theta}) \quad \forall i = 0, \dots, N, \tag{80}$$

$$\bar{\alpha}(\bar{r}, \bar{\theta}, \zeta_i) = A_{ij} \hat{\alpha}_j(\bar{r}, \bar{\theta}) \quad \forall i = 0, \dots, N, \tag{81}$$

with the second order tensor $A_{ij} = P_j(\zeta_i)$. Note that the Einstein summation convention is used in Eqs. (79)–(81) and in the following equations, in which double indices occur. The polynomial coefficients \hat{T}_j , $\hat{\rho}_j$ and $\hat{\alpha}_j$ can now be calculated by inverting A_{ij} , see [9,11,12], which results in

$$\hat{T}_j(\bar{r}, \bar{\theta}) = I_{ji} \bar{T}(\bar{r}, \bar{\theta}, \zeta_i) \quad \forall j = 0, \dots, N, \tag{82}$$

$$\hat{\rho}_j(\bar{r}, \bar{\theta}) = I_{ji} \bar{\rho}(\bar{r}, \bar{\theta}, \zeta_i) \quad \forall j = 0, \dots, N, \tag{83}$$

$$\hat{\alpha}_j(\bar{r}, \bar{\theta}) = I_{ji} \bar{\alpha}(\bar{r}, \bar{\theta}, \zeta_i) \quad \forall j = 0, \dots, N, \tag{84}$$

with $I_{ji} = (A^{-1})_{ji}$.

According to Elrod and Brewé [11], Elrod [9] and Moraru [12], the integrals (37)–(43) are numerically calculated using a Lobatto point quadrature method, see Section 3.2.1. It should finally be stressed that due to the approximation (73), the 3D energy equation is reduced to 2D space, see Section 3.2.2.

3.2.1. Simplification of the generalized Reynolds equation

The generalized Reynolds equation (34) is simplified by calculating the Dowson integrals (37)–(43) in the generalized Reynolds equation using Legendre polynomials for approximating density and fluidity across the fluid film, see Eqs. (74) and (75). In order to apply the polynomial approximation to the Dowson integrals, we firstly carry out a coordinate transformation according to Eq. (78), which results in

$$\bar{F}_0 = \frac{1}{2} \int_{-1}^1 \bar{\alpha} \, d\zeta = \frac{1}{2} \hat{F}_0, \tag{85}$$

$$\bar{F}_1 = \frac{1}{4} \int_{-1}^1 \bar{\alpha}(\zeta + 1) \, d\zeta = \frac{1}{4} \hat{F}_1, \tag{86}$$

$$\bar{F}_2 = \frac{1}{8} \int_{-1}^1 \bar{\alpha} \bar{\rho}(\zeta + 1) [(\zeta + 1) - \zeta^*] \, d\zeta = \frac{1}{8} \hat{F}_2, \tag{87}$$

$$\bar{F}_3 = \frac{1}{4} \int_{-1}^1 \bar{\alpha} \bar{\rho}(\zeta + 1) \, d\zeta = \frac{1}{4} \hat{F}_3, \tag{88}$$

$$\bar{G}_1 = \frac{1}{8} \int_{-1}^1 \left[(\zeta + 1) \frac{\partial \bar{\rho}}{\partial \zeta} \left(\int_{-1}^{\zeta} (\zeta + 1) \bar{\alpha} \, d\zeta - \zeta^* \int_{-1}^{\zeta} \bar{\alpha} \, d\zeta \right) \right] \, d\zeta = \frac{1}{8} \hat{G}_1, \tag{89}$$

$$\bar{G}_2 = \frac{1}{4} \int_{-1}^1 \left[(\zeta + 1) \frac{\partial \bar{\rho}}{\partial \zeta} \int_{-1}^{\zeta} \bar{\alpha} \, d\zeta \right] \, d\zeta = \frac{1}{4} \hat{G}_2, \tag{90}$$

$$\bar{G}_3 = \frac{1}{2} \int_{-1}^1 (\zeta + 1) \frac{\partial \bar{\rho}}{\partial \zeta} \, d\zeta = \frac{1}{2} \hat{G}_3, \tag{91}$$

with

$$\zeta^* = \frac{\hat{F}_1}{\hat{F}_0}. \tag{92}$$

Substituting Eqs. (74) and (75) into Eqs. (85)–(91) yields

$$\hat{F}_0 = 2\hat{\alpha}_0, \tag{93}$$

$$\hat{F}_1 = \frac{2}{3}\hat{\alpha}_1 + 2\hat{\alpha}_0, \tag{94}$$

$$\hat{F}_2 = \hat{\rho}_j(\bar{r}, \bar{\theta}) \hat{\alpha}_k(\bar{r}, \bar{\theta}) \int_{-1}^1 P_j(\zeta) P_k(\zeta) (\zeta + 1) [(\zeta + 1) - \zeta^*] \, d\zeta, \tag{95}$$

$$\hat{F}_3 = \hat{\rho}_j(\bar{r}, \bar{\theta}) \hat{\alpha}_k(\bar{r}, \bar{\theta}) \int_{-1}^1 P_j(\zeta) P_k(\zeta) (\zeta + 1) \, d\zeta, \tag{96}$$

$$\hat{G}_1 = \hat{\rho}_j(\bar{r}, \bar{\theta}) \hat{\alpha}_k(\bar{r}, \bar{\theta}) \int_{-1}^1 \left[(\zeta + 1) \frac{\partial P_j(\zeta)}{\partial \zeta} \left(\int_{-1}^{\zeta} (\zeta + 1) P_k(\zeta) \, d\zeta - \zeta^* \int_{-1}^{\zeta} P_k(\zeta) \, d\zeta \right) \right] \, d\zeta, \tag{97}$$

$$\hat{G}_2 = \hat{\rho}_j(\bar{r}, \bar{\theta}) \hat{\alpha}_k(\bar{r}, \bar{\theta}) \int_{-1}^1 \left[(\zeta + 1) \frac{\partial P_j(\zeta)}{\partial \zeta} \int_{-1}^{\zeta} P_k(\zeta) \, d\zeta \right] \, d\zeta, \tag{98}$$

$$\hat{G}_3 = \hat{\rho}_j(\bar{r}, \bar{\theta}) \int_{-1}^1 (\zeta + 1) \frac{\partial P_j(\zeta)}{\partial \zeta} \, d\zeta, \tag{99}$$

with

$$\zeta^* = \left(\frac{1}{3} \hat{\alpha}_1 + 1 \right). \tag{100}$$

It should be mentioned that in Eqs. (93), (94) and (100), the coefficients $\hat{\alpha}_j$ vanish for $j > 1$, see [12]. With the Dowson integrals (93)–(99), the generalized Reynolds equation reads as

$$\begin{aligned} & \frac{\rho_0 h_2^3 p_a}{8 \eta_R (\Delta r)^2} \frac{\partial}{\partial \bar{r}} \left[\bar{h}^{-3} (r_1 + \Delta r \bar{r}) (\hat{F}_2 + \hat{G}_1) \frac{\partial \bar{p}}{\partial \bar{r}} \right] \\ & + \frac{\rho_0 h_2^3 p_a}{8 (r_1 + \Delta r \bar{r}) \theta_0^2 \eta_R} \frac{\partial}{\partial \bar{\theta}} \left[\bar{h}^{-3} (\hat{F}_2 + \hat{G}_1) \frac{\partial \bar{p}}{\partial \bar{\theta}} \right] \\ & = \frac{\Omega (r_1 + \Delta r \bar{r}) h_2 \rho_0}{2 \theta_0} \frac{\partial}{\partial \bar{\theta}} \left[\bar{h} \left(\frac{\hat{F}_3 + \hat{G}_2}{\hat{F}_0} - \hat{G}_3 \right) \right]. \end{aligned} \tag{101}$$

For incompressible fluids, the above equation is simplified to

$$\begin{aligned} & \frac{\rho_0 h_2^3 p_a}{8 \eta_R (\Delta r)^2} \frac{\partial}{\partial \bar{r}} \left[\bar{\rho} \bar{h}^{-3} (r_1 + \Delta r \bar{r}) \left(\frac{2}{3} \hat{\alpha}_0 + \frac{4}{15} \hat{\alpha}_2 + \frac{2}{9} \frac{\hat{\alpha}_1^2}{\hat{\alpha}_0} \right) \frac{\partial \bar{p}}{\partial \bar{r}} \right] \\ & + \frac{\rho_0 h_2^3 p_a}{8 (r_1 + \Delta r \bar{r}) \theta_0^2 \eta_R} \frac{\partial}{\partial \bar{\theta}} \left[\bar{\rho} \bar{h}^{-3} \left(\frac{2}{3} \hat{\alpha}_0 + \frac{4}{15} \hat{\alpha}_2 + \frac{2}{9} \frac{\hat{\alpha}_1^2}{\hat{\alpha}_0} \right) \frac{\partial \bar{p}}{\partial \bar{\theta}} \right] \\ & = \frac{\Omega (r_1 + \Delta r \bar{r}) h_2 \rho_0}{2 \theta_0} \frac{\partial}{\partial \bar{\theta}} \left[\bar{\rho} \bar{h} \left(\frac{1}{3} \hat{\alpha}_1 + 1 \right) \right]. \end{aligned} \tag{102}$$

It should be pointed out that for the incompressible case, the coefficients $\hat{\alpha}_j$ vanish in all Dowson integrals for $j > 2$.

3.2.2. Simplification and reduction of the 3D energy equation

To calculate fluid density $\bar{\rho}(\bar{r}, \bar{\theta}, \zeta_i)$ and fluidity $\bar{\alpha}(\bar{r}, \bar{\theta}, \zeta_i)$ at the Lobatto-points ζ_i with the constitutive equations (52) and (53), the temperature at the Lobatto points must be known. Therefore, the 3D energy equation (45) has to be solved. In this section, we discuss four different approaches – namely the *Quadrature Method*, the *Modified Quadrature Method*, the *Point Collocation Method* and the *Galerkin Method* – to simplify and reduce the 3D energy

equation. Within the *Quadrature Method* and the *Modified Quadrature Method*, the 3D energy equation is solved without reduction; only density and fluidity are approximated by Legendre polynomials. Within the *Point Collocation Method* and the *Galerkin Method*, fluidity, density and temperature are approximated by Legendre polynomials so that the 3D energy equation is solved in 2D space. For all four methods, the transformation (78) has to be used to transform the energy equation to the dimensionless $(\bar{r}, \bar{\theta}, \zeta)$ -space. This results in

$$\begin{aligned} & \underbrace{\rho_0 r_2 \Omega c_p \bar{\rho} T_a \left[\frac{\bar{v}_r}{\Delta r} \frac{\partial \bar{T}}{\partial \bar{r}} + \frac{\bar{v}_\theta}{(r_1 + \Delta r \bar{r}) \theta_0} \left(\frac{\partial \bar{T}}{\partial \bar{\theta}} - \frac{\partial \bar{T}}{\partial \zeta} \frac{\zeta + 1}{\bar{h}} \frac{\partial \bar{h}}{\partial \bar{\theta}} \right) \right]}_{\dot{e}_{conv}} \\ &= p_a r_2 \Omega \underbrace{\left(\frac{\bar{v}_r}{\Delta r} \frac{\partial \bar{p}}{\partial \bar{r}} + \frac{\bar{v}_\theta}{(r_1 + \Delta r \bar{r}) \theta_0} \frac{\partial \bar{p}}{\partial \bar{\theta}} \right)}_{\dot{e}_{comp}} \\ &+ \underbrace{\frac{4(r_2 \Omega)^2 \eta_R \bar{\eta}}{h_2^2 \bar{h}^2} \left[\left(\frac{\partial \bar{v}_r}{\partial \zeta} \right)^2 + \left(\frac{\partial \bar{v}_\theta}{\partial \zeta} \right)^2 \right]}_{\dot{e}_{dis}} \\ &+ T_a \lambda \underbrace{\left[\frac{1}{(r_1 + \Delta r \bar{r}) (\Delta r)^2} \frac{\partial}{\partial \bar{r}} \left((r_1 + \Delta r \bar{r}) \frac{\partial \bar{T}}{\partial \bar{r}} \right) + \frac{4}{h_2^2 \bar{h}^2} \frac{\partial^2 \bar{T}}{\partial \zeta^2} \right]}_{\dot{e}_{cond}}. \end{aligned} \tag{103}$$

Herein, \dot{e}_{conv} , \dot{e}_{comp} , \dot{e}_{dis} and \dot{e}_{cond} denote the heat flux per fluid volume due to convection, compression, dissipation and conduction, respectively. Next, the four different methods are explained in detail.

Quadrature Method: In the framework of this method, density and fluidity in the Dowson integrals (37)–(43) are approximated by Legendre polynomials, see Eqs. (93)–(99). Furthermore, the approximation of fluidity and density is used to calculate the integrals in the fluid velocities (46) and (47), which results in

$$\begin{aligned} \bar{v}_r &= \frac{h_2^2 \bar{h}^2 p_a \hat{\alpha}_k}{4 \eta_R \Delta r r_2 \Omega} \frac{\partial \bar{p}}{\partial \bar{r}} \left(\int_{-1}^{\zeta} (\zeta + 1) P_k(\zeta) d\zeta \right. \\ &\quad \left. - \left(\frac{1 \hat{\alpha}_1}{3 \hat{\alpha}_0} + 1 \right) \int_{-1}^{\zeta} P_k(\zeta) d\zeta \right), \end{aligned} \tag{104}$$

$$\begin{aligned} \bar{v}_\theta &= \frac{h_2^2 \bar{h}^2 p_a \hat{\alpha}_k}{4 (r_1 + \Delta r \bar{r}) \theta_0 \eta_R r_2 \Omega} \frac{\partial \bar{p}}{\partial \bar{\theta}} \left(\int_{-1}^{\zeta} (\zeta + 1) P_k(\zeta) d\zeta \right. \\ &\quad \left. - \left(\frac{1 \hat{\alpha}_1}{3 \hat{\alpha}_0} + 1 \right) \int_{-1}^{\zeta} P_k(\zeta) d\zeta \right) \\ &\quad - \frac{(r_1 + \Delta r \bar{r}) \hat{\alpha}_k}{2 \hat{\alpha}_0 r_2} \int_{-1}^{\zeta} P_k(\zeta) d\zeta + \frac{(r_1 + \Delta r \bar{r})}{r_2}. \end{aligned} \tag{105}$$

Temperature is not approximated by Legendre polynomials and the 3D energy equation (103) is solved by a finite element method.

Modified Quadrature Method: A further simplification of the 3D energy equation can be obtained by approximating density and fluidity not only in the Dowson integrals and in the fluid velocity equations, but also in the convection term \dot{e}_{conv} and in the dissipation term \dot{e}_{dis} of the 3D energy equation (103). As a consequence, the convection term results in

$$\begin{aligned} \dot{e}_{conv} &= \rho_0 r_2 \Omega c_p \hat{\rho}_j(\bar{r}, \bar{\theta}) P_j(\zeta) T_a \left[\frac{\bar{v}_r}{\Delta r} \frac{\partial \bar{T}}{\partial \bar{r}} \right. \\ &\quad \left. + \frac{\bar{v}_\theta}{(r_1 + \Delta r \bar{r}) \theta_0} \left(\frac{\partial \bar{T}}{\partial \bar{\theta}} - \frac{\partial \bar{T}}{\partial \zeta} \frac{\zeta + 1}{\bar{h}} \frac{\partial \bar{h}}{\partial \bar{\theta}} \right) \right] \end{aligned} \tag{106}$$

and the dissipation term reads as

$$\begin{aligned} \dot{e}_{dis} &= 4 \frac{(r_2 \Omega)^2 \eta_R}{h_2^2 \bar{h}^2} I_{j_i} \bar{\alpha}(\bar{r}, \bar{\theta}, \zeta_i) P_j(\zeta) \\ &\quad \left[\left(\frac{h_2^2 \bar{h}^2 p_a}{4 \eta_R \Delta r r_2 \Omega} \frac{\partial \bar{p}}{\partial \bar{r}} \left((\zeta + 1) - \left(\frac{1 \hat{\alpha}_1}{3 \hat{\alpha}_0} + 1 \right) \right) \right)^2 \right. \\ &\quad \left. + \left(\frac{h_2^2 \bar{h}^2 p_a}{4 (r_1 + \Delta r \bar{r}) \theta_0 \eta_R r_2 \Omega} \frac{\partial \bar{p}}{\partial \bar{\theta}} \left((\zeta + 1) - \left(\frac{1 \hat{\alpha}_1}{3 \hat{\alpha}_0} + 1 \right) \right) \right) \right. \\ &\quad \left. - \frac{(r_1 + \Delta r \bar{r})}{2 \hat{\alpha}_0 r_2} + \frac{(r_1 + \Delta r \bar{r})}{r_2} \right]^2. \end{aligned} \tag{107}$$

The advantage of this approach compared to the *Quadrature Method* is that density and fluidity are generally calculated at the Lobatto points, only.

Remark on the discretization approach and the solution procedure for the Quadrature Method and the Modified Quadrature Method: The 3D energy equation (103) is discretized by 3D hexahedral Lagrange elements of order two. The generalized Reynolds equation (101) is discretized by 2D quadrilateral Lagrange elements of order two. A segregated solution approach is applied for solving the discretized system:

- *Stage 1:* In the first solution step, pressure is kept constant and the 3D energy equation (103) is solved for the temperature.
- *Stage 2:* In the second solution step, the Dowson integrals are approximated by a Lobatto quadrature method according to Eqs. (93)–(99).
- *Stage 3:* In the third solution step, the 2D pressure field is calculated based on the approximated Dowson integrals from stage 2 by solving the generalized Reynolds equation (101).

Stages 1–3 are repeated until global convergence of all variables is achieved.

Point Collocation Method: The method is based on the approach of Elrod [9] with the only difference that the finite element method is used instead of the finite difference method to discretize the partial differential equations. In this method, density, fluidity and temperature are approximated by Legendre polynomials. To calculate the temperature at the Lobatto points, the 3D energy equation is discretized across the fluid film using point collocation method, see [9,12]. Therefore, the following $N-1$ weighted residuals of the 3D energy equation (103) are forced to be zero

$$\begin{aligned} \int_{-1}^1 \dot{e}_{conv} \vartheta^{col}(\zeta) d\zeta &= \int_{-1}^1 \dot{e}_{comp} \vartheta^{col}(\zeta) d\zeta \\ &+ \int_{-1}^1 \dot{e}_{dis} \vartheta^{col}(\zeta) d\zeta + \int_{-1}^1 \dot{e}_{cond} \vartheta^{col}(\zeta) d\zeta \\ \forall l &= 1, \dots, N-1, \end{aligned} \tag{108}$$

where the weighting functions are the Dirac-delta functions:

$$\vartheta_l^{col} = \delta(\zeta - \zeta_l), \tag{109}$$

with ζ_l denoting the l -th Lobatto point. Due to the sifting property of the Dirac-delta function, the weighted residuals (108) are simplified to (see [9,12])

$$\begin{aligned} \dot{e}_{conv}(\bar{r}, \bar{\theta}, \zeta_l) &= \dot{e}_{comp}(\bar{r}, \bar{\theta}, \zeta_l) + \dot{e}_{dis}(\bar{r}, \bar{\theta}, \zeta_l) \\ &+ \dot{e}_{cond}(\bar{r}, \bar{\theta}, \zeta_l) \quad \forall l = 1, \dots, N-1. \end{aligned} \tag{110}$$

The above equation represents $N-1$ 2D partial differential equations for the $N+1$ unknown temperatures at the Lobatto points. The remaining two unknown temperatures at the top and bottom of the fluid film are determined by boundary conditions. The Dirichlet boundary condition g_1 at the runner can simply be

implemented by setting

$$\bar{T}(\bar{r}, \bar{\theta}, \zeta = -1) = g_1. \tag{111}$$

The Neumann boundary condition f_2 at the thrust plate can be incorporated into the solution process by taking into account the additional field equation (see [15]):

$$\left. \frac{\partial \bar{T}(\bar{r}, \bar{\theta}, \zeta)}{\partial \zeta} \right|_{\zeta=1} = I_{ji} \bar{T}(\bar{r}, \bar{\theta}, \zeta_i) \left. \frac{\partial P_j(\zeta)}{\partial \zeta} \right|_{\zeta=1} = f_2. \tag{112}$$

Galerkin Method: In the framework of this method, density, fluidity and temperature are approximated by Legendre polynomials. The method is similar to the *Point Collocation Method*. The main difference is that the Dirac-delta functions (109) are replaced by the Legendre polynomials as weighting functions, see [11]. Applying the *Galerkin Method* to the 3D energy equation (103), we get the following $N+1$ 2D partial differential equations:

$$\int_{-1}^1 \dot{e}_{conv} \vartheta^{gal}(\zeta) d\zeta = \int_{-1}^1 \dot{e}_{comp} \vartheta^{gal}(\zeta) d\zeta + \int_{-1}^1 \dot{e}_{dis} \vartheta^{gal}(\zeta) d\zeta + \int_{-1}^1 \dot{e}_{cond} \vartheta^{gal}(\zeta) d\zeta \quad \forall l = 0, \dots, N, \tag{113}$$

with

$$\vartheta_l^{gal} = P_l(\zeta). \tag{114}$$

Neumann and Dirichlet boundary conditions at the runner $\zeta = -1$ and at the thrust plate $\zeta = 1$ are incorporated by means of the weak formulation for the heat conduction term according to

$$\int_{\zeta=-1}^1 \dot{e}_{cond} P_l(\zeta) d\zeta = T_a \lambda \left[\int_{\zeta=-1}^1 \frac{1}{(r_1 + \Delta r \bar{r})(\Delta r)^2} \frac{\partial}{\partial \bar{r}} \left((r_1 + \Delta r \bar{r}) I_{ji} \frac{\partial \bar{T}(\bar{r}, \bar{\theta}, \zeta)}{\partial \bar{r}} \right) P_l(\zeta) P_l(\zeta) d\zeta + \frac{4}{h_2^2 h} \left[\left. \frac{\partial \bar{T}(\bar{r}, \bar{\theta}, \zeta)}{\partial \zeta} P_l(\zeta) \right|_{\zeta=-1} - I_{ji} \bar{T}(\bar{r}, \bar{\theta}, \zeta_i) \int_{\zeta=-1}^1 \frac{\partial P_j(\zeta)}{\partial \zeta} \frac{\partial P_l(\zeta)}{\partial \zeta} d\zeta \right] \right] \quad \forall l = 0, \dots, N. \tag{115}$$

Neumann boundary conditions may now simply be implemented both at the runner and at thrust plate by specifying the term

$$\left[\frac{\partial \bar{T}(\bar{r}, \bar{\theta}, \zeta)}{\partial \zeta} P_l(\zeta) \right]_{\zeta=-1} = \left. \frac{\partial \bar{T}(\bar{r}, \bar{\theta}, \zeta)}{\partial \zeta} \right|_{\zeta=1} P_l(\zeta=1) - \left. \frac{\partial \bar{T}(\bar{r}, \bar{\theta}, \zeta)}{\partial \zeta} \right|_{\zeta=-1} P_l(\zeta=-1). \tag{116}$$

The Neumann boundary condition f_2 at the thrust plate can be incorporated by setting

$$\left. \frac{\partial \bar{T}(\bar{r}, \bar{\theta}, \zeta)}{\partial \zeta} \right|_{\zeta=1} = f_2. \tag{117}$$

Dirichlet boundary conditions can in a similar manner be incorporated by making use of a penalty approach. Specifying the Dirichlet boundary condition g_1 at the runner is simply accomplished by setting

$$\left. \frac{\partial \bar{T}(\bar{r}, \bar{\theta}, \zeta)}{\partial \zeta} \right|_{\zeta=-1} = c \left(\bar{T}(\bar{r}, \bar{\theta}, \zeta = -1) - g_1 \right), \tag{118}$$

where c denotes the penalty factor.

Remark on the discretization approach and the solution procedure for the Point Collocation Method and the Galerkin Method: The $N+1$ 2D field equations (110)–(112) of the *Point Collocation Method* and the $N+1$ 2D field equations (113) of the *Galerkin Method* for the unknown temperatures at the Lobatto points are discretized by 2D quadrilateral Lagrange elements of order two. The generalized Reynolds equation (101) is also discretized by 2D quadrilateral Lagrange elements of order two. Again, a segregated solution approach is applied for solving the discretized system:

- *Stage 1:* In the first solution step, pressure is kept constant and the $N+1$ 2D field equations are solved for the unknown temperatures at the Lobatto points.
- *Stage 2:* In the second solution step, the Dowson integrals are approximated by a Lobatto point quadrature method according to Eqs. (93)–(99).
- *Stage 3:* In the third solution step, the 2D pressure field is calculated based on the approximated Dowson integrals from stage 2 by solving the generalized Reynolds equation (101).

Stages 1–3 are repeated until global convergence of all variables is achieved.

Remark on possible numerical instabilities in connection with the discretization of the 3D energy equation: The numerical solution of the 3D energy equation (103) with a finite element approach may result in numerical instabilities. Instabilities are frequently observed in connection with pure convection and convection–diffusion problems, see [16,17]. Instabilities associated with convection–diffusion problems occur if the convection terms in the 3D energy equation are significantly larger than the diffusion terms. A characteristic number for the ratio of convection and diffusion in the \bar{r} -, $\bar{\theta}$ - and ζ -direction are given by the (local) element Péclet numbers, see e.g. [17]:

$$Pe_{\bar{r}}^e = \frac{\Delta l_{\bar{r}} \rho c_p v_r}{\lambda}, \tag{119}$$

$$Pe_{\bar{\theta}}^e = \frac{\Delta l_{\bar{\theta}} \rho c_p v_{\theta}}{\lambda}, \tag{120}$$

$$Pe_{\zeta}^e = \frac{\Delta l_{\zeta} \rho c_p w}{\lambda}. \tag{121}$$

Herein, $\Delta l_{\bar{r}}$, $\Delta l_{\bar{\theta}}$ and Δl_{ζ} describe the element size in the \bar{r} -, $\bar{\theta}$ - and ζ -direction. Instabilities may occur, if one of the three element Péclet numbers exceeds a critical value. Considering the linear 1D case, the critical value of the local Péclet number can be obtained analytically [17]. Instability effects for 3D problems are more complicated. In the 3D case, stabilizing and destabilizing effects exist between the different directions. For instance, a convection dominated flow in the $\bar{\theta}$ -direction (i.e. the \bar{x} -direction for the oil slider bearing) may be stabilized by heat conduction in the ζ -direction. A thorough stability analysis for nonlinear 3D problems is very complicated and strongly depends on the system parameters, on the discretization and on the boundary conditions. According to assumptions 7 and 8 in Sections 2.1 and 2.2, heat conduction in the $\bar{\theta}$ -direction has been neglected in context of this paper so that a typical convection–diffusion instability cannot occur in the $\bar{\theta}$ -direction. However, pure convection in the $\bar{\theta}$ -direction may also entail numerical instabilities, if the system parameters and the boundary conditions are chosen inappropriately. Since a detailed analytical stability analysis is not possible for the considered nonlinear 3D problem, numerical simulations for different system parameters and different discretizations have

been carried out. The results of our simulations can be summarized as follows:

- For the gas bearing, instabilities have not been observed, even for larger element lengths and larger runner velocities.
- For the oil bearing, we detected instabilities for larger runner velocities in connection with larger element sizes.

For the parameters, discretizations and boundary conditions chosen in Section 4, we have not detected any numerical instabilities.

4. Results

The presented five reduction approaches – namely the *Averaging Approach* of Section 3.1 and the *Quadrature Method*, the *Modified Quadrature Method*, the *Point Collocation Method* and the *Galerkin Method* of Section 3.2 – are now compared with respect to numerical efficiency, accuracy and convergence behavior for the gas thrust bearing (see Section 4.1) and the oil slider bearing (see Section 4.2). The accuracy of the different approaches is estimated using the following error definitions (see e.g. [18]):

$$\bar{e}_{r,\bar{T}}(D_i) = \frac{\sqrt{\frac{1}{N_{a,\bar{T}}} \sum_{k=1}^{N_{a,\bar{T}}} (\bar{T}_k(D_i) - \bar{T}_k(\Delta l_{ref}))^2}}{\sqrt{\frac{1}{N_{a,\bar{T}}} \sum_{k=1}^{N_{a,\bar{T}}} (\bar{T}_k(\Delta l_{ref}))^2}}, \quad (122)$$

$$\bar{e}_{r,\bar{p}}(D_i) = \frac{\sqrt{\frac{1}{N_{a,\bar{p}}} \sum_{k=1}^{N_{a,\bar{p}}} (\bar{p}_k(D_i) - \bar{p}_k(\Delta l_{ref}))^2}}{\sqrt{\frac{1}{N_{a,\bar{p}}} \sum_{k=1}^{N_{a,\bar{p}}} (\bar{p}_k(\Delta l_{ref}))^2}}. \quad (123)$$

Herein, $\bar{e}_{r,\bar{T}}(\Delta l_i)$ and $\bar{e}_{r,\bar{p}}(\Delta l_i)$ denote, respectively, the relative error in temperature and pressure for a given discretization D_i across the fluid film. The discretization parameter D_i denotes either the dimensionless length $\Delta l_{\bar{z}}$ of a finite element across the fluid film in case of the *Averaging Approach* or the polynomial order N in case of the *Polynomial Approach*. Furthermore, $N_{a,\bar{T}}$ and $N_{a,\bar{p}}$ denote the number of nodes used for the error estimation. As a reference model, we use an unreduced 3D bearing model, which is solved by a finite element approach with a fine mesh (element length Δl_{ref}).

4.1. Results for the gas thrust bearing

Accuracy and convergence behavior of the different approaches are compared by using the error definitions (122) and (123). Numerical efficiency is compared by evaluating the computation time and the accuracy of the different approaches. In the following investigations, the discretization in the \bar{r} - and $\bar{\theta}$ -direction is kept constant using $32 \times 32 = 1024$ elements. Discretization across the fluid film is varied. For the *Averaging Approach* the number of elements across the fluid film is changed (i.e. the element length $\Delta l_{\bar{z}}$ is varied). For the *Polynomial Approach* the polynomial order N is varied. In the reference model, $32 \times 32 \times 40 = 40,960$ hexahedral Lagrange elements of order two are used in the \bar{r} -, $\bar{\theta}$ - and $\bar{\zeta}$ -direction.

The calculations have been carried out with the subsequent air thrust bearing parameters:

$$\begin{aligned} r_1 &= 13.5 \times 10^{-3} \text{ m}, & r_2 &= 30 \times 10^{-3} \text{ m}, \\ \theta_0 &= \frac{2}{3} \pi, & h_1 &= 2h_2 = 20 \times 10^{-6} \text{ m}, \\ \Omega &= 3000 \text{ 1/s}, & \rho &= 1.1197 \text{ kg/m}^3, \\ \lambda &= 0.0262 \text{ W/m K}, & \eta_0 &= \eta_R = 18.27 \times 10^{-6} \text{ Pa s}, \end{aligned}$$

$$\begin{aligned} T_a &= 311.11 \text{ K}, & c_p &= 1005 \text{ J/kg K}, \\ T_R &= 291.15 \text{ K}, & C &= 120 \text{ K}, \\ R &= 287.058 \text{ J/kg K}, & p_a &= 10^5 \text{ Pa}, \\ R_{th} &= 21 \text{ K/W}. \end{aligned}$$

Fig. 3 shows the temperature field (left) and the pressure field (right) in the air thrust bearing calculated with the reference model. The pressure profile shows the typical pressure increase from pad inlet to outlet. The maximum pressure of $p - p_a = 0.42$ bar is located close to the pad outlet. The pressure distribution is unsymmetrical, since the circumferential velocity of the runner increases in the radial direction, see Fig. 3 (right). Because of the large pressure gradient at the pad outlet, the circumferential fluid velocity increases from the inlet to the outlet. Hence, the gradient of the circumferential velocity in the $\bar{\zeta}$ -direction – and therefore the temperature – has its maximum at $\bar{r} = \bar{\theta} = 1$, see Fig. 3 (left). As can be seen in Fig. 3 (left), the temperature across the fluid film only varies about in maximum 4 K in maximum. This low temperature increase in the $\bar{\zeta}$ -direction is caused by the dominance of the heat conduction compared to the heat convection, which is typical for air thrust bearings.

Fig. 4 shows the relative error in temperature $\bar{e}_{r,\bar{T}}^{Av}(\Delta l_{\bar{z}})$ (left) and pressure $\bar{e}_{r,\bar{p}}^{Av}(\Delta l_{\bar{z}})$ (right) for the *Averaging Approach* over the element length $\Delta l_{\bar{z}}$. The error has been calculated for three different element sizes, namely for $\Delta l_{\bar{z}} = \{0.25, 0.125, 0.0625\}$. The corresponding simulation times are $t_c^{Av} = \{29.7691 \text{ s}, 69.4204 \text{ s}, 191.7250 \text{ s}\}$. As can be seen, the errors are very small, even for the case that only four elements are used in the $\bar{\zeta}$ -direction. This is reasonable, since for gas bearings the temperature varies only little across the fluid film.

Results for the *Quadrature Method* (*Quad* [2]), the *Modified Quadrature Method* (*Quad,mod* [2]), the *Point Collocation Method* (*Col*) and the *Galerkin Method* (*Gal*) are collected in Figs. 5 and 6. Fig. 5 shows the relative error in temperature (left) and pressure (right) over the polynomial order N . Fig. 6 depicts the computation time over the polynomial order N . For the *Quadrature Method* and the *Modified Quadrature Method*, the 3D energy equation is discretized. The number of elements in the $\bar{\zeta}$ -direction is adopted to the polynomial order N by using $2(N+2)$ elements across the fluid film.

As can be seen in Fig. 5, the largest error in temperature and pressure exhibits the *Point Collocation Method*. It can further be observed that the error is not significantly reduced for $N > 4$. However, the *Point Collocation Method* shows the smallest simulation time. The large error mainly results from the Neumann boundary conditions at the top and bottom of the fluid film, see [15]. It should be stressed that the *Point Collocation Method* entails a significantly larger error than the *Averaging Approach*.

The *Quadrature Method* and the *Modified Quadrature Method* yield similar errors. For the *Galerkin Method*, the error in temperature is larger compared with the *Quadrature Method*. For $N \geq 4$, however, the error in pressure for the *Galerkin Method* is smaller than that for the *Quadrature Method*. Obviously, the temperatures at the Lobatto points are calculated more accurately if Legendre polynomials are used for approximating the temperature (*Galerkin Method*) in contrast to the *Quadrature Method*, where quadratic Lagrange polynomials are applied. For $N \geq 6$, the computation time for the *Galerkin Method* is larger than for the *Quadrature Method*.

Applying the *Quadrature Method* and the *Modified Quadrature Method*, the 3D energy equation has to be discretized in the $\bar{\zeta}$ -direction. Figs. 7 and 8 show the influence of the discretization in the $\bar{\zeta}$ -direction on the error in temperature and on the computation time. Therefore, $1(N+2)$, $2(N+2)$ and $3(N+2)$ elements are used for discretizing the 3D energy equation in the $\bar{\zeta}$ -direction. As expected, the error is reduced if the number of elements is increased. The plots also contain error and computation time for the *Galerkin Method*.

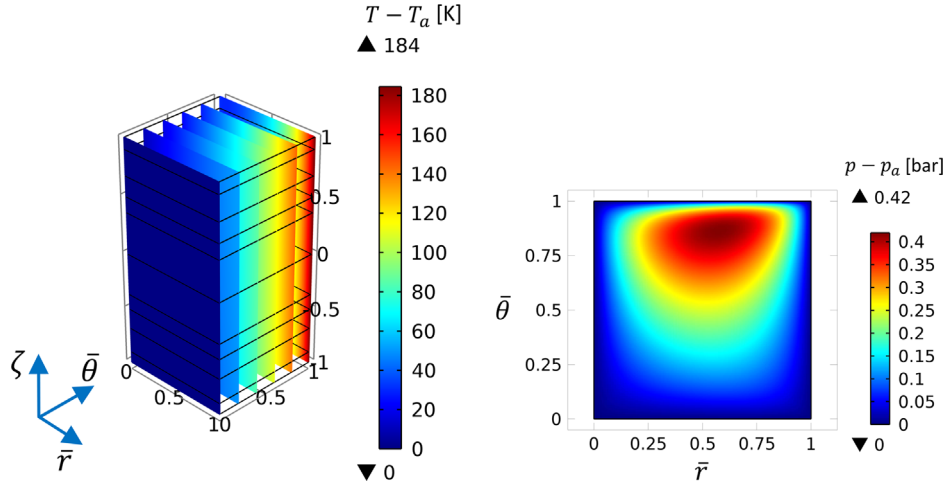


Fig. 3. Temperature field (left) and pressure field (right) for the inclined air thrust bearing.

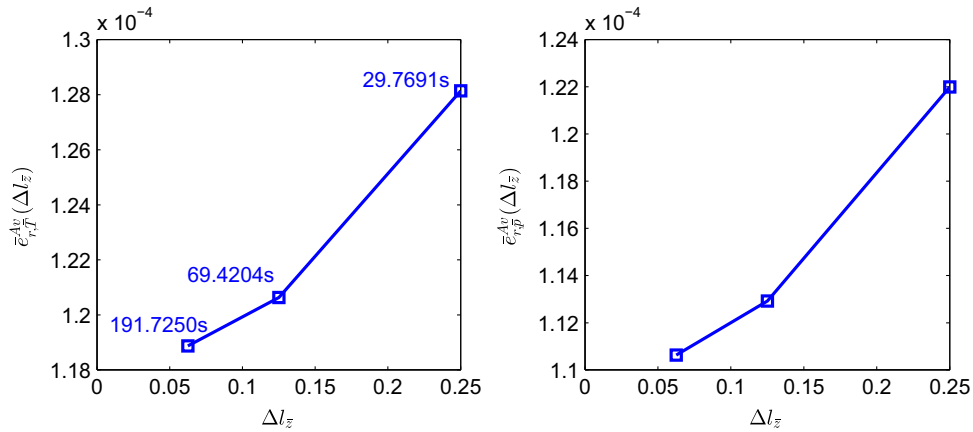


Fig. 4. Relative error in temperature (left) and pressure (right) for the *Averaging Approach* over the element size (air thrust bearing).

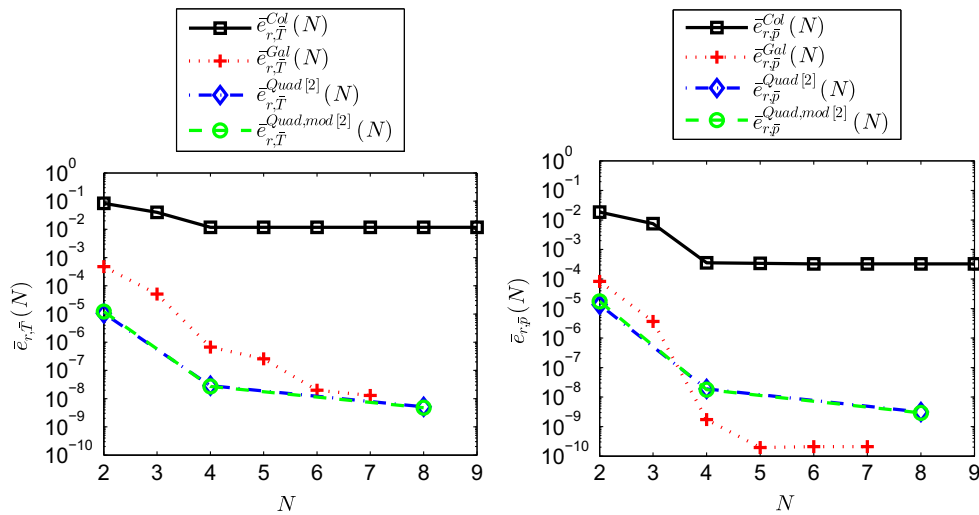


Fig. 5. Relative error in temperature (left) and pressure (right) for the *Quadrature Method*, the *Modified Quadrature Method*, the *Point Collocation Method* and the *Galerkin Method* over the polynomial order N (air thrust bearing).

Comparing the results for the gas bearing, we observe that the *Quadrature Method (Quad [2])* for $N=4$ yields very accurate results and a moderate computation time. The computational effort may further be reduced by using the *Averaging Approach* with $\Delta l_z = 0.25$ or the *Galerkin Method* in combination with $N=3$.

For the unreduced model, the same grid in the \bar{r} , $\bar{\theta}$ -plane has been used as for the reduction approaches. In the \bar{z} -direction, four

hexahedral Lagrange elements of order two have been used. Using only four elements, the simulation time for the unreduced model is significantly larger ($t_c = 2227.72$ s) compared to the simulation time observed for the *Averaging Approach*, the *Galerkin Method*, the *Quadrature Method* and the *Modified Quadrature Method*. Also, the numerical error is significantly larger (Error in temperature: $\bar{e}_{r,T}^{unred}(\Delta l_z) = 0.0016825$; error in pressure: $\bar{e}_{r,p}^{unred}(\Delta l_z) = 0.0214762$).

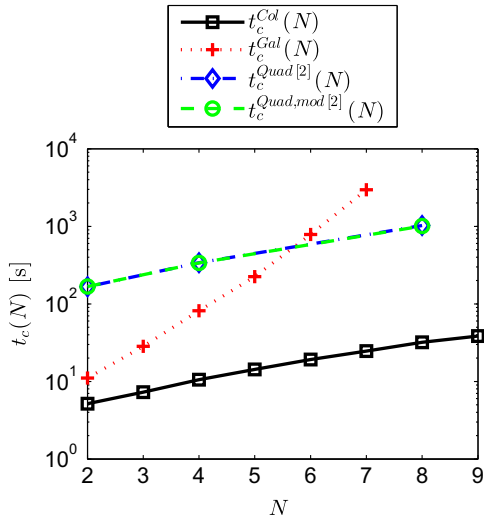


Fig. 6. Computation time for the *Quadrature Method*, the *Modified Quadrature Method*, the *Point Collocation Method* and the *Galerkin Method* over the polynomial order N (air thrust bearing).

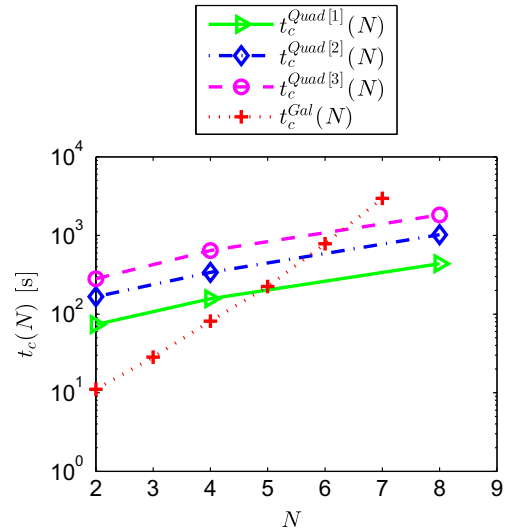


Fig. 8. Computation time for the *Quadrature Method* and for the *Galerkin Method* over the polynomial order N for different discretizations (air thrust bearing).

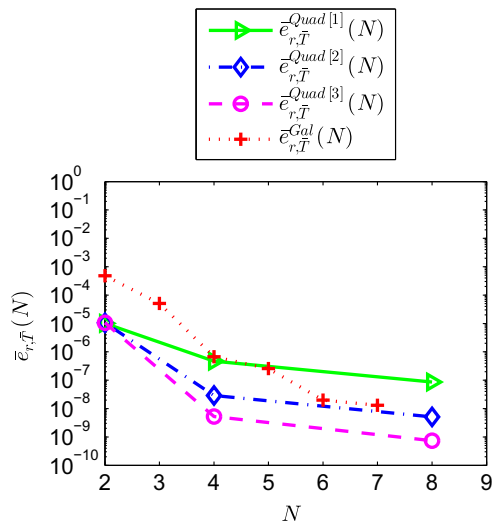


Fig. 7. Relative error in temperature for the *Quadrature Method* and for the *Galerkin Method* over the polynomial order N for different discretizations (air thrust bearing).

4.2. Results for the oil slider bearing

In this section, the reduction approaches are compared with respect to numerical efficiency, accuracy, and convergence behavior for the oil slider bearing. In the reference model, $40 \times 40 \times 40 = 64,000$ hexahedral Lagrange elements of order two are used in the \bar{x} -, \bar{y} - and \bar{z} -direction.

Simulations have been accomplished using the subsequent bearing parameters (see [4]):

$$\begin{aligned}
 L = B &= 91.44 \times 10^{-3} \text{ m}, & h_1 = 2h_2 &= 1.3026 \times 10^{-4} \text{ m}, \\
 U_1 &= 30.48 \text{ m/s}, & \rho &= 874.5 \text{ kg/m}^3, \\
 \nu_0 &= 142.4 \times 10^{-6} \text{ m}^2/\text{s}, & \nu_1 &= 14.4 \times 10^{-6} \text{ m}^2/\text{s}, \\
 \lambda &= 0.1298 \text{ W/m K}, & c_p &= 2010 \text{ J/kg K}, \\
 T_0 = T_a &= 310.92 \text{ K}, & T_1 &= 372.04 \text{ K}, \\
 p_a &= 10^5 \text{ Pa}.
 \end{aligned}$$

Fig. 9 shows the temperature field (left) and the pressure field (right) for the oil slider bearing calculated with the reference model. In contrast to the air thrust bearing, the pressure

distribution is now symmetrical, see Fig. 9 (right). The maximum temperature in the fluid film is located at the pad outlet on the top surface of the bearing, see Fig. 9 (left). In contrast to the air thrust bearing, the temperature varies significantly across the fluid film. Fig. 10 shows the relative error in temperature (left) and pressure (right) for different element lengths ($\Delta l_z = \{0.25, 0.125, 0.0625, 0.03125\}$) for the *Averaging Approach*. The corresponding simulation times are $t_c^{Av} = \{10.483 \text{ s}, 23.3351 \text{ s}, 54.4416 \text{ s}, 144.724 \text{ s}\}$. Due to the large temperature variation across the oil film, the relative errors in temperature and pressure calculated with the *Averaging Approach* are quite large. Hence, the *Averaging Approach* is not suitable to reduce the computational effort with an acceptable error for oil slider bearings.

Fig. 11 shows the relative error in temperature (left) and pressure (right) for the *Quadrature Method* (*Quad* [2]), the *Modified Quadrature Method* (*Quad,mod* [2]), the *Point Collocation Method* (*Col*) and the *Galerkin Method* (*Gal*) over the polynomial order N . The corresponding computation times are plotted in Fig. 12 over the polynomial order N .

As in the Section 4.1, the *Point Collocation Method* shows the largest error in temperature and pressure as well as the shortest computation time. For the *Galerkin Method* with $N=4$, the error in temperature is about 21% larger than the error for the *Point Collocation Method* with $N=6$. Moreover, the *Galerkin Method* shows a 34% larger computation time. In order to achieve small errors with the *Point Collocation Method*, higher order polynomials are required. Using however higher order polynomials ($N \geq 11$) in combination with the *Point Collocation Method* often leads to numerical instabilities. A clear explanation for the numerical convergence problems observed with the *Point Collocation Method* for $N \geq 11$ is difficult. Using higher order approximation polynomials, convergence problems are frequently detected in numerical analyses. Applying higher order approximation, oscillation effects are often detected, see e.g. [19]. Such oscillation effects could be the reason for the observed convergence problems in connection with the *Point Collocation Method*. It should however be stressed again that the governing integro-differential equation system is highly nonlinear so that the convergence problems might simply be traced back to the nonlinearity of the equation system. Therefore, the *Point Collocation Method* is not well-suited to generate very accurate simulation results. In contrast to the air thrust bearing, the error for the *Point Collocation Method* decreases if N is increased. This is caused by the fact that in case of the oil slider

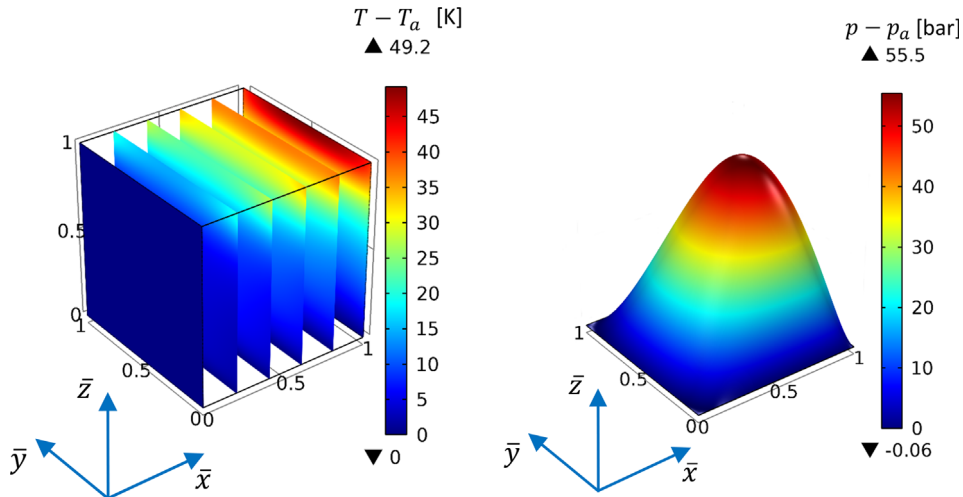


Fig. 9. Temperature field (left) and pressure field (right) for the inclined oil slider bearing.

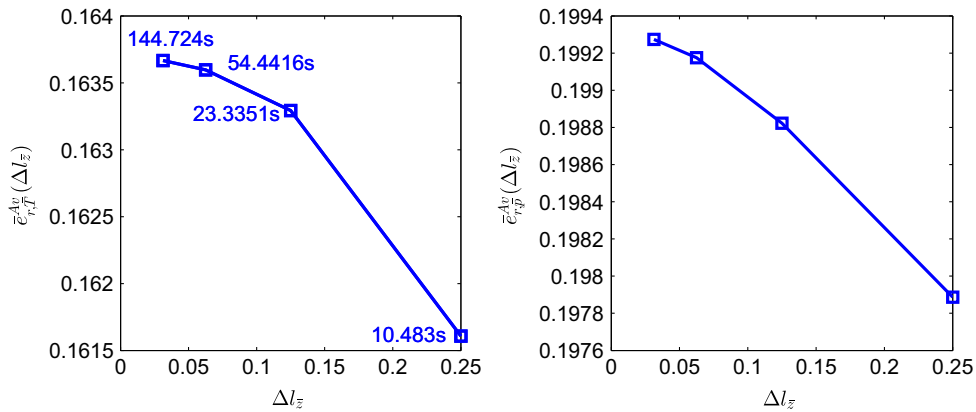


Fig. 10. Relative error in temperature (left) and pressure (right) for the Averaging Approach over the element size (oil slider bearing).

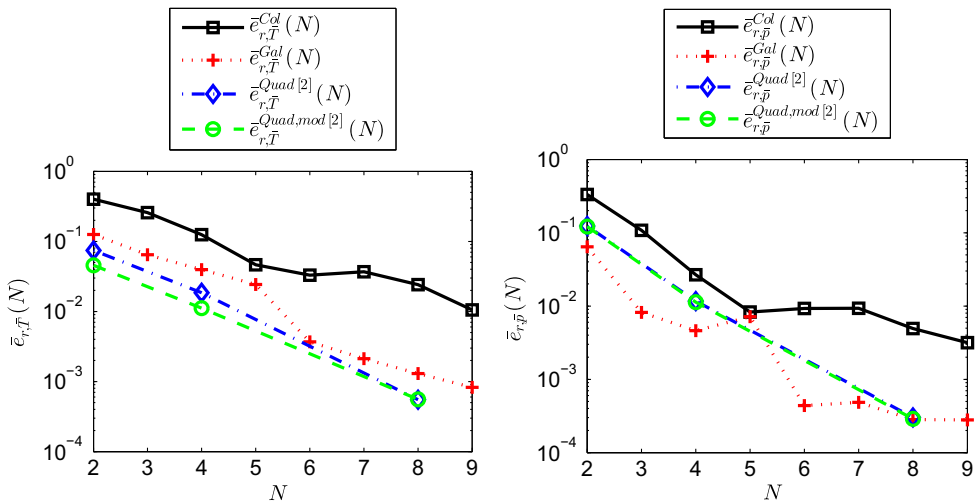


Fig. 11. Relative error in temperature (left) and pressure (right) for the Quadrature Method, the Modified Quadrature Method, the Point Collocation Method and the Galerkin Method over the polynomial order N (oil slider bearing).

bearing only one Neumann boundary condition is implemented at the top of the fluid film, see Section 2.2.

The Quadrature Method and the Modified Quadrature Method show nearly the same computation time. For $N=2$ and $N=4$, the Modified Quadrature Method exhibits a lower error than the Quadrature Method. For $N=8$, the computation time for the Quadrature Method is about 4.6 times larger than the computation

time for the Galerkin Method. However, for the Galerkin Method the error in temperature is about 137% larger than the error for the Quadrature Method. Except for the case $N=5$, the Galerkin Method shows a smaller error in the pressure than the Quadrature Method.

Using the Quadrature Method and the Modified Quadrature Method, the 3D energy equation has also to be discretized in the ζ -direction. Figs. 13 and 14 depict the influence of the

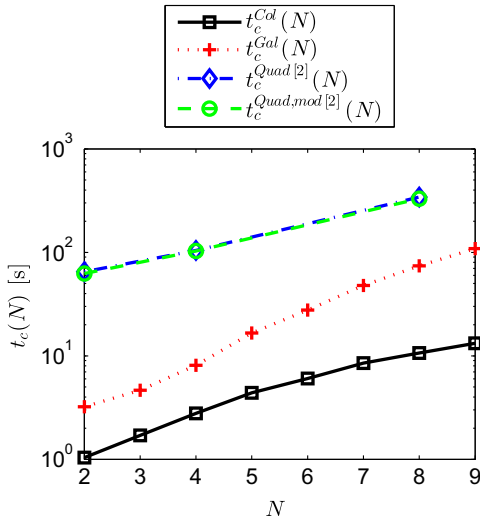


Fig. 12. Computation time for the Quadrature Method, the Modified Quadrature Method, the Point Collocation Method and the Galerkin Method over the polynomial order N (oil slider bearing).

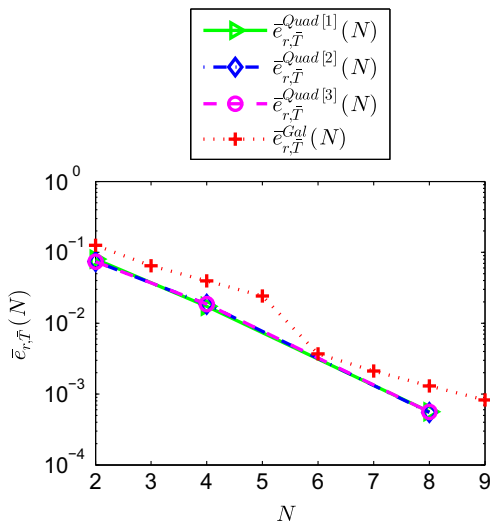


Fig. 13. Relative error in temperature for the Quadrature Method and for the Galerkin Method over the polynomial order N for different discretizations (oil slider bearing).

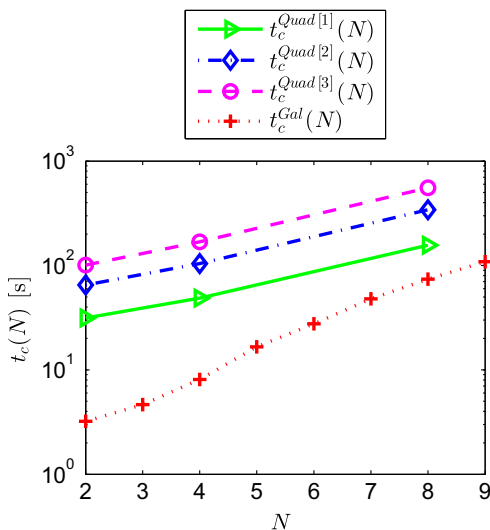


Fig. 14. Computation time for the Quadrature Method and for the Galerkin Method over the polynomial order N for different discretizations (oil slider bearing).

discretization in the ζ -direction on the error in temperature and on the computation time. Therefore, $1(N+2)$, $2(N+2)$ and $3(N+2)$ elements have been used for discretizing the 3D energy equation in the ζ -direction. As can be seen, the number of elements has very little influence on the relative error in temperature. The computation time, however, increases significantly with the number of elements. For $N=8$, the Quadrature Method (Quad [3]) and the Galerkin Method show comparable results with respect to numerical error and computation time.

The error in temperature for the unreduced finite element model with 16 elements across the fluid film is 1.8% larger than the error observed with the Quadrature Method (Quad [1]) with $N=8$. Furthermore, the error in pressure for the unreduced model is 122.62% larger than the error for the Quadrature Method (Quad [1]). The computation time of both models are equal.

5. Conclusions

Five different techniques have been presented for reducing thermogas- and thermohydrodynamic bearing models. The first method is based on averaging the fluid temperature across the fluid film. Within the second and the third method (Quadrature Method and Modified Quadrature Method), fluidity and density are approximated by Legendre polynomials across the fluid film. In the fourth and the fifth method (Point Collocation Method and Galerkin Method), temperature is also approximated using Legendre polynomials. For gas thrust bearings, all reduction approaches yielded a significant reduction in the computation time compared to the unreduced finite element model. Good performance with respect to accuracy and computation time showed the Quadrature Method. Very low computation times and moderate errors have been achieved with the Averaging Method and with the Galerkin Method. The Galerkin Method yielded very accurate results for the pressure. For oil slider bearings, the Galerkin Method and the Quadrature Method showed very accurate results. Numerical instabilities have been observed for the Point Collocation Method in combination with higher order polynomials. Furthermore, it has been shown that the Averaging Approach is not suitable for calculating the temperature and pressure field in oil bearings due to the large temperature gradient across the oil film.

In summary, application of reduction methods may be very useful for gas bearings. For oil bearings, however, making use of reduction approaches may not be very beneficial, since a direct implementation of the unreduced model yields similar results with comparable computation times.

References

- [1] Gunter EJ, Chen WJ. Dynamic analysis of a turbocharger in floating bushing bearings. In: Proceedings of the third international symposium on stability control of rotating machinery, Cleveland, OH; 2005.
- [2] Kirk RG, Alsaeed AA, Gunter EJ. Stability analysis of a high-speed automotive turbocharger. Tribol Trans 2007;50(3):427–34.
- [3] Schweizer B, Sievert M. Nonlinear oscillations of automotive turbocharger turbines. J Sound Vib 2009;321:955–75.
- [4] Ezzat A, Rohde SM. A study of the thermohydrodynamic performance of finite slider bearings. J Lubr Technol 1973;95:298–307.
- [5] Huebner KH. A three-dimensional thermohydrodynamic analysis of sector-thrust bearings. Tribol Trans 1974;17(1):62–73.
- [6] Dowson D. A generalized Reynolds equation for fluid-film lubrication. Int J Mech Sci 1961;4:150–70.
- [7] Dellacorte C, Valco MJ. Load capacity estimation of foil air journal bearings for oil-free turbomachinery applications. Tribol Trans 2000;43(4):795–801.
- [8] Radil K, Howard S, Dykas B. The role of radial clearance on the performance of foil air bearings. Tribol Trans 2002;45(4):485–90.
- [9] Elrod HG. Efficient numerical method for computation of thermohydrodynamics of laminar lubricating films, Technical report. NASA Lewis Research Center; 1989.
- [10] Feng K, Kaneko S. A thermohydrodynamic sparse mesh model of bump-type foil bearings. J Eng Gas Turb Power; 135(2).

- [11] Elrod HG, Bewe DE. Thermohydrodynamic analysis for laminar lubricating films, Technical report, NASA technical memorandum 88845; 1986.
- [12] Moraru LE. Numerical prediction and measurements in the lubrication of aeronautical engine and transmission components [Ph.D. thesis]. University of Toledo; 2005.
- [13] Lee D, Kim D. Three-dimensional thermohydrodynamic analysis of Rayleigh step air foil thrust bearings with radial arranged bump foils. *Tribol Trans* 2011;54(3):432–48.
- [14] Sutherland W. LII. The viscosity of gases and molecular forces. *Philos Mag* 1893;5:505–31.
- [15] Wang J-P, Nakamura Y, Yasuhara M. Global coefficient adjustment method for Neumann condition in explicit Chebyshev collocation method and its application to compressible Navier–Stokes equations. *J Comput Phys* 1993;107:160–75.
- [16] Press WH, Teukolsky SA, Vetterling WT, Flannery BP. Numerical recipes, the art of scientific computing. 3rd edition Cambridge University Press; 2007.
- [17] Bathe KJ. Finite element procedures. Prentice-Hall International, Inc.; 1996.
- [18] Schweizer B. Numerical approach for solving Reynolds equation with JFO boundary conditions incorporating ALE techniques. *J Tribol* 2009;131:1–14.
- [19] Davis PJ. Interpolation & approximation. Dover Publications, Inc.; 1975.



Paper III

M. Mahner, M. Bauer, and B. Schweizer, Numerical Analyzes and Experimental Investigations on the Fully-Coupled Thermo-Elasto-Gasdynamic Behavior of Air Foil Journal Bearings, Mechanical Systems and Signal Processing 149 (2021): 107221.

©2021. This manuscript version is made available under the CC-BY-NC-ND 4.0 license <http://creativecommons.org/licenses/by-nc-nd/4.0/>



Contents lists available at ScienceDirect

Mechanical Systems and Signal Processing

journal homepage: www.elsevier.com/locate/ymssp

Numerical analyzes and experimental investigations on the fully-coupled thermo-elasto-gasdynamics behavior of air foil journal bearings



Marcel Mahner*, Marcel Bauer, Bernhard Schweizer

Technical University of Darmstadt, Department of Mechanical Engineering, Institute of Applied Dynamics, Otto-Berndt-Strasse 2, 64287 Darmstadt, Germany

ARTICLE INFO

Article history:

Received 31 January 2020
 Received in revised form 23 May 2020
 Accepted 11 August 2020
 Available online 2 October 2020

For the MSSP Special Issue in Honor of Professor Lothar Gaul.

2010 MSC:

00–01
 99–00

Keywords:

Air Foil Bearings
 Thermo-Elasto-Gasdynamics
 Reduction Approaches
 Temperature Measurements

ABSTRACT

Air foil journal bearings are an important component in high-speed, oil-free turbomachinery applications. In order to optimize the performance of rotor systems supported by air foil journal bearings, detailed numerical models are needed. In this paper, a fully-coupled thermo-elasto-gasdynamics bearing model is presented. Using this model, the thermo-elasto-gasdynamics behavior of a mechanically preloaded three-pad air foil journal bearing is investigated numerically. Furthermore, experiments are accomplished in order to validate the results obtained with the numerical model. The 3D thermo-elasto-gasdynamics bearing model comprises the description of bump and top foil deflection and the calculation of the pressure and temperature distribution in the air film as well as the temperature distributions in the surrounding structure, namely in the rotor, in the bearing sleeve and in the top and bump foil. The bump and top foil deflection are described by a nonlinear beamshell theory according to Reissner. The model accounts for the contact between the bump and the top foil and between the bump foil and the bearing sleeve. The pressure distribution is calculated by solving the generalized Reynolds equation according to Dowson. Temperature distributions in the air film and in the surrounding structure are obtained from the 3D energy equation and appropriate heat equations. In order to reduce the computational effort of the thermo-elasto-gasdynamics problem, the 3D energy equation and the generalized Reynolds equation are reduced by an averaging approach. The governing equations are solved by a finite element method.

© 2020 Elsevier Ltd. All rights reserved.

1. Introduction

Due to their simple and inexpensive design, the small maintenance effort and the ability to accommodate shaft growth induced by centrifugal and thermal effects, air foil bearings are widely used in high speed, low weight applications, like in micro gas turbines or compressors for fuel cell applications, see e.g. [1,2].

In contrast to rigid air bearings, an elastic foil structure is placed inside the bearing sleeve. In bump-type air foil journal bearings, this foil structure consists of bump and a top foils, see Fig. 1. The bump foil is a corrugated foil which induces compliance and damping to the bearing. The top foil provides a smooth surface for the pressure built-up in the air film.

* Corresponding author.

E-mail address: mahner@ad.tu-darmstadt.de (M. Mahner).

Nomenclature

A_{pad}	pad area [m ²]
C	Fluid dependent constant in the Sutherland equation [K]
E	Young's modulus [N/m ²]
F_b	bearing load [N]
F_y, F_z	resulting fluid film forces on the rotor in y- and z-direction [N]
H	thickness of top and bump foil [m]
H_{cot}	top foil coating thickness [m]
M	bending moment about the z-axis, related to the beamshell width [N]
N	normal force, related to the beamshell width [N/m]
Nu	Nusselt number
Pr	Prandtl number
Q	shear force, related to the beamshell width [N/m]
R_t	friction force [N]
Ra_{av}	arithmetic average surface roughness of top and bump foil [m]
Re	Reynolds number
W_D	energy dissipation [J]
\bar{p}	averaged pressure across the bearing width [Pa]
δ_{art}	artificial diffusion factor
\dot{q}	heat flux [W/m ²]
${}^0x_{tbij}$	limits of the contact region between bump and top foil [m]
\underline{n}_{M_k}	normal vector of the master surface at the contact node $s_{M_k}^*$
a_p	bump pitch [m]
a_{se}	segment length [m]
b	bearing width [m]
c	penalty stiffness [N/m]
c_p	isobaric heat capacity [J/(kgK)]
$c_{f_{hor}}$	foil structural stiffness in the direction of the horizontal bearing displacement [N/μm]
e_r	rotor eccentricity [m]
$f(\pm {}^0x_{tbij})$	function of the contact region limits; used in the calculation of the thermal contact resistance between bump and top foil [rad]
g_t	relative sliding distance in the tangential direction of the contacting master surface [m]
h	fluid film height [m]
h	gap function [m]
h_b	bump height [m]
h_{mesh}	element size [m]
k	heat conductivity [W/(m ² K)]
k_φ	stiffness of a torsional spring at the mounting suspension of top and bump foil [N]
l	length of bump or segment [m]
l_r	rotor length [m]
l_{ms}	length of the top and bump foil mounting suspension [m]
n	total number of bumps and segments per bumpfoil, $n = n_{bu} + n_s$
n	total number of bumps and segments
n_r	rotational speed [rpm]
n_s	number of segments per bump foil
n_{bu}	number of bumps per bump foil
n_{sl}	number of slave nodes per bump foil
p	two-dimensional pressure field in the fluid film [Pa]
p_y, p_z	pressure on the beamshell in y and z-direction [Pa]
r_{t_o}	outer top foil radius [m]
r_{bu_o}	outer bump radius [m]
s	material coordinate [m]
u	displacement in the global y- or z-direction [m]
x_a, y_a, z_a	longitudinal, transversal and cross-film coordinate of the fluid film [m]
x_{tb}	local tangential coordinate at the bump and top foil contact region [m]
z_r	axial position of the air foil journal bearing on the rotor [m]
F_0, F_1	Dowson integrals (m/(Pa s), m ² /(Pa s))
F_2, F_3	Dowson integrals (kg/(Pa s), kg/(Pa s m))
G_1, G_2, G_3	Dowson integrals (kg/(Pa s), kg/(Pa s m), kg/m ²)
z_a^*	Ratio of Dowson integrals, $z^* = F_1/F_0$ (m)

$\Delta\varphi$	rotation about the global x-axis [rad]
Ω	rotor angular velocity [s^{-1}]
Π	potential energy [J]
α_s	shear correction factor
δW	virtual work [J]
δW_f	virtual work of the friction forces [J]
$\delta \Pi_c$	virtual potential energy of the contact forces [J]
δ_D	Dirac delta function
δ_k	distance between a slave node k and the master surface [m]
δ_n	normal distance between slave/ node and master surface/ node [m]
$\delta_{n_{tr}}$	normal distance between top foil and rotor [m]
$\delta_{n_{tr}}^+$	contact switch function [m]
δ_{min_k}	minimum distance between a slave node k and the master surface [m]
η	dynamic fluid viscosity [Pa s]
γ_r	angle under which the bearing load is applied [rad]
κ	beamshell bending strain [m^{-1}]
λ	Lagrange multiplier [N]
ν	Poisson's ratio
ψ	angle between the rotor normal and the z-axis [rad]
ρ	fluid density [kg/m^3]
σ	rotor stress [N/m^2]
σ	signum function [m]
$\underline{\delta}_{min_k}$	vectorial distance between the contacting slave and master node in the global y- and z-direction [m]
ε, γ	beamshell normal and shear strain
$s_{M_k}^*$	arc length at which the minimum distance δ_{min_k} occurs [m]
φ_0, φ	orientation of the beamshell cross section about the global x-axis in the initial and in the current configuration [rad]

Subscripts

a	air film
AL	Augmentes Lagrange
amb	ambient air
amb	ambient
b	bump foil
bs	bearing sleeve
bu	bump
c	center
$comp$	compression
$cond$	conduction
$conv$	convection
dis	dissipation
gr	growth
gr	growth
i	i -th bearing pad
in	inner
j	index for indicating bump or segment, $j = 1, \dots, n = n_b + n_s$
l	leading edge
l	lightly
lt	leading/trailing edge
M	Master
mes	measurement
ms	mounting suspension
n	normal
o	outer
p	penalty
R	reference
r	rotor
s	segment
sim	simulation
t	top foil
tr	topfoil/rotor contact

tr	trailing edge
y, z	y- and z-direction
<i>Superscripts</i>	
AL	Augmented Lagrange
o	outer
i	inner
p	penalty

Rotors supported by air foil journal bearings often show subharmonic vibrations and fluid film induced instabilities, see e.g. [3]. The introduction of a mechanical preload in air foil journal bearings can significantly improve the dynamic performance of air bearing supported rotors, e.g. the amplitudes of sup- and superharmonic motions and the onset speed of the rotor instability, as shown for example by Sim et al. [4]. In their study, Sim et al. [4] used shims to mechanically preload a one-pad air foil journal bearing. The three shims locally reduce the bearing clearance. Thereby, a wedge is introduced which affects the bearing mainly aerodynamically, while the foil structural stiffness of bump and top foil is not affected significantly, see the static stiffness measurements in [4].

In this manuscript, a three-pad air foil journal bearing is preloaded by using bump and top foils whose initial undeformed radii are significantly larger than the inner radius of the bearing sleeve and the outer radius of the shaft, see Fig. 2. The foils are elastically bent during their assembly in the bearing sleeve. In order to assemble the bearing on a rotor, the foils have to be pushed towards the bearing sleeve. When this force is released, the foils will push against the rotor creating a preload. This preload is defined as an assembly preload, see [5,6]. Note, that even when rotor and bearing are perfectly aligned, there is no radial clearance between the rotor and the top foils like in other air foil journal bearing designs, see e.g. [2]. In contrast to the mechanical preload introduced by shims, like in [4], the assembly preload significantly increases the foil structural stiffness as well as the bearing damping, see [5,6]. Thereby, the bearing will operate mostly in the linear region of the bearing force–displacement relationship. This improves the rotor dynamic behavior of the supported rotor.

Besides these rotor dynamic advantages, the assembly preload has an important downside: It increases the drag torque during airborne operation [5,6] as well as the startup and shutdown torque, see [7]. Latter results in larger power requirements during rotor startup, increased wear and rotor lift-off at higher rotational speeds. The larger frictional losses during airborne operation lead to higher temperatures with the risk of a bearing failure due to thermal runaway, see e.g. [8].

Even for the case that air foil journal bearings are not preloaded, the thermal behavior is a crucial issue which can lead to bearing failure. This results from the low heat capacity of air, see e.g. [9]. Although the frictional losses are comparatively small, the low heat capacity can result in a significant rise of the bearing temperature.

Therefore, a lot of researchers have investigated the thermal behavior of air foil journal and thrust bearings numerically and experimentally. Due to the low heat capacity of air, the thermal behavior of air foil journal bearings strongly depends on the heat transfer in the surrounding components, e.g. in the rotor, in the foil structure and in the bearing sleeve, see. [9]. Out of this reason, numerical models have to account for the different heat paths through the bearing and the rotor which makes the models quite complex.

The numerical models in literature can be distinguished with respect to their level of detail: In lumped thermal models, the temperature of the different bearing components are calculated from global heat balances using thermal resistances to

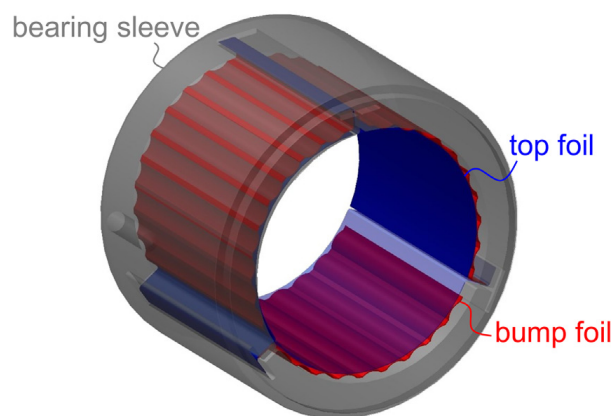


Fig. 1. Bump-type three-pad air foil journal bearing with top and bump foils.

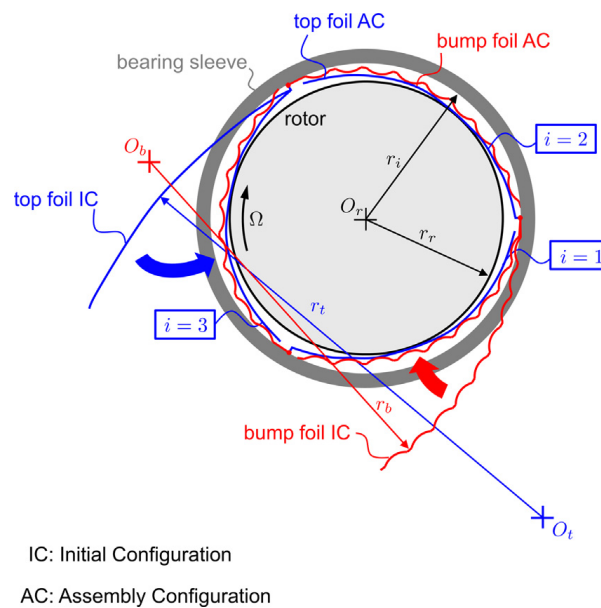


Fig. 2. Preloaded three-pad air foil journal bearing in the initial and in the assembly configuration [5,6].

account for the heat transfer through and between different bearing parts, see [10–16]. The thermal resistances are either calculated from Fourier's law for heat conduction or from Nusselt numbers for convective heat transfer. Although, global heat balances for the surrounding components are used in these studies, the temperature distribution of the air film between the top foil and the rotor is described by the energy equation implying different simplifications.

In more detailed models, the temperature of the surrounding structure is calculated from partial differential equations, e.g. the energy equation for fluids and the heat equation for solids, see [17–24,9,25,26]. Different approaches for calculating the temperature distribution in the foil structure are employed in these studies.

Besides these predominately numerical works, a lot of researchers have analyzed the thermal behavior of air foil bearings [27–32,8,33] and the behavior of the foil structure under elevated temperatures [34–37] experimentally using different types of test rigs.

In the following, the main ideas, methods and results of the numerical studies are summarized.

Salehi et al. [10] described the temperature distribution of a cooled air foil journal bearing with a 1D energy equation in circumferential direction. This simplification of the general 3D energy equation was obtained by neglecting the heat conduction and the heat convection in axial direction and across the fluid film. Furthermore, the Couette approximation was applied to the energy equation. By this approach all terms which comprise pressure gradients were neglected. For this reduced 1D energy equation, an analytical solution could be obtained yielding the temperature distribution in the circumferential direction. Afterwards, the axial temperature distribution was obtained by dividing the solution domain in axial direction into control volumes. For each control volume, a global heat balance was applied. In their approach, measured temperatures of the axial cooling flow through the foil structure were used to calculate the heat transfer from the fluid film to the cooling flow. The temperature measurements were accomplished on a test rig where the rotor was driven by an electric motor at speeds up to 36krpm. For a given speed and load, the temperatures at the backside of the top foil were measured using K-type thermocouples. The predicted temperatures showed a good agreement to the measurements. The experimental results indicate that the top foil temperature increases both with the bearing load and the rotor speed. Latter had a more significant influence on the bearing temperature than the bearing load. It was obtained from the numerical model that about 75 – 80% of the heat which is generated in the air film is conducted into the surrounding structure and the cooling flow. The air side flow of the bearing transfers the rest of the heat into the environment. Hence, it is important that the different heat paths through the surrounding structure are correctly accounted for in thermo-elasto-gasdynamic air foil journal bearing models.

Bruckner [11] described the temperature distribution in the air film of a bump-type thrust bearing using a simplified form of the 3D energy equation in which the heat conduction and the heat convection across the fluid film were neglected yielding a 2D energy equation in circumferential and in radial direction. Both the heat flux through the rotor and through the foil structure were considered as a lumped variable in this 2D energy equation. Bruckner [11] did not specify how the heat flux in the surrounding structure was calculated. The predicted bump foil temperature was compared with measurements showing a good agreement.

Peng and Khonsari [12] described the temperature distribution in the fluid film of an air foil journal bearing by the 3D energy equation. The pressure distribution was obtained from the Reynolds equation. While taking into account the density-temperature-relationship in the Reynolds equation, the dependency of the viscosity on the temperature was

neglected. In contrast to Salehi et al. [10], they neglected only the heat conduction in circumferential and in axial direction. It was assumed that the rotor temperature equals the average temperature of the bearing side flow. The heat conduction through the foil structure as well as the heat convection to the axial cooling flow was modeled by thermal resistances. Furthermore, a mixing model was introduced for calculating the inlet temperature at the top foil leading edge. The 3D energy equation and the Reynolds equation were solved by a finite-difference approach. The predicted increase of the top foil temperature was compared with measurements from [10] showing a good agreement. The authors showed that the axial cooling flow through the foil structure significantly decreases the temperature rise in the bearing. It was also demonstrated that an isothermal approach underestimates the load capacity of air foil journal bearings.

Feng and Kaneko [13] expanded the model of Peng and Khonsari [12] for a numerical investigation of multiwound foil bearings. In their study, the generalized Reynolds equation according to Dowson [38] was employed for the description of the pressure distribution in the air film. This equation accounts for the change of viscosity and density across the fluid film by the so called Dowson integrals. The authors solved the set of integro-differential equations by a Lobatto point quadrature method in which the fluidity, the density and the temperature were approximated by Legendre polynomials across the fluid film. In contrast to Peng and Khonsari [12], Feng and Kaneko assumed that the average heat flux from the air film to the shaft is zero. For air foil thrust and oil slider bearings, Mahner et al. [39] have systematically shown that a significant reduction in computation time may be achieved by the Lobatto point quadrature method and by an averaging approach.

San Andrés and Kim [14], described the temperature distribution in the air film of a foil journal bearing by a 2D bulk flow equation. This equation was derived by integrating the 3D energy equation across the fluid film. The 2D bulk flow equation accounted for the heat flux at the top foil and the rotor interface. The heat fluxes were calculated by using appropriate relationships for the thermal resistances for heat conduction through the rotor, the foils and the bearing sleeve as well as for the heat convection to an inner and outer cooling flow. To account for the change of the temperature of the surrounding structure in circumferential direction, the solution domain was divided into several control volumes. The authors also analytically calculated the thermal expansion of the rotor and bearing sleeve as well as the centrifugal growth of the rotor. The results were validated against temperature measurements from Radil and Zeszotek [27] showing a good agreement. Based on the numerical results, it was obtained that the temperature changes little in axial direction and that the maximum temperature occurs in the bearing mid plane. By comparing the results of the described thermo-elasto-gasdynamics model with the results of an isothermal model, San Andrés and Kim [14] analyzed the effect of the bearing temperature on the load capacity and attitude angle. This run-time efficient bulk-flow model was used in further studies to investigate the thermal management of air foil bearing supported rotors [40,41,32].

Lee and Kim [15] described the temperature distribution of the air film in a foil journal bearing by the 3D energy equation without further assumptions. The Reynolds equation for compressible fluids was employed for the description of the pressure in the air film. Herein, density and viscosity were calculated at an averaged cross-film temperature. Again, thermal resistances were used for approximation of the heat fluxes through the surrounding structure. In contrast to the models explained above, Lee and Kim [15] account for the thermal contact resistance at the top and bump foil and at the bump foil and bearing sleeve interface. They measured the thermal contact resistance at different contact pressures using a top and bump foil which were clamped between a heated and a non-heated block. The temperatures of the upper and the lower block were measured using K-type thermocouples. In a further study, Lee et al. [42] used the described model to analyze the overall thermal behavior of an oil-free gas turbine.

In another work, Lee et al. [16] accomplished transient simulations with the model presented in [15] by accounting for the change of temperature with time. In their work, also thermal instabilities were discussed. Their findings were proofed by experiments.

As stated above, the summarized studies have in common that the heat paths through the surrounding structure are described by lumped mass models. In other works, which will briefly be summarized hereafter, heat equations for the surrounding structure are employed.

Lee and Kim [17] investigated the thermal behavior of a Rayleigh step air foil thrust bearing numerically. They used a model which was quite similar to the one employed in [15] for an air foil journal bearing. Instead of the thermal resistance for the whole foil structure as in [15], only the bump foils and the contact between the top foils and the bump foils and between the bump foils and the thrust plate were described by thermal resistances, whereas the temperature distribution of the top foil was calculated by a 2D heat equation. Furthermore, the temperature of the runner disk was described by a 1D heat equation in radial direction assuming a constant disk temperature in circumferential and in axial direction. Their results showed that the thrust plate temperature increases parabolically with the rotational speed.

Kim et al. [19] extended the model of Lee and Kim [15] to investigate the thermal behavior of a cooled three-pad air foil journal bearing in a gas turbine simulator. The cooling was accomplished by providing an axial cooling flow from a plenum through the foil structure of the air foil journal bearing. In their study, a CFD model was used to calculate the recirculation ratio in the mixing zone between two bearing pads. Furthermore, the bearing sleeve and the housing were modeled by employing the 3D heat equation. In their model, the cooling plenums were represented by lumped thermal masses. Kim et al. found that the recirculation ratio is nearly 1 for small cooling flow pressures (< 1500 Pa) across the bearing width. Thus, all of the air which leaves the upstream pad enters the downstream pad for small cooling flow pressures [19].

Sim and Kim [4] derived an analytical formula for the thermal resistance of the bump contacts. They assumed most of the heat to be conducted through the solid contact area, which was calculated by the Hertzian elastic contact theory. Thereby, Sim and Kim showed a high dependency of the thermal contact resistance on the contact pressure. This result is not in consistency with the experimental findings from [15].

Feng et al. [21] applied their sparse mesh model presented in [13] to an air foil journal bearing. While the temperature distribution of the rotor and of the bearing sleeve were described by 1D and 2D heat equations, the temperature of the foil structure was modeled using lumped thermal masses. The thermal model of bump and top foil did account for the thermal contact resistance at the bump and top foil contact and at the contact between the bump foil and the bearing sleeve. The authors account for the thermal expansion of the rotor, of the bearing sleeve and of the foil structure as well as for the centrifugal growth of the rotor. The predicted temperatures were compared with measurements from [27] showing a good agreement.

Aksoy and Aksit [22] presented a comprehensive thermo-elasto-gasdynamics model of an air foil journal bearing in which the temperature of the foil structure, of the rotor and of the bearing sleeve were described by 3D heat equations. The temperature distribution of the fluid film was calculated from a 2D bulk flow equation, see [14]. While a finite element approach was used for the solution of the heat equations, the Reynolds equation and the 2D plane strain equations for top and bump foil, the 2D bulk flow equation was solved by a finite difference approach. From the predicted results, the temperature distribution of the foil structure could be analyzed in detail.

Lehn [9,25] presented a detailed thermo-elasto-gasdynamics model of an air foil thrust bearing. As in [17], the bump foil was modeled as a lumped thermal mass while the temperature distribution of the top foil was described by a 2D heat equation. Instead of the measured contact resistance used in [17], an analytical formula for the thermal contact resistance was employed in [25]. This formula was first derived in [43]. In contrast to Sim and Kim [4], their formula was based on the assumption that most of the heat in the contact zone is transferred through the thin air film in the vicinity of the contact, see [43]. Lehn et al. showed a good agreement with the experimental results from [15]. Furthermore, the turbulent flow at the backside of the runner disk was modeled in [25] using boundary layer equations. The disk deformation due to thermal and centrifugal effects was calculated with the 2D axisymmetric Lamé-Navier equations. With this model, the authors [25] showed that the load capacity of air foil thrust bearings is restricted by the thermal distortion of the runner disk. In [44], the model from [9,25] was used in order to optimize the thermal behavior of air foil thrust bearings by the use of different foil materials.

Different reduction approaches have been developed in order to solve the generalized Reynolds equation in conjunction with the 3D energy equation, see [45–48,21]. In [39], these approaches were systematically compared with respect to accuracy and computation time for oil slider and air thrust bearings. The authors pointed out two approaches which yield a significant decrease in computation time and a small numerical error for air bearings: In the first approach (averaging approach), the air film temperature obtained from the 3D energy equation is averaged across the fluid film. The viscosity and density of the air film are calculated using the averaged temperature. Thereby, the generalized Reynolds equation is reduced to the simple Reynolds equation for compressible fluids. Within the second approach (Galerkin method), temperature, density and fluidity are approximated across the fluid film by Legendre polynomials of order N . As a result, the Dowson integrals are calculated by a Lobatto point quadrature method. Inserting the temperature approximation into the 3D energy equation and weighting with the Legendre polynomials, the 3D energy equation is reduced to $N + 1$ 2D partial differential equations.

Different authors investigated the thermal behavior of foil journal and thrust bearings which were operated with CO_2 , [18,30,24,23,26]. Due to the higher density of CO_2 in comparison to air, centrifugal effects as well as turbulence have to be taken into account. This was done by either using a CFD based approach [26] or by employing a modified form of the Reynolds equation which accounts for these effects [18,30,24,23]. In these models, the temperature distribution in the surrounding structure is mostly described by heat equations.

In the paper at hand, the thermal behavior of a preloaded three-pad air foil journal bearing is investigated numerically and experimentally. In the numerical model, the pressure distribution in the air film between the top foils and the rotor is described by the generalized Reynolds equation according to Dowson [38]. The deflection of top and bump foil is accounted for by the nonlinear beamshell theory according to Reissner [49], see also [5,6]. The normal and tangential behavior at the contact between bump foil and top foil and between bump foil and bearing sleeve are described by an augmented Lagrange approach and Coulomb's law of friction, respectively. The temperature distribution in the air film is calculated by solving the 3D energy equation.

Since the thermal paths through the surrounding structure, e.g. the rotor and the foil structure, have a crucial influence on the thermal behavior of the bearing, detailed thermal models are implemented for these components. The temperature distribution of the rotor is calculated from an axisymmetric 2D heat equation. In addition, the thermal and centrifugal growth of the rotor is accounted for by the axisymmetric Lamé-Navier equations. The temperature distribution of the top and bump foils are modeled by a 2D heat equation. In this model, the thermal contact resistance at the top and bump foil is calculated from an analytical formula. This formula is based on an approach developed in [43], but also accounts for a gap between top and bump foil as well as for the curvature of top and bump foil. While at the contact points of top and bump foil lumped thermal resistances are used for calculating the transferred heat, the heat exchange between the bump foil and the bearing sleeve is calculated by modeling the air film between these components by a 1D heat equation. The bearing sleeve is the only component which is modeled as a lumped thermal mass. The heat transferred at the bearing sleeve outer surface by convec-

tion is calculated from an initial temperature measurement at the bearing sleeve. The set of nonlinear fully-coupled integro-differential equations is reduced by applying the averaging approach described in [39]. Thereby, the computational effort for solving the generalized Reynolds equation and the 3D energy equation is significantly reduced. The remaining set of nonlinear partial differential equations is solved by a finite element approach.

For the purpose of validating the numerical model, experiments are accomplished on an automated high-speed test rig. For a given rotational speed and bearing load, this test rig allows for the measurement of the bearing and rotor temperature, the horizontal and vertical bearing displacement and of the bearing drag torque.

The main contributions of this work are:

- Development of a detailed fully-coupled thermo-elasto-gasdynamic model of a preloaded three-pad air foil journal bearing.
- Extension of the analytical formula for the thermal contact resistance developed by Lehn et al. [43] for the use of curved foils and consideration of a small air gap between the top foil and the bumps which are not in contact.
- Numerical investigation of the temperature distribution in bump and top foil and numerical analyzes of the influence of the bump foil deformation on the heat transfer through the foil structure.
- Experimental validation of the model for different bearing loads.

2. Thermo-elasto-gasdynamic bearing model

The thermo-elasto-gasdynamic model presented in this manuscript comprises the description of the pressure and temperature distribution in the air film. Due to the pressure acting on the top foil, the foil structure will deform affecting the fluid film height between the top foil and the rotor. This is accounted for by a detailed elastic model of top and bump foil considering the assembly preload and the contact between the bump and the top foil and between the bump foil and the bearing sleeve. Furthermore, the temperature distribution in the air film is strongly influenced by the heat transfer in the surrounding structure, as stated already in Section 1. Hence, these heat paths are modeled in detail using appropriate heat equations for the surrounding structure.

In this section, the gasdynamic model is presented firstly. Then, the elastic model of the foil structure as well as the thermal model of the air film and the surrounding structure incorporating all relevant heat paths are explained. In the last subsection, the numerical solution procedure is described.

2.1. Gasdynamic Model of the Air Film

The well-known Reynolds equation for compressible fluids can be applied to describe the pressure distribution in the air film of foil journal bearings considering isothermal conditions, see e.g. [5,6]. When taking thermal effects into account, as it is done in this study, the air density and viscosity will change across the fluid film due to their temperature dependency. Since in the classical Reynolds equation for compressible fluids density and the viscosity are assumed to be constant across the fluid film, this equation is not suitable for a correct calculation of the pressure distribution when thermal effects have to be considered. A general form of the Reynolds equation taking into account the discussed effects was derived by Dowson [38]. Further assumptions regarding the surface speeds of the rotor and the top foil can be made, see e.g. [39]:

1. The surface velocity of the top foil is negligible compared to the rotor speed.
2. Since the pressure distribution is calculated for a stationary rotor position, the transversal and cross-film surface velocity of the rotor are zero. Furthermore, the squeeze term can be neglected for the same reason.
3. The longitudinal rotor speed equals $-r_r\Omega$, see Fig. 3.

Applying these assumptions, the generalized Reynolds equation for the i -th pad, see Fig. 3, of a three-pad air foil journal bearing reads

$$\frac{\partial}{\partial x_{a_i}} \left[(F_{2_i} + G_{1_i}) \frac{\partial p_i}{\partial x_{a_i}} \right] + \frac{\partial}{\partial y_{a_i}} \left[(F_{2_i} + G_{1_i}) \frac{\partial p_i}{\partial y_{a_i}} \right] = - \frac{\partial}{\partial x_{a_i}} \left[r_r \Omega \left(\frac{F_{3_i} + G_{2_i}}{F_{0_i}} - G_{3_i} \right) \right] \quad \forall i = 1, \dots, 3. \quad (1)$$

Herein, x_{a_i} , y_{a_i} and z_{a_i} describe the longitudinal, the transversal and the cross-film coordinate of the i -th air film, see Fig. 3. The variable p_i denotes the two-dimensional pressure field in i -th air film in x_{a_i} - and y_{a_i} -direction. The change of the fluid viscosity η_i and the fluid density ρ_i across the fluid film is accounted for by the quantities F_{0_i} - F_{3_i} and G_{1_i} - G_{3_i} which are defined by the following integral expressions [38]:

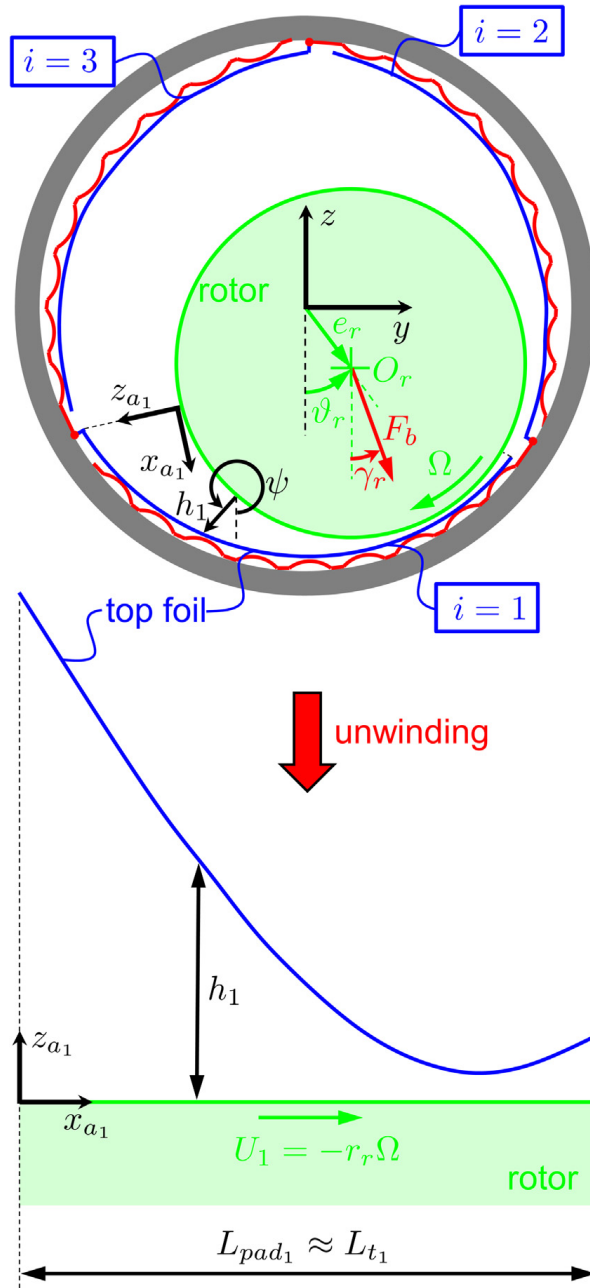


Fig. 3. Unwinding of the air film in a three-pad air foil journal bearing.

$$F_{0i} = \int_0^{h_i} \frac{dz_{a_i}}{\eta_i}, \tag{2}$$

$$F_{1i} = \int_0^{h_i} \frac{z_{a_i}}{\eta_i} dz_{a_i}, \tag{3}$$

$$F_{2i} = \int_0^{h_i} \frac{\rho z_{a_i}}{\eta_i} (z_{a_i} - z_{a_i}^*) dz_{a_i}, \tag{4}$$

$$F_{3i} = \int_0^{h_i} \frac{\rho z_{a_i}}{\eta_i} dz_{a_i}, \tag{5}$$

$$G_{1i} = \int_0^{h_i} \left[z_{a_i} \frac{\partial \rho_i}{\partial z_{a_i}} \left(\int_0^{z_{a_i}} \frac{z_{a_i}}{\eta_i} dz_{a_i} - z_{a_i}^* \int_0^{z_{a_i}} \frac{dz_{a_i}}{\eta_i} \right) \right] dz_{a_i}, \tag{6}$$

$$G_{2_i} = \int_0^{h_i} \left(z_{a_i} \frac{\partial \rho_i}{\partial z_{a_i}} \int_0^{z_{a_i}} \frac{dz_{a_i}}{\eta_i} \right) dz_{a_i}, \tag{7}$$

$$G_{3_i} = \int_0^{h_i} z_{a_i} \frac{\partial \rho_i}{\partial z_{a_i}} dz_{a_i}, \tag{8}$$

with

$$z_{a_i}^* = \frac{F_{1_i}}{F_{0_i}}. \tag{9}$$

The integrals are evaluated across the fluid film height h_i .

Since in air foil journal bearings, the air film height is considerably smaller than the radius of the rotor and of the top foil, the curvature of the air film can be neglected, see Fig. 3. This means that the air film between rotor and top foil can be unwounded yielding the geometry shown in Fig. 3. Due to the small fluid film height, the pad length L_{pad} on the rotor surface equals nearly the top foil length L_t , see Fig. 3. While it is possible to neglect the curvature of the air film, the curvature of the foil structure cannot be neglected when calculating the elastic deformation of bump and top foil, see Section 2.2. Thus, the generalized Reynolds equation can be formulated in Cartesian coordinates as stated in Eq. 1. It is assumed that the pressure at each side of the bearing pads equals the ambient pressure p_{amb} :

$$p(x_{a_i} = 0, y_{a_i}) = p(x_{a_i} = L_t, y_{a_i}) \tag{10}$$

$$= p(x_{a_i}, y_{a_i} = 0) = p(x_{a_i}, y_{a_i} = b) = p_{amb}. \tag{11}$$

Herein, b denotes the bearing width.

In this manuscript, the air film height h is defined as the actual normal distance between the rotor and the top foil taking into account the rotor eccentricity e_r under the bearing load F_b as well as the deformation of the foil structure. The deformation of bump and top foil is described by a nonlinear beamshell theory according to Reissner [49]. The elastic model also accounts for the contact between bump foil and top foil and between bump foil and bearing sleeve. In Section 2.2, the elastic model will be described in detail. The actual position of the rotor is found from the equilibrium of forces

$$\begin{bmatrix} F_y \\ F_z \end{bmatrix} + F_b \begin{bmatrix} \sin(\gamma_r) \\ -\cos(\gamma_r) \end{bmatrix} = \begin{bmatrix} 0 \\ 0 \end{bmatrix} \tag{12}$$

in y - and z -direction.

Herein, γ_r describes the angle under which the bearing load is applied, see Fig. 3. The forces F_y and F_z result from the air film pressure between the rotor and the three bearing pads. These are calculated from the 2D pressure distribution by using the relationships

$$\begin{bmatrix} F_y \\ F_z \end{bmatrix} = \sum_{i=1}^3 \begin{bmatrix} - \int \int_{A_{pad_i}} p_i \sin(\psi) dA \\ \int \int_{A_{pad_i}} p_i \cos(\psi) dA \end{bmatrix}. \tag{13}$$

In the above equation, $A_{pad_i} \approx L_t \cdot b$ denotes the area of the i -th bearing pad. The angle ψ occurs between the rotor normal and the z -axis, see Fig. 3.

2.2. Elastic Model

In the paper at hand, the deformation of the foil structure under the air film pressure p is calculated using a geometrically nonlinear 1D elastic model of top and bump foil [5,6].

In contrast to other models, see e.g. [50–52,22], the presented model correctly accounts for the preload of bump and top foil. For this purpose, the initial undeformed configuration of top and bump foil before their assembly in the bearing sleeve is considered, see Fig. 2. Afterwards, the assembly configuration and the preload are calculated by simulating the assembly process of the bump foils, the top foils and of the rotor. Note that in contrast to other air foil journal bearing concepts, see e.g. [2], there is no initial clearance between the top foil and the rotor, even when rotor and bearing sleeve are perfectly aligned. Instead, the top foils push against the rotor. The resultant contact force between the rotor and each top foil is defined as an assembly preload.

Due to the low curvature of the bump and top foils in the initial configuration compared to the curvature in their assembly configuration, large deformations will occur during the assembly process. In order to correctly calculate these deformations, the elastic model of bump and top foil accounts for a geometrical nonlinearity. While the deformations are large, the membrane, bending and shear stress are assumed to be small. Thus, linear elastic material behavior is considered. Furthermore, a constant foil thickness and Reissner–Mindlin kinematics are assumed. As a consequence of the membrane stresses in

the bump and top foil, the deformations are considered to be constant across the foil width, see e.g. [53,54]. Since the top and bump foil width is significantly larger than the foil height, plane strain theory is used. Applying the above assumptions to the general 3D theory of elasticity, one gets the nonlinear 1D beamshell theory according to Reissner, see [49,55,56]. Using this theory, the deformation of bump and top foil at every material coordinate s is described by the two displacements u and v in the global y - and z -direction and by the rotation $\Delta\varphi = \varphi - \varphi_0$ about the global x -axis, where φ and φ_0 denote the orientation of the beamshell cross section about the global x -axis in the initial and in the current configuration. The two displacements and the rotation are calculated from the following three coupled partial differential equations

$$\frac{\partial}{\partial s} [N \cos(\varphi) + Q \sin(\varphi)] = -p_y(1 + \varepsilon), \tag{14}$$

$$\frac{\partial}{\partial s} [N \sin(\varphi) - Q \cos(\varphi)] = -p_z(1 + \varepsilon), \tag{15}$$

$$\frac{\partial M}{\partial s} = (1 + \varepsilon)Q - \gamma N, \tag{16}$$

which represent the equilibrium of forces in the y - and z -direction (Eqs. (14) and (15)) as well as the law of moment of momentum about the x -axis (Eq. (16)), see [5,6]. Herein, p_y and p_z denote the pressure on the beamshell in y - and z -direction. Note that Eq. (14)–(16) are valid for top and bump foil. In order to distinguish between bump and top foil hereafter, the subscripts b and t are introduced. The pressure p_{y_t} and p_{z_t} on the top foil result from the aerodynamic pressure p in the air film between rotor and top foil. The two-dimensional pressure distribution p_i resulting from the generalized Reynolds Eq. (1) for each bearing pad is averaged across the bearing width according to

$$\bar{p}_i = \frac{1}{b_t} \int_0^{b_t} p_i dy \quad \forall i = 1, \dots, 3 \tag{17}$$

in order to be used in conjunction with the one-dimensional beamshell theory (14)–(16). From the averaged pressure \bar{p}_i , the pressure components p_{y_t} and p_{z_t} are calculated as follows

$$p_{y_t}(1 + \varepsilon_t) = \sin(\varphi_{t_i})(1 + \varepsilon_t)\bar{p}_i - \gamma_{t_i} \cos(\varphi_{t_i})\bar{p}_i, \tag{18}$$

$$p_{z_t}(1 + \varepsilon_t) = -\cos(\varphi_{t_i})(1 + \varepsilon_t)\bar{p}_i - \gamma_{t_i} \sin(\varphi_{t_i})\bar{p}_i, \tag{19}$$

$$\forall i = 1, \dots, 3.$$

In Eqs. (14)–(16), N , Q and M represent the normal force, the shear force and the bending moment about the x -axis, see Fig. 4. Note that N , Q and M are related to the beamshell width. They are calculated from the membrane strain ε , the shear strain γ and the bending strain κ using the relationships for linear elastic material behavior

$$N = \frac{EH}{1 - \nu^2} \varepsilon, \tag{20}$$

$$Q = \alpha_s GH \gamma, \tag{21}$$

$$M = \frac{EH^3}{12(1 - \nu^2)} \kappa. \tag{22}$$

Herein, E , $G = E/(2(1 + \nu))$ and ν represent the Young's modulus, the shear modulus and the Poisson's ratio. The beamshell thickness is denoted by H . To account for the correct distribution of the shear stress across the beamshell thickness, a shear correction factor α_s is introduced. The relationship between the three strains and the displacements and the rotation is described by the kinematic equations

$$\varepsilon = \frac{\partial(y + u_y)}{\partial s} \cos \varphi + \frac{\partial(z + u_z)}{\partial s} \sin(\varphi) - 1, \tag{23}$$

$$\gamma = \frac{\partial(y + u_y)}{\partial s} \sin \varphi - \frac{\partial(z + u_z)}{\partial s} \cos(\varphi), \tag{24}$$

$$\kappa = \frac{\partial}{\partial s} (\varphi - \varphi_0). \tag{25}$$

For the investigated three-pad air foil journal bearing, the top and bump foils are free at the one end and mounted in suspensions at the other end. Fig. 5 shows the location of the mounting suspension as well as an illustration of the boundary conditions of top and bump foil. The boundary conditions at the mounting suspension at the top foil read

$$Q_t(s_t = 0) = 0 \tag{26}$$

$$u_{t_z}(s_t = 0) = -\frac{u_{t_y}(s_t = 0)}{\tan(\varphi_t(s_t = 0))}, \tag{27}$$

$$M_t(s_t = 0) = k_{\varphi_t}(\varphi_t(s_t = 0) - \varphi_{t0}(s_t = 0)). \tag{28}$$

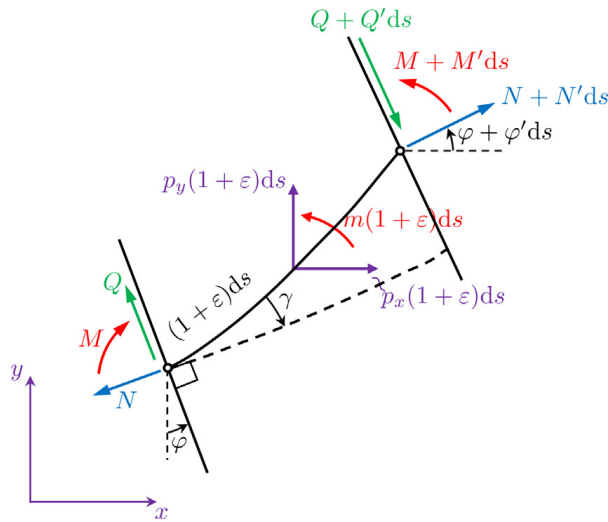


Fig. 4. Free body diagram of an infinitesimal beamshell segment [49,5,6].

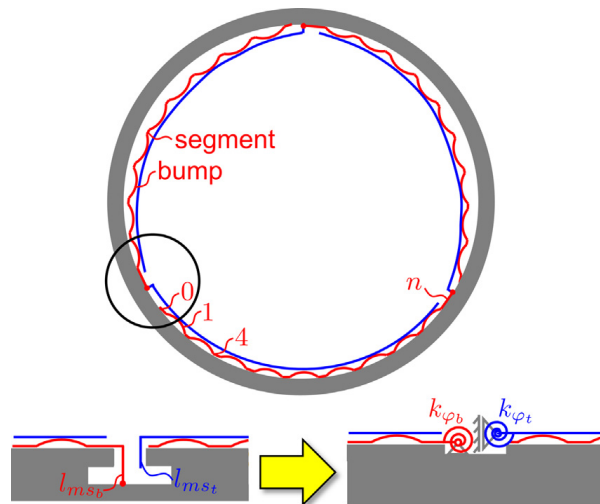


Fig. 5. Location of the top and bump foil mounting suspensions, illustration of the boundary conditions of top and bump foil and naming/ numbering convention for the bumps and segments.

According to the first two boundary conditions (Eqs. (26)), the top foil mounting suspension can move freely in normal direction while the displacement in tangential direction is restricted. To account for the deformation of the top foil mounting suspension due to bending moments, a torsional spring with the stiffness k_{φ_t} is introduced at the top foil fixed end, see Eq. (28). This spring stiffness k_{φ_t} is calculated from the relationship

$$k_{\varphi_t} = \frac{EH^3}{12l_{ms_t}}, \tag{29}$$

where l_{ms_t} denotes the length of the top foil mounting suspension, see Fig. 5.

In contrast to the top foil, it is assumed that the bump foil cannot move in y- and in z-direction:

$$u_{b_{y,n}}(s_n = l_n) = 0, \tag{30}$$

$$u_{b_{z,n}}(s_n = l_n) = 0. \tag{31}$$

Herein, n denotes the total number of bumps and segments of each bump foil, see Fig. 5. Accordingly, l_n represents the length of the last segment at the bump foil fixed end. Again, the deformation of the bump foil mounting suspension due to bending moments is calculated using the relationship

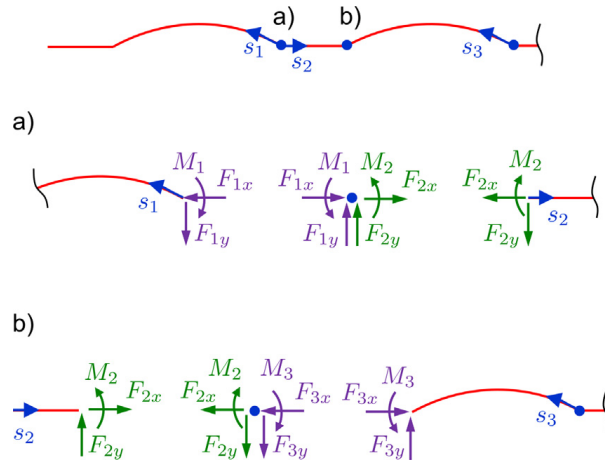


Fig. 6. Free body diagram at the leading (a) and the trailing (b) edge of bump and segment.

$$M_n(s_n = l_n) = k_{\phi_b}(\varphi_n(s_n = l_n) - \varphi_{n0}(s_n = l_n)). \tag{32}$$

This spring stiffness k_{ϕ_b} is calculated from the relationship

$$k_{\phi_b} = \frac{EH^3}{12l_{ms_b}}, \tag{33}$$

where l_{ms_b} denotes the length of the bump foil mounting suspension, see Fig. 5.

As stated in Section 1, the bump foil consists of n_{bu} bumps and n_s segments, see Fig. 2.

The bumps and segments are numbered in ascending order ($j = 0, \dots, n_{bu} + n_s - 1$) from the free end of the bump foil to the fixed end of the bump foil, see Fig. 6 and 5. While uneven numbers indicate bumps, even numbers refer to segments. For each bump and each segment, the three partial differential Eqs. (14)–(16) are formulated. At the intersection of bump and segment, coupling constraints for the forces and the bending moment as well as for the displacements and the rotation are applied. Fig. 6 shows the free body diagram of the intersections at the bump and segment leading (a) and trailing edge (b). The kinematic coupling constraints at the leading and the trailing edge of bumps and segments read

$$u_{b_{y_j}}(s_{l_{t_j}}) = u_{b_{y_{j+1}}}(s_{l_{t_{j+1}}}), \tag{34}$$

$$v_{b_{z_j}}(s_{l_{t_j}}) = v_{b_{z_{j+1}}}(s_{l_{t_{j+1}}}), \tag{35}$$

$$\Delta\varphi_{b_j}(s_{l_{t_j}}) = \Delta\varphi_{b_{j+1}}(s_{l_{t_{j+1}}}), \tag{36}$$

$$\forall j = 1, \dots, n_{bu} + n_s - 1, \tag{37}$$

with the arc length

$$s_{l_{t_j}} = \begin{cases} 0 & j = 2k_{bu} - 1 \quad \forall k_{bu} = 1, \dots, n_{bu}, \\ l_{b_j} & j = 2k_s - 2 \quad \forall k_s = 1, \dots, n_s, \end{cases} \tag{38}$$

at the bump leading and the segment trailing edge.

Herein, l_{b_j} denotes the length of a bump or segment. In addition, the equilibrium of forces and the moment equilibrium at the intersections yield further coupling equations

$$F_{b_{jy}}(s_{l_{t_j}}) = -F_{b_{(j+1)y}}(s_{l_{t_{j+1}}}), \tag{39}$$

$$F_{b_{jz}}(s_{l_{t_j}}) = -F_{b_{(j+1)z}}(s_{l_{t_{j+1}}}), \tag{40}$$

$$M_{b_j}(s_{l_{t_j}}) = -M_{b_{j+1}}(s_{l_{t_{j+1}}}), \tag{41}$$

$$\forall j = 1, \dots, n_{bu} + n_s - 1.$$

In Eqs. (39) and (40), $F_{b_{jy}}$ and $F_{b_{jz}}$ represent the stress resultants of the j -th bump/ segment in the global y - and z -direction. These forces are calculated from the stress resultants N_{b_j} and Q_{b_j} in the tangential and normal direction of the j -th bump/ segment by employing the transformations

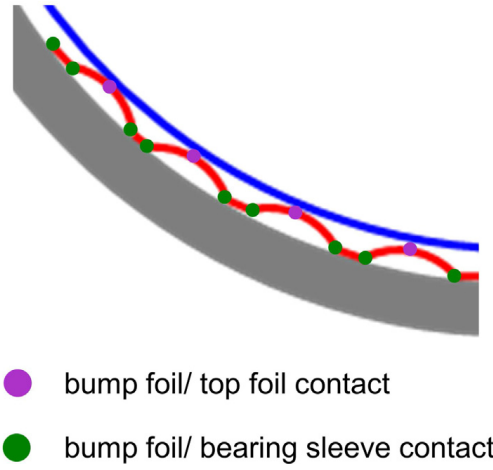


Fig. 7. Slave nodes at the bump foil for the contact approach between bump and top foil and between bump foil and bearing sleeve.

$$F_{b_{jy}} = N_{b_j} \cos(\varphi_j) + Q_{b_j} \sin(\varphi_{b_j}), \tag{42}$$

$$F_{b_{jz}} = N_{b_j} \sin(\varphi_j) - Q_{b_j} \cos(\varphi_{b_j}), \tag{43}$$

$$\forall j = 1, \dots, n_{bu} + n_s - 1.$$

The contact between bump and top foil and between bump foil and bearing sleeve is accounted for by a nonlinear contact approach. Specifying the slave nodes at the bump foil, the contacting master nodes at the top foil and at the bearing sleeve are calculated using a nonlinear search algorithm. Assuming that the bump center will come into contact with an arbitrary point of the top foil, the nodes at the bump centers are defined as slave nodes for the bump/top foil interaction, see Fig. 7. For the contact between bump foil and bearing sleeve, the nodes at the leading and trailing edge of each segment are defined as slave nodes, see Fig. 7. From these nodes, the contacting master nodes are calculated by solving the minimization problem

$$\delta_{\min_k}(\mathbf{s}_{M_k}^*) = \min_{S_M} \delta_k(S_M), \quad \forall k = 1, \dots, n_{sl}, \tag{44}$$

with $\delta_k(S_M)$ depicting the distance between a slave node k and the master surface.

From the minimum distance δ_{\min_k} at the master node $\mathbf{s}_{M_k}^*$, the normal distance δ_{n_k} is calculated by employing the projection

$$\delta_{n_k} = -\underline{\mathbf{n}}_{M_k}(\mathbf{s}_{M_k}^*) \cdot \underline{\delta}_{\min_k} \quad \forall k = 1, \dots, n_{sl}. \tag{45}$$

Herein, $\underline{\mathbf{n}}_{M_k}(\mathbf{s}_{M_k}^*)$ depicts the normal vector of the master surface at the contact node $\mathbf{s}_{M_k}^*$.

The normal distance δ_{n_k} is used for formulating the no-penetration constraint at the contacting nodes. The nonlinear beamshell Eqs. (14)–(16) and the no-penetration constraint can be rewritten as Signorini’s problem [56]

$$\Pi^i + \Pi^o \rightarrow \text{Min}, \tag{46}$$

$$\delta_{n_k} \leq 0 \quad \forall k = 1, \dots, n_{sl}. \tag{47}$$

Eq. (46) defines the well-known minimum total potential energy principle which describes that the total potential energy $\Pi^i + \Pi^o$ reaches a minimum in the equilibrium state [57].

The solution space for the minimum total potential energy principle (46) is restricted by the no-penetration constraint (47) at the bump foil slave nodes $k = 1, \dots, n_{sl}$. In order to solve Signorini’s problem stated in Eqs. (46) and (47), the problem is reformulated using the principal of virtual displacements

$$\delta W^i + \delta \Pi_c = \delta W^o + \delta W_f. \tag{48}$$

Herein, δW^i and δW^o depict the virtual work of the inner and outer forces, respectively. As can be seen, the virtual potential energy $\delta \Pi_c$ is introduced in Eq. (48) to account for the virtual potential energy of the contact forces. Thereby, no constraints are explicitly used in Eq. (48). Depending on the formulation of the virtual potential energy $\delta \Pi_c$, several indirect solution approaches for Signorini’s problem are distinguished. In this work, the Augmented Lagrange approach is used for enforcing the contact constraints at the bump foil slave nodes. Following this approach, the virtual potential energy $\delta \Pi_c^{AL}$ reads

$$\delta\Pi_c^{AL} = \sum_{k=1}^{n_{sl}} \max(0, \lambda_k + c_{AL} \delta_{n_k}) \delta(\delta_{n_k}) + \frac{1}{k} [\lambda_k + c_{AL} \delta_{n_k} - \lambda_k] \delta(\lambda_k). \tag{49}$$

Herein, λ_k and c_{AL} depict the Lagrange multiplier and the penalty stiffness, respectively. The sum $\lambda_k + c_{AL} \delta_{n_k}$ represents the resultant contact force at each slave node.

To account for the friction between bump foil and top foil and between bump foil and bearing sleeve, the outer virtual work of the friction forces δW_f is introduced in Eq. (48). This work reads

$$\delta W_f = \sum_{k=1}^{n_{sl}} R_{t_k} \delta g_{t_k}. \tag{50}$$

The friction force R_{t_k} at each slave node k is calculated using Coulomb's law of friction

$$R_{t_k} = -\mu_b \frac{\dot{g}_{t_k}}{|\dot{g}_{t_k}|} \max(0, \lambda_k + k_{AL} \delta_{n_k}). \tag{51}$$

Herein, \dot{g}_{t_k} represents the first time derivative of the relative sliding distance at each slave node k in the tangential direction of the contacting master surface. The signum function at time iteration n

$$\frac{\dot{g}_{t_k}}{|\dot{g}_{t_k}|} = \frac{g_{t_k}^n - g_{t_k}^{n-1}}{|g_{t_k}^n - g_{t_k}^{n-1}|} = \text{sgn}(g_{t_k}^n - g_{t_k}^{n-1}) =: \sigma_k \quad \forall k = 1, \dots, n_{sl} \tag{52}$$

is regularized using an elastic slip approach, see Fig. 8. In the highlighted transition zone stiction occurs. According to elastic slip approach applied in this study, a small elastic slip takes place while sticking, see Fig. 8.

Before bearing lift-off and in case of a non-rotating shaft, the contact between top foil and rotor is accounted for. In this context, the no-penetration condition is enforced by applying a penalty approach. Using this method, the virtual potential energy of the contact forces reads

$$\delta\Pi_C^p = \int_{x=0}^{L_t} c_p \delta_{n_{tr}}^+ \delta(\delta_{n_{tr}}^+) ds_t. \tag{53}$$

Herein, c_p describes the penalty stiffness which is chosen sufficiently high to assure that the contact constraint is fulfilled. The penalty springs are active only if the top foil penetrates the rotor. Therefore, the corresponding contact switch function

$$\delta_{n_{tr}}^+ = \begin{cases} \delta_{n_{tr}}, & \delta_{n_{tr}} > 0 \\ 0, & \delta_{n_{tr}} \leq 0 \end{cases} \tag{54}$$

is introduced. The variable $\delta_{n_{tr}}$ depicts the normal distance between top foil and rotor. This distance corresponds with the gap function in the generalized Reynolds Eq. (48)

$$h_{a_i} = -\delta_{n_{tr,i}}. \tag{55}$$

2.3. Thermal model

As stated above, the air density and viscosity show a strong dependency on the temperature. Therefore, it is essential to calculate the air film temperature along with the air film pressure and the elastic top and bump foil deformation. Owing to the low heat capacity of air, the bearing temperature is mostly determined by the heat paths through the structure at the top and bottom of the air film. Fig. 9 shows the heat paths through this surrounding structure.

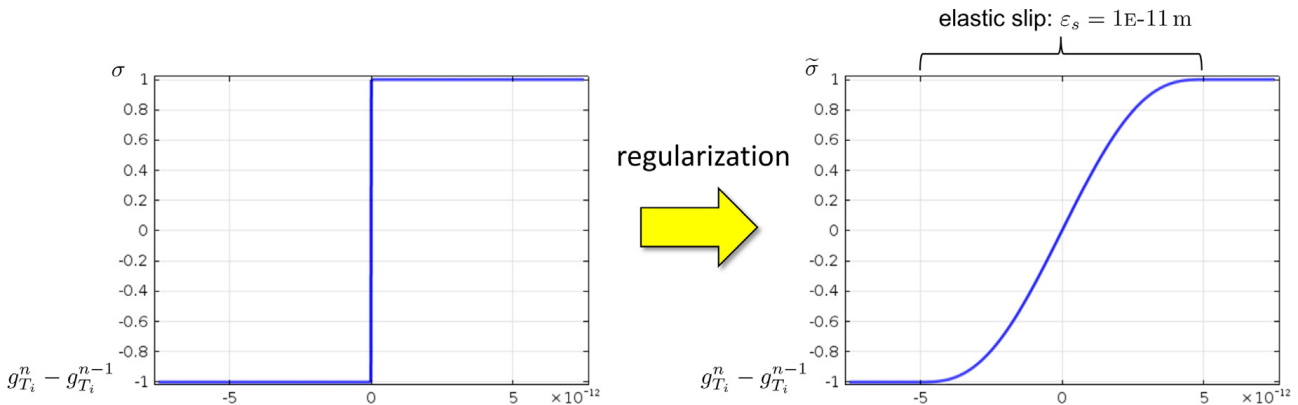
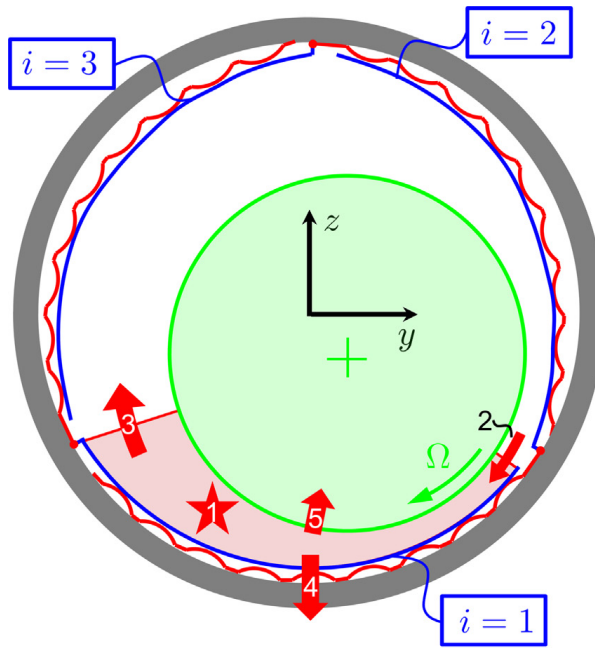


Fig. 8. Ideal (left) and regularized (right) signum function in Coulomb's law of friction, see Eq. (51).



- 1 Dissipation and heat transfer inside the air film
- 2 Heat transfer from the upstream mixing zone
- 3 Heat transfer to the downstream mixing zone
- 4 Heat transfer through the elastic foil structure and the bearing sleeve
- 5 Heat transfer through the rotor

Fig. 9. Heat paths through the surrounding structure of a single pad in a three-pad air foil journal bearing.

The heat inside the air film is generated by energy dissipation and is transferred by convection and conduction to the surrounding structure. At the axial bearing ends - not shown in Fig. 9 - a part of the heat leaves the bearing by the leakage flow. At the top foil leading edge, air from the upstream mixing zone enters the bearing pad while at the top foil trailing edge, heat is transferred to the downstream mixing zone. Furthermore, heat is transferred through the elastic foil structure and the bearing sleeve as well as through the rotor by heat conduction.

In the subsequent sections, the thermal model of the air film and of the surrounding structure are discussed in detail.

2.3.1. Thermal model of the air film

The temperature distribution inside the i -th air film of the three-pad air foil journal bearing is described by the 3D energy equation

$$\rho_i c_{p_i} \left(\frac{\partial T_{a_i}}{\partial x_{a_i}} v_{x_{a_i}} + \frac{\partial T_{a_i}}{\partial y_{a_i}} v_{y_{a_i}} \right) = \frac{\partial p_i}{\partial x_{a_i}} v_{x_{a_i}} + \frac{\partial p_i}{\partial y_{a_i}} v_{y_{a_i}} + k_{a_i} \left(\frac{\partial^2 T_{a_i}}{\partial y_{a_i}^2} + \frac{\partial^2 T_{a_i}}{\partial z_{a_i}^2} \right) + \eta_{a_i} \left[\left(\frac{\partial v_{x_{a_i}}}{\partial z_{a_i}} \right)^2 + \left(\frac{\partial v_{y_{a_i}}}{\partial z_{a_i}} \right)^2 \right] \quad \forall i = 1, \dots, 3. \tag{56}$$

Following an order of magnitude analysis in [9] for air foil thrust bearings, the heat conduction in circumferential direction as well as the heat convection across the fluid film are neglected in Eq. (56). Furthermore, the energy dissipation term is reduced according to the order analysis in [38]. In Eq. (56), c_{p_i} , k_{a_i} and η_{a_i} depict the isobaric heat capacity, the heat conductivity and the dynamic viscosity of the air film in the i -th pad. The properties of the air film depend on the temperature T_{a_i} . The well-known Sutherland equation [58]

$$\eta_{a_i} = \eta_R \frac{T_R + C}{T_{a_i} + C} \left(\frac{T_{a_i}}{T_R} \right)^{\frac{3}{2}} \quad \forall i = 1, \dots, 3. \tag{57}$$

is used for calculating the air film viscosity at a given temperature T_{a_i} . Herein, η_R describes the reference viscosity at the reference temperature T_R . The parameter C defines a fluid dependent constant. The dependency of the isobaric heat capacity on the air film temperature is described by the empiric relationship [9]

$$c_{p_i} = \left(2.43 \cdot 10^{-4} \left(\frac{T_{a_i}}{|\text{K}|} \right)^2 - 7.70 \cdot 10^{-2} \left(\frac{T_{a_i}}{|\text{K}|} \right) + 1008 \right) \left[\frac{\text{J}}{\text{kgK}} \right], \quad \forall i = 1, \dots, 3. \quad (58)$$

For the thermal conductivity, the empiric formula

$$k_{a_i} = \left(-2.1 \cdot 10^{-8} \left(\frac{T_{a_i}}{|\text{K}|} \right)^2 + 8.46 \cdot 10^{-5} \left(\frac{T_{a_i}}{|\text{K}|} \right) + 2.89 \cdot 10^{-3} \right) \left[\frac{\text{J}}{\text{kgK}} \right], \quad \forall i = 1, \dots, 3, \quad (59)$$

is applied to describe the dependency on the air film temperature T_{a_i} in the i -th pad. Eqs. (58) and (59) were developed in [9] by a regression analysis of measured data. Following the assumptions by Dowson [38] stated in Section 2.1, the circumferential and axial fluid film velocity in Eq. (56) are calculated from the simplified Navier–Stokes equation to

$$v_{x_{a_i}} = \frac{\partial p_i}{\partial x_{a_i}} \left(\int \frac{z_{a_i}}{\eta_{a_i}} dz_{a_i} - z_{a_i}^* \int \frac{dz_{a_i}}{\eta_{a_i}} \right) + \frac{r_R \Omega}{F_{0_i}} \int \frac{dz_{a_i}}{\eta_{a_i}} - r_R \Omega, \quad (60)$$

$$v_{y_{a_i}} = \frac{\partial p_i}{\partial y_{a_i}} \left(\int \frac{z_{a_i}}{\eta_{a_i}} dz_{a_i} - z_{a_i}^* \int \frac{dz_{a_i}}{\eta_{a_i}} \right), \quad (61)$$

$\forall i = 1, \dots, 3.$

Herein, the integral expressions account for the temperature induced change of the viscosity across the fluid film. To account for the heat transfer to the surrounding structure, the boundary conditions

$$T_{a_i}(x_{a_i} = L_{t_i}, y_{a_i}, z_{a_i}) = T_r(r = r_r, z_r), \quad (62)$$

$$T_{a_i}(x_{a_i}, y_{a_i}, z_{a_i} = 0) = T_r(r = r_r, z_r), \quad (63)$$

$$T_{a_i}(x_{a_i}, y_{a_i}, z_{a_i} = h_{a_i}) = T_{t_i}, \quad (64)$$

$$k_{a_i} \frac{\partial T_{a_i}}{\partial y_{a_i}} \Big|_{y_{a_i}=0,b} = 0, \quad (65)$$

$$\forall i = 1, \dots, 3,$$

are applied to the energy Eq. (56). It is assumed that the temperature of the air, which enters each pad at the top foil trailing edge, equals the temperature of the rotor surface $T_r(r = r_r, z_r)$, see Eq. (62). Herein, r and z_r indicate the radial and the axial coordinate of the rotor. The z_r -axis of the rotor and the y_{a_i} -axis of each air film are collinear. In contrast to other works, see e.g. [12,19], a mixing model for the area between two neighboring pads is not used in this study in order to calculate the inlet temperature. In fact, the inlet temperature is mostly determined by the temperature of the rotor boundary layer, see [9]. Furthermore, it is assumed that the heat does not leaves the air foil journal bearing by conduction at the axial bearing ends, see Eq. (65). At the rotor and the top foil interface, the air temperature T_{a_i} equals the rotor temperature $T_r(r = r_r, z_r)$ and the top foil temperature T_{t_i} , see Eqs. (63) and (65). Rotor and top foil temperature are calculated using detailed thermo-elastic models which will be described in the subsequent sections.

2.3.2. Thermo-Elastic Rotor Model

Due to the high rotational speed of the rotor, the temperature T_r is assumed to be constant in circumferential direction. Therefore, the 2D axisymmetric energy equation

$$k_r \left(\frac{\partial^2 T_r}{\partial r^2} + \frac{1}{r} \frac{\partial T_r}{\partial r} + \frac{\partial^2 T_r}{\partial z_r^2} \right) = 0 \quad (66)$$

is applied for calculating the temperature distribution of the rotor. Herein, k_r depicts the thermal conductivity of the rotor.

Eq. (66) is solved on the rotor domain which is shown in Fig. (10). This figure also depicts the heat transfer at the rotor boundaries. This comprises the heat transfer from the air foil journal bearing to the rotor and from the rotor to the ambient air. As shown in Fig. (10), the position of the air foil journal bearing on the rotor is described by the axial coordinate z_{r_b} . The parameter l_r depicts the length of the rotor.

The heat transfer from the air foil journal bearing is calculated by averaging the heat flux at the air film/ rotor interface in circumferential direction

$$k_r \frac{\partial T_r}{\partial r} \Big|_{r=r_r} = \sum_{i=1}^3 \frac{1}{L_{t_i}} \int_0^{L_{t_i}} k_a \frac{\partial T_{a_i}}{\partial z_{a_i}} \Big|_{z_{a_i}} dx_{a_i}, \quad \forall z_{r_b} \leq z_r \leq z_{r_b} + b. \quad (67)$$

Next to the air foil journal bearing, the heat is transferred to the ambient air by forced convection induced by the high rotational speed of the shaft. Here, the boundary condition

$$-k_r \frac{\partial T_r}{\partial r} \Big|_{r=r_r} = \alpha_r (T_r(r = r_r, z_r) - T_{amb}), \quad \forall 0 \leq z_r < z_{r_b} \cup z_{r_b} + b < z_r \leq l_r \quad (68)$$

is applied at the outer radial surface of the rotor. Following the approach by Sim and Kim [4], the heat transfer coefficient at the free rotor surface is calculated from the empirical Nusselt relationship

$$Nu := \frac{2\alpha_r r_r}{k_{amb}} = 0.133 Re^{2/3} Pr^{1/3}. \tag{69}$$

Herein, Nu , Re and Pr denote the dimensionless Nusselt, Reynolds and Prandtl number which are defined by

$$Re = \frac{4\Omega r_r^2 \rho_{amb}}{\eta_{amb}}, \tag{70}$$

$$Pr = \frac{\eta_{amb} c_p}{k_{amb}}. \tag{71}$$

In this study, the axial rotor ends are assumed to be adiabatic

$$k_r \frac{\partial T_r}{\partial r} \Big|_{z_r=0, l_r} = 0. \tag{72}$$

Alternatively, a heat transfer coefficient may be applied to the rotor ends following the approach used at the outer radial surface of the rotor, see Eq. (68). At the rotor center, the symmetry condition

$$k_r \frac{\partial T_r}{\partial r} \Big|_{r=0} = 0 \tag{73}$$

holds.

To account for the change of the air film height by the rotor thermal and centrifugal growth, the elastic deformation of the rotor is calculated. Therefore, the equilibrium conditions, the material law and the kinematic relations are defined subsequently.

Since the temperature distribution and the centrifugal load are axisymmetric, the 2D axisymmetric equilibrium conditions

$$\frac{\partial \sigma_r}{\partial r} + \frac{1}{r}(\sigma_r - \sigma_\phi) + \frac{\partial \sigma_{rz}}{\partial z_r} = \rho \Omega^2 r \tag{74}$$

$$\frac{\partial \sigma_{rz}}{\partial r} + \frac{1}{r} \sigma_{rz} + \frac{\partial \sigma_z}{\partial z_r} = 0 \tag{75}$$

are applied on the rotor domain which is shown in Fig. (10). The term on the right side of Eq. (74) represents the centrifugal load.

The generalized Hooke's law

$$\sigma_r = \frac{(1-\nu)E_r}{(1+\nu)(1-2\nu)} \left[\varepsilon_r + \frac{\nu}{1-\nu}(\varepsilon_\phi + \varepsilon_z) - \frac{1+\nu}{1-\nu} \beta_r(T_r - T_{r_0}) \right], \tag{76}$$

$$\sigma_\phi = \frac{(1-\nu)E_r}{(1+\nu)(1-2\nu)} \left[\varepsilon_\phi + \frac{\nu}{1-\nu}(\varepsilon_r + \varepsilon_z) - \frac{1+\nu}{1-\nu} \beta_r(T_r - T_{r_0}) \right], \tag{77}$$

$$\sigma_z = \frac{(1-\nu)E_r}{(1+\nu)(1-2\nu)} \left[\varepsilon_z + \frac{\nu}{1-\nu}(\varepsilon_r + \varepsilon_\phi) - \frac{1+\nu}{1-\nu} \beta_r(T_r - T_{r_0}) \right] \tag{78}$$

describes the relationship between the normal and shear stresses σ_r , σ_z and σ_{rz} and the normal strains ε_r , ε_ϕ and ε_z . Note that the term $\beta_r(T_r - T_{r_0})$ in Eqs. (76)–(78) represents the thermal strains.

The elastic strains are calculated from the radial and axial rotor displacement u_r and u_z using the kinematic relations

$$\varepsilon_r = \frac{\partial u_r}{\partial r}, \tag{79}$$

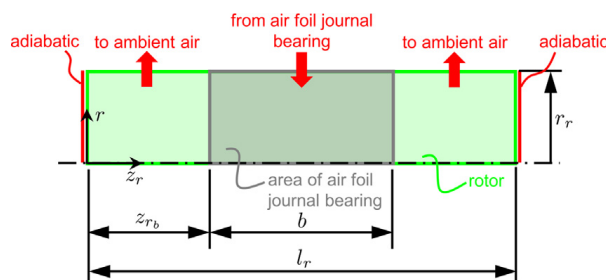


Fig. 10. Rotor domain and heat transfer at the rotor boundaries.

$$\varepsilon_\varphi = \frac{u_r}{r}, \tag{80}$$

$$\varepsilon_z = \frac{\partial u_z}{\partial z_r}. \tag{81}$$

Using the kinematic relations (79)–(81) and the Hooke’s law (76)–(78), the equilibrium conditions (74) and (75) can be solved for the radial and axial rotor displacement u_r and u_z . The originating two partial differential equations in the radial and axial rotor displacement are called as Lamé-Navier equations. The boundary conditions

$$u_r(r = 0, z_r) = 0, \tag{82}$$

$$u_z(r, z_r = 0) = 0, \tag{83}$$

$$n_r \cdot \begin{bmatrix} \frac{\partial u_r}{\partial r} \\ \frac{\partial u_z}{\partial z_r} \end{bmatrix} = 0 \text{ on all other boundaries}, \tag{84}$$

are applied in order to solve Eqs. (74) and (75) for the rotor displacements. The boundary condition (83) is used to constrain the rotor displacement in axial direction. The radial growth of the rotor corresponds with the radial rotor displacement at the outer radius

$$u_{gr} = u_r(r = r_r). \tag{85}$$

The radial growth u_{gr} is used in the calculation of the air film height between each top foil and the rotor surface.

2.3.3. Thermal Model of the Elastic Foil Structure

As shown in Fig. 9, a part of the heat generated in the air film is transferred through the foil structure and the bearing sleeve to the ambient air (heat path 4). In this study, the heat transfer through the foil structure is calculated using a 2D heat equation for top and bump foil. Furthermore, the analytical formula from [9,25] for the thermal contact resistance of top and bump foil is extended to account for the distance between each bump and the top foil as well as for the distance between the bump foil and the bearing sleeve.

Since the top foil thickness is significantly smaller than the top foil length and width, the 2D heat equation

$$k_{t_i} H_{t_i} \left(\frac{\partial^2 T_{t_i}}{\partial s_{t_i}^2} + \frac{\partial^2 T_{t_i}}{\partial y_{t_i}^2} \right) = -\dot{q}_{t_{in_i}} + \dot{q}_{t_{out_i}}, \quad \forall i = 1, \dots, 3, \tag{86}$$

is used to describe the temperature distribution of each top foil. Note, that the s_{t_i} - and y_{t_i} -coordinate of the top foil correspond with the x_{a_i} - and y_{a_i} -coordinate of the air film. At the axial top foil ends, it is assumed that there is no heat flux

$$k_{t_i} \frac{\partial T_{t_i}}{\partial y_{t_i}} \Big|_{y_{t_i}=0,b} = 0, \quad \forall i = 1, \dots, 3, \tag{87}$$

while at the top foil leading edge, the heat is transferred through the mounting suspension to the bearing sleeve

$$k_{t_i} \frac{\partial T_{t_i}}{\partial s_{t_i}} \Big|_{s_{t_i}=0} = k_{t_i} \frac{H_{t_i}}{l_{ms_{t_i}}} (T_{t_i}(s_{t_i} = 0) - T_{bs}), \quad \forall i = 1, \dots, 3. \tag{88}$$

Herein, T_{bs} denotes the temperature of the bearing sleeve, see Section 2.3.4. At the top foil trailing edge, the temperature $T_{t_i}(s_{t_i} = L_{t_i})$ equals the incoming air film temperature $T_{a_i}(x_{a_i} = L_{t_i})$, see [9,25].

The quantity $\dot{q}_{t_{in_i}}$ in Eq. (86) depicts the heat flux from each air film to the adjacent top foil

$$\dot{q}_{t_{in_i}} = -k_{a_i} \frac{\partial T_{a_i}}{\partial z_{a_i}} \Big|_{z_{a_i}=h_i} \quad \forall i = 1, \dots, 3. \tag{89}$$

The outgoing heat flux $\dot{q}_{t_{out_i}}$ is transferred to the bump foil. It is assumed that the heat leaves the top foil only in the regions where the bumps contact the top foil

$$\dot{q}_{t_{out_i}} = \sum_{j=1}^{n_{bu}} \frac{1}{R_{th_{ij}} b} (T_{t_i} - T_{b_i}(s_{bu_{c_{ij}}})) \delta_D(s_{M_{ij}}^*) \quad \forall i = 1, \dots, 3. \tag{90}$$

Herein, $\delta_D(s_{M_{ij}}^*)$ defines the Dirac delta function at the master node $s_{M_{ij}}^*$ ($j = 1, \dots, n_{bu}$) which contacts the j -th bump at the bump center $s_{bu_{c_{ij}}}$. These master nodes are obtained from the contact algorithm described in Section 2.2. The thermal contact resistance $R_{th_{ij}}$ is calculated using an analytical formula. The derivation of the formula is based on the assumption that the heat

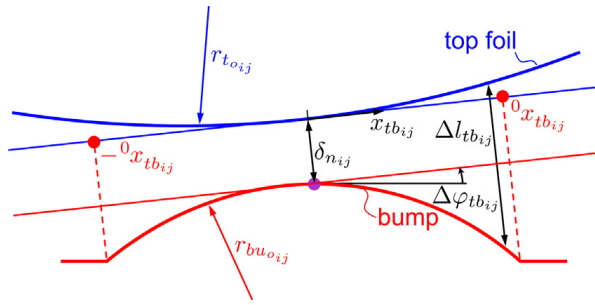


Fig. 11. Contact region between the top foil and a single bump.

in the contact region of bump and top foil is transferred by the small air film near the contact points, see [9,25]: In [9,25] it is shown that the thermal resistance of the solid contact is significantly larger than the thermal resistance of the neighboring air film. Thus, the thermal resistance of the air film determines the overall thermal behavior of the bump and top foil contact.

The thermal resistance of the air film depends on the air film thickness near the contact region. Fig. 11 shows the geometrical conditions in the contact region of a single bump j .

Assuming that the relative angle $\Delta\varphi_{tbij}$ between the top and bump foil tangent is small, the distance Δl_{tbij} is calculated as

$$\begin{aligned} \Delta l_{tbij} &= r_{bu_{oij}} - \sqrt{r_{bu_{oij}}^2 - x_{tbij}^2} + r_{t_{oij}} - \sqrt{r_{t_{oij}}^2 - x_{tbij}^2} + \Delta\varphi_{tbij} x_{tbij} + |\delta_{n_{ij}}| + Ra_{av}, \quad \forall i = 1, \dots, 3, j = 1, \dots, n_{bu} \quad \forall -^0x_{tbij} \\ &\leq x_{tbij} \leq ^0x_{tbij}. \end{aligned} \tag{91}$$

Herein, x_{tbij} describes the local tangential coordinate at the bump and top foil contact region, see Fig. 11. The limits of the contact region are denoted by $^0x_{tbij}$. In this manuscript, the limits correspond with the bump ends. Ra_{av} represents the arithmetic average surface roughness of top and bump foil. Furthermore, $r_{bu_{oij}}$ and $r_{t_{oij}}$ denote the outer bump and top foil radius in the current configuration. The radii are obtained from the current rotation angle of bump and top foil

$$r_{bu_{oij}} = \left(\frac{\partial \Delta\varphi_{bij}}{\partial s_{bu_{ij}}} \Big|_{s_{bu_{ij}}=l_{bu_{ij}}/2} \right)^{-1} + \frac{H_b}{2}, \tag{92}$$

$$\begin{aligned} r_{t_{oij}} &= \left(\frac{\partial \Delta\varphi_{t_i}}{\partial s_{t_i}} \Big|_{s_{t_i}=s_{M_{ij}}} \right)^{-1} + \frac{H_t}{2}, \tag{93} \\ \forall i &= 1, \dots, 3, j = 1, \dots, n_{bu}. \end{aligned}$$

It is further assumed that the radius of top and bump foil are constant within the considered contact region, see Fig. 11. From the distance Δl_{tbij} , the heat conductance K_{tbij} of the bump and top foil contact is calculated by using the relationship

$$K_{tbij} = bk_a \int_{-^0x_{tbij}}^{^0x_{tbij}} \frac{1}{\Delta l_{tbij}} dx_{tbij}, \quad \forall i = 1, \dots, 3, j = 1, \dots, n_{bu}. \tag{94}$$

By performing the integration in Eq. (94) and building the reciprocal of the thermal conductance, a formula for the thermal contact resistance between bump and top foil

$$R_{thij} = \frac{1}{K_{tbij}} = \frac{\sqrt{2 \frac{r_{bu_{oij}} + r_{t_{oij}}}{r_{bu_{oij}} r_{t_{oij}}} (|\delta_{n_{ij}}| + Ra_{av}) - \Delta\varphi_{tbij}^2}}{2ka b} \frac{1}{\arctan f(^0x_{tbij}) - \arctan f(-^0x_{tbij})}, \quad \forall i = 1, \dots, 3, j = 1, \dots, n_{bu} \tag{95}$$

is derived. The function $f(\pm^0x_{tbij})$ of the contact region limits is defined as

$$f(\pm^0x_{tbij}) = \frac{\pm \frac{r_{bu_{oij}} + r_{t_{oij}}}{r_{bu_{oij}} r_{t_{oij}}} ^0x_{tbij} + \Delta\varphi_{tbij}}{\sqrt{2 \frac{r_{bu_{oij}} + r_{t_{oij}}}{r_{bu_{oij}} r_{t_{oij}}} (|\delta_{n_{ij}}| + Ra_{av}) - \Delta\varphi_{tbij}^2}}, \quad \forall i = 1, \dots, 3, j = 1, \dots, n_{bu}. \tag{96}$$

As explained above, the heat from the top foil $\dot{q}_{t_{out_i}}$ is transferred to the bump foil in the contact region, see Fig. 11. As for the top foil, the temperature distribution of the bump foil is described by a 2D heat equation. In Eq. (86), the curvature of the top foil is neglected since the top foil radius is significantly larger than the top foil thickness. The same holds for the bump foil segments. Here, the 2D heat equation

$$k_{b_i} H_{b_i} \left(\frac{\partial^2 T_{b_i}}{\partial s_{b_i}^2} + \frac{\partial^2 T_{b_i}}{\partial y_{b_i}^2} \right) = \dot{q}_{b_{out_i}}, \quad \forall s_{s_{ij}} \leq s_{b_i} \leq s_{s_{rj}}, \quad \forall i = 1, \dots, 3, j = 1, \dots, n_s \tag{97}$$

is applied. Herein, $s_{s_{ij}}$ and $s_{s_{trj}}$ denote the coordinates of the leading and trailing edge of the j -th segment in the i -th bump foil. In contrast to the segments, the curvature of the bumps has to be considered when calculating the temperature distribution. This is caused by the small radius of the bumps compared to the foil thickness. Assuming a linear heat flux distribution across the bump foil thickness in radial direction

$$\dot{q}_{b_{ri}} = \frac{\dot{q}_{b_{out_i}} - \dot{q}_{b_{in_i}}}{H} (r_{bu_{ij}} - r_{bu_{in_{ij}}}) - \dot{q}_{b_{out_i}}, \forall s_{bu_{ij}} \leq s_{b_i} \leq s_{bu_{trj}}, \forall i = 1, \dots, 3, j = 1, \dots, n_{bu}, \quad (98)$$

the general 3D heat equation in cylindrical coordinates

$$k_{b_i} \frac{1}{r_{bu_{ij}}} \frac{\partial}{\partial r_{bu_{ij}}} \left(r_{bu_{ij}} \frac{\partial T_{b_i}}{\partial r_{bu_{ij}}} \right) + k_{b_i} \frac{1}{r_{bu_{ij}}^2} \frac{\partial^2 T_{b_i}}{\partial \varphi_{bu_{ij}}^2} + k_{b_i} \frac{\partial^2 T_{b_i}}{\partial y_{b_i}^2} = 0 \quad \forall s_{bu_{ij}} \leq s_{b_i} \leq s_{bu_{trj}}, \quad \forall i = 1, \dots, 3, j = 1, \dots, n_{bu} \quad (99)$$

is reduced to the 2D heat equation

$$\begin{aligned} H_{b_i} k_{b_i} \frac{\partial^2 T_{b_i}}{\partial s_{b_i}^2} + H_{b_i} k_{b_i} \left(1 + \frac{H_{b_i}}{r_{bu_{in_{ij}}}} \right) \frac{\partial^2 T_{b_i}}{\partial y_{b_i}^2} = \\ \left\{ 2 \left(\dot{q}_{b_{out_i}} - \dot{q}_{b_{in_i}} \right) - \left[\dot{q}_{b_{out_{ij}}} + \frac{r_{bu_{in_{ij}}}}{H_{b_i}} \left(\dot{q}_{b_{out_i}} - \dot{q}_{b_{in_i}} \right) \right] \right. \\ \left. \ln \left(1 + \frac{H_{b_i}}{r_{bu_{in_{ij}}}} \right) \right\} \left(1 + \frac{H_{b_i}}{r_{bu_{in_{ij}}}} \right), \\ \forall s_{bu_{ij}} \leq s_{b_i} \leq s_{bu_{trj}}, \\ \forall i = 1, \dots, 3, j = 1, \dots, n_{bu}, \end{aligned} \quad (100)$$

by integrating Eq. (99) across the bump foil thickness in radial direction. Herein, $r_{bu_{ij}}$ denote the radial coordinate of the j -th bump, running from the inner bump radius $r_{bu_{in_{ij}}}$ to the outer bump radius $r_{bu_{o_{ij}}}$. It is assumed, that the heat flux is zero at the bump foil at the free ends. At the bump foil leading edge, the bump foil temperature $T_{b_i}(s_{b_i} = L_{b_i})$ equals the bearing sleeve temperature T_{bs} .

As stated in Eq. (90), it is assumed that the heat from the top foil

$$\dot{q}_{b_{in_i}} = \dot{q}_{t_{out_i}} = \sum_{j=1}^{n_{bu}} \frac{1}{R_{th_{ij}} D} (T_{t_i}(s_{M_{ij}}^*) - T_{b_i}) \delta_D(s_{bu_{c_{ij}}}), \quad \forall i = 1, \dots, 3, \quad (101)$$

enters the bump foil at the bump centers $s_{bu_{c_{ij}}}$ ($j = 1, \dots, n_{bu}$). The outgoing heat flux from the bump foil $\dot{q}_{b_{out_i}}$ is transferred to the bearing sleeve. Here, the same assumptions as for the top and bump foil contact are made, see [9,25]: The thermal resistance is mainly determined by the air film in the contact region. From Eq. (45) the distance $\delta_{n_{b,bs}}$ between bump foil and bearing sleeve is calculated. In contrast to the contact algorithm, where the distance is only evaluated at single slave nodes, see Fig. 7, a surface-to-surface approach is applied for the thermal contact model. Thereby, the distance $\delta_{n_{b,bs}}(s_b)$ is calculated as a function of the bump foil material coordinate s_b . Assuming a 1D heat transfer and a constant heat flux through the thin air film between bump foil and bearing sleeve, the out streaming heat flux is calculated as

$$\dot{q}_{b_{out_i}} = k_a \frac{T_{b_i} - T_{bs}}{\delta_{n_{b,bs}}}, \quad \forall i = 1, \dots, 3. \quad (102)$$

The bearing sleeve temperature T_{bs} is obtained from the heat equation of the bearing sleeve, explained in detail in the subsequent section.

Table 1
Number of finite elements for the different domains of the numerical model.

Gasdynamic Model	
Reynolds Equation	50 × 50
Elastic Model	
Top foil	1000
Bump/ segment	50
Thermal model	
3D Air Film	50 × 20 × 8
Rotor	60 × 20
Top foil	50 × 50
Bump foil	126 × 50

2.3.4. Thermal Model of the Bearing Sleeve

In this study, a lumped thermal model is used in order to obtain the temperature of the bearing sleeve

$$T_{bs} = T_a + \dot{Q}_{bsin} (R_{thbs} + R_{tho}). \tag{103}$$

The thermal resistance of the bearing sleeve R_{thbs} is calculated from the relationship

$$R_{thbs} = \frac{\ln\left(\frac{r_{bs0}}{r_{bsi}}\right)}{2\pi b_{bs} k_{bs}}, \tag{104}$$

while the thermal resistance of the convective heat transfer at the outer bearing sleeve R_{tho} is obtained from measurements, see Section 3. The in streaming heat flux \dot{Q}_{bsin} results from the heat transfer at the bump foil contact as well as from heat transfer at the top and bump foil leading edge

$$\dot{Q}_{bsin} = \sum_{i=1}^3 \left(\int_{A_i} \dot{q}_{bout_i} dA_i + k_t \frac{\partial T_{t_i}}{\partial s_{t_i}} \Big|_{s_{t_i}=0} - k_b \frac{\partial T_{b_i}}{\partial s_{b_i}} \Big|_{s_{b_i}=L_{b_i}} \right). \tag{105}$$

Assuming that the bearing sleeve can freely expand in radial direction, the thermal growth of the bearing sleeve inner surface is calculated by

$$u_{gr_{bs}} = \beta_{bs} r_i (T_{bs} - T_{bs0}). \tag{106}$$

The thermal growth is used in the calculation of the normal distance between the bearing sleeve and bump foils.

2.4. Numerical solution procedure

As shown in Sections 2.1–2.3, the thermo-elasto-gasdynamic model of preloaded three-pad air foil journal bearings is described by a set of nonlinear fully-coupled integro-differential equations. In this section, the numerical solution schema for this set of equations is described. First, a reduction approach for the generalized Reynolds Eq. (1) and the 3D energy equation of the air film (56) is presented. Afterwards, the different steps of the numerical solution procedure are explained.

2.4.1. Reduction approach

By considering the change of density and viscosity across the air film, the generalized Reynolds Eq. (1) and the 3D energy Eq. (56) have to be solved. The generalized Reynolds equation and the fluid velocity expressions (60) and (61) within the 3D energy equation include the Dowson integrals (2)–(7). Hence, the generalized Reynolds equation and the 3D energy equation build a set of nonlinear fully-coupled integro-differential equations.

The numerical solution of this equation system implies a high computational effort, see e.g. [45]. Therefore, different reduction approaches were developed by several authors, see Section 1. In this study, an averaging approach is applied. This approach yields a significant reduction of computation time but still with sufficient accuracy, see [39]. In [39] this method has been used in order to efficiently calculate the temperature and pressure distribution of an air foil thrust bearing. In this section, the averaging approach is applied to air foil journal bearings.

The averaging approach is based on the assumption that the temperature changes only moderately across the fluid film. As shown in [39], this assumption holds for air bearings. In the framework of the averaging approach, the air film temperature - obtained from the 3D energy Eq. (56) - is averaged across the air film

$$T_{a,avg_i}(x_{a_i}, y_{a_i}) = \frac{1}{h_{a_i}} \int_0^{h_{a_i}} T_{a_i}(x_{a_i}, y_{a_i}, z_{a_i}) dz, \quad \forall i = 1, \dots, 3, \tag{107}$$

yielding a 2D temperature distribution $T_{a,avg_i}(x_{a_i}, y_{a_i})$, see [39]. Density and viscosity of the air film are calculated at the averaged temperature. Thereby, the generalized Reynolds Eq. (1) is reduced to the simple Reynolds equation

$$\frac{\partial}{\partial x_{a_i}} \left(\frac{\rho_i(T_{a,avg_i}) h_{a_i}^3}{\eta_{a_i}(T_{a,avg_i})} \frac{\partial p_i}{\partial x_{a_i}} \right) + \frac{\partial}{\partial z_{a_i}} \left(\frac{\rho_i(T_{a,avg_i}) h_{a_i}^3}{\eta_{a_i}(T_{a,avg_i})} \frac{\partial p_i}{\partial z_{a_i}} \right) = -6r_R \Omega \frac{\partial(\rho_i(T_{a,avg_i}) h_{a_i})}{\partial x_{a_i}}, \quad \forall i = 1, \dots, 3, \tag{108}$$

for compressible fluids. Furthermore, the fluid velocity expressions (60) and (61) in the 3D energy Eq. (56) are simplified to

$$v_{x_{a_i}} = \frac{1}{2\eta_{a_i}(T_{a,avg_i})} \frac{\partial p_i}{\partial x_{a_i}} z_{a_i} (z_{a_i} - 1) - r_R \Omega (1 - z_{a_i}) \tag{109}$$

$$v_{y_{a_i}} = \frac{1}{2\eta_{a_i}(T_{a,avg_i})} \frac{\partial p_i}{\partial y_{a_i}} z_{a_i} (z_{a_i} - 1), \tag{110}$$

$$\forall i = 1, \dots, 3,$$

by using the air film viscosity at the averaged temperature T_{a,avg_i} , see [39].

2.4.2. Numerical solution procedure

The governing equations, see Section 2.1–2.4.1, are discretized by a finite element approach. As for the generalized Reynolds equation and the 3D energy equation, the solution space of all other partial differential equations is transformed to a uniform domain by a non-dimensionalization of the corresponding coordinates. The non-dimensional domains are discretized using different types and numbers of finite elements. For the nonlinear beamshell Eqs. (14)–(16), quintic Lagrange elements are used in order to avoid shear locking. All other equations are discretized with quadratic Lagrange elements. Table 1 gives an overview on the number of finite elements for the different domains of the numerical model.

In order to prevent numerical instabilities in connection with convection–diffusion problems an artificial diffusion approach is applied in this study. In context of this approach, a diffusion term is added to the 3D energy Eq. (56) in circumferential direction. The numerical diffusion coefficient reads

$$k_{art_i} = \delta_{art} h_{mesh} \rho_i c_p \left\| v_{x_{ai}} \right\|, \quad \forall i = 1, \dots, 3. \quad (111)$$

Herein, δ_{art} and h_{mesh} describe a sufficiently small artificial diffusion factor and the element size, respectively. In general, the introduction of an artificial diffusion term prevents numerical instabilities but may cause numerical errors in the temperature results. In this study, an artificial diffusion factor of $\delta_{art} = 0.25$ is chosen.

The discretization of the partial differential equations by the finite element method yields a set of fully-coupled nonlinear algebraic equations. This set of equations is solved by an automated Newton–Raphson method. To achieve a convergence of the numerical solution, a special procedure is introduced which comprises the subsequent study steps:

1. Calculation of the top and bump foil deformation during bending into the bearing sleeve. The assembly pressure is modeled as a uniform pressure acting on each top foil and each penultimate bump foil segment.
2. Evaluation of the bump foil deformation after release of the assembly pressure. The bump foils come into contact with the bearing sleeve inner surface.
3. Determination of the top foil deformation after release of the assembly pressure. The top foils come into contact with the bump foil.
4. In order to assemble the bearing sleeve on the rotor shaft, the elastic foil structure is pushed towards the bearing sleeve. This process is realized in the fourth study step by applying a constant assembly pressure on each top foil.
5. Release of the assembly pressure on the top foils. The top foils come into contact with the rotor surface.
6. The shaft rotates at a constant speed. The resulting pressure distribution inside each air film is calculated by gradually decreasing the uniform boundary layer on the rotor shaft.
7. A harmonic load $F_b = \widehat{F}_b/2(1 - \cos(2\pi t))$ is applied on the rotor. To avoid a dependency of the resulting solution on the initial conditions obtained from the previous study step, two periods are simulated. Since transient and inertia effects are neglected in this study, the mathematical problem is frequency independent and quasi-static. Therefore, t is regarded as a non-dimensional parameter.
8. The temperature and pressure distribution of the air films as well as the temperature distribution of all other components are calculated, while all other dependent variables (deformation/ displacement of the components) are held constant.
9. The elastic deformation of the foil structure as well as the thermal distortion of the rotor belonging to the previous obtained temperature field are determined.
10. The fully-coupled thermo-elasto-gasdynamic solution is obtained.

Note, that in study steps 1–6 only the non-linear equations belonging to the elastic model are solved, while all other dependent variables and corresponding equations are excluded from the study steps.

Fig. 12 illustrates the described solution procedure. In the last step, the fully-coupled thermo-elasto-gasdynamic problem is solved. To obtain a solution, a segregated solution procedure is applied in this study. In context of this procedure, the total number of dependent variables and corresponding equations describing the presented thermo-elasto-gasdynamic model, see Section 2, is divided into three segregated groups:

1. Elasto-gasdynamic variables and equations: Top and bump foil displacement, rotor eccentricity, air film pressure.
2. Thermal variables and equations: Air film temperature, top and bump foil temperature, rotor temperature, bearing sleeve temperature and expansion.
3. Lamé-Navier equations of the rotor: Centrifugal and thermal rotor expansion.

Each group of equations is solved for the corresponding variables using a fully-coupled solution approach, while the variables of the other groups are held at a constant value. Thereby, the numerical solution is obtained in a blockwise manner. The group of variables introduced above define the sub steps of the solution procedure. The sub steps 1–3 are repeated until a global convergence of all variables is achieved. In each sub step, a damped Newton–Raphson approach is applied, in which the Jacobian matrix is calculated analytically.

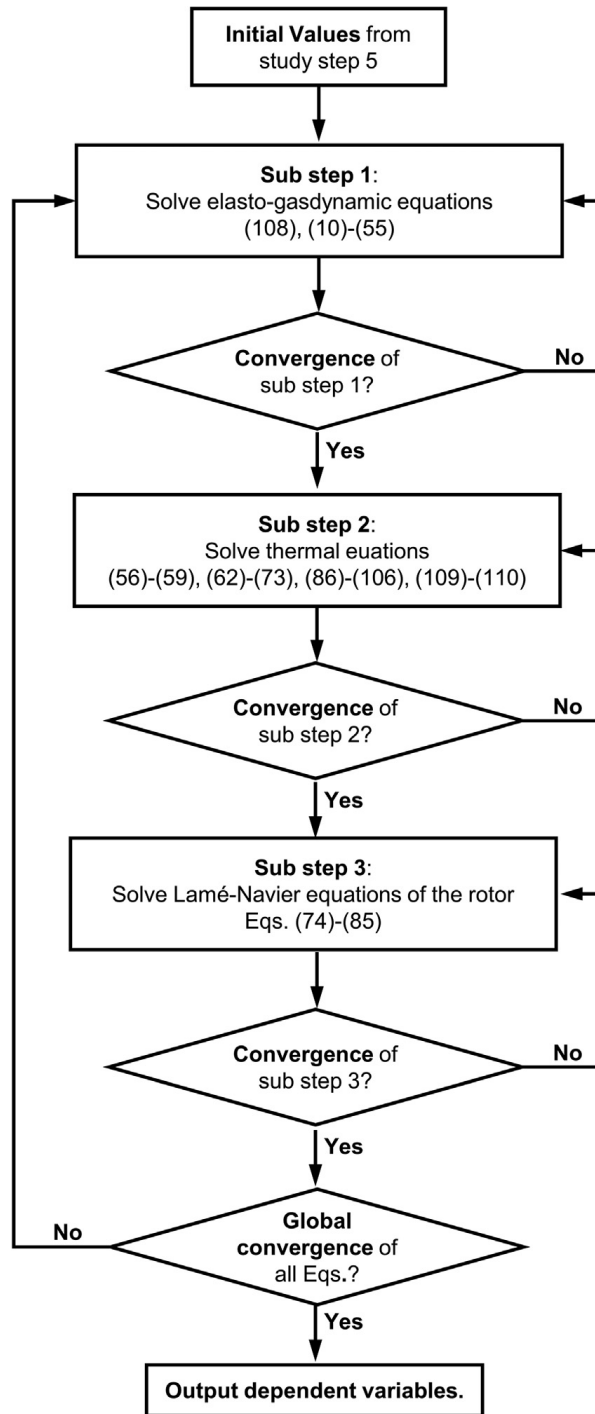


Fig. 12. Flowchart of the solution procedure in the last study step.

3. Experimental procedure

In order to validate the numerical results, experiments are accomplished on two different test rigs. The test rigs are described in detail in [7]. In this work, the employed test rigs and the test bearing are briefly summarized. For more details, the reader is referred to Ref. [7].

The first test rig - the hysteresis device - is used for validating the elastic model of the foil structure, see Section 3.1. With the second test rig, temperature measurements of the bearing and the rotor are examined in order to validate the thermal model, see Section 3.2. The geometry of the investigated test bearing is presented in Section 3.2.1.

3.1. Static hysteresis measurement

In order to validate the elastic model of the foil structure, static hysteresis measurements are performed on a hysteresis device first. This hysteresis device is presented in [5,6]. Fig. 13 shows a CAD-model of the hysteresis device. In this test rig, a horizontal, linear bearing movement along a linear guiding is automatically applied by a hybrid linear actuator. The acting horizontal force on the shaft $F_{s_{hor}}$ and the relative bearing displacement $s_{b_{hor}}$ are measured by a strain-gauge based load cell and an eddy current sensor. With this device, static hysteresis curves for the bearing are measured. The direction of motion is automatically reversed when the shaft force reaches 30N. The procedure is accomplished until the hysteresis curve describes a closed loop. The horizontal movement is applied via the hybrid linear actuator while the vertical movement is restricted. A positive displacement is defined as a relative displacement of the rotor in the direction of the center of the first pad. Negative values correspond to a motion in the opposite direction, between the second and the third pad. In this study, the measurement results used for validation are taken from [7].

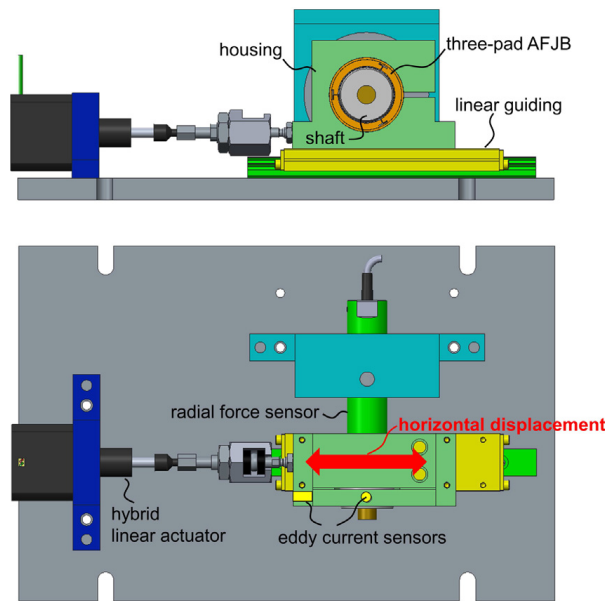


Fig. 13. Test rig 1: Hysteresis device for the measurement of static bearing hystereses [7,6].

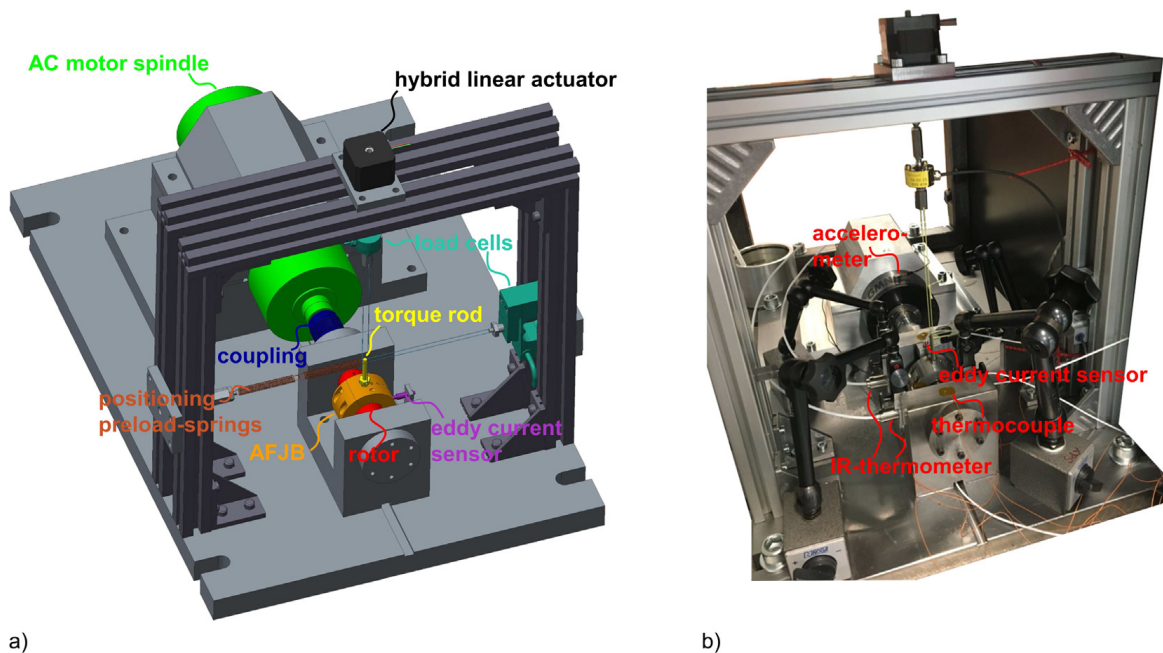


Fig. 14. Test rig 2: CAD-model (a) and photo (b) of the automated high-speed air foil journal bearing test rig, see [7].

Table 2
Overall measurement errors of the bearing load as well as of the bearing and rotor temperatures, see [7].

Bearing load σ_{F_b}	0.06 N at $F_b = 5$ N
Bearing temperature σ_{T_b}	1.12 K
Rotor temperature σ_{T_r}	1 K

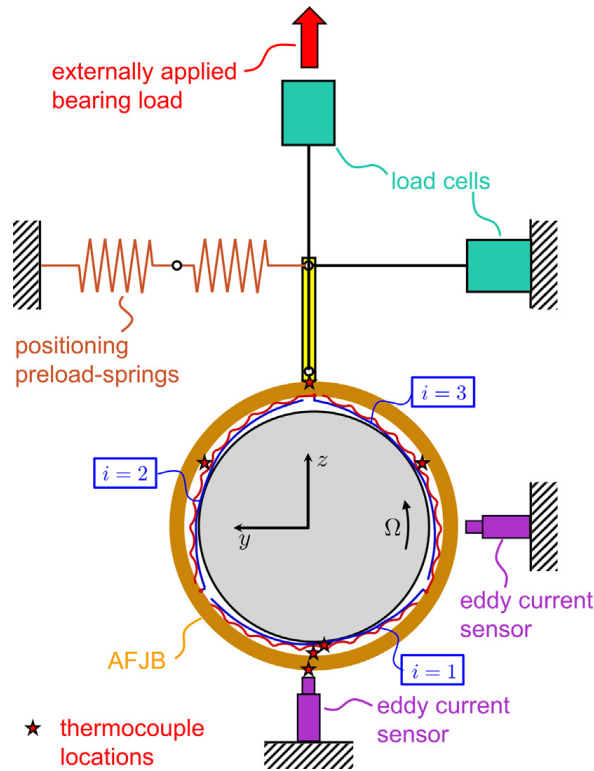


Fig. 15. Test rig 2: Schematic representation of the automated high-speed air foil journal bearing test rig including the thermocouple locations at the bearing components, see [7].

Table 3
Nominal parameters of the heavily preloaded three-pad air foil journal bearing, see [7].

Overall bearing parameters	
Bearing width b	27 mm
Rotor radius r_r	15 mm
Bearing sleeve inner radius r_i	15.789 mm
Number of pads	3
Top and bump foil parameters	
Top foil radius r_{t_b}	57.3 mm
Top foil length L_t	30 mm
Number of bumps per bump foil	9
Bump foil radius r_b	30 mm
Segment length a_{se}	0.65 mm
Minimum bump height at the fixed end $h_{b_{min}}$	0.554 mm
Maximum bump height at the free end $h_{b_{max}}$	0.578 mm
Bump pitch a_p	3.15 mm
Top and bump foil thickness H	100 μ m
Top foil coating thickness H_{cot}	20 μ m

3.2. Temperature measurements

For the purpose of validating the thermal model of the preloaded three-pad air foil journal bearing, thermal measurements at different bearing loads are performed on an automated high-speed test rig. This test is described in detail in [7]. The test device, illustrated in Figs. 14 and 15, is briefly explained in this section.

The test rig consists of a rotor which is supported by four grease lubricated angular contact ball bearings in a spring-preloaded X-arrangement. The rotor is driven by an AC motor spindle at speeds up to 60krpm.

The investigated air foil journal bearing is located in the middle of a rotor. The rotor is driven by an AC motor spindle at speeds up to 60krpm. The bearing sleeve is divided into two parts in order to allow for a simple and fast assembling and disassembling of the foil bearing on the rotor. The bearing sleeve has a total of ten radial threaded holes to allow a torque rod to be attached to the bearing sleeve at different angular locations. The free end of the torque rod is connected to a load cell via a horizontal cable. Thereby, the bearing drag torque is measured. Furthermore, two serially combined springs are attached to the free end of the torque rod. These springs preload the load cell. A vertical load is applied to the bearing sleeve by a hybrid linear actuator. Therefore, the bearing sleeve end of the torque rod is connected via a second cable to another load cell located at the linear actuator. This actuator has a minimum macro step size of $1.5\ \mu\text{m}$. The strain gauge based load cell has a sensitivity of $0.09994\ \text{V/N}$ and a linearity error of less than $0.2\ \%$. The load is controlled by adjusting the hybrid linear actuator step size using a P-controller design.

The rotor motion as well as the current machine operation are monitored by several eddy current sensors and accelerometers which are located near the rotor and the spindle.

Furthermore, the temperature of the foil bearing, of the rotor and of the angular ball bearing housings are measured. The temperature of the foil bearing is measured at the top and bottom of the bearing sleeve, at the backside of the loaded top foil between the fourth and the fifth bump and at the backside of the fifth bump of each bump foil using T-type thermocouples, Fig. 15. The same thermocouples are used for the measurement of the temperature at the angular ball bearing housings. These thermocouples have a measurement error of $0.75\ \%$, but at least $1\ ^\circ\text{C}$. The thermocouples are attached to the surfaces with special adhesive strips.

The rotor temperature is measured with two infrared thermometers in an axial distance of approximately $6\ \text{mm}$ to the air foil bearing sides. The infrared thermometers have a system accuracy of $\pm 1\ \%$ or $\pm 1\ ^\circ\text{C}$ and a repeatability error of $\pm 0.5\ \%$ or $\pm 0.5\ ^\circ\text{C}$.

Table 2 gives an overview of the measurement error of the bearing load as well as of the bearing and rotor temperatures.

The temperature measurements are accomplished at a rotor speed of $n_r = 35\ \text{krpm}$. At the rotor startup, the air foil journal bearing is not subjected to a load. When the final rotor speed is reached, the particular load is applied to the bearing using a specified loading procedure [7]. The loading schema comprises 2.5 cycles of loading and unloading with the particular bearing load. This is done to ensure that the bearing operates at a repeatable point of the bearing hysteresis curve which is independent of the initial conditions, see [7]. This is especially important for a comparison with the simulation results. The measurements are performed until all components reach steady state temperatures after about half an hour ($t \approx 1800\ \text{s}$), see [7].

From the temperature measurements at the bearing sleeve, the thermal resistance of the convective heat transfer at the outer bearing sleeve R_{th_o} is obtained. Therefore, the measured bearing temperature T_{bs_o} is used in the thermo-elasto-gasdynamic bearing model instead of solving the employed heat transfer Eq. (103). From the model, the heat flux $\dot{Q}_{bs_{in}}$ entering the bearing sleeve is obtained. The thermal resistance is then calculated by solving the relationship

$$R_{th_o} = \frac{T_{bs_o} - T_a}{\dot{Q}_{bs_{in}}}. \quad (112)$$

3.2.1. Test bearing

In this paper, a heavily preloaded three-pad air foil journal bearing is investigated. The bearing consists of three pairs of bump and top foil, Fig. 2. As can be seen from Fig. 2, each top and bump foil is free at one end and fixed in a mounting suspension at the other end. In order to decrease the startup and shutdown torque, the direction of rotation of the rotor is from the free end to the fixed end of the top foils. The bump foils are mounted opposite to the top foils. The bump heights increase by about $24\ \mu\text{m}$ from the fixed end to the free end creating an aerodynamic wedge when all bumps are in contact with the top foil and the bearing sleeve. As shown in Fig. 2, the pads are numbered opposite to the direction of rotation.

Top and bump foils are made from X10CrNi18-8 (1.4310), a stainless spring steel, which can be used at temperatures up to $250\ ^\circ\text{C}$. The bearing sleeve is made from the stainless steel X5CrNiMo17-12-2 (1.4401).

As already described in Section 1, the assembly preload is introduced by using bump and top foils whose initial undeformed radii are significantly larger than the inner radius of the bearing sleeve. The relevant geometrical data of the bearing under investigation are listed in Table 3.

The top foils are coated with a $20\ \mu\text{m}$ PTFE layer to reduce friction and wear during sliding contact at the rotor startup and shutdown [59]. Furthermore, the rotor is coated with a $2 - 4\ \mu\text{m}$ diamond-like carbon (DLC) layer in order to further reduce friction and wear. The rotor radius listed in Table 3 already includes the diamond-like carbon coating thickness.

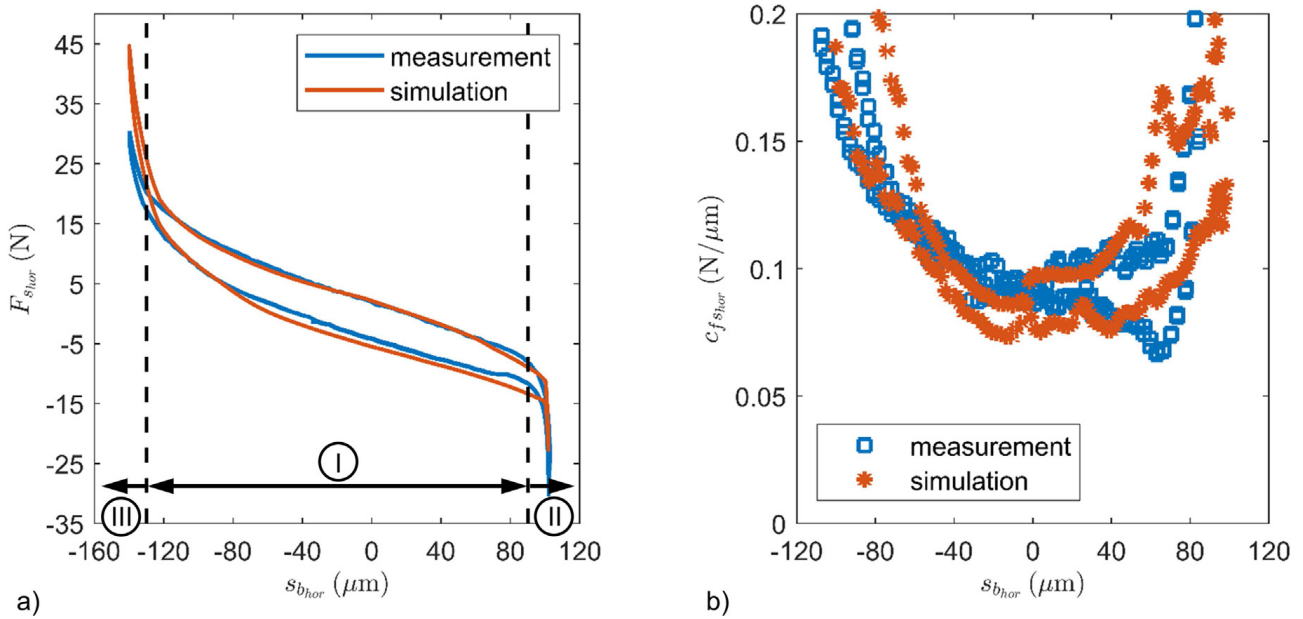


Fig. 16. Measured and predicted hysteresis curve (a) and foil structural stiffness (b) of the investigated three-pad air foil journal bearing. Measurement results from [7].

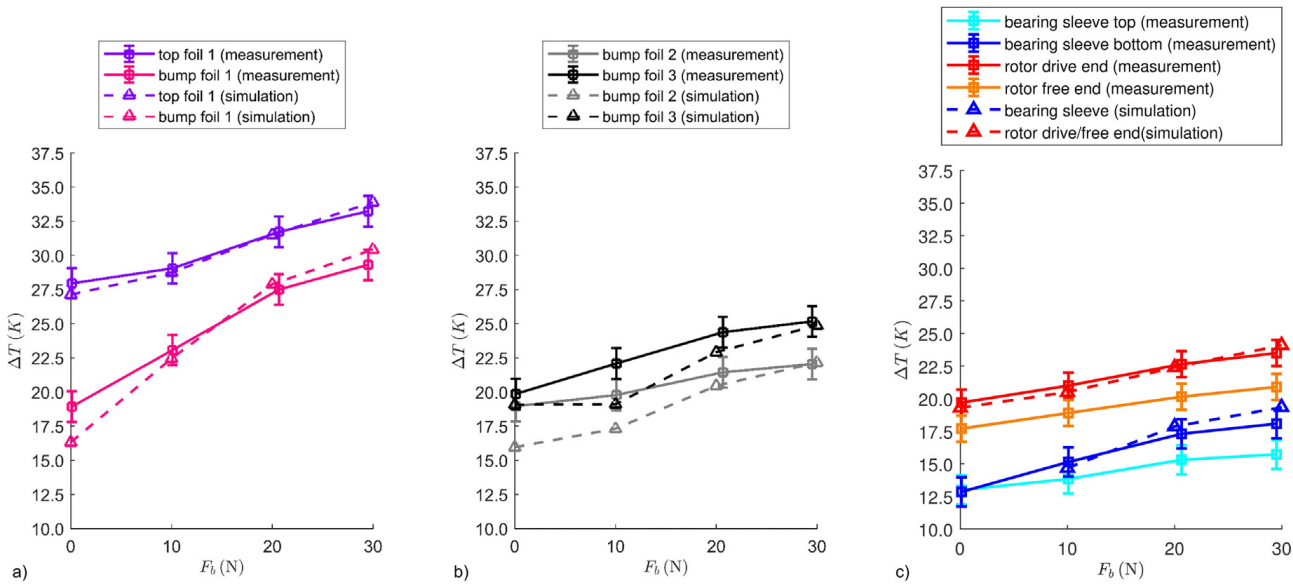


Fig. 17. Measured and predicted temperatures of the first bearing pad (a), of the second and third bump foil (b) and of the bearing sleeve and the rotor (c). Measurement results from [7].

4. Results

In this section, the bearing hysteresis and stiffness as well as the temperature distribution of the heavily preloaded bearing introduced in Section 3.2.1 are analyzed and compared to the experimental results.

4.1. Bearing hysteresis and stiffness

Fig. 16 depicts the predicted and the measured hysteresis curve (a) as well as the foil structural stiffness $c_{f_{s_{hor}}}$ (b) of the investigated bearing. The measured hysteresis curve, see Fig. 16a), has been acquired using the test rig described in Section 3.1. The measured hysteresis curve has first been presented in [7]. Note that two measured hysteresis loops are depicted in Fig. 16. These curves are almost coincident. The foil structural stiffness in the direction of the horizontal bearing displacement, see Fig. 16b), is calculated from the hysteresis curves by the use of first-order central differences.

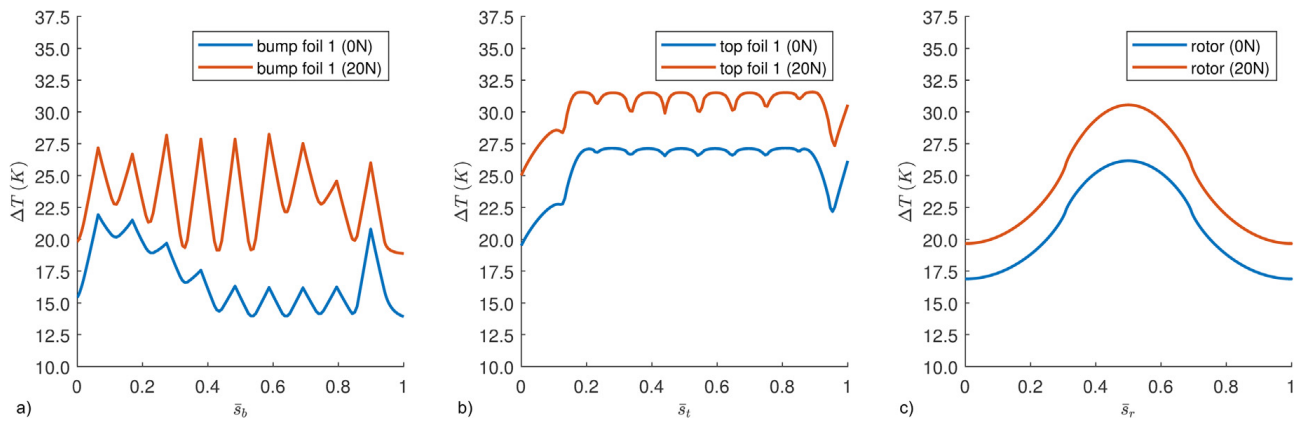


Fig. 18. Temperature distribution of the first bump (a) and top foil (b) as well as of the rotor (c) over the corresponding non-dimensional coordinates for two different load cases.

As can be seen, both hysteresis curves (measured and predicted) can be subdivided into three main regions. The first region I, see Fig. 16, is characterized by a moderate stiffness ($c_{fs_{hor}} < 0.2 \text{ N}/\mu\text{m}$). This stiffness is mainly determined by the introduced assembly preload. In this region, only a small number of bumps are in contact either with the top foil or the bearing sleeve. The second and third region are characterized by a strongly increasing foil structural stiffness. For larger displacements towards the pad center - region II - or towards the opposite foil suspension - region III - more bumps come into contact with either the top foil or the bearing sleeve. This explains the strong increase of the foil structural stiffness. Therefore, the foil structural stiffness in the second and third region mainly depends on the bump stiffness. Note, that the bearing is mostly operated in the region of moderate foil stiffness. Due to rarely occurring shock loads an operation in region II or III may take place.

As shown in Fig. 16, the predicted and measured hysteresis curve agree well. In region III, slight discrepancies between measurement and simulation occur. This might be traced back to manufacturing deviations of the bump foil height which are not captured by the simulation.

The area enclosed by the hysteresis loop equals the energy dissipation W_D during one cycle. The energy dissipation is caused by the friction occurring in the contact between top and bump foil, bump foil and bearing sleeve as well as between top foil and rotor. The energy dissipation can be calculated from the measured and predicted hysteresis curve by evaluating the ring integral

$$W_D = \oint F_{b_{hor}} ds_{b_{hor}}. \tag{113}$$

This integral expression is approximated from the measured and predicted results by a trapezoidal quadrature method. From Eq. 113, the dissipated energy is calculated to $W_{D_{mes}} = 1.3 \text{ mJ}$ and $W_{D_{sim}} = 1.5 \text{ mJ}$ for the measurement and the simulation, respectively. The measured and predicted energy differ by about 15%. This discrepancy might be traced back to the uncertainty of the friction coefficient between the different surfaces. In this study, the friction coefficient between bump and top foil and between bump foil and bearing sleeve is chosen to $\mu = 0.1$. Due to the PTFE coating on the top foil and the diamond-like-carbon coating on the shaft, the friction coefficient between the top foil and the shaft is significantly smaller, see [7]. This friction coefficient is chosen to $\mu_s = 0.035$.

Summarizing, measured and predicted bearing hysteresis agree favorably validating the presented elastic model of the foil structure.

4.1.1. Temperature distribution

In order to validate the thermal model, the temperature results obtained with the fully-coupled thermo-elasto-gasdynamic bearing model are compared to measurement results for a load-on-pad configuration, see Fig. 15. Note, that the measurement results have first been presented in [7].

For several bearing loads, Fig. 17 depicts the measured and predicted temperatures at different bearing components: The temperatures of the top and bump foil of the first bearing pad are shown in Fig. 17a). Fig. 17b) and 17c) illustrate the temperatures of the second and third bump foil as well as the temperatures of the bearing sleeve and of the rotor drive end and drive end. Since the bearing sleeve temperatures at zero bearing load have been used to determine the thermal resistance of the bearing sleeve using Eq. (112), the corresponding predicted temperature is not depicted in Fig. 17c). For the measured temperatures, error bars indicate the overall measurement error, see Table 2.

As can be seen, the predicted temperatures are mostly located inside the error bars of the corresponding measurement result showing a good agreement between measurement and simulation. For the temperatures of the second and third bump foil, the largest discrepancies occur. These discrepancies may be traced back to manufacturing deviations of the bump foil - especially of the bump height - which result in different thermal contact resistances. These measurement uncertainties have

a larger effect on the temperature distribution in lightly loaded pads as it is the case for the second and third pad as well as for the first pad at zero bearing load. Therefore, the deviations between measurement and simulation are larger here. For larger bearing loads, the distance between top and bump foil decreases. When the bumps are in contact, the thermal resistance is determined by the gap function in the vicinity of the contact point rather than by the distance between bump foil slave nodes and the top foil and bearing sleeve. The dependency of this gap function on the bump height is quite small. Hence, the deviations between the measured and predicted temperatures of the first bump foil are small for larger loads.

Due to the symmetric axial boundary conditions chosen for the heat equations for the bearing and the rotor, the predicted temperature distribution of the rotor is symmetric as well, see Fig. 18c). Therefore, the numerical model predicts an equal temperature at the rotor drive end and the rotor free end, see Fig. 18c). In contrast, small differences between the temperature at the rotor free end and at the rotor drive end are measured, see Fig. 17c). These differences might be traced back to deviations in the axial position of the infrared thermometer. Another reason might be a small angular misalignment of the air foil journal bearing. The predicted rotor temperatures agree favorably with the measured temperatures at the rotor drive end. Note, that the heat transferred to the rotor by the angular ball bearings and the motor spindle are not directly taking into account in the thermal model of the rotor. Instead, the axial rotor end are assumed as adiabatic walls, see Eq. (72). Due to temperature measurements of the test rotor at the given rotor speed without the air foil journal bearing, it was found that the heat flux due to the angular ball bearings and the motor spindle is negligible compared to the energy dissipation of the investigated air foil journal bearing.

As shown in Fig. 17, the temperatures of the top and bump foil increase with increasing bearing load. The temperature rise in the first bearing pad is significantly larger than in the other bearing pads, since the bearing load is directed towards the center of the first pad. Besides the loading condition, the rise of the temperature of the first bump foil may be explained by a second effect: Due to the load, the distance between the contacting points decreases. Thereby, the thermal resistance at the contact points decreases which leads to a rise of the bump foil temperature and the bearing sleeve temperature. Hence, the temperature difference between top and bump foil decreases, see Fig. 17a).

Fig. 18 depicts the temperature distribution of the first bump (a) and top foil (b) as well as of the rotor (c) over the corresponding non-dimensional coordinate \bar{s} for zero bearing load and for a bearing load of $F_b = 20\text{ N}$. The temperature distribution of top and bump foil clearly reflects the shape of the bump foil as well as the contact situation between bump and top foil and between bump foil and bearing sleeve: The temperature peaks at the bump foil are located at the nine bump centers while the temperature minima correspond to the segments between the bumps. For the top foil, the local temperature minima are located at the nearby bump centers.

At zero external load, the heat enters the bump foil mainly at the first and at the last bump. These bumps are in contact with the top foil. The heat is further transferred to the bearing sleeve at the center bumps, whose temperatures are close to the bearing sleeve temperature, see Fig. 17c). Due to the small number of bumps, which are in contact with the top foil, the peak values differ significantly. For the highly loaded bearing however, the peak temperatures do not differ that significantly, since more bumps are in contact with the top foil or they are close to come into contact. Hence, the contact between the different foils and the bearing sleeve has a significant effect on the heat transfer through the foil structure.

Summarizing, measured and predicted temperatures agree well validating the presented thermo-elasto-gasdynamic model of the three-pad air foil journal bearing.

5. Conclusion

In this paper a detailed thermo-elasto-gasdynamic model has been presented. In this model, the bump and top foil deflection are described by a non-linear beamshell equation according to Reissner. The contact of top and bump foil and of the bump foil and the bearing sleeve is accounted for by a contact algorithm which is based on the augmented Lagrange approach and Coulomb's law of friction. The pressure in the fluid film is calculated by the Reynolds equation for compressible fluids. To account for the temperature change across the fluid film, the density and viscosity in the Reynolds equation and in the fluid velocity expressions are calculated at a cross-film averaged temperature, see [39]. The temperature distribution of the air film as well as of the surrounding structure are described by appropriate energy and heat equations. Furthermore, an analytical formula for the thermal contact resistance between bump and top foil has been developed.

The predicted bearing hysteresis and stiffness as well as the temperature distribution have been analyzed and compared with measurements obtained with two automated test rigs. The prediction and measurements agree favorably, thus validating the thermo-elasto-gasdynamic bearing model. The results clearly show a strong dependency of the thermal resistance of the foil structure on the number of bumps which are in contact either with the bearing sleeve or the top foil. In a future study, different cooling strategies for preloaded air foil journal bearings will be examined both numerically and experimentally.

CRedit authorship contribution statement

Marcel Mahner: Conceptualization, Formal analysis, Investigation, Methodology, Software, Validation, Visualization, Writing - original draft, Writing - review & editing. **Marcel Bauer:** Investigation, Writing - review & editing. **Bernhard Schweizer:** Conceptualization, Methodology, Writing - review & editing.

Declaration of Competing Interest

The authors declare that they have no known competing financial interests or personal relationships that could have appeared to influence the work reported in this paper.

References

- [1] C. Dellacorte, M.J. Valco, Load capacity estimation of foil air journal bearings for oil-free turbomachinery applications, *Tribol. Trans.* 43 (4) (2000) 795–801, <https://doi.org/10.1080/10402000008982410>.
- [2] K. Radil, S. Howard, B. Dykas, The role of radial clearance on the performance of foil air bearings, *Tribol. Trans.* 45 (4) (2002) 485–490, <https://doi.org/10.1080/10402000208982578>.
- [3] C. Baum, H. Hetzler, W. Seemann, On the stability of balanced rigid rotors in air foil bearings, in: 11th International Conference on Vibrations in Rotating Machines (SIRM), Magdeburg, Germany, Feb, 2015, pp. 23–25.
- [4] K. Sim, L. Yong-Bok, T. Ho Kim, J. Lee, Rotordynamic performance of shimmed gas foil bearings for oil-free turbochargers, *Journal of Tribology* 134 (3) (2012) 031102–1 – 031102–11. doi:10.1115/1.4005892..
- [5] M. Mahner, P. Li, A. Lehn, B. Schweizer, Numerical and experimental investigations on preload effects in air foil journal bearings, in: ASME Turbo Expo, Vol. Volume 7A: Structures and Dynamics, Place of Conference, 2017, p. V07AT34A006, DOI: 10.1115/GT2017-63284. doi:10.1115/GT2017-63284. doi:10.1115/GT2017-63284..
- [6] M. Mahner, P. Li, A. Lehn, B. Schweizer, Numerical and experimental investigations on preload effects in air foil journal bearings, *J. Eng. Gas Turbines Power* 140 (3) (2018), <https://doi.org/10.1115/1.4037965>, pp. 032505–1–032505–9.
- [7] M. Mahner, M. Bauer, A. Lehn, B. Schweizer, An experimental investigation on the influence of an assembly preload on the hysteresis, the drag torque, the lift-off speed and the thermal behavior of three-pad air foil journal bearings, *Tribol. Int.* 137 (2019) 113–126.
- [8] K. Ryu, L. San Andres, On the failure of a gas foil bearing: High temperature operation without cooling flow, *J. Eng. Gas Turbines Power* 135 (11) (2013), <https://doi.org/10.1115/1.4025079>, pp. 112506–1 – 112506–10.
- [9] A. Lehn, Air foil thrust bearings: A thermo-elasto-hydrodynamic analysis, Ph.d. thesis, Technical University Darmstadt (2017)..
- [10] M. Salehi, E. Swanson, H. Heshmat, Thermal features of compliant foil bearingstheory and experiments, *J. Tribol.* 123 (3) (2001) 566, <https://doi.org/10.1115/1.1308038>.
- [11] R.J. Bruckner, Simulation and modeling of the hydrodynamic, thermal, and structural behavior of foil thrust bearings, Case Western Reserve University, 2004, Thesis.
- [12] Z.C. Peng, M.M. Khonsari, A thermohydrodynamic analysis of foil journal bearings, *J. Tribol.* 128 (3) (2006) 534, <https://doi.org/10.1115/1.2197526>.
- [13] K. Feng, S. Kaneko, Thermohydrodynamic study of multiwound foil bearing using lobatto point quadrature, *J. Tribol.* 131 (2) (2009), <https://doi.org/10.1115/1.3070579>, 021702.
- [14] L. San Andres, T.H. Kim, Thermohydrodynamic analysis of bump type gas foil bearings: A model anchored to test data, *J. Eng. Gas Turbines Power* 132 (4) (2010), <https://doi.org/10.1115/1.3159386>, 042504.
- [15] D. Lee, D. Kim, Thermohydrodynamic analyses of bump air foil bearings with detailed thermal model of foil structures and rotor, *J. Tribol.* 132 (2) (2010), <https://doi.org/10.1115/1.4001014>, 021704.
- [16] D. Lee, D. Kim, R.P. Sadashiva, Transient thermal behavior of preloaded three-pad foil bearings: Modeling and experiments, *J. Tribol.* 133 (2) (2011), <https://doi.org/10.1115/1.4003561>, 021703.
- [17] D. Lee, D. Kim, Three-dimensional thermohydrodynamic analyses of rayleigh step air foil thrust bearing with radially arranged bump foils, *Tribol. Trans.* 54 (3) (2011) 432–448, <https://doi.org/10.1080/10402004.2011.556314>.
- [18] T. A. Munroe, Comsol multiphysics predictions of pressurized co2 foil thrust bearing characteristics, in: Supercritical CO2 Power Cycle Symposium, Place of Conference, 2011..
- [19] D. Kim, J. Ki, Y. Kim, K. Ahn, Extended three-dimensional thermo-hydrodynamic model of radial foil bearing: Case studies on thermal behaviors and dynamic characteristics in gas turbine simulator, *J. Eng. Gas Turbines Power* 134 (5) (2012), <https://doi.org/10.1115/1.4005215>, 052501.
- [20] K. Sim, T.H. Kim, Thermohydrodynamic analysis of bump-type gas foil bearings using bump thermal contact and inlet flow mixing models, *Tribol. Int.* 48 (2012) 137–148, <https://doi.org/10.1016/j.triboint.2011.11.017>.
- [21] K. Feng, S. Kaneko, A thermohydrodynamic sparse mesh model of bump-type foil bearings, *J. Eng. Gas Turbines Power* 135 (2) (2013), <https://doi.org/10.1115/1.4007728>, 022501.
- [22] S. Aksay, M.F. Aksit, A fully coupled 3d thermo-elastohydrodynamics model for a bump-type compliant foil journal bearing, *Tribol. Int.* 82 (2015) 110–122, <https://doi.org/10.1016/j.triboint.2014.10.001>.
- [23] F. Xu, D. Kim, Three-dimensional turbulent thermo-elastohydrodynamic analyses of hybrid thrust foil bearings using real gas model, in: ASME Turbo Expo 2016: Turbomachinery Technical Conference and Exposition, American Society of Mechanical Engineers, Place of Conference, 2016, pp. V07BT31A030–V07BT31A030..
- [24] D. Kim, Design space of foil bearings for closed-loop supercritical co2power cycles based on three-dimensional thermohydrodynamic analyses, *J. Eng. Gas Turbines Power* 138 (3) (2016), <https://doi.org/10.1115/1.4031433>, 032504.
- [25] A. Lehn, M. Mahner, B. Schweizer, A thermo-elasto-hydrodynamic model for air foil thrust bearings including self-induced convective cooling of the rotor disk and thermal runaway, *Tribol. Int.* 119 (2018) 281–298, <https://doi.org/10.1016/j.triboint.2017.08.015>, URL: <http://www.sciencedirect.com/science/article/pii/S0301679X17303936>.
- [26] K. Qin, P.A. Jacobs, J.A. Keep, D. Li, I.H. Jahn, A fluid-structure-thermal model for bump-type foil thrust bearings, *Tribol. Int.* 121 (2018) 481–491, <https://doi.org/10.1016/j.triboint.2018.02.008>, <http://www.sciencedirect.com/science/article/pii/S0301679X18300859>.
- [27] K. Radil, M. Zeszotek, An experimental investigation into the temperature profile of a compliant foil air bearing, *Tribol. Trans.* 47 (4) (2004) 470–479, <https://doi.org/10.1080/05698190490501995>.
- [28] L. San Andres, T.A. Chirathadam, K. Ryu, T.H. Kim, Measurements of drag torque, lift-off journal speed, and temperature in a metal mesh foil bearing, *J. Eng. Gas Turbines Power* 132 (11) (2010), <https://doi.org/10.1115/1.4000863>, pp. 112503–1 – 112503–7.
- [29] L. San Andres, K. Ryu, T.H. Kim, Thermal management and rotordynamic performance of a hot rotor-gas foil bearings systempart i: Measurements, *J. Eng. Gas Turbines Power* 133 (6) (2011), <https://doi.org/10.1115/1.4001826>, 062501.
- [30] D. Kim, G. Zimbru, Start-stop characteristics and thermal behavior of a large hybrid airfoil bearing for aero-propulsion applications, *Journal of Engineering for Gas Turbines and Power* 134 (3) (2012) 032502–1 – 032502–9. doi:10.1115/1.4004487..
- [31] T.H. Kim, J.W. Song, Y.-B. Lee, K. Sim, Thermal performance measurement of a bump type gas foil bearing floating on a hollow shaft for increasing rotating speed and static load, *J. Eng. Gas Turbines Power* 134 (2) (2012), <https://doi.org/10.1115/1.4004401>, 024501.
- [32] K. Ryu, L. San Andres, Effect of cooling flow on the operation of a hot rotor-gas foil bearing system, *J. Eng. Gas Turbines Power* 134 (10) (2012), <https://doi.org/10.1115/1.4007067>, 102511.
- [33] S.K. Shrestha, D. Kim, Y. Cheol Kim, Experimental feasibility study of radial injection cooling of three-pad air foil bearings, *J. Tribol.* 135 (4) (2013), <https://doi.org/10.1115/1.4024547>, 041703.
- [34] S.A. Howard, C. Dellacorte, M.J. Valco, J.M. Prael, H. Heshmat, Steady-state stiffness of foil air journal bearings at elevated temperatures, *Tribol. Trans.* 44 (3) (2001) 489–493, <https://doi.org/10.1080/10402000108982486>.
- [35] T. H. Kim, A. W. Breedlove, L. San Andres, Characterization of foil bearing structure for increasing shaft temperatures: Part istatic load performance (43116) (2008) 671–678, DOI: 10.1115/GT2008-50567..

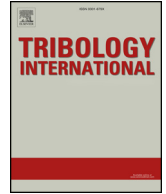
- [36] T. H. Kim, L. San Andres, A. W. Breedlove, Characterization of foil bearing structure for increasing shaft temperatures: Part i: dynamic force performance (43116) (2008) 689–695, DOI: 10.1115/GT2008-50570.
- [37] T.H. Kim, A.W. Breedlove, L. San Andres, Characterization of a foil bearing structure at increasing temperatures: Static load and dynamic force performance, *J. Tribol.* 131 (4) (2009), <https://doi.org/10.1115/1.3195042>, pp. 041703–041703-9.
- [38] D. Dowson, A generalized reynolds equation for fluid-film lubrication, *Int. J. Mech. Sci.* 4 (2) (1962) 159–170, [https://doi.org/10.1016/S0020-7403\(62\)80038-1](https://doi.org/10.1016/S0020-7403(62)80038-1), URL: <http://www.sciencedirect.com/science/article/pii/S0020740362800381>.
- [39] M. Mahner, A. Lehn, B. Schweizer, Thermogas- and thermohydrodynamic simulation of thrust and slider bearings: Convergence and efficiency of different reduction approaches, *Tribol. Int.* 93 (2016) 539–554, <https://doi.org/10.1016/j.triboint.2015.02.030>.
- [40] T.H. Kim, L. San Andres, Thermohydrodynamic model predictions and performance measurements of bump-type foil bearing for oil-free turboshaft engines in rotorcraft propulsion systems, *J. Tribol.* 132 (1) (2010), <https://doi.org/10.1115/1.4000279>, 011701.
- [41] L. San Andres, K. Ryu, T.H. Kim, Thermal management and rotordynamic performance of a hot rotor-gas foil bearings system part ii: Predictions versus test data, *J. Eng. Gas Turbines Power* 133 (6) (2011), <https://doi.org/10.1115/1.4001827>, 062502.
- [42] D. Lee, H. Lim, B. Choi, B. Kim, J. Park, J. Bang, Thermal behavior of radial foil bearings supporting an oil-free gas turbine: Design of the cooling flow passage and modeling of the thermal system, *J. Eng. Gas Turbines Power* 139 (6) (2017), <https://doi.org/10.1115/1.4035324>, 061902.
- [43] A. Lehn, M. Mahner, B. Schweizer, A contribution to the thermal modeling of bump type air foil bearings: Analysis of the thermal resistance of bump foils, *J. Tribol.* 139 (6) (2017), <https://doi.org/10.1115/1.4036631>, pp. 061702-1–061702-10.
- [44] M. Rieken, M. Mahner, B. Schweizer, Thermal optimization of air foil thrust bearings using different foil materials, in: ASME Turbo Expo 2019: Turbomachinery Technical Conference and Exposition, Vol. Volume 7B: Structures and Dynamics, Place of Conference, 2019. doi:10.1115/gt2019-91207. doi: 10.1115/GT2019-91207..
- [45] H.G. Elrod, D.E. Brewster, Thermohydrodynamic analysis for laminar lubricating films, Tech. rep., NASA Technical Memorandum 88845 (1986)..
- [46] H.G. Elrod, Efficient numerical method for computation of thermohydrodynamics of laminar lubricating films, Tech. rep., NASA Lewis Research Center (1989)..
- [47] L.E. Moraru, Numerical prediction and measurements in the lubrication of aeronautical engine and transmission components, Ph.D. thesis, University of Toledo (2005)..
- [48] D. Lee, D. Kim, Three-dimensional thermohydrodynamic analysis of Rayleigh step air foil thrust bearings with radial arranged bump foils, *Tribol. Trans.* 54 (3) (2011) 432–448.
- [49] E. Reissner, On one-dimensional finite-strain beam theory: the plane problem, *J. Appl. Math. Phys. (ZAMP)* 23 (5) (1972) 795–804.
- [50] H. Heshmat, J.A. Walowit, O. Pinkus, Analysis of gas-lubricated foil journal bearings, *J. Lubr. Technol.* 105 (1983) 647–655.
- [51] S. Le Lez, M. Arghir, J. Frene, A new bump-type foil bearing structure analytical model, *J. Eng. Gas Turbines Power* 129 (4) (2007) 1047–1057, <https://doi.org/10.1115/1.2747638>.
- [52] L. San Andrés, T.H. Kim, Analysis of gas foil bearings integrating fe top foil models, *Tribol. Int.* 42 (1) (2009) 111–120, <https://doi.org/10.1016/j.triboint.2008.05.003>.
- [53] M. Carpino, L.A. Medvetz, J.-P. Peng, Effects of membrane stresses in the prediction of foil bearing performance, *Tribol. Trans.* 37 (1) (1994) 43–50, <https://doi.org/10.1080/10402009408983264>.
- [54] D.-H. Lee, Y.-C. Kim, K.-W. Kim, The static performance analysis of foil journal bearings considering three-dimensional shape of the foil structure, *J. Tribol.* 130 (3) (2008), <https://doi.org/10.1115/1.2913538>, pp. 031102–031102-10.
- [55] A. Libai, J.G. Simmonds, *The nonlinear theory of elastic shells*, Cambridge University Press, 2005.
- [56] P. Wriggers, *Computational Contact Mechanics*, Springer-Verlag, Berlin, Heidelberg, 2006.
- [57] W. Becker, D. Gross, *Mechanik elastischer Krper und Strukturen*, Springer-Verlag, Berlin u.a., 2002.
- [58] W. Sutherland, III, the viscosity of gases and molecular forces, *Philosophical Magazine* 5 (1893) 505–531..
- [59] C. DellaCorte, K.C. Radil, R.J. Bruckner, S.A. Howard, Design, fabrication, and performance of open source generation I and II compliant hydrodynamic gas foil bearings, *Tribol. Trans.* 51 (3) (2008) 254–264, <https://doi.org/10.1080/10402000701772579>.



Paper IV

M. Mahner, M. Bauer, A. Lehn, B. Schweizer, An experimental investigation on the influence of an assembly preload on the hysteresis, the drag torque, the lift-off speed and the thermal behavior of three-pad air foil journal bearings, Tribology International, 2019, vol. 137: pp. 113-126.

©2019. This manuscript version is made available under the CC-BY-NC-ND 4.0 license <http://creativecommons.org/licenses/by-nc-nd/4.0/>



An experimental investigation on the influence of an assembly preload on the hysteresis, the drag torque, the lift-off speed and the thermal behavior of three-pad air foil journal bearings

Marcel Mahner*, Marcel Bauer, Andreas Lehn, Bernhard Schweizer

ARTICLE INFO

Keywords:

Air foil bearings
Torque measurement
Lift-off speed
Temperature measurement

ABSTRACT

Rotors supported by air foil journal bearings often show distinctive subharmonic oscillations arising from the nonlinear force-displacement relationship of the elastic foil structure. Also, air film induced instabilities may be observed in such bearings. A straightforward possibility to decrease the amplitude of subharmonic vibrations and to increase the onset speed of rotor instability is to introduce a mechanical assembly preload to the bearing. The resultant rise in stiffness and damping and the improved rotor dynamic behavior goes along with a larger drag torque. This leads to an increase in the bearing power loss and temperature with the risk of a thermal runaway, which may cause bearing failure. In this manuscript, the influence of an assembly preload on the bearing hysteresis, the startup and shutdown torque and the bearing temperature at different bearing loads is investigated experimentally. The experiments are accomplished on an automated high-speed test rig which can run at speeds up to 60,000 rpm. Specifying the external bearing load and the rotor speed, this test rig allows for a measurement of the bearing drag torque, the horizontal and vertical displacement of the bearing and of different temperatures of the rotor and the bearing. It is observed that the lift-off speed changes with the bearing load. The experimental results also show that the shutdown torque increases with the bearing load and the assembly preload, whereas the bearing coefficient of friction and the bearing temperature does not significantly change with the assembly preload. The measured coefficient of friction is compared with results from literature which were obtained from pin-on-disk tests at different speeds and loads. It is shown that the discrepancies between the measured coefficient of friction and corresponding values from pin-on-disk tests reported in literature can be traced back to the high dependency of the friction coefficient on the sliding speed.

1. Introduction

Bump-type air foil journal bearings are self-acting aerodynamic bearings. They consist of one or several pairs of bump and top foils, see Fig. 1. While circular one-pad air foil journal bearings show a high load capacity, three-pad designs are characterized by an improved whirl stability, see Ref. [1]. The bump foil is a corrugated foil which induces compliance and friction to the bearing. The top foil is a smooth foil on which the pressure in the air film builds up.

Air Foil bearings have many advantages compared to oil lubricated bearings which arise mainly from the omission of oil and from the elastic foil structure. Air foil bearings are environmentally friendly [2] and can be used in applications where an oil-free medium is mandatory like in air cycle machines or in compressors for fuel cells. Incorporating air bearings instead of oil bearings in machines can significantly reduce the maintenance effort and the weight of the machine because an oil

supply system is not necessary, see Ref. [3]. Furthermore, the maximum operating temperature of oil bearings is limited due to oil degradation, see Ref. [2]. Air bearings, in contrast, have no such temperature limits. The operating temperature of air bearings is only restricted by the maximum tolerable temperature of the surrounding materials and the coatings of the top foil and the rotor.

Due to the elastic foil structure, air foil bearings may compensate larger shaft radial and angular misalignment [4] and tolerate thermal and centrifugal growth of the shaft, see e.g. Ref. [5].

Besides these advantages, air foil bearings have some downsides. As a result of the low air viscosity, air foil bearings have a small load capacity when compared to oil bearings of the same nominal size, see Ref. [6]. Therefore, rotors supported by air foil bearings must either have a larger journal diameter or operate at higher speeds. Thus, air foil bearings are mainly used in low load, high speed applications like in air cycle machines, compressors for fuel cells or in micro gas turbines, see

* Corresponding author. Technical University Darmstadt, Department of Mechanical Engineering, Institute of Applied Dynamics, Otto-Berndt-Straße 2, 64287 Darmstadt, Germany

E-mail address: mahner@sds.tu-darmstadt.de (M. Mahner).

<https://doi.org/10.1016/j.triboint.2019.02.026>

Received 14 September 2018; Received in revised form 13 February 2019; Accepted 15 February 2019

Available online 29 April 2019

0301-679X/ © 2019 Published by Elsevier Ltd.

rig, the load was applied using dead weights. The friction torque was measured via a torque rod and a strain gauge bridge located in the room temperature section of the test rig. The experiments showed that the materials form Ni-Cr and Al oxides at elevated temperatures which led to a reduction in friction. All materials exhibited moderate to high wear indicating the need of solid lubricants on the top foil and the shaft.

DellaCorte [12] used the same test rig as in Ref. [21] in order to analyze the friction and wear properties of an Al_2O_3 pin and an Inconel X-750 pin sliding against a PS300 coated disk at different temperatures. The test results demonstrated that friction and wear increased with temperature for the metal pin, while friction and wear decreased with temperature for the Al_2O_3 pin. At room temperature, the wear and the friction coefficient of the Al_2O_3 pin was higher compared to the metal pin.

Heshmat et al. [17] used a very similar test rig as in Ref. [21], but in a pad-on-disk configuration. The presented test rig could run up to speeds of 50 m/s. The authors analyzed the friction coefficient between an air foil thrust bearing pad with different top foil coatings sliding against a disk with several runner coatings. As a result of the high maximum disk speed, the drag torque after pad lift-off could be measured besides the startup and shutdown torque.

Bhushan and Gray [10] presented the first single bearing device for a partial arc air foil journal bearing. The test rig consists of a ball bearing supported rotor. At the rotor end, a test journal was mounted using a tie bolt. Using an electric motor, the rotor was driven at speeds up to 13,800 rpm via a flat belt transmission. The partial arc air foil journal bearing was installed on the test journal at the free end of the rotor and loaded with deadweights via a cable. The bearing drag torque was measured with a capacitive proximity probe and a calibrated flexure plate at the end of a torque rod which was connected to the bearing sleeve. By the application of quartz heaters near the test bearing, the ambient temperature near the air foil bearing was controlled. Four K-type thermocouples were used to measure the bearing sleeve temperature. Bhushan and Gray [10] evaluated different top foil and journal coatings on the described test rig. The same device was later used by several authors [9,11,13,14] to gain further progress in the development of durable high-temperature foil and journal coatings for air foil bearing applications.

Later, DellaCorte [13] enhanced the test rig of Bushan and Gray for the accomplishment of measurements at temperatures up to 700 °C and rotational speeds up to 70 krpm. Instead of the electric motor and the flat belt transmission used in Ref. [10], the rotor was driven by a turbine. Furthermore, a preloaded load cell instead of the flexure plate was used at the end of the torque rod to measure the bearing drag torque. The bearing load was adjusted by a pneumatic cylinder and measured with a load cell. DellaCorte [13] studied the drag torque and the load capacity of a circular one-pad air foil journal bearing on this test rig. He showed that the drag torque during airborne operation increases linearly with the bearing load and the journal speed. Furthermore, DellaCorte's results exhibit that for the analyzed speed range, the load capacity increases linear with the rotational speed and decreases with temperature mostly due to a softening effect in the elastic foil structure.

DellaCorte [15] investigated the wear and friction of an air foil journal bearing at different loads and temperatures for a huge number (up to 100,000) of 20 s lasting start-stop-cycles using the test rig presented in Ref. [13]. The obtained results demonstrate that the foil and journal wear as well as the startup and shutdown torque increase linear with the bearing load. It was further observed that the startup and shutdown torque decreases with the bearing temperature.

In another study, DellaCorte et al. [37] accomplished experiments on a slightly modified test rig in order to measure air foil bearing performance maps. The modification affects the loading mechanism: Instead of the pneumatic cylinder, cylindrical deadweights are used which are mounted directly onto the bearing sleeve. The performance maps are obtained by plotting the bearing power loss over a modified Sommerfeld number. The modified Sommerfeld number accounts for

the load due to external static and dynamic loads, the bearing preload and loads induced by centrifugal and thermal growth of the journal and the bearing sleeve. The performance map shows a minimum which separates the operating regime of air foil journal bearings in a heavily and lightly loaded region.

Radil and DellaCorte [38] experimentally obtained three-dimensional performance maps by plotting the bearing power loss over the rotational speed and the bearing load. The test rig explained above was extended by a pneumatic cylinder which balanced the deadweight force during the startup and the shutdown. The pneumatic cylinder was not connected to the bearing housing during airborne operation to reduce the measurement error which a slight misalignment in the pneumatic cylinder cable would induce. The obtained performance maps showed that the power loss minimum increases to higher rotational speeds with increasing load thus decreasing the lightly loaded operation region of the bearing.

Kim et al. [23] presented a test rig for the measurement of bearing load, torque and temperature. In this test rig, the air foil journal bearing was placed in the middle of the rotor between two supporting ball bearings. The rotor was driven using an electric motor at speeds up to 15 krpm. The bearing load was applied with a pneumatic cylinder via a cable and a load cell. The torque rod was mounted in the same direction as the loading cable. At the end of the torque rod, a preloaded load cell acquired the transmitted friction force. Bearing temperatures were measured using thermocouples which were placed in the bearing sleeve. The presented results showed that the shutdown torque is larger than the startup torque and that both increase slightly with the number of start-stop cycles, whereas the bearing maximum and minimum temperature are nearly constant over the number of start-stop cycles.

Bruckner and Puleo [24] experimentally investigated the effect of pressure and temperature on the performance of air foil journal bearings. The tests were performed on two test rigs: An ambient pressure test rig for experiments at pressures from 0.1 – 2.5 bar and a high pressure test rig for investigations at pressures from 0.1 – 48 bar. The ambient pressure test rig was quite similar to the one used in Ref. [16] with modifications regarding the loading and drive mechanism. In Ref. [24], an electric motor instead of a turbine was used to drive the test journal at speeds up to 30,000 rpm. The high pressure test rig had several simplifications compared to the ambient pressure test rig regarding the loading mechanism. With this two devices, Bruckner and Puleo [24] obtained performance maps for air foil journal bearings at different temperatures and pressures. The results indicated that the load capacity and the power loss increase with pressure, while the load capacity decreases with temperature, as already observed by DellaCorte [13].

Conlon et al. [25] presented a test rig for highly loaded air foil journal bearings. The turbine driven rotor was supported by ball bearings. The air foil journal bearing floated on the rotor between the ball bearings. A static load was applied to the air foil bearing using an aerostatic bearing. The drag torque was measured with a torque arm and a load cell. With this test rig, Conlon et al. measured the load capacity of a first generation air foil journal bearing. In a later study [39], Conlon et al. used this test rig to measure 3D performance maps of first and second generation air foil bearings. The results indicate that the operating region of first generation air foil bearings is smaller than that of second generation bearings.

Kim et al. [2,26] experimentally investigated the performance, the startup and shutdown behavior as well as the thermal behavior of hybrid air foil journal bearings with a single bearing test rig. They showed that the startup and shutdown friction is significantly decreased by the hybrid bearing operation. In contrast to not externally pressurized bearings, it was shown that the lowest temperature occurs in the bearing mid plane, see Ref. [33] for comparison.

Chirathadam [28] presented a test device for air foil journal bearings whose test journal was driven by a turbocharger. The load was applied using a positioning table. Again, a preloaded torque arm was used for the transmission of the friction force. A calibrated spring and a

proximity probe at the end of the torque arm acquired the transmitted friction force. This design is advantageous since it decreases the interaction between the cross coupled bearing stiffness and the transmitted friction force. San Andrés et al. [34,40,41] used this device in part with slight modifications to study the performance of metal mesh foil bearings. In Ref. [34], the bearing sleeve temperature of the metal mesh foil bearing was measured besides the drag torque. It was observed that the temperature increases with load and speed, as already obtained by other authors [32,33]. San Andrés et al. [40] compared the performance of a metal mesh foil bearing with that of a bump-type foil bearing. They obtained a larger startup torque for the metal mesh foil bearing compared to the bump-type foil bearing, while the drag torque in airborne operation is nearly the same. This behavior could be explained by the larger preload of the metal mesh foil bearing. A comparison between measured and predicted drag torque in Ref. [41] showed a good agreement in the airborne operation region. In Ref. [42], San Andrés and Kim predicted also the startup and shutdown torque for an air foil journal bearing using the model for the elastic foil structure presented in Ref. [43].

Furthermore, San Andrés and Norsworthy [44] experimentally evaluated the effect of a mechanical preload, induced by shims underneath the bump foil, on the drag torque and the lift-off speed of air foil journal bearings. The experiments were performed on the test rig presented in Ref. [28]. In contrast to the assembly preload investigated in the paper at hand, shims underneath the bump foil locally decrease the radial clearance of the bearing. This leads to a wedge which preloads the bearing aerodynamically leading to an increase in the fluid film stiffness, while the structural foil stiffness at small loads is not changed significantly, see Ref. [18]. In their experiments, San Andrés and Norsworthy [44] showed that the startup torque increases with the shim thickness, whereas the lift-off speed and the drag torque during airborne operation are not affected significantly. From this result it can be concluded that the shims mechanically preload the bearing.

Rudloff et al. [29] experimentally analyzed the startup and shutdown torque of a first generation air foil journal bearing at different loads. They mounted the air foil bearing sleeve inside a ball bearing in order to decouple the loading mechanism from the torque measurement mechanism. As the results show, this configuration is not suitable for the measurement of the bearing drag torque after lift-off since the friction torque of the ball bearing is larger than that of the investigated air foil bearing.

Heshmat et al. [1] described a test rig which can either be used for rotor dynamic measurements or drag torque measurements. Howard [30] presented a rotor dynamic test rig in which the drag torque could be measured by torque rods attached to the two air foil bearing sleeves. Like in Ref. [29], the bearing sleeves were mounted in ball bearings. This led to the same errors when measuring the bearing drag torque during airborne operation. Kim and San Andrés [5] and Lai [31] measured the coastdown time of a rotor supported by air foil journal bearings in order to qualitatively compare the frictional behavior of different bearing designs. Kim and San Andrés [5] showed that the coastdown time of a shim-preloaded bearing is smaller than that of a not preloaded bearing thus indicating an increased shutdown torque, see also [44].

Salehi et al. [32] investigated the thermal behavior of a large air foil journal bearing experimentally with a single bearing device. For a given speed and load, Salehi et al. [32] measured the temperatures at the backside of the top foil using K-type thermocouples. The experimental results indicate that the top foil temperature increases both with the bearing load and the rotor speed. Latter had a more significant influence on the bearing temperature than the bearing load. It was obtained from a numerical model that about 75 – 80 % of the heat which is generated in the air film is conducted into the surrounding structure and the cooling flow while the rest leaves the bearing by the side flow.

Radil and Zeszotek [33] measured the temperature profile of a circular one-pad air foil journal bearing at different loads and speeds

using the test rig of DellaCorte [22]. They used nine K-type thermocouples at the backside of the bump foil. The results showed that the bump foil temperatures increase both with speed and load. It was observed, that the rotational speed had a more significant influence on the bearing temperature than the bearing load. The measured temperatures were fairly symmetric in axial direction. Furthermore, the thermal gradient in axial direction was larger than in circumferential direction.

Kim et al. [35] investigated the thermal behavior of air foil journal bearings with different radial clearances experimentally using a single bearing device. They used twelve thermocouples at the bearing housing. The bearing clearance was obtained by a hysteresis measurement with the same test rig. The results showed that the temperature is higher at the bearing mid plane compared to the bearing edges. As expected, the temperatures slightly increase with a decreasing bearing clearance.

Keun and San Andrés [45] analyzed the effect of a secondary cooling flow through the foil structure on the thermal and rotor dynamic behavior of a rotor supported by two air foil journal bearings experimentally and numerically. They measured the temperatures with thermocouples at both bearing sleeves, at the cooling plenum and at a cartridge heater which was used to heat the hollow rotor. It was shown that the bearing and the cooling plenum temperature increase with decreasing cooling flow. For very large cooling flows, no further reduction in the bearing temperature was achieved. The influence of the cooling flow on the rotor dynamic behavior was not significant.

In a later study, Keun and San Andrés [8] used the above test rig to investigate the thermal failure of an uncooled air foil journal bearing. They heated the rotor via the cartridge heater until a thermal-runaway occurred which led to a bearing seizure and a catastrophic bearing failure.

Shrestha et al. [36], accomplished an experimental investigation on the effect of a radial injection cooling on the thermal behavior of three-pad air foil journal bearings. In their study, a three-pad air foil journal bearing was cooled by a radial cooling flow which was injected between the three pads. They showed that the radial cooling flow was as effective as an axial cooling flow. But, in contrast to the axial cooling flow, the radial flow showed no saturation at higher flow rates.

In this paper, the effect of a mechanical assembly preload on the hysteresis, the drag torque, the lift-off speed and on the thermal behavior of three-pad air foil journal bearings is investigated experimentally, see Fig. 1 and 1. The experiments are accomplished on an automated high-speed test rig which can run at speeds up to 60 krpm. From the shutdown torque measurements, the coefficient of friction and the assembly preload of the bearings can be obtained. The coefficient of friction is compared with results from pin-on-disk tests at different speeds and loads available in the literature. Furthermore, the bearing lift-off speed is determined from Stribeck curves which are obtained for different bearing loads and assembly preloads. To quantify the influence of the assembly preload on the thermal behavior of air foil journal bearings, the temperature at several bearing locations is measured for differently preloaded bearings.

The main contributions of this work are:

- Presenting a high-speed test rig for the simultaneous measurement of all relevant bearing quantities: the load capacity, the drag torque, the stiffness in two perpendicular directions, the friction loss (damping) and the temperature of all bearing components.
- Systematic comparison of the drag torque of differently preloaded air foil journal bearings.
- Evaluation of the influence of the bearing load and of the assembly preload on the bearing lift-off speed.
- Explanation of the discrepancies between the sliding torque measured in high-speed test rigs and the values obtained in pin-on-disk tests.
- Comparison of the thermal behavior of differently preloaded bearings.

The air foil journal bearing is located in the middle of the rotor. In order to allow for a simple and fast assembling and disassembling of the foil bearing on the rotor, the bearing sleeve is divided into two parts which are aligned and fixed by two cylindrical bolts and two screws. Measurements of the cylindrical shape of the bearing sleeve inner surface with a micrometer after repeated assemblies have proofed a very good positioning repeatability. The bearing sleeve has a total of ten radial threaded holes to allow a torque rod to be attached to the bearing sleeve at different angular locations. A horizontal cable connects the free end of the torque rod with a strain gauge based load cell. Thereby, the drag torque acting on the foil bearing can be measured. Furthermore, two serial combined springs are attached to the free end of the torque rod. These springs preload the load cell. The preload force acting on the load cell due to the springs is 1.357 N. The load cell has a sensitivity of 1.000505 V/N and a linearity error of 0.02 %. A vertical load is applied to the bearing sleeve via a second cable connecting the bearing sleeve end of the torque rod with another load cell, which is attached to a hybrid linear actuator. This actuator has a minimum macro step size of 1.5 μm which can be subdivided into 64 micro steps. The strain gauge based load cell has a sensitivity of 0.09994 V/N and a linearity error of less than 0.2 %. The load is controlled by adjusting the hybrid linear actuator step size using a P-controller design in the measurement processing software LabVIEW.

The rotor motion is measured by two perpendicular eddy current sensors which are located at the free end and the drive end of the rotor. A perpendicular pair of eddy current sensors measures the horizontal and vertical displacement of the bearing sleeve. Two piezoelectric accelerometers, one at the drive end ball bearing pair and another one at the spindle, are used to monitor the current machine operation. The eight signals from the two load cells, from the four eddy current sensors and from the two accelerometers are acquired at a sampling frequency of 20 kHz with a measuring board using an anti-aliasing filter, simultaneous sample and hold functionality and an analog-digital converter.

Besides these predominately mechanical quantities, the temperature of the foil bearing, of the rotor and of the angular ball bearing housings are measured. The temperature of the foil bearing is measured at the top and bottom of the bearing sleeve, at the backside of the loaded top foil between the fourth and the fifth bump and at the backside of the fifth bump of each bump foil using T-type thermocouples, see Fig. 3. The same thermocouples are used for the measurement of the temperature at the angular ball bearing housings. These thermocouples have a measurement error of 0.75 %, but at least 1 °C. The thermocouples are attached to the surfaces with special adhesive strips.

The rotor temperature is measured with two infrared thermometers in an axial distance of approximately 6 mm to the air foil bearing sides. Each infrared thermometers has a lens to reduce the measurement diameter on the rotor to 5.92 mm when located in a radial distance of 17 mm. The infrared thermometers have a system accuracy of $\pm 1\%$ or $\pm 1\text{ °C}$ and a repeatability error of $\pm 0.5\%$ or $\pm 0.5\text{ °C}$. The data acquired by the infrared thermometers are processed in a separate software provided with the hardware. Since the change in temperature is significantly slower than the change of the mechanical quantities, smaller sampling frequencies are used for the acquisition of the temperatures.

3. Test specimen

In this paper, two three-pad air foil journal bearings with different assembly preloads are investigated. The two bearings will be referred to as a ‘lightly’ and a ‘heavily’ preloaded bearing. The bearings consist of three pairs of bump and top foil, see Fig. 1. As can be seen from Fig. 1, each top and bump foil is free at one end and fixed in a mounting suspension at the other end. In order to decrease the startup and shutdown torque, the direction of rotation of the rotor is from the free end to the fixed end of the top foils. The bump foils are mounted opposite to the top foils. The bump heights increase by about 24 μm from

Table 1

Nominal parameters of the lightly and heavily preloaded three-pad air foil journal bearing. The two bearings differ only in their nominal top foil radii.

Overall bearing parameters	
Bearing width b	27 mm
Rotor radius r_r	15 mm
Bearing sleeve inner radius r_i	15.789 mm
Number of pads	3
Top and bump foil parameters	
Top foil radius (lightly preloaded) r_{li}	28.4 mm
Top foil radius (heavily preloaded) r_{lh}	57.3 mm
Top foil length L_t	30 mm
Number of bumps per bump foil	9
Bump foil radius r_b	30 mm
Segment length a_{se}	0.65 mm
Minimum bump height at the fixed end h_{bmin}	0.554 mm
Maximum bump height at the free end h_{bmax}	0.578 mm
Bump pitch a_p	3.15 mm
Top and bump foil thickness H	100 μm
Top foil coating thickness H_{cot}	20 μm

the fixed end to the free end creating an aerodynamic wedge when all bumps are in contact with the top foil and the bearing sleeve. As shown in Fig. 1, the pads are numbered opposite to the direction of rotation.

Top and bump foils are made from X10CrNi18-8 (1.4310), a stainless spring steel, which can be used at temperatures up to 250 °C. The bearing sleeve is made from the stainless steel X5CrNiMo17-12-2 (1.4401).

As already described in section 1, the assembly preload is introduced by using bump and top foils whose initial undeformed radii are significantly larger than the inner radius of the bearing sleeve. The two bearings investigated in this study differ only in their nominal top foil radii creating different assembly preloads, while the nominal bump foil radius and the preload induced by the bump foil shape are equal. The dimensions of the two bearings under investigation are listed in Table 1.

The top foils are coated with a 20 μm PTFE layer to reduce friction and wear during sliding contact at the rotor startup and shutdown, see Ref. [46]. This coating has a maximum operating temperature of 285 °C, which is higher than the suggested maximum temperature of the stainless steel from which the top foils are made. The PTFE coating is realized by spraying PTFE onto the top foil surface at a process temperature of about 250 °C.

To further reduce friction and wear, the rotor is coated with a 2 – 4 μm diamond-like carbon (DLC) layer. This coating is applied to the rotor surface by PVD sputtering at a process temperature of 150 °C. The maximum operating temperature of this coating is 400 °C. The rotor radius listed in Table 1 already includes the diamond-like carbon coating thickness. The DLC-coating has been chosen since the friction coefficient of PTFE on diamond-like carbon is even smaller than the friction coefficient of PTFE sliding against itself, see Ref. [47]. For a sliding speed of 5.86 mm s^{-1} and a contact pressure of 0.97 MPa, Yang et al. [47] obtained a friction coefficient of about 0.035 for a PTFE/diamond-like carbon contact in a pin-on-disk test.

4. Test procedure

The test procedure for each bearing comprises four steps: A sequence of start-stop cycles to assure that the top foil and rotor coating are broken in, the measurement of the drag torque of the run-in bearing, the acquisition of the steady state bearing temperatures and a static hysteresis measurement at zero running speed to quantify the effect of the assembly preload on the bearing stiffness and damping.

The bearing test starts with a run-in procedure on the described test

rig. This is realized as a sequence of start-stop cycles at several bearing loads from 0 – 30 N in 5 N-steps. For all experiments, the load is applied in a load-on-pad configuration on the first pad, see Fig. 3. One start-stop cycle comprises a 13.33 s lasting acceleration up to 40 krpm, followed by a constant operation regime at this speed for about 10 s and ends with a controlled deceleration over 13.33 s to zero running speed. At each load, the start-stop cycles are repeated until no significant change in the temperature rise of the rotor is observed anymore. Fig. 4 shows exemplary the rotor temperature during the run-in procedure of the heavily preloaded bearing at an externally applied bearing load of 20 N. Note, that the first and second cycles start at smaller rotor temperatures compared to the subsequent cycles. As shown in Fig. 4, the maximum rotor temperature at both bearing sides differ slightly by about 2 – 3 K caused by a small misalignment of the rotor/foil bearing assembly.

In the second step, the drag torque of the run-in bearings is measured with the described test rig. Note, that no thermocouples are used in this step at the bump and top foils to assure that the torque measurement will not be affected by an eventual increase in the preload by the thermocouples.

As mentioned in section 1, the bearing load applied via the vertical cable will have an effect on the measured friction force even when the rotor does not rotate. This effect is caused by the cross-coupled stiffness of the air foil journal bearing. The cross-coupled stiffness induces a horizontal movement s_{by} of the bearing when a vertical force is applied, see Fig. 5. Fig. 5 shows the measured and smoothed horizontal displacement of the heavily preloaded air foil journal bearing at a rotor speed of $n_r = 35$ krpm when the bearing is quasi-statically subjected to a steadily increasing load (up to 30 N). For the measurement whose results are collected in Fig. 5, the positioning preload-springs are not connected to the torque rod. To assure that the bearing can move freely in the horizontal direction, the horizontal cable is fixed at the torque rod in a way that it is saggy when the torque rod stands perfectly vertically. As can be seen in Fig. 5, the horizontal displacement increases to a maximum value of about $18 \mu\text{m}$ at a bearing load of 30 N. It should be mentioned that for loads larger than about 5 N, the displacement-force-relationship is nearly linear.

During the drag torque measurement, this horizontal movement of the bearing sleeve is restricted by the horizontal cable, see Fig. 3. Thereby, a reaction force will act on the torque measuring load cell producing an apparent torque signal. To compensate this effect properly, the relationship between the bearing load and the apparent torque of the bearing at zero running speed is measured before the drag torque measurement with the running rotor is accomplished. This is realized by quasi-statically applying a periodic load of $F_b = 30 \text{ N}/2 \left(1 - \cos\left(\frac{2\pi}{20 \text{ s}} t\right)\right)$ over four periods to the bearing using the hybrid linear actuator. Again, each period lasts 20 s. Afterwards, the measured load and apparent torque are smoothed by the use of a moving average approach with an averaging interval of 0.5 s. The relationship between the bearing load and the apparent torque is obtained from the last pulling phase of the periodic loading cycle. Subsequently, this relationship is fitted with a smoothing spline. Fig. 6 shows the measured and the smoothed and fitted relationship between the bearing load and the apparent torque for the heavily preloaded air foil journal bearing at zero running speed. As can be seen from the smoothed and fitted curve, the relationship is nearly linear. The obtained relationship is used to eliminate the apparent torque from the drag torque measurement acquired during rotor operation. For the lightly preloaded bearing, the apparent torque is so small that a compensation is not necessary.

The bearing startup and shutdown torque as well as the bearing drag torque in airborne operation is measured during a slightly different start-stop cycle as compared to the cycle used in the run-in procedure. While the acceleration and controlled deceleration times are the same, the operation time at the maximum speed of 40 krpm is 1.67 s

longer. Since the bearings are already run in, the start-stop cycle is only accomplished once. The bearing torque is measured for the two bearings at loads from 0 – 30 N in 5 N-steps. At each bearing load, the measurement is started at an initial rotor temperature between 22 – 26 °C. Again, the acquired bearing torque and load are smoothed applying a moving averaging approach. For the heavily preloaded bearing, the apparent torque is eliminated from the measured drag torque afterwards by using the measured curve shown in Fig. 6.

In the third step, the thermal behavior of the lightly and the heavily preloaded bearing under steady state conditions is analyzed for bearing loads up to 30 N in steps of 10 N. The locations of the temperature measurement points at the air foil journal bearing and the rotor are explained in detail in section 2, see Fig. 3. The temperature measurements are accomplished at a rotor speed of $n_r = 35$ krpm. Again, the measurements are started at a rotor temperature between 22 – 26 °C. At the rotor startup, the air foil journal bearing is not subjected to a load. When the final rotor speed is reached, the particular load is applied to the bearing. The measurement is realized until all components reach steady state temperatures, see Fig. 7. As shown in Fig. 7 for the heavily preloaded bearing at a load of 10 N, all components approach steady state temperatures after about half an hour ($t \approx 1800$ s). These temperatures are used for characterizing the thermal behavior of the two differently preloaded air foil journal bearings. To compare the temperature of the different components at different loads for the two bearings, the temperature difference ΔT is calculated by subtracting the ambient temperature T_{amb} from the absolute (steady state) temperature T .

For the purpose of comparing the stiffness and damping of the two differently preloaded bearings, a static hysteresis measurement at zero running speed is accomplished in the fourth step of the test procedure. This measurement is performed on a second test rig, which allows for the measurement of a full hysteresis cycle. is described in detail in Refs. [19,20]. In this test rig, a horizontal, linear bearing movement along a linear guiding is automatically applied by a hybrid linear actuator. The acting horizontal force on the shaft F_{hor} and the relative bearing displacement s_{bhor} are measured by a strain-gauge based load cell and an eddy current sensor. With this device, static hysteresis curves for the both bearings are measured. The direction of motion is automatically reversed when the shaft force reaches 30 N. The procedure is accomplished until the hysteresis curve describes a closed loop. Since the drag

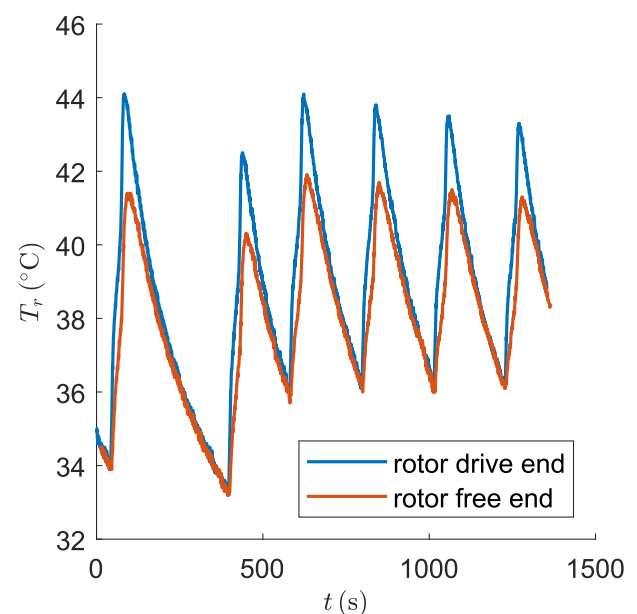


Fig. 4. Rotor temperature during run-in procedure of the heavily preloaded bearing at a bearing load of 20 N.

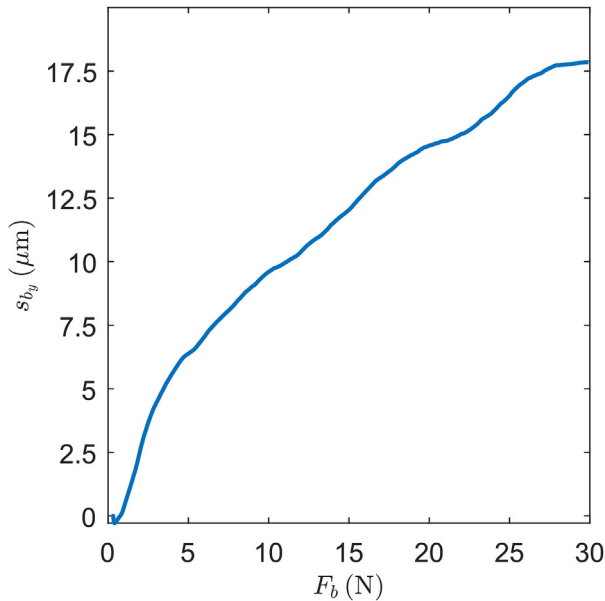


Fig. 5. Horizontal displacement of the heavily preloaded bearing over the bearing load.

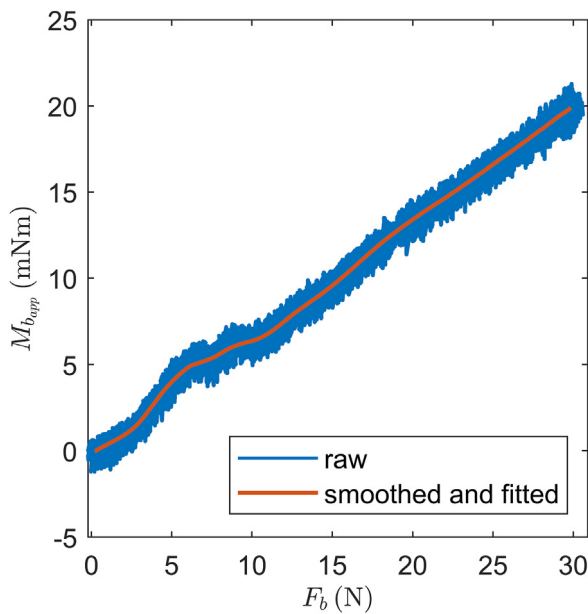


Fig. 6. Measured as well as smoothed and fitted relationship between the bearing load and the apparent torque for the heavily preloaded bearing at zero running speed.

torque measurements are accomplished with the load acting on the first pad in a load-on-pad configuration, the bearing sleeve is mounted in the housing of the hysteresis device such that the center of the first pad is in coincidence with direction of motion. A positive displacement is defined as a relative displacement of the rotor in the direction of the center of the first pad. Negative values correspond to a motion in the opposite direction, between the second and the third pad.

5. Results and discussion

Based on the experimental results, the influence of the assembly preload on the bearing properties is shown in this section. First, the stiffness and damping of the two differently preloaded bearings are compared. Afterwards, the drag torque and the lift-off speed of the

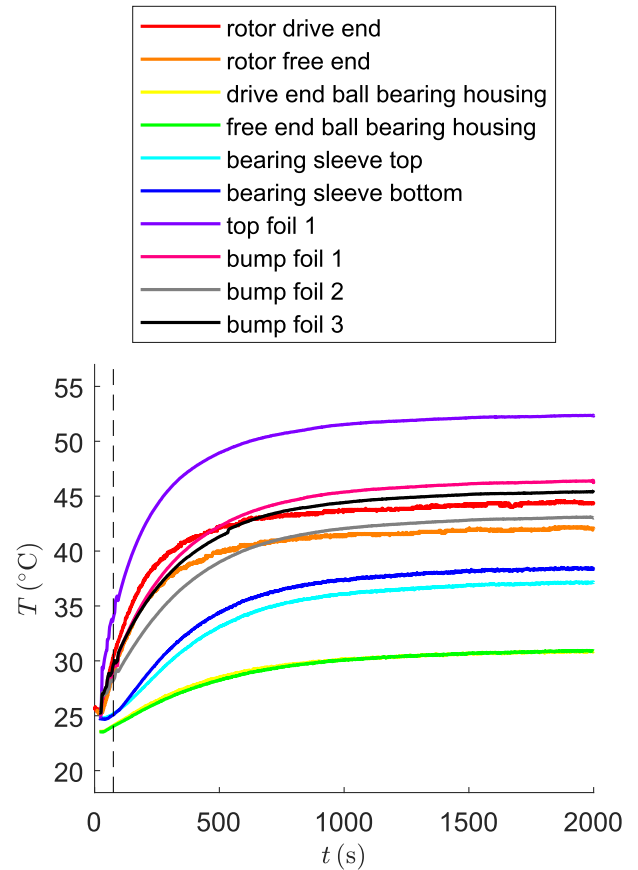


Fig. 7. Measured temperature increase during the steady state test of the heavily preloaded bearing at a load of 10 N

bearings are analyzed. In the last step, the thermal behavior of the air foil journal bearings is investigated.

5.1. Bearing stiffness and damping

Fig. 8 shows the hysteresis curves and the stiffness for the lightly and the heavily preloaded bearing over two periods. In Fig. 8a), the operation regime of the bearing under normal loads is marked. For larger displacements, which may appear under shock loads, a significant rise in the bearing stiffness is obtained. This results from the increasing number of bumps coming into contact either with the bearing sleeve or the top foil, see Fig. 8a). As can be seen in Fig. 8a), both hysteresis curves are fairly closed. The horizontal distance between the bearing displacement at the maximum and the minimum bearing force equals approximately 247 μm for the lightly preloaded bearing. Radil et al. [7], who used a bearing with a clearance between top foil and rotor in the aligned condition, defined this distance as a diametrical clearance. Nevertheless, one has to keep in mind that for the investigated bearing there is no clearance between the top foil and the rotor due to the assembly preload. In contrast, the defined radial distance here corresponds with the distance between the top foil and the bump foil and with the distance between the bump foil and the bearing sleeve in the aligned assembly configuration. Compared to the lightly preloaded bearing, the horizontal distance for the heavily preloaded bearing is only about 5 μm smaller. This indicates that the higher assembly preload does not significantly influence the described diametrical distance.

While the diametrical distance is nearly identical, the slopes of the hysteresis curves in the region before the abrupt rise in bearing stiffness are significantly different. As expected, the highly preloaded bearing shows a larger stiffness in this region. For a better quantitative

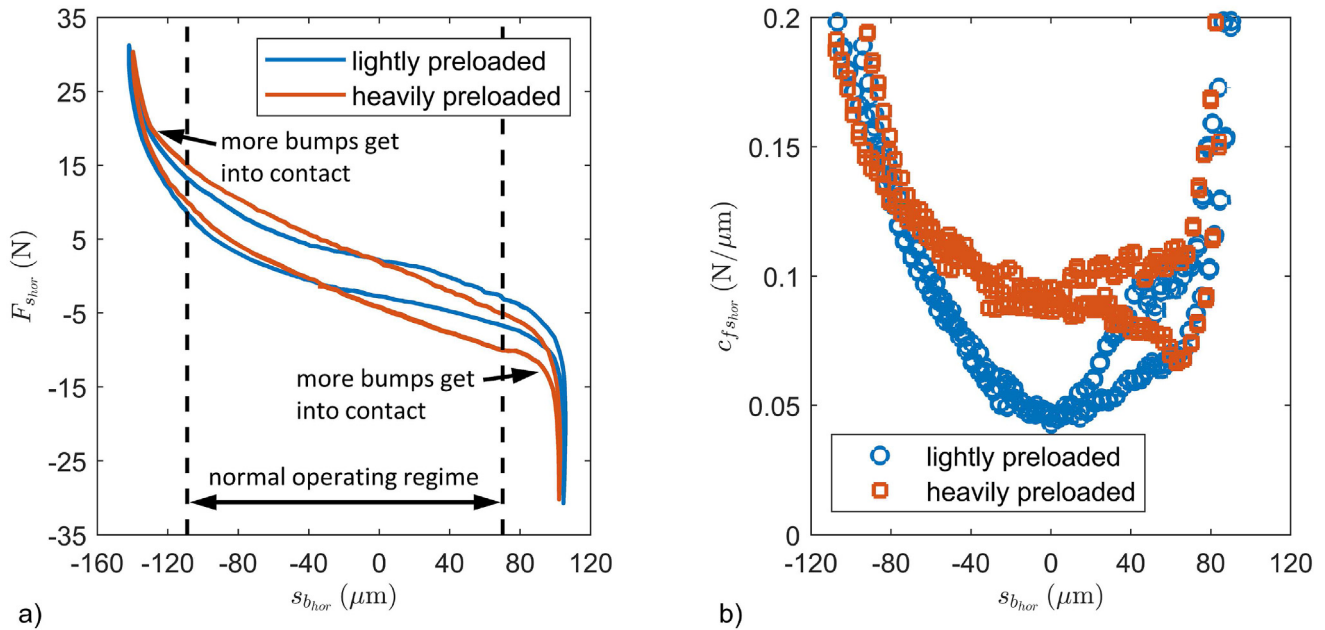


Fig. 8. Measured hysteresis curves (a) and stiffness (b) for the lightly and the heavily preloaded bearing.

comparison, Fig. 8b) presents the obtained stiffness from the hysteresis curves for the lightly and the heavily preloaded bearing. The stiffness is calculated from the measured hysteresis curves by the use of first-order central differences. Note, that only stiffness values up to $c_b = 0.2 \text{ N}/\mu\text{m}$ have been plotted in order to emphasize the influence of the assembly preload within the normal operating regime. As can be seen from the figure, the stiffness for small loads and displacements increases significantly with the assembly preload. The stiffness at zero relative bearing displacement increases from about $c_b = 0.045 \text{ N}/\mu\text{m}$ for the lightly preloaded bearing to $c_b = 0.086 \text{ N}/\mu\text{m}$ for the heavily preloaded bearing. This is an increase by 91.1%. While the stiffness differs for small loads and bearing displacements, the stiffness of the lightly and the heavily preloaded bearing are approaching for higher loads and displacements. It can be concluded, that the foil structural stiffness gets more and more dominated by the bump foil as the number of bumps coming into contact with either the top foil or the bearing sleeve steadily increases, see Fig. 8.

The area enclosed by the hysteresis curves in Fig. 8a) represents the energy dissipated during one cycle. The dissipation of energy originates from the friction between the top foil and the bump foil, between the bump foil and the bearing sleeve as well as from the friction between the top foil and the rotor. The energy dissipated during one cycle corresponds with the bearing damping. The dissipated energy W_D can be calculated with the ring integral

$$W_D = \oint F_{b_{hor}} ds_{b_{hor}} \quad (1)$$

In this study, the ring integral in Eq. (1) is approximated by a trapezoidal quadrature method. This approach is applied over the two hysteresis cycles for each bearing and the result is halved afterwards to yield the dissipated energy during one cycle. The dissipated energy of the heavily preloaded bearing equals 1.3 mJ, while for the lightly preloaded bearing a dissipated energy of 1.1 mJ is obtained. This corresponds to an increase of about 18.2% due to the larger assembly preload.

Concluding, the increase in the bearing preload significantly increases the bearing stiffness and the dissipated energy during one cycle, while the diametrical distance in the hysteresis curves stays nearly the same.

5.2. Bearing drag torque and lift-off speed

Fig. 9 exemplarily shows the rotor speed and the bearing drag torque of the heavily preloaded bearing at a bearing load of $F_b = 10 \text{ N}$ over one start-stop-cycle. The characteristic points of the torque curve are numbered and will be explained in detail hereafter.

When the rotor starts to accelerate (at $t \approx 76 \text{ s}$), the bearing drag torque increases sharply to a local peak of about 159 mNm (point 1 in Fig. 9). Up to the peak, pure boundary lubrication (dry friction) between the rotor and the top foils occurs. The peak value is defined as the startup torque, see e.g. Refs. [13,44]. Between point 1 and point 2 in Fig. 9, the bearing operates in the mixed lubrication regime. The mixed lubrication regime is characterized by a decreasing drag torque with increasing rotational speed, see Fig. 9. Point 2 depicts a drag torque local minimum of about 2.3 mNm. This point defines the transition from the mixed lubrication to the fluid film lubrication regime, see Ref. [44]. The corresponding rotor speed is the bearing lift-off speed. For the presented case, the bearing lift-off occurs at approximately 22.5 krpm. After this point is passed, the drag torque increases with the rotational speed. This behavior is characteristic for the fluid film lubrication regime. When the maximum rotor speed of 40 krpm is reached, the drag torque has a nearly constant value of about 3.7 mNm (point 3).

An equivalent behavior occurs in the deceleration phase of the start-stop cycle: The drag torque decreases with decreasing rotational speed up to point 4 (2.7 mNm). The corresponding speed is the touch-down speed, which equals about 28.9 krpm. After passing this point, mixed lubrication occurs again and the drag torque steadily increases up to a peak value of approximately 317 mNm (point 5). This peak defines the shutdown torque, see e.g. Ref. [13]. Again, boundary lubrication occurs for larger speeds and the drag torque sharply decreases.

The variation in torque before rotor startup and after rotor shutdown is induced by the spindle speed controller.

As can be seen from Fig. 9, the startup and shutdown torque are significantly different. This behavior results from the abrupt acceleration of the bearing sleeve when the rotor speeds up. When applying the moment of momentum principle to the bearing sleeve, one obtains the relationship

$$M_{b_{acc}} = M_b - \theta_{bs} \ddot{\phi}_{bs} \quad (2)$$

for the measured drag torque $M_{b_{acc}}$ during the bearing sleeve

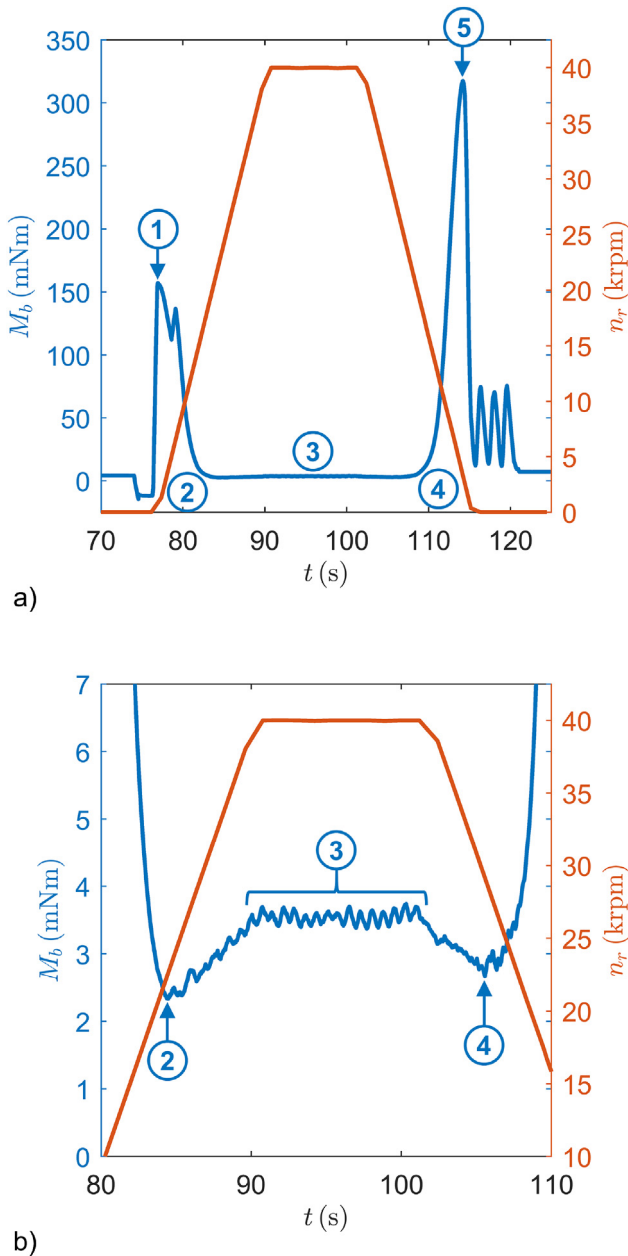


Fig. 9. Measured drag torque and rotational speed of the heavily preloaded bearing at a bearing load of $F_b = 10\text{ N}$: a) Complete start-stop cycle, b) Zoom for emphasizing the drag torque after bearing lift-off.

acceleration. Herein, $\hat{\theta}_{bs}$ and $\hat{\varphi}_{bs}$ denote the mass moment of inertia and the angular acceleration of the bearing sleeve including the torque rod. The quantity M_b is the correct drag torque of the air foil journal bearing. As stated in Eq. (2), the measured drag torque is reduced by the moment of inertia. This effect is known in literature. For instances, Kim et al. [2] measured the acceleration of the torque rod in order to compensate the moment of inertia. At the rotor shutdown, this effect does not appear since no bearing sleeve acceleration occurs. For that reason, the bearing shutdown torque for the two different bearings is used for characterizing the dry friction of the differently preloaded bearings.

Subsequently, the lift-off speed (point 2 in Fig. 9) and the shutdown torque (point 5 in Fig. 9) of the lightly and the heavily preloaded bearing are compared.

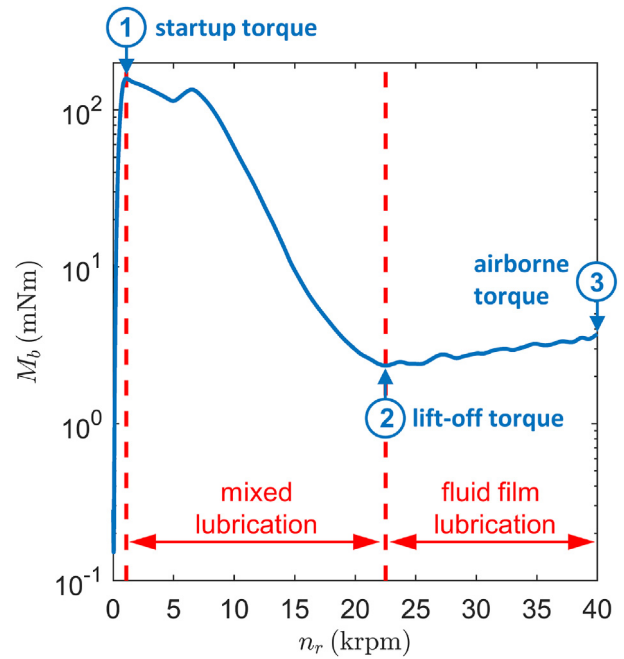


Fig. 10. Measured Stribeck curve of the heavily preloaded bearing at a bearing load of $F_b = 10\text{ N}$

5.2.1. Bearing lift-off speed

As stated in section 5.2, the bearing lift-off speed is defined as the speed where the transition between the mixed and the fluid film lubrication regime occurs (point 2 in Fig. 9). At the transition point, a local minimum in the bearing drag torque is observed. In order to obtain the lift-off speed, the relationship between the drag torque and rotor speed is smoothed and fitted by a smoothing spline, first. Afterwards, the local minimum is calculated from the smoothing spline.

Fig. 10 shows the smoothed and fitted relationship between the bearing drag torque and the rotor speed in the acceleration phase of the rotor for the heavily preloaded bearing at a bearing load of $F_b = 10\text{ N}$. The depicted curve is called Stribeck curve. Note, that the ordinate in Fig. 10 is log-scaled to present the values of the drag torque during rotor startup and in airborne operation. The bearing drag torque during these operations differ by about two order of magnitudes, see Fig. 10. Again, the characteristic points of the depicted Stribeck curve are marked according to the points in Fig. 9. Furthermore, the mixed and fluid film lubrication regimes are highlighted. Boundary lubrication occurs for rotational speeds below 1,100 rpm.

The bearing lift-off speed can easily be obtained from the Stribeck curve by determining the location of the local drag torque minimum. For the presented case in Fig. 10, the bearing lift-off speed equals 22.5 krpm, see section 5.2. The described procedure for determining the bearing lift-off speed is accomplished for the lightly and the heavily preloaded bearing at different bearing loads.

Fig. 11 depicts the bearing lift-off speed for the lightly and the heavily preloaded bearing over the bearing load. As shown in Fig. 11, the lift-off speed of the lightly and the heavily preloaded bearing change with the bearing load. For the lightly preloaded bearing, the lift-off speed increases nearly linearly with the bearing load. The bearing lift-off speed of the lightly preloaded bearing is fitted using a linear regression model, see Fig. 11. For the heavily preloaded bearing, the bearing lift-off speed is nearly constant at bearing loads between $F_b = 5\text{ N}$ and $F_b = 20\text{ N}$. At increasing bearing loads, a significant rise in the lift-off speed is observed.

As shown in Fig. 11, the lift-off speed of the heavily preloaded bearing is smaller compared to the lift of speed of the lightly preloaded bearing for bearing loads larger than 0 N. This might be traced back to

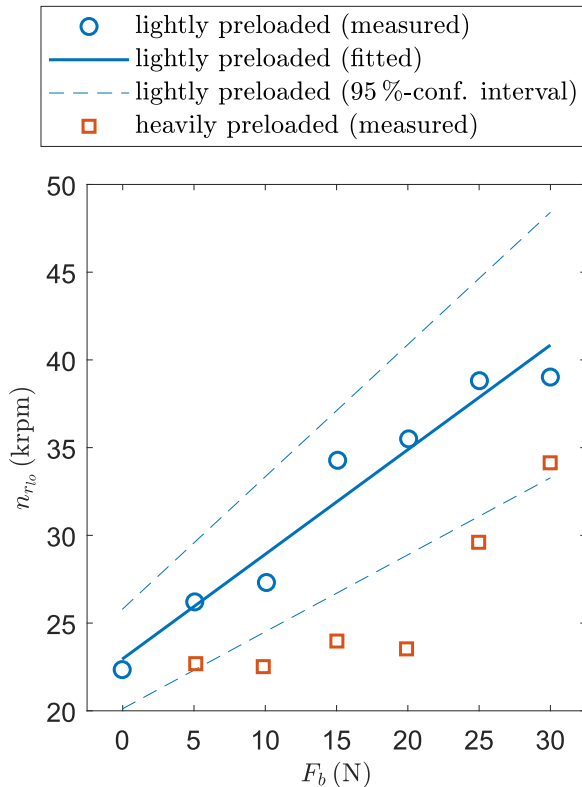


Fig. 11. Measured and fitted lift-off speed for the lightly and the heavily preloaded bearing over the bearing load.

the larger initial top foil radius of the heavily preloaded bearing. In the assembly configuration, the larger top foil radius could improve the air inlet at the top foil leading edge since the gap between top foil and rotor is larger. In comparison, San Andrés and Norsworthy [44] obtained only slight differences in the lift-off speed of differently shim-preloaded air foil journal bearings.

5.2.2. Bearing shutdown torque

Fig. 12 shows the measured and linear fitted shutdown torque of the lightly and the heavily preloaded bearing over the bearing load. The coefficient of determination of the linear regression for the lightly and the heavily preloaded bearing are 0.969 and 0.965, respectively. Thus, the shutdown torque of both bearings increases nearly linearly with the bearing load as already observed by DellaCorte et al. [15]. As expected, the shutdown torque of the heavily preloaded bearing is larger compared to the lightly preloaded bearing. While the larger assembly preload leads to an increase of 91.1 % in the bearing stiffness, like shown in section 5.1, the rise in the shutdown torque at zero bearing load is smaller (about 17.9 %).

On the other hand, the slope of the curves are nearly the same. From the slope of the curves the coefficient of friction can be obtained, see Ref. [15]. This is done by dividing the slope by the rotor radius. The resultant coefficient of friction from the fitted curves are $\mu_{trl} = 0.42$ for the lightly preloaded bearing and $\mu_{trh} = 0.39$ for the heavily preloaded bearing. Since both values lie inside each others 95 %-confidence interval, the measured difference in the coefficient of friction is not statistically significant. This is plausible because the same top foil and rotor coatings are used in both bearing tests. The obtained coefficient of friction are significantly larger than the values reported for instances by Yang et al. [47] for the same surface pairing. As stated in section 3, they measured a coefficient of friction of about 0.035 between PTFE and diamond-like carbon in a pin-on-disk test at a sliding speed of 5.86 mm s^{-1} and a contact pressure of 0.97 MPa. Wagner and Harold [11] first reported the discrepancies between the friction values

measured in an air foil journal bearing test rig and the ‘generally accepted values’ [11] for certain surface pairings. They called the coefficient of friction measured within their study as apparent friction and traced the discrepancies back to the elastic foil structure.

Contrary to their hypothesis, the discrepancies result from the strong dependency of the friction on the sliding speed. While the friction values stated in literature are often obtained in pin-on-disk test rigs at low sliding speeds, see e.g. Ref. [47], the shutdown torque appears at much higher sliding speeds. For the lightly preloaded bearing, the shutdown torque occurs at rotor speeds between 3242 rpm and 6021 rpm. This corresponds to surface speeds of 5.1 m/s to 9.5 m/s. In case of the heavily preloaded bearing, the shutdown torque appears at sliding speeds between 3.7 m/s and 7 m/s.

These values correspond quite well with the speed at which the maximum coefficient of friction occurs in a PTFE/PTFE surface pairing, see Fig. 13. Fig. 13 is taken from Ref. [48] and shows the friction coefficient μ_{PTFE} of PTFE sliding against PTFE over the sliding speed v_s for an ambient temperature of 22 °C. For sliding speeds below 10 m/s, the presented coefficient of friction was measured in a pin-on-disk test rig by Ref. [48]. For higher sliding speeds, the coefficient of friction was obtained in a bouncing ball experiment by Bowden and Persson [49]. As can be seen from the figure, the friction coefficient at low speeds agrees well with the values often reported in literature for PTFE, see e.g. Ref. [47]. The coefficient of friction increases with the sliding speed first until a maximum is reached at a sliding speed of about 300 – 400 cm/s. For larger speeds, the friction coefficient steadily decreases. Although a different counter surface is used in this study, the general behavior can be expected to be qualitatively the same, see e.g. Ref. [50]. The large friction coefficient obtained for the lightly and the heavily preloaded bearing compared to the smaller values often reported in literature can therefore be traced back to the increase of the friction coefficient with the sliding speed. Furthermore, the decrease in the drag torque from point 5 in Fig. 9 to rotor rest may be explained by the decreasing coefficient of friction with decreasing speed.

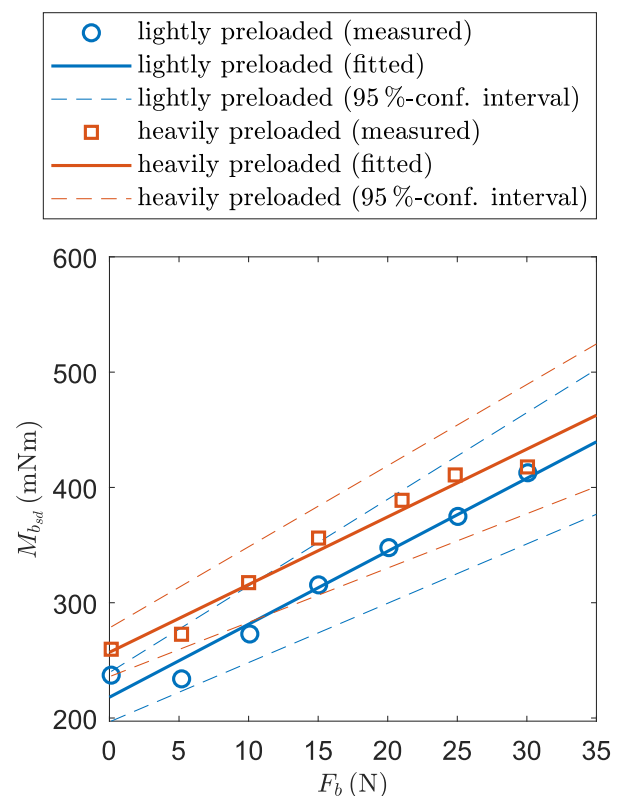


Fig. 12. Measured and fitted shutdown torque of the heavily and the lightly preloaded bearing over the bearing load.

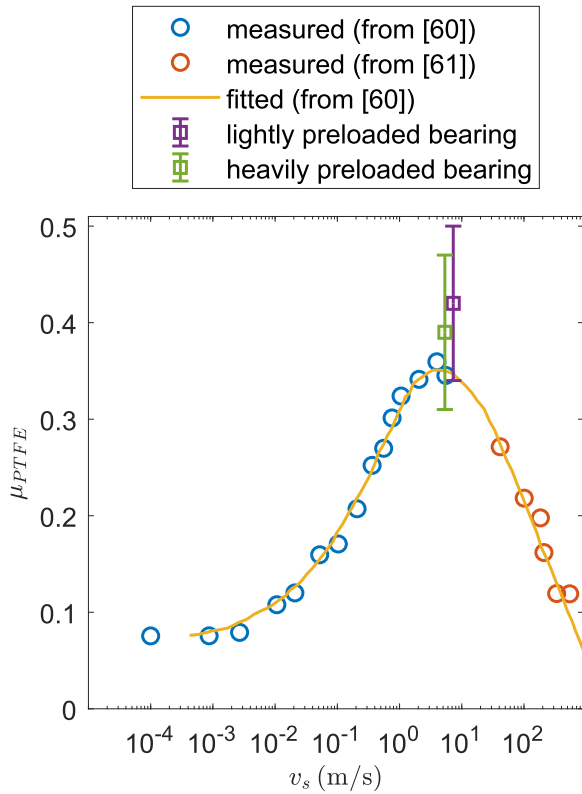


Fig. 13. Measured and fitted coefficient of friction over the sliding speed for PTFE sliding against PTFE. The points and curves are taken from Refs. [48,49].

With the coefficient of friction and the drag torque at zero bearing load, both from Fig. 12, the mechanical preload per pad can be approximated using the relationship, see Ref. [15],

$$F_p = \frac{M_b}{3r_r \mu_{tr}} \quad (3)$$

Employing this relationship, the assembly preload of the lightly and the heavily preloaded are $F_{pl} = 11.5 \text{ N}$ and $F_{ph} = 14.6 \text{ N}$. This corresponds to a rise of the assembly preload of 27 %.

5.3. Thermal behavior

For characterizing the thermal behavior of the lightly and the heavily preloaded bearing after bearing lift-off, the steady state temperatures of the bearing and the rotor are analyzed for different bearing loads. Fig. 14 presents the measured temperature increase for the lightly (a) and the heavily (b) preloaded bearing over the bearing load. As can be seen from the figure, the temperatures of all bearing components and of the rotor increase moderately with the bearing load.

More importantly, the figure shows that the bearing and rotor temperature do not rise with assembly preload. In contrast, the temperature of the lightly preloaded bearing is even slightly larger than the temperature of the heavily preloaded bearing, especially for higher bearing loads. It can be concluded that while the assembly preload significantly increases the shutdown torque, its influence on the drag torque during airborne operation is negligible.

When analyzing the temperature of the different components for the heavily preloaded bearing, it can be seen that the loaded top foil (top foil 1) always has the largest temperature since it is nearest to the air film in which the energy dissipation occurs. The rotor temperatures are smaller than the top foil temperatures as they could not be measured in the vicinity of the air foil bearing, see section 2. Instead, the rotor temperatures were measured in an axial distance to the air foil bearing sides. As can be seen from Fig. 14, the rotor temperature at the rotor free end and the rotor drive end differ by about 2 K, see also Fig. 4. As already explained in section 4, this difference might be traced back to a small misalignment in the rotor/air foil bearing system.

For the lightly preloaded bearing, a quite similar behavior is obtained with the difference that the first and third bump foil have nearly the same temperature for all tested bearing loads.

At zero bearing load, the bump foil temperatures are nearly the same. When the load is increased, the loaded bump foil shows the largest temperature. This can be explained by two effects: On the one hand, the power loss in the loaded pad is higher than the power loss in the two neighboring pads. On the other hand, the number of bumps coming into contact with the top foil and the bearing sleeve increases with the bearing load, especially in the middle of the bump foil, where the thermocouples are fixed. Thereby, more heat is transferred through the bump foil of the first pad which increases the temperature. The temperature of the third pad is larger than the temperature of the second pad since the hot air which leaves the first pad enters the third pad, see Fig. 1.

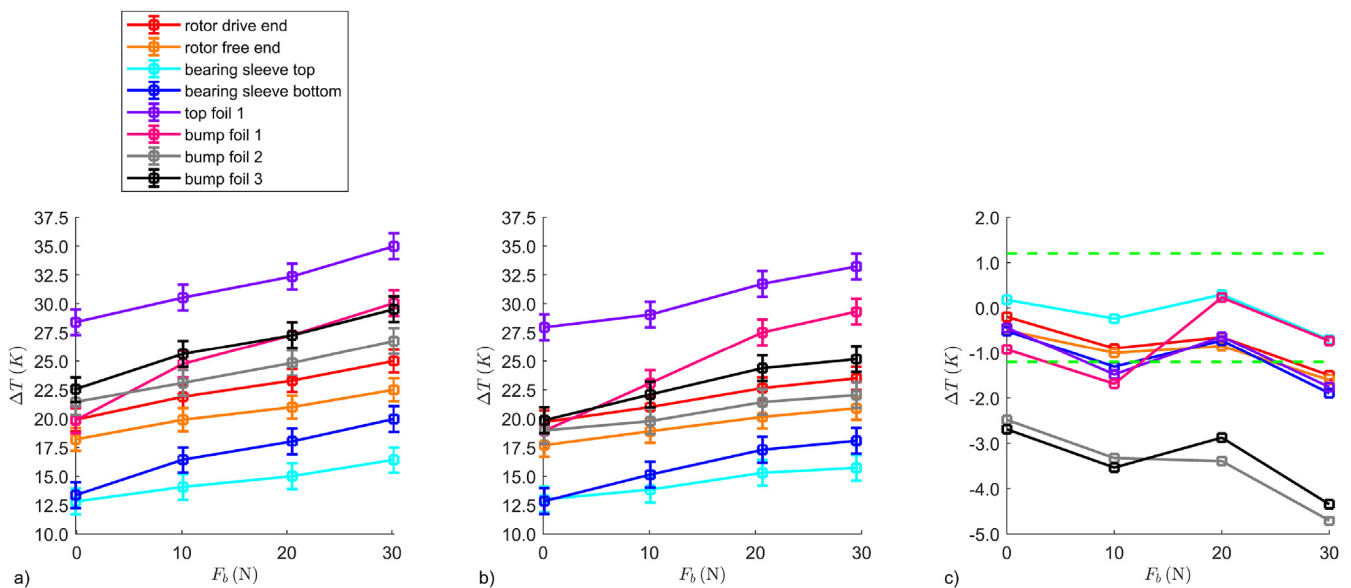


Fig. 14. Measured temperature increase for the lightly (a) and the heavily (b) preloaded bearing over the bearing load.

A similar behavior can be obtained for the bearing sleeve temperatures. At zero bearing load, the top and bottom temperature are nearly the same. As the bearing load increases, the difference between the top and bottom temperature rises. The temperature at the bearing sleeve bottom is larger than the temperature at the top since the loaded pad is at the bottom of the bearing sleeve. Again, this behavior can be explained by the larger power loss and the improved heat transfer which can be traced back to a higher number of contacting bumps in the loaded pad.

Concluding, the assembly preload has no significant influence on the thermal behavior of air foil journal bearings after bearing lift-off. Furthermore, the measured temperature distribution in the bearing can be explained by the larger power loss and the improved heat transfer in the loaded pad.

6. Conclusions

An automated high-speed test rig for air foil journal bearings has been presented. This test rig allows for the measurement of the bearing load, the drag torque, the vertical and horizontal displacement of the bearing sleeve and of the temperature at different locations.

In this study, the drag torque of a lightly and a heavily preloaded three-pad air foil journal bearing has been analyzed. The assembly preload is introduced by using bump and top foils whose initial undeformed radii are significantly larger than the bearing sleeve inner radius and the rotor radius. The analyzed bearings differ only in their nominal top foil radii while the nominal bump foil radii are equal.

During the test procedure, the PTFE coating on the top foils and the diamond-like carbon coating on the rotor were run in during repeated start-stop cycles at increasing bearing loads first. Afterwards, the drag torque of the two bearings was measured during one start-stop cycle. In order to quantify stiffness and damping of the investigated bearings, a static hysteresis measurement was accomplished on a second test rig which is described in detail in Refs. [19,20].

The experimental results indicate that the assembly preload significantly increase the bearing stiffness (91.1 %) and the dissipated energy during one hysteresis cycle (18.2 %) while the diametrical distance in the hysteresis curves does not change. From the drag torque measurement, characteristic points, like the startup and shutdown torque as well as the bearing lift-off and touchdown speeds, could be obtained. It has been shown, that the lift-off speed increases with bearing load. Contrary to expectations, the heavily preloaded bearing showed smaller lift-off speeds compared to the lightly preloaded bearing. This might be traced back to an improved geometrical air inlet condition at the top foil leading edge due to the larger initial top foil radius. The shutdown torque at zero bearing load increases by about 17.9 % due to the larger assembly preload. By plotting the shutdown torque over the bearing load, the coefficient of friction and the mechanical preload between the top foils and the rotor were obtained. As expected, the coefficient of friction of both bearings does not differ significantly. On the other hand, the mechanical preload increases by using top foils with a larger radius. The difference between the obtained coefficient of friction and values for the same surface pairing found in literature can be explained by a strong dependency of the coefficient of friction on the sliding speed. The temperatures of the lightly and the heavily preloaded bearing did not differ significantly. Furthermore, the larger temperature in the loaded pad could be explained by the larger power loss and the improved heat transfer due to more bumps which are in contact with the bearing sleeve and the top foil.

Summarizing, the results show that the larger top foil radius increases the bearing preload and the shutdown torque moderately while the bearing stiffness is increased significantly by the larger assembly preload. This is advantageous, since a large rise in bearing stiffness may lead to an improved dynamic behavior. The lift-off speed of the heavily preloaded bearing is even smaller than the lift-off speed of the lightly preloaded bearing. The thermal behavior of air foil journal bearings is

not affected significantly by an increase in the assembly preload.

References

- [1] Heshmat H, Shapiro W, Gray S. Development of foil journal bearings for high load capacity and high speed whirl stability. *J Lubr Technol* 1982;104(2):149–56. <https://doi.org/10.1115/1.3253173>
- [2] Kim D, Park S. Hydrostatic air foil bearings: analytical and experimental investigation. *Tribol Int* 2009;42(3):413–25. <https://doi.org/10.1016/j.triboint.2008.08.001>.
- [3] Dellacorte C, Valco MJ. Load capacity estimation of foil air journal bearings for oil-free turbomachinery applications. *Tribol Trans* 2000;43(4):795–801. <https://doi.org/10.1080/10402000008982410>.
- [4] Howard SA. Misalignment in gas foil journal bearings: an experimental study. *ASME turbo expo: power for land, sea and air*, Vol. 1, place of conference 2008. p. 741–9. <https://doi.org/10.1115/GT2008-50806>
- [5] Kim TH, San Andrés L. Effects of a mechanical preload on the dynamic force response of gas foil bearings: measurements and model predictions. *Tribol Trans* 2009;52(4):569–80. <https://doi.org/10.1080/10402000902825721>.
- [6] Lehn A. Air foil thrust bearings: a thermo-elasto-hydrodynamic analysis Phd. thesis Technical University Darmstadt; 2017.
- [7] Radil K, Howard S, Dykas B. The role of radial clearance on the performance of foil air bearings. *Tribol Trans* 2002;45(4):485–90. <https://doi.org/10.1080/10402000208982578>.
- [8] Ryu K, San Andrés L. On the failure of a gas foil bearing: high temperature operation without cooling flow. *J Eng Gas Turbines Power* 2013;135(11). <https://doi.org/10.1115/1.4025079>. 112506–1 – 112506–10.
- [9] Dellacorte C. Composition optimization of chromium carbide based solid lubricant coatings for foil gas bearings at temperatures up to 650 °C, Report Contractor Report No. 179649. NASA; 1987.
- [10] Bhushan B, Gray S. Development of surface coatings for air-lubricated, compliant journal bearings to 650 °C. *ASLE Trans* 1980;23(2):185–96. <https://doi.org/10.1080/05698198008982959>.
- [11] Wagner RC, Sliney HE. Durable solid lubricant coatings for foil gas bearings to 315 °C Report NASA Technical Memorandum 83596 NASA; 1984
- [12] DellaCorte C. The effect of counterface on the tribological performance of a high temperature solid lubricant composite from 25 °C to 650 °C. *Surf Coating Technol* 1996;86:486–92.
- [13] Dellacorte C, Fellenstein JA, Benoy PA. Evaluation of advanced solid lubricant coatings for foil air bearings operating at 25 °C and 500C. *Tribol Trans* 1999;42(2):338–42. <https://doi.org/10.1080/10402009908982226>.
- [14] Dellacorte C. The evaluation of a modified chrome oxide based high temperature solid lubricant coating for foil gas bearings. *Tribol Trans* 2000;43(2):257–62. <https://doi.org/10.1080/10402000008982337>.
- [15] Dellacorte C, Lukaszewicz V, Valco MJ, Radil KC, Heshmat H. Performance and durability of high temperature foil air bearings for oil-free turbomachinery. *Tribol Trans* 2000;43(4):774–80. <https://doi.org/10.1080/10402000008982407>.
- [16] Radil KC, Dellacorte C. The effect of journal roughness and foil coatings on the performance of heavily loaded foil air bearings, Report NASA/TM-2001-210941. NASA; 2001.
- [17] Heshmat H, Hryniewicz P, Walton Ii JF, Willis JP, Jahanmir S, DellaCorte C. Low-friction wear-resistant coatings for high-temperature foil bearings. *Tribol Int* 2005;38(11–12):1059–75. <https://doi.org/10.1016/j.triboint.2005.07.036>.
- [18] Sim K, Yong-Bok L, Ho Kim T, Lee J. Rotordynamic performance of shimmed gas foil bearings for oil-free turbochargers. *J Tribol* 2012;134(3). <https://doi.org/10.1115/1.4005892>. 031102–1 – 031102–11.
- [19] Mahner M, Li P, Lehn A, Schweizer B. Numerical and experimental investigations on preload effects in air foil journal bearings. *ASME turbo expo*, Vol. Volume 7A: structures and dynamics, place of conference 2017. <https://doi.org/10.1115/GT2017-63284>. p. V07AT34A006 <https://doi.org/10.1115/GT2017-63284>.
- [20] Mahner M, Li P, Lehn A, Schweizer B. Numerical and experimental investigations on preload effects in air foil journal bearings. *J Eng Gas Turbines Power* 2018;140(3). <https://doi.org/10.1115/1.4037965>. 032505–1–032505–9.
- [21] Laskowski J, DellaCorte C. Friction and wear characteristics of candidate foil bearing materials from 25 °C to 800 °C. Report NASA TM107082. NASA; 1996.
- [22] Dellacorte C. A new foil air bearing test rig for use to 700 °C and 70,000 rpm. *Tribol Trans* 1998;41(3):335–40. <https://doi.org/10.1080/10402009808983756>.
- [23] Kim T-H, Lee Y-B, Kim C-H, Lee N-S. A study on the reliability of an air foil journal bearing for high speed turbomachinery. *KSPM J Fluid Mach* 2003;6(2):7–14. <https://doi.org/10.5293/KFMA.2003.6.2.007>.
- [24] Bruckner RJ, Puleo BJ. Compliant foil journal bearing performance at alternate pressures and temperatures. *ASME turbo expo: power for land, sea and air*, vol. 1. 2008. p. 587–94. <https://doi.org/10.1115/GT2008-50174>
- [25] Conlon M, Dadouche A, Dmochowski W, Payette R, Bédard J-P, Likó B. Experimental evaluation of foil bearing performance: steady-state and dynamic results. *ASME turbo expo 2009: power for land, sea, and air*. American Society of Mechanical Engineers; 2009. p. 981–92.
- [26] Kim D, Zimbru G. Start-stop characteristics and thermal behavior of a large hybrid airfoil bearing for aero-propulsion applications. *J Eng Gas Turbines Power* 2012;134(3). <https://doi.org/10.1115/1.4004487>. 032502–1 – 032502–9.
- [27] Radil KC, Dellacorte C. Foil bearing starting considerations and requirements for rotorcraft engine applications, Report ARL-TR-4873. Army Research Laboratory; 2009.
- [28] Chirathadam TA. Measurements of drag torque and lift off speed and identification

- of stiffness and damping in a metal mesh foil bearing, Master thesis. Texas A & M University; 2010.
- [29] Rudloff L, Arghir M, Bonneau O, Matta P. Experimental analyses of a first generation foil bearing: startup torque and dynamic coefficients. *J Eng Gas Turbines Power* 2011;133(9). <https://doi.org/10.1115/1.4002909>. 092501–1 – 092501–9.
- [30] Howard SA. A new high-speed oil-free turbine engine rotordynamic simulator test rig NASA; 2007. Report NASA/TM2007-214489.
- [31] Lai T, Chen S, Ma B, Zheng Y, Hou Y. Effects of bearing clearance and supporting stiffness on performances of rotor-bearing system with multi-decked protuberant gas foil journal bearing. *Proc IME J J Eng Tribol* 2014;228(7):780–8. <https://doi.org/10.1177/1350650114531406>.
- [32] Salehi M, Swanson E, Heshmat H. Thermal features of compliant foil bearings theory and experiments. *J Tribol* 2001;123(3):566. <https://doi.org/10.1115/1.1308038>.
- [33] Radil K, Zeszotek M. An experimental investigation into the temperature profile of a compliant foil air bearing. *Tribol Trans* 2004;47(4):470–9. <https://doi.org/10.1080/05698190490501995>.
- [34] San Andrés L, Chirathadam TA, Ryu K, Kim TH. Measurements of drag torque, lift-off journal speed, and temperature in a metal mesh foil bearing. *J Eng Gas Turbines Power* 2010;132(11). <https://doi.org/10.1115/1.4000863>. 112503–1 – 112503–7.
- [35] Kim TH, Song JW, Lee Y-B, Sim K. Thermal performance measurement of a bump type gas foil bearing floating on a hollow shaft for increasing rotating speed and static load. *J Eng Gas Turbines Power* 2012;134(2):024501. <https://doi.org/10.1115/1.4004401>.
- [36] Shrestha SK, Kim D, Cheol Kim Y. Experimental feasibility study of radial injection cooling of three-pad air foil bearings. *J Tribol* 2013;135(4):041703. <https://doi.org/10.1115/1.4024547>.
- [37] Dellacorte C, Radil KC, Bruckner R, Howard SA. A preliminary foil gas bearing performance map, Report NASA/TM2006-214343. NASA; 2006.
- [38] Radil KC, Dellacorte C. A three-dimensional foil bearing performance map applied to oil-free turbomachinery. *Tribol Trans* 2010;53(5):771–8. <https://doi.org/10.1080/10402001003797942>.
- [39] Conlon M, Dadouche A, Dmochowski W, Payette R, Bédard J-P. A comparison of the steady-state and dynamic performance of first-and second-generation foil bearings. *ASME turbo expo 2010: power for land, sea, and air*. American Society of Mechanical Engineers; 2010. p. 453–62.
- [40] San Andrés L, Abraham Chirathadam T. A metal mesh foil bearing and a bump-type foil bearing: comparison of performance for two similar size gas bearings. *J Eng Gas Turbines Power* 2012;134(10). <https://doi.org/10.1115/1.4007061>. 102501–1 – 102501–13.
- [41] San Andrés L, Abraham Chirathadam T. Performance characteristics of metal mesh foil bearings: predictions versus measurements. *J Eng Gas Turbines Power* 2013;135(12). <https://doi.org/10.1115/1.4025146>. 122503–1 – 122503–8.
- [42] San Andrés L, Kim TH. Forced nonlinear response of gas foil bearing supported rotors. *Tribol Int* 2008;41(8):704–15. <https://doi.org/10.1016/j.triboint.2007.12.009>.
- [43] San Andrés L, Kim TH. Improvements to the analysis of gas foil bearings: integration of top foil 1d and 2d structural models. *ASME turbo expo 2007: power for land, sea, and air*. American Society of Mechanical Engineers; 2007. p. 779–89.
- [44] San Andrés L, Norsworthy J. Measurement of drag torque, lift off speed and rotordynamic force coefficients in a shimmed BFB. *Proceedings of the 9th IFTOMM international conference on rotor dynamics*. Springer International Publishing; 2015. p. 909–19.
- [45] Ryu K, San Andrés L. Effect of cooling flow on the operation of a hot rotor-gas foil bearing system. *J Eng Gas Turbines Power* 2012;134(10):102511. <https://doi.org/10.1115/1.4007067>.
- [46] DellaCorte C, Radil KC, Bruckner RJ, Howard SA. Design, fabrication, and performance of open source generation I and II compliant hydrodynamic gas foil bearings. *Tribol Trans* 2008;51(3):254–64. <https://doi.org/10.1080/10402000701772579>.
- [47] Yang EL, Anttila A, Toivanen RO, Hirvonen JP. Friction and wear of polytetrafluoroethylene on diamond-like carbon film. *Thin Solid Films* 1991;196(1):L25–9. URL [https://doi.org/10.1016/0040-6090\(91\)90190-9](https://doi.org/10.1016/0040-6090(91)90190-9)<http://www.sciencedirect.com/science/article/pii/0040609091901909>.
- [48] McLaren KG, Tabor D. Visco-elastic properties and the friction of solids: friction of polymers : influence of speed and temperature. *Nature* 1963;197:856–8. <https://doi.org/10.1038/197856a0>. URL <https://doi.org/10.1038/197856a0>.
- [49] Bowden FP, S FR, Persson PA. Deformation, heating and melting of solids in high-speed friction. *Proc Roy Soc Lond Math Phys Sci* 1961;260(1303):433–58. <https://doi.org/10.1098/rspa.1961.0044><http://rspa.royalsocietypublishing.org/content/royprsa/260/1303/433.full.pdf>.
- [50] Uchiyama Y, Tanaka K. Wear laws for polytetrafluoroethylene. *Wear* 1980;58(2):223–35 [https://doi.org/10.1016/0043-1648\(80\)90152-0](https://doi.org/10.1016/0043-1648(80)90152-0)<http://www.sciencedirect.com/science/article/pii/0043164880901520>.